

1-1-2006

## Delineating anomalous layers in soil profiles using seismic surface wave methods

Xiaohui Jin

*University of Nevada, Las Vegas*

Follow this and additional works at: <https://digitalscholarship.unlv.edu/rtds>

---

### Repository Citation

Jin, Xiaohui, "Delineating anomalous layers in soil profiles using seismic surface wave methods" (2006). *UNLV Retrospective Theses & Dissertations*. 2703.  
<http://dx.doi.org/10.25669/9pbl-5yj4>

This Dissertation is protected by copyright and/or related rights. It has been brought to you by Digital Scholarship@UNLV with permission from the rights-holder(s). You are free to use this Dissertation in any way that is permitted by the copyright and related rights legislation that applies to your use. For other uses you need to obtain permission from the rights-holder(s) directly, unless additional rights are indicated by a Creative Commons license in the record and/or on the work itself.

This Dissertation has been accepted for inclusion in UNLV Retrospective Theses & Dissertations by an authorized administrator of Digital Scholarship@UNLV. For more information, please contact [digitalscholarship@unlv.edu](mailto:digitalscholarship@unlv.edu).

DELINEATING ANOMALOUS LAYERS IN SOIL PROFILES  
USING SEISMIC SURFACE WAVE METHODS

by

Xiaohui Jin

Bachelor of Engineering  
Tian Jin University, China  
1997

Master of Engineering  
Tian Jin University, China  
2002

A dissertation submitted in partial fulfillment  
of the requirements for the

**Doctor of Philosophy Degree in Civil and Environmental Engineering**  
**Department of Civil and Environmental Engineering**  
**Howard R. Hughes College of Engineering**

**Graduate College**  
**University of Nevada, Las Vegas**  
**December 2006**

UMI Number: 3256290

Copyright 2007 by  
Jin, Xiaohui

All rights reserved.

#### INFORMATION TO USERS

The quality of this reproduction is dependent upon the quality of the copy submitted. Broken or indistinct print, colored or poor quality illustrations and photographs, print bleed-through, substandard margins, and improper alignment can adversely affect reproduction.

In the unlikely event that the author did not send a complete manuscript and there are missing pages, these will be noted. Also, if unauthorized copyright material had to be removed, a note will indicate the deletion.

**UMI**<sup>®</sup>

---

UMI Microform 3256290

Copyright 2007 by ProQuest Information and Learning Company.

All rights reserved. This microform edition is protected against  
unauthorized copying under Title 17, United States Code.

ProQuest Information and Learning Company  
300 North Zeeb Road  
P.O. Box 1346  
Ann Arbor, MI 48106-1346



**Dissertation Approval**  
The Graduate College  
University of Nevada, Las Vegas

December 01, 2006

The Dissertation prepared by

Xiaohui Jin

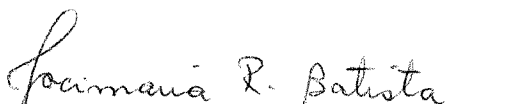
Entitled

DELINEATING ANOMALOUS LAYERS IN SOIL PROFILES USING  
SEISMIC SURFACE WAVE METHODS

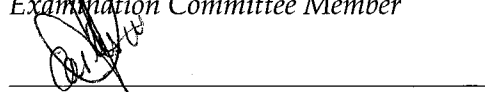
is approved in partial fulfillment of the requirements for the degree of


Doctor of Philosophy Degree in Civil and Environmental Engineering

  
Examination Committee Chair

  
Examination Committee Member

  
Examination Committee Member

  
Examination Committee Member

  
Graduate College Faculty Representative

  
Dean of the Graduate College

## ABSTRACT

### **Delineating Anomalous Layers in Soil Profiles Using Seismic Surface Wave Methods**

by

Xiaohui Jin

Dr. Barbara Luke, Examination Committee Chair  
Associate Professor of Civil Engineering  
University of Nevada, Las Vegas

Soil profiles with an included carbonate-cemented layer, a high velocity layer (HVL), are commonly encountered in Las Vegas, Nevada and other arid settings. Knowledge of the presence, geometry and hardness of the carbonate-cemented inclusions is important for civil engineering site investigation. Active-source seismic surface wave methods were tested to detect this HVL. An optimization method consisting of simulated annealing followed by linearized inversion was applied to the data.

The purpose of this study was to improve the ability to detect and delineate the HVL using surface wave methods. Two approaches are followed. One is inversion of the effective dispersion curve with the cylindrical wave forward model (EDC/CM). This corresponds to two-channel data acquisition followed by the phase spectral method for

dispersion curve (DC) extraction. The other is simultaneous inversion of the first two modes of the DC with plane wave forward model (MDC/PM). This corresponds to multi-channel data acquisition followed by the frequency-slowness method for DC extraction. The applicability of the two approaches was tested with a normally dispersive (ND) profile and a HVL profile, which were solutions from forward models. Then it was tested through finite-difference (FD) simulation. Lastly, the approaches were applied to experimental datasets collected at a site known to have a carbonate-cemented layer.

Both approaches achieved limited success. In the synthetic study, they were able to provide close-to-target results. The MDC/PM analysis showed significant improvement with respect to inversion of the fundamental mode alone. The FD simulation demonstrated that (1) for the MDC approach, accurate interpretation of the DC can be challenging for HVL systems; and (2) for the EDC approach, the EDC/CM analysis failed to resolve an HVL when a similar analysis using a plane wave forward model was successful. For the experimental study, the best results in both cases came from the less complex approach: modeling the fundamental-mode alone for the multi-channel measurement and modeling plane-wave propagation for the two-channel measurement. The simpler approaches succeed because the shape of the fundamental-mode DC carries the characteristics of the HVL.

## LIST OF ACRONYMS, SYMBOLS AND ABBREVIATIONS

CM	Covariance matrix
DC	Dispersion curve
DD	Data difference
DP	Depth of HVL increased 10% with respect to the reference profile
EDC/CM	Inversion of effective dispersion curve with cylindrical wave forward model
EDC/CM/NPI	Inversion of effective dispersion curve with cylindrical wave forward model with prior information
EDC/CM/BL	Inversion of effective dispersion curve with cylindrical wave forward model with prior information from borehole log
EDC/CM/R	Inversion of effective dispersion curve with cylindrical wave forward model with prior information from refraction
EDC/PF	Inversion of effective dispersion curve with fundamental mode of plane wave forward model
EDC/PF/NPI	Inversion of effective dispersion curve with fundamental mode of plane wave forward model with prior information
EDC/PF/BL	Inversion of effective dispersion curve with fundamental mode of plane wave forward model with prior information from borehole log

EDC/PF/R	Inversion of effective dispersion curve with fundamental mode of plane wave forward model with prior information from refraction
EGTS	Engineering Geophysics Test Site
EM	Equivalent mean profile
FD	Finite difference
HP	Thickness of HVL increased 10% with respect to the reference profile
HVL	High velocity layer
LI	Linearized inversion
LVL	Low velocity layer
MDC/PF	Inversion of multi-mode dispersion curve with fundamental mode of plane wave forward model
MDC/PF/NPI	Inversion of multi-mode dispersion curve with fundamental mode of plane wave forward model without prior information
MDC/PF/BL	Inversion of multi-mode dispersion curve with fundamental mode of plane wave forward model with prior information from borehole log
MDC/PF/R	Inversion of multi-mode dispersion curve with fundamental mode of plane wave forward model with prior information from refraction
MDC/PM	Inversion of multi-mode dispersion curve with the first two modes of plane wave forward model
MDC/PM/NPI	Inversion of multi-mode dispersion curve with the first two modes of plane wave forward model without prior information
MDC/PM/BL	Inversion of multi-mode dispersion curve with the first two modes of plane wave forward model with prior information from borehole log



MDC/PM/R	Inversion of multi-mode dispersion curve with the first two modes of plane wave forward model with prior information from refraction
ND	Normally dispersive
PD	Profile difference
RM	Resolution matrix
RP	Reference profile
SA	Simulated annealing
SR	Search range
VP	Velocity of HVL increased 10% with respect to the reference profile
$V_P$	Compressional wave velocity
$V_S$	Shear wave velocity
$V_{S30}$	Slowness-averaged shear wave velocity in the top 30 m or 100 ft
$V_R$	Rayleigh wave velocity

## TABLE OF CONTENTS

ABSTRACT .....	iii
LIST OF ACRONYMS, SYMBOLS AND ABBREVIATIONS .....	v
LIST OF TABLES .....	xi
LIST OF FIGURES .....	xii
ACKNOWLEDGMENTS .....	xviii
 CHAPTER 1 INTRODUCTION .....	 1
1.1 Problem Statement and Motivation .....	1
1.2 Objectives .....	4
1.3 Dissertation Outline .....	4
 CHAPTER 2 STATE OF KNOWLEDGE AND METHODOLOGY .....	 7
2.1 Data Collection .....	7
2.1.1 Active-Source Methods .....	8
2.1.2 Passive-Source Methods .....	11
2.1.3 Combined Active-Source and Passive-Source Methods.....	13
2.2 Dispersion Relation Generation.....	15
2.2.1 Active-Source Methods .....	15
2.2.2 Passive-Source Methods .....	25
2.3 Inversion and Interpretation.....	29
2.3.1 Forward Modeling Methods .....	29
2.3.2 Optimization Methods .....	34
2.4 Detection of Anomalous Layers with Surface Wave Methods.....	38
2.5 Methodology of this Study .....	42
 CHAPTER 3 IMPLEMENTATION OF THE TWO APPROACHES .....	 45
3.1 Introduction.....	45
3.2 Model and Parameter Description .....	45
3.3 Theoretical Dispersion Curves Generation.....	48
3.4 Starting Model Generation.....	48
3.5 Inversion .....	51
3.6 Interpretation of Results.....	54
3.6.1 Results for the ND Profile.....	55
3.6.2 Results for the HVL Profile .....	57
3.6.3 Results for the ND Profile with Incorrect HVL Expectation.....	59

3.7 Discussion.....	60
CHAPTER 4 PRACTICAL STUDIES ON DELINEATING THE HVL SYSTEM ...	83
4.1 Introduction.....	83
4.2 Effect of HVL in Soil Profiles on DCs .....	83
4.3 Inversion with Prior Information from Refraction Measurement.....	86
CHAPTER 5 FINITE-DIFFERENCE SIMULATION OF MULTI-CHANNEL <i>f-p</i> METHOD .....	101
5.1 Introduction.....	101
5.2 E3D Model and Parameter Description .....	102
5.3 Multi-Channel <i>f-p</i> Method Simulation .....	103
5.4 Effects of Some Factors on <i>f-p</i> Image .....	104
5.4.1 Real Source Effect .....	104
5.4.2 Effect of Numbers and Spacing of Receivers .....	105
5.5 Dispersion Curve Picking .....	106
5.6 Inversion and Interpretation.....	108
5.6.1 Results for the ND Profile .....	108
5.6.2 Results for the HVL Profile .....	108
5.7 Discussion.....	110
CHAPTER 6 FINITE-DIFFERENCE SIMULATION OF TWO-CHANNEL PHASE SPECTRAL METHOD .....	128
6.1 Introduction.....	128
6.2 E3D Model and Parameter Description .....	128
6.3 Two-Channel Phase Spectral Method Simulation.....	130
6.4 Inversion and Interpretation.....	131
6.4.1 Results for the ND Profile.....	131
6.4.2 Results for the HVL Profile .....	132
CHAPTER 7 EXPERIMENTAL STUDY .....	147
7.1 Introduction.....	147
7.2 Study Site.....	148
7.3 Seismic Downhole Measurement .....	149
7.3.1 Data Acquisition .....	149
7.3.2 Data Analysis .....	150
7.4 P-wave Refraction measurement .....	153
7.5 SASW Measurement.....	154
7.5.1 Data Acquisition .....	154
7.5.2 Inversion .....	154
7.6 MASW Measurements.....	158
7.6.1 Data Acquisition .....	158
7.6.2 Data Processing and DC Generation.....	159
7.6.3 Inversion .....	161
7.7 Comparison.....	163
7.8 Discussion.....	164

CHAPTER 8 SYNTHESIS, CONCLUSIONS AND RECOMMENDATIONS .....	198
8.1 Synthesis .....	198
8.1.1 Dispersion Curve .....	198
8.1.2 Inversion .....	199
8.1.3 Evaluating Quality of the Results .....	203
8.2 Conclusions.....	204
8.2 Future Research Recommendations.....	205
APPENDIX A INSTRUCTION MANUAL FOR STARTING MODEL GENERATION, SA AND SA-LI INVERSION ANALYSES .....	207
APPENDIX B DEVELOPMENT OF DISPERSION CURVE FOR THE ND AND HVL PROFILES .....	211
APPENDIX C DOWNHOLE MEASUREMENT TIME HISTORIES WITH PICKS .....	220
APPENDIX D P-WAVE REFRACTION DATA WITH PICKS .....	226
REFERENCES .....	228
VITA .....	248

## LIST OF TABLES

Table 3.1 Layer properties of the ND profile. Water table assumed to be at 2 m depth .....	62
Table 3.2 Layer properties of the HVL profile. Water table assumed to be at 3.5 m depth .....	62
Table 3.3 Summary of the results for the ND profile .....	63
Table 3.4 Summary of the results for the HVL profile.....	63
Table 3.5 Summary of the results for the ND profile with incorrect HVL expectation ...	64
Table 4.1 Layer properties of four target profiles.....	90
Table 4.2 Summary of the results for study incorporating refraction data .....	90
Table 5.1 Parameters of seven different array setups .....	112
Table 5.2 Summary of the results for the ND profile with DCs from FD simulation of multi-channel <i>f-p</i> method .....	112
Table 5.3 Summary of the results for the HVL profile with DCs from FD simulation of multi-channel <i>f-p</i> method .....	113
Table 6.1 Layer properties of the ND profile for the 3-D model.....	135
Table 6.2 Layer properties of the HVL profile for the 3-D model .....	135
Table 6.3 Spacings and corresponding central frequencies of Ricker wavelet for the ND and HVL profiles.....	136
Table 6.4 Summary of the results for the ND profiles with DC from FD simulation of two-channel phase spectral method.....	136
Table 6.5 Summary of the results for the HVL profiles with DC from FD simulation of two-channel phase spectral method.....	137
Table 7.1 Summary of the prior information settings from borehole log and refraction data.....	167
Table 7.2 Summary of $V_{S30}$ from downhole, SASW and MASW measurements .....	167

## LIST OF FIGURES

Figure 1.1 Example of a sample $V_S$ profile with a carbonate-cemented layer .....	6
Figure 2.1 Basic configuration for SASW testing .....	44
Figure 2.2 Basic configuration for MASW testing.....	44
Figure 3.1 ND profile: (a) DCs; (b) velocity ratio between EDC and fundamental mode DC .....	65
Figure 3.2 HVL profile: (a) DCs; (b) velocity ratio between EDC and fundamental mode DC .....	65
Figure 3.3 ND profile: starting model for the EDC approach .....	66
Figure 3.4 ND profile: starting model for the MDC approach .....	66
Figure 3.5 HVL profile: starting model for the EDC approach.....	67
Figure 3.6 HVL profile: starting model for the MDC approach.....	67
Figure 3.7 ND profile: comparison of (a) DD values, (b) PD values .....	68
Figure 3.8 ND profile, EDC/CM: comparison of DCs.....	68
Figure 3.9 ND profile, EDC/CM: $V_S$ profiles for (a) three runs (b) average .....	69
Figure 3.10 ND profile, EDC/CM: RMs and CMs.....	69
Figure 3.11 ND profile: comparison of DCs for (a) MDC/PF, (b) MDC/PM.....	70
Figure 3.12 ND profile: $V_S$ profiles from three runs (a) MDC/PF, (b) MDC/PM.....	70
Figure 3.13 ND profile: average $V_S$ profiles from MDC approach.....	71
Figure 3.14 ND profile: RMs and CMs from (a) MDC/PF, (b) MDC/PM.....	72
Figure 3.15 HVL profile: comparison of (a) DD values, (b) PD values.....	73
Figure 3.16 HVL profile, EDC/CM: comparison of DCs.....	73
Figure 3.17 HVL profile, EDC/CM: $V_S$ profile from (a) three runs (b) average .....	74
Figure 3.18 HVL profile, EDC/CM: RMs and CMs .....	74
Figure 3.19 HVL profile: comparison of DCs for (a) MDC/PF, (b) MDC/PM.....	75
Figure 3.20 HVL profile: $V_S$ profile from three runs for (a) MDC/PF, (b) MDC/PM.....	75
Figure 3.21 HVL profile: average $V_S$ profile (a) MDC/PF, (b) MDC/PM .....	76
Figure 3.22 HVL profile: RMs and CMs from (a) MDC/PF, (b) MDC/PM .....	77
Figure 3.23 ND profile with incorrect HVL expectation: comparison of (a) DD values, (b) PD values.....	78
Figure 3.24 ND profile with incorrect HVL expectation, EDC/CM: comparison of DCs .....	78
Figure 3.25 ND profile with incorrect HVL expectation, EDC/CM: $V_S$ profiles for (a) three runs (b) average .....	79
Figure 3.26 ND profile with incorrect HVL expectation, EDC/CM: RMs and CMs.....	79
Figure 3.27 ND profile with incorrect HVL expectation: comparison of DCs for (a) MDC/PF, (b) MDC/PM .....	80
Figure 3.28 ND profile with incorrect HVL expectation: $V_S$ profiles for three runs from (a) MDC/PF, (b) MDC/PM .....	80

Figure 3.29 ND profile with incorrect HVL expectation: average profiles from (a) MDC/PF, (b) MDC/PM.....	81
Figure 3.30 ND profile with incorrect HVL expectation: RMs and CMs for (a) MDC/PF, (b) MDC/PM.....	82
Figure 4.1 Four target profiles .....	91
Figure 4.2 Dispersion curves of the RP in terms of a) frequency, b) wavelength .....	91
Figure 4.3 Sensitivity of wave velocity to perturbations of depth (top), thickness (middle) and velocity (bottom) in the HVL .....	92
Figure 4.4 Maximum values of sensitivity for EDC, fundamental and first higher mode to perturbations in HVL.....	93
Figure 4.5 Incorporating refraction data, starting model for EDC approach: comparison of (a) DCs and (b) $V_S$ profiles .....	94
Figure 4.6 Incorporating refraction data, starting model for MDC approach: comparison of (a) DCs and (b) $V_S$ profiles .....	95
Figure 4.7 Incorporating refraction data: comparison of (a) DD values, (b) PD values...	96
Figure 4.8 Incorporating refraction data, EDC/CM: comparison of DCs.....	96
Figure 4.9 Incorporating refraction data, EDC/CM: $V_S$ profile from (a) three runs (b) average (black dashed line is the SR for the HVL) .....	97
Figure 4.10 Incorporating refraction data, EDC/CM: RMs and CMs .....	97
Figure 4.11 Incorporating refraction data: comparison of DCs for (a) MDC/PF and (b) MDC/PM.....	98
Figure 4.12 Incorporating refraction data: $V_S$ profile from three runs for (a) MDC/PF (b) MDC/PM .....	98
Figure 4.13 Incorporating refraction data: average $V_S$ profile (a) MDC/PF (b) MDC/PM .....	99
Figure 4.14 Incorporating refraction data: RMs and CMs from (a) MDC/PF (b) MDC/PM .....	100
Figure 5.1 Ricker wavelet source with 100 & 25 Hz central frequencies: (a) time- and (b) frequency- domain representations .....	113
Figure 5.2 Synthetic time histories for 81 receivers, 0.5 m spacing with superposed 25 & 100 Hz Ricker wavelet sources for (a) ND and (b) HVL profiles.....	114
Figure 5.3 Time-offset, $p-t$ and $f-p$ images of the (a) ND and (b) HVL profiles.....	115
Figure 5.4 Real source time and frequency domain .....	116
Figure 5.5 Source effect: (a) superposed 25 & 100 Hz Ricker wavelet sources (b) real source, on the $f-p$ images for the ND (top) and HVL profiles (bottom) .....	117
Figure 5.6 Effects of numbers of receivers and spacing of receivers on $f-p$ images .....	118
Figure 5.7 ND profile: (a) $f-p$ image alone, (b) superposed with picks of the first two modes and (c) superposed with the solution from plane wave forward model (black: fundamental mode; red: first higher mode) .....	119
Figure 5.8 HVL profile: (a) $f-p$ image alone, (b) superposed with picks of the first two modes and (c) superposed with the solution from plane wave forward model (black: fundamental mode; red: first higher mode) .....	119

Figure 5.9 FD study, ND profile: comparison of DCs from picked modes, cubic spline fit of picked modes and solution from plane wave forward model .....	120
Figure 5.10 FD study, HVL profile: comparison of DCs from picked modes, cubic spline fit of picked modes and solution from plane wave forward model .....	120
Figure 5.11 FD study, ND profile, MDC approach: comparison of (a) DD values, (b) PD values .....	121
Figure 5.12 FD study, ND profile, MDC approach: comparison of DCs for (a) MDC/PF, (b) MDC/PM .....	121
Figure 5.13 FD study, ND profile, MDC approach: $V_S$ profiles from three runs for (a) MDC/PF, (b) MDC/PM .....	122
Figure 5.14 FD study, ND profile, MDC approach: average $V_S$ profiles .....	122
Figure 5.15 FD study, ND profile, MDC approach: RMs and CMs from (a) MDC/PF, (b) MDC/PM .....	123
Figure 5.16 FD study, HVL profile, MDC approach: comparison of (a) DD values, (b) PD values .....	124
Figure 5.17 FD study, HVL profile, MDC approach: comparison of DCs from (a) MDC/PF, (b) MDC/PM .....	124
Figure 5.18 FD study, HVL profile, MDC approach: $V_S$ profiles from three runs MDC/PF, (b) MDC/PM .....	125
Figure 5.19 FD study, HVL profile, MDC approach: average profiles from (a) MDC/PF, (b) MDC/PM .....	125
Figure 5.20 FD study, HVL profile, MDC approach: RMs and CMs from MDC/PF, (b) MDC/PM .....	126
Figure 5.21 Comparison of $V_S$ profiles from two averaging methods .....	127
Figure 5.22 Comparison of DCs from two averaging methods .....	127
Figure 6.1 ND profile: Phase of the cross power spectrum of each spacing (2, 4, 8 and 16 m from top to bottom) .....	137
Figure 6.2 ND profile: Composite DC .....	138
Figure 6.3 ND profile: comparison of DCs from 3-D simulation .....	138
Figure 6.4 HVL profile: phase of the cross power spectrum of each spacing (2, 4, 8 and 16 m from top to bottom) .....	139
Figure 6.5 HVL profile: composite DC .....	139
Figure 6.6 HVL profile: comparison of DCs from 3-D simulation .....	140
Figure 6.7 FD study, ND profile, EDC/CM: comparison of (a) DD values, (b) PD values .....	140
Figure 6.8 FD study, ND profile, EDC/CM: comparison of DCs .....	141
Figure 6.9 FD study, ND profile, EDC/CM: $V_S$ profile from (a) three runs (b) average .....	141
Figure 6.10 FD study, ND profile, EDC/CM: RMs and CMs .....	142
Figure 6.11 FD study, HVL profile, EDC: Comparison of (a) DD values, (b) PD values .....	142
Figure 6.12 FD study, HVL profile, EDC/CM: comparison of DCs .....	143
Figure 6.13 FD study, HVL profile, EDC/CM: $V_S$ profile from (a) three runs (b) average .....	143



Figure 6.14 FD study, HVL profile, EDC/CM: RMs and CMs.....	144
Figure 6.15 FD study, HVL profile, EDC/PF: comparison of DCs.....	144
Figure 6.16 FD study, HVL profile, EDC/PF: $V_S$ profile from (a) three runs (b) average .....	145
Figure 6.17 FD study, HVL profile, EDC/PF: RMs and CMs .....	145
Figure 6.18 Comparison of four DCs .....	146
Figure 7.1 (a) Engineering Geophysics Test Site (EGTS) as located on the UNLV campus ( <a href="http://www.unlv.edu/campus_map">http://www.unlv.edu/campus_map</a> ) (b) EGTS map ( <a href="http://www.ce.unlv.edu/egl">http://www.ce.unlv.edu/egl</a> ) .....	168
Figure 7.2 Aerial view of the EGTS showing the location of the measurements.....	169
Figure 7.3 Donwhole measurements.....	170
Figure 7.4 Orientation of the three-component geophones in downhole measurement. (not to scale) .....	171
Figure 7.5 The $V_P$ , $V_S$ and Poisson's ratio from the direct method with respect to the borehole log.....	172
Figure 7.6 The $V_P$ , $V_S$ and Poisson's ratio from the ray path method with respect to the borehole log.....	173
Figure 7.7 Comparison of the $V_P$ , $V_S$ and Poisson's ratio from the direct method (thinner line) and ray-path method .....	174
Figure 7.8 The $V_P$ profile from refraction measurement .....	175
Figure 7.9 SASW: DCs for each receiver spacing and the composite DC .....	175
Figure 7.10 SASW: comparison of DD values from inversions.....	176
Figure 7.11 SASW, EDC/CM/NPI: comparison of DCs.....	176
Figure 7.12 SASW, EDC/CM/NPI: $V_S$ profiles for (a) three runs (b) average.....	177
Figure 7.13 SASW, EDC/CM/NPI: RMs and CMs.....	177
Figure 7.14 SASW, EDC/CM/BL: comparison of DCs .....	178
Figure 7.15 SASW, EDC/CM/BL: $V_S$ profiles for (a) three runs (b) average .....	178
Figure 7.16 SASW, EDC/CM/BL: RMs and CMs.....	179
Figure 7.17 SASW, EDC/PF/BL: comparison of DCs.....	179
Figure 7.18 SASW, EDC/PF/BL: $V_S$ profiles for (a) three runs (b) average .....	180
Figure 7.19 SASW, EDC/PF/BL: RMs and CMs.....	180
Figure 7.20 SASW, EDC/CM/R: comparison of DCs.....	181
Figure 7.21 SASW, EDC/CM/R: $V_S$ profiles for (a) three runs (b) average .....	181
Figure 7.22 SASW, EDC/CM/R: RMs and CMs .....	182
Figure 7.23 SASW, EDC/PF/R: comparison of DCs .....	182
Figure 7.24 SASW, EDC/PF/R: $V_S$ profiles for (a) three runs (b) average .....	183
Figure 7.25 SASW, EDC/PF/R: RMs and CMs.....	183
Figure 7.26 $V_S$ profiles from SASW inversion analyses with respect to the borehole log .....	184
Figure 7.27a Time history images of each single record after vibroseis correlation.....	185
Figure 7.27b Time history images of the combined record after vibroseis correlation.....	186
Figure 7.28 The $f$ - $p$ images from (a) Minivib source and (b) hammer source.....	187
Figure 7.29 (a) The combined $f$ - $p$ images alone and (b) superposed with picks for two modes .....	187
Figure 7.30 DCs from MASW measurement .....	188

Figure 7.31 MASW: comparison of DD values from inversions .....	188
Figure 7.32 MASW, MDC/PF/NPI: comparison of DCs .....	189
Figure 7.33 MASW, MDC/PF/NPI: $V_S$ profiles for (a) three runs (b) average .....	189
Figure 7.34 MASW, MDC/PF/NPI: RMs and CMs .....	190
Figure 7.35 MASW, MDC/PF/BL: comparison of DCs.....	190
Figure 7.36 MASW, MDC/PF/BL: $V_S$ profiles for (a) three runs (b) average.....	191
Figure 7.37 MASW, MDC/PF/BL: RMs and CMs .....	191
Figure 7.38 MASW, MDC/PM/BL: comparison of DCs .....	192
Figure 7.39 MASW, MDC/PM/BL: $V_S$ profiles for (a) three runs (b) average .....	192
Figure 7.40 MASW, MDC/PM/BL: RMs and CMs.....	193
Figure 7.41 MASW, MDC/PF/R: comparison of DCs .....	193
Figure 7.42 MASW, MDC/PF/R: $V_S$ profiles for (a) three runs (b) average .....	194
Figure 7.43 MASW, MDC/PF/R: RMs and CMs.....	194
Figure 7.44 MASW, MDC/PM/R: comparison of DCs.....	195
Figure 7.45 MASW, MDC/PM/R: $V_S$ profiles for (a) three runs (b) average .....	195
Figure 7.46 MASW, MDC/PM/R: RMs and CMs .....	196
Figure 7.47 $V_S$ profiles from MASW inversion analyses with respect to the borehole log .....	196
Figure 7.48 Comparison of DCs from MASW and SASW measurements .....	197
Figure 7.49 Comparison of best $V_S$ profiles from MASW and SASW measurements with respect to the borehole log .....	197

## ACKNOWLEDGMENTS

I would like to thank my advisor, Dr. Barbara Luke, for introducing me to the extremely interesting area of research and supervising me throughout the research work. I would like to express my thanks to my other committee members, Drs. Jacimaria Batista, Carlos Calderon-Macias, Catherine Snelson and Wanda Taylor. I benefited tremendously from insightful advice, wonderful teaching and kind encouragement of the entire committee.

For the first two years, this research was funded by the National Science Foundation under Grant No. CMS-9734000. For the last two years, this research was funded partly by UNLV graduate assistantship and partly by Lawrence Livermore National Laboratory (LLNL) under contract No. W-7405-ENG-48, and directly by the U. S. Department of Energy under contract No. DE-FG02-04ER63855 and DE-FG52-03NA99204.

I would like to thank the Kansas Geological Survey for the training on MASW measurement. I would like to thank Aasha Pancha and Dr. John Louie at UNR for their training on the E3D program. Also, many thanks go to Dr. Shawn Larsen at LLNL who was extremely patient in guiding me through every problem I ran into with E3D. I would like to thank Dr. David Boore at U. S. Geological Survey and Bruce Redpath for helpful discussion on downhole measurements and data processing. I would like to thank Graduate student Eric Thompson at Tufts University for an introduction to the R language and Dr. Boore's downhole code. I would like to thank Dr. Glenn Rix at Georgia

Tech for sharing the code “SWAMI”; Dr. Kenneth Stokoe at University of Texas at Austin and Dr. Jose Roësset at Texas A&M University for sharing the code “SASWFI”; and Dr. Mauricio Sacchi at University of Alberta for sharing the frequency-slowness transformation code. I would like to thank Geometrics for sharing their refraction processing software Plotrefa. Next, I would like to thank Jim O’Donnell for his discussion, kind encouragement and useful guidance in the field.

UNLV students and staff Erik Peters, Qiuhong Su, Sandra Saldaña and Helena Murvosh helped with data collection. A special word of thanks goes to Helena Murvosh for her friendship and assistance in editing this work.

Finally, I would like to extend my profound appreciation and love for my husband Jiangong Xu and our parents who are always with me.

## CHAPTER 1

### INTRODUCTION

#### 1.1 Problem Statement and Motivation

Some buried anomalous layers that might be important in civil engineering site development include coal seams containing extensive abandoned excavations, loose and saturated sand deposits which might be liquefiable, and carbonate-cemented layers. A sediment profile with carbonate-cemented layers is commonly encountered in Las Vegas, Nevada and other arid settings. The rock-hard carbonate-cemented material, which is a high velocity layer (HVL), causes a high contrast in *impedance* (the product of density and shear wave velocity ( $V_s$ ) or compression wave velocity ( $V_p$ )) with respect to uncemented soil layers. These cemented layers are well known as "caliche" among local geotechnical engineers. Solely for purposes of discussion, a sample profile with a carbonate-cemented layer is shown in Figure 1.1. In the sample, the  $V_s$  of the HVL differs from those of the layers above and underneath by factors of 10 and 5, respectively.

This carbonate-cemented material is commonly found at or near the ground surface in semi-arid and arid areas of the world (Reeves 1976). Various degrees of cementation can be found throughout the Las Vegas Valley; the most extensively cemented soils generally occur in the western and central portion of the valley (Wyman et al. 1993). The carbonate-cemented soils may be formed by the evaporation of either descending surface water or ascending ground water. Thus, the calcium carbonate

dissolved in the water is left behind in the soil. As much calcium carbonate is deposited over thousands of years, the carbonate-cemented soil is formed (Nowatzki and Almasmoum 1988).

Knowledge of the presence and hardness of carbonate-cemented inclusions is extremely important for civil engineers. A fully developed deposit of carbonate-cemented inclusions can be used as a bearing stratum for structural foundations, because it can have strength and stiffness similar to that of concrete (Stone and Luke 2001). However, it can also be an expensive nuisance for excavations, especially if it is discontinuous or if it is encountered unexpectedly. Normally, with increasing degree of hardness, the unconfined compressive strength (Gile 1961) and seismic velocity (Nowatzki and Almasmoum 1988) also increase. Nowatzki and Almasmoum (1988) used seismic compression wave velocity to define the cemented soil's excavatability.

With respect to geotechnical boring or drilling to detect the anomalies, geophysical methods present unique advantages, including the ability to cover broad volumes of soil, and the noninvasive nature of many of the tests (Stokoe and Santamarina 2000). Among the geophysical methods, various seismic methods have been used to detect anomalous layers.

The surface-based geophysical methods have several advantages over intrusive methods (cross-hole and down-hole). The most attractive feature of surface-based methods is that they are nonintrusive, hence time saving, economical and convenient. Furthermore, they might be the only possible choice for *in situ* investigations where subsurface conditions, environmental concerns or accessibility restrict the use of boreholes or trenches. The surface-based seismic methods involve sampling a much

larger volume of soil than that sampled in crosshole or downhole tests; thus properties determined represent a larger area over the site.

The surface-based seismic methods include refraction, reflection and surface wave methods. The reflection method requires many source and receiver locations to produce meaningful images. Furthermore, the data interpretation is complex. Therefore, it is labor-intensive. The refraction method has difficulty in detecting velocities of layers if the layer below has a lower velocity than the layer above or the layer is too thin (e.g., Mussett and Khan 2000).

Surface wave methods use the *dispersive* behavior of Rayleigh waves in layered media (waves of different frequency travel at different velocities) to characterize  $V_s$  profiles of the subsurface. The  $V_s$  is also an important mechanical soil property for the evaluation of dynamic soil behavior (e.g., Richart et al. 1970). It is used as a key index property to indicate stiffness of the ground in civil engineering. From a wave propagation point of view, using Rayleigh waves instead of body waves has several advantages. First, a higher percentage of the energy generated by a surface-based source travels in the form of Rayleigh waves (e.g., Richart et al. 1970). Second, the geometrical attenuation of Rayleigh waves is much lower than that of body waves.

Despite the proliferation of surface wave methods for subsurface profiling today, there are difficulties in detecting velocity reversals (where the velocity of a soil layer decreases with increasing depth), especially when the impedance contrast is high. In those cases, one or more higher Rayleigh modes instead of the fundamental mode may dominate the wave field (Gucunski and Woods 1991a; Roësset et al. 1991; Tokimatsu et al. 1992c). Also, the impedance contrasts cause scattering of seismic energy of all wave

types, which results in interference from body wave reflection, refraction and conversion (Van Wijk 2003; Xia et al. 2000, 2003). The scattering decreases the dominance of Rayleigh waves, complicates the wave train, and adds noise to the base condition. Thus, the simplest-case assumption that the fundamental Rayleigh mode is dominant and the effects of other waves and higher-mode Rayleigh waves can be neglected may not be appropriate for complex profiles.

## 1.2 Objectives

This research covers the detection of layered velocity anomalies using seismic surface wave methods, with specific focus upon carbonate-cemented horizons in arid soil profiles.

The main objectives of this research include:

- Build a reliable process to resolve a HVL system using surface wave methods. This process includes tools and algorithms.
- Evaluate the quality of the outcomes from the process.
- Study the applicability and limitations of the process.

## 1.3 Dissertation Outline

Chapter 2 consists of a comprehensive review and evaluation of current surface wave methods with emphasis on detecting anomalous layers. Based on the literature, two promising approaches to the problem are put forward. The two approaches apply to two widely used data acquisition methods correspondingly.



Chapter 3 illustrates the implementation of the two approaches using synthetic data in a so-called “synthetic” approach. Two profiles including a normally dispersive (ND) system and a HVL system are studied.

Chapter 4 focuses on the HVL system. Two cases are designed. Firstly, the capability to resolve the depth, thickness and velocity of the HVL are investigated. Secondly, the interpretations of refraction data are incorporated into the inversion of surface wave data by an enhanced starting model generation method. The effect on quality of the inversion results is investigated.

Chapters 5 and 6 use synthetic time histories created using a finite-difference (FD) code to further investigate the applicability of the two approaches. This is also a synthetic study. However, in this dissertation, it is called “FD simulation” to distinguish it from the studies in Chapter 3. In Chapter 7, experimental datasets collected at a site known to have a HVL are analyzed using the two approaches. The results are compared to the outcome from a 30 m downhole seismic measurement.

Finally, conclusions and recommendations are given in Chapter 8.

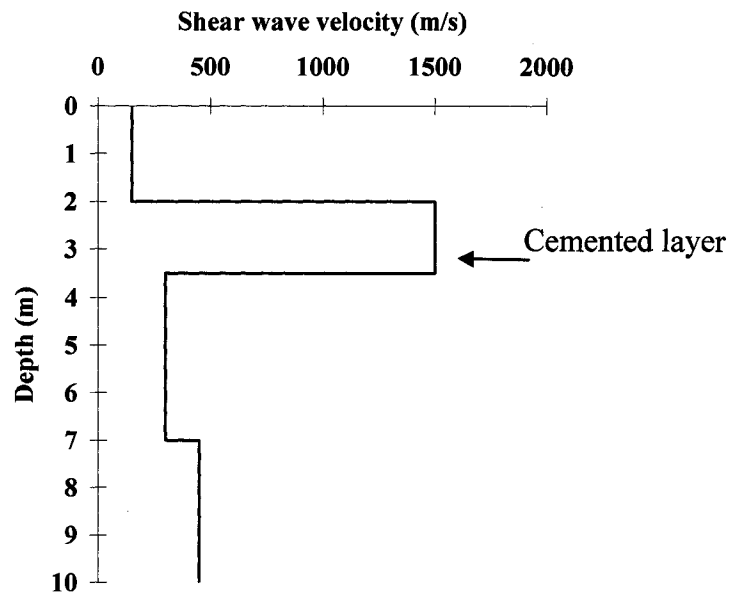


Figure 1.1. Sample  $V_s$  profile with a carbonate-cemented layer.

## CHAPTER 2

### STATE OF KNOWLEDGE AND METHODOLOGY

Surface wave methods remains a rapidly developing subject. In recent years, surface wave methods have continued to develop through the use of powerful and robust wave propagation, signal processing, and inversion techniques (e.g., O'Neill 2005). They are all based on the following three steps:

1. Data collection, in which elastic waves are generated by active or passive means, detected by one or more receivers and recorded;
2. Signal processing and construction of experimental DCs or panels (phase velocity versus wavelength or frequency); and
3. Inversion of the dispersion data to obtain the one-dimensional  $V_s$  profile or vertical slice of the site.

Those three steps are elaborated in the following discussion.

#### 2.1 Data Collection

For data collection, essentially two methods exist, active-source, which is also known as controlled-source, and passive-source. In the active-source method Rayleigh waves are captured in vertical ground vibrations induced either by an impulsive source or an exciter oscillating with a vertical harmonic motion (Stokoe et al. 1994; Tokimatsu et al. 1992b) or by a random-noise source such as the deliberate motion of heavy tracked equipment.

In the active-source methods, one, two or more sensors are placed on the ground surface in a line with the source. In the passive-source methods either vertical or three-component orthogonal motions of multiple sensors are observed, without actively generating any vibrations (e.g., Tokimatsu 1995; Louie 2001).

### 2.1.1 Active-Source Methods

The active-source methods are described below in order of number of receivers used.

#### Single sensor

A seismic technique for nondestructive testing of pavement layer moduli has been introduced by Rydén et al. (2001; 2002a; 2002b) and Park et al. (2001a; 2001b; 2002). This method, called the Multi-channel Simulation with One Receiver (MSOR) method, is based on the Multi-channel Analysis of Surface Waves (MASW) method (Park et al. 1999b; Xia et al. 1999), which is described in more detail below. The MSOR technique uses a laptop computer, one accelerometer (receiver) and a light hammer (source). With this system, a multi-channel measurement is simulated through repetitive generation of seismic energy along a survey line at different distances from the receiver, which is fixed in place on the surface. Compared with the MASW method, this method might be cost-saving, but not time-saving or effort-saving. Because the principle is the same as MASW method, the data quality should be comparable.

#### Two sensors

The Spectral Analysis of Surface Wave (SASW) method was originally introduced by Stokoe and his colleagues in the early 1980's (Stokoe et al. 1994). A typical experimental setup for SASW testing is shown in Figure 2.1. The test is performed with a single source,

paired transducers sensitive to vertical motions and a signal analyzer which can transfer the data into frequency domain in near-real time. The testing is repeated for several receiver spacings to cover a desired range of Rayleigh wave wavelengths. The testing is sometimes performed in opposite directions along the linear array to account for effects of dipping layers and any internal phase shifts due to receivers and instrumentation (Stokoe et al. 1994). Hammers, mallets, sledgehammers, dropped weights, and shakers, as well as ambient noise (e.g., traffic) and motion of tracked vehicles can be used to generate the necessary seismic energy. Typically, frequencies corresponding to wavelengths from  $1/3d$  to  $2d$ , where  $d$  is the receiver spacing, are of interest at each spacing. Multiple source activations at each spacing are performed, and the results are averaged in the frequency domain. The result of an SASW test is a single DC, which is then inverted to determine the  $V_s$  profile with depth. An extensive set of early references pertaining to the SASW method is provided in the annotated bibliography prepared by Hiltunen and Gucunski (1994).

The SASW method has been used for a number of applications including nondestructive pavement evaluation (e.g., Hossain and Drnevich 1989; Hiltunen 1991; Haegeman and Van Impe 1997; Ganji and Gucunski 1998), evaluation of soil liquefaction potential (e.g., Stokoe and Nazarian 1985), evaluation of the integrity of a concrete beam (Kalinski et al. 1994), determination of elastic properties of hard-to-sample soils (e.g., Haegeman and Van Impe 1997), underwater site characterization (Luke and Stokoe 1998), near surface anomalies identification (Luke and Tsarev 2000) and as a diagnostic tool for determining the effectiveness of soil improvement techniques

(Stokoe and Nazarian 1983). The SASW method has proven to be a valuable tool for determining detailed  $V_s$  profiles.

#### Multiple sensors

Rix et al. (2001) and Lai (1998) used multiple sensors, on the order of ten, to measure surface wave dispersion and attenuation curves from a single set of measurements. Then, the  $V_s$  profile and shear damping ratio profile are obtained by inverting them simultaneously. The approach is motivated by the recognition that in dissipative media, Rayleigh phase velocity and attenuation are not independent as a result of material dispersion. The technique is based on displacement transfer functions for the solution of the strongly coupled Rayleigh-wave eigenproblem in linear viscoelastic media (Lai 1998). This method provides a way to combine two datasets,  $V_s$  measurement and attenuation measurement. However, this new method cannot identify multiple modes of surface wave propagation, just like the traditional SASW method that will be discussed below. Others have argued that the damping ratio is negligible for surface wave measurements because the shear strain is below about 0.001% (Stokoe et al. 1994).

At the Kansas Geological Survey, Park et al. (1999b; Xia et al. 1999) developed the multi-channel analysis of surface waves (MASW) method. The basic field configuration and acquisition routine for the MASW method is shown in Figure 2.2. The equipment includes a 12- or more channel seismograph with vertical geophones in a line, recording cable and source. Sources used in this method are the same as those used in SASW method. Use of multi-channel arrays instead of the receiver pairs used in SASW testing is advantageous for two reasons. The first reason is that it permits the user to visually distinguish the fundamental mode of the Rayleigh wave DC from higher modes and body

waves (Xia et al. 1999). The fundamental mode of the Rayleigh wave DC alone or with higher modes then serve as experimental DCs for  $V_s$  profile searching (Xia et al. 2003). The MASW method has been applied to numerous sites to solve various problems such as characterization of pavement systems (Park et al. 2001b; Rydén et al. 2001), investigation of sea-bottom sediments (Park et al. 2000; Ivanov et al. 2000b) and detecting near-surface anomalies (Park et al. 1998a; 1999a). Similar multi-channel methods have also been used by other researchers including Tselentis and Delis (1998), Lai (1998), Foti (2000), and Beaty (2000).

#### 2.1.2 Passive-Source Methods

Passive-source surface wave methods measure small oscillations known as microtremors. Microtremors are also referred to as ambient noise. Microtremors are classified as either long-period (greater than 1 second), which are the result of natural phenomena such as wave action at coastlines, winds and atmospheric variations; or short-period (less than 1 second), which tend to be produced by cultural sources such as industrial activity or traffic energy (Okada, 2003; Roberts and Asten 2004). Passive-source methods have three properties which are advantageous with respect to active-source methods (Tokimatsu et al. 1992c):

- Deeper depths can be measured because of the potential to sample longer wavelengths;
- No active source is required;

- The assumption of dominance of Rayleigh wave energy is more likely to be true because the Rayleigh waves are generated by a source that is sufficiently distant that related body wave components are negligible.

However, the passive-source method requires more complex signal processing procedures, lacks resolution in the near-surface layers and does not work as well in seismically quiet places (Tokimatsu 1995).

Passive-source methods include the array microtremor and Refraction Microtremor (ReMi) methods. Tokimatsu et al. (1992a, 1992b) used a two-dimensional array of six vertical sensors to determine the  $V_s$  up to 150 m depth. Five vertical sensors are placed on the ground surface to form a circular array, with a sixth in the center. The sensor spacing depends on wavelengths of interest: the radius of the array is initially set at 5 m and expanded or contracted by factors of about two until the range of array radii covers the range of wavelengths to be measured. Suzuki and Takahashi (2002) made passive-source surface wave measurements using four sensors in a triangular configuration with one sensor in the center, and Suzuki and Hayashi (2003) also used eleven sensors configured in an “L” shape. Zywicki (1999) studied several different array geometries chosen to minimize spatial aliasing at high frequencies and maximize wavenumber resolution. A sixteen-sensor circular array, without a center sensor, was selected because of its good resolution characteristics. The ReMi method (Louie 2001) provides a way to collect ambient noise data with a linear geometry.



### 2.1.3 Combined Active-Source and Passive-Source Methods

The active-source method is depth-restricted (up to hundreds of meters) because of the limitations in energy output of the active sources. The passive-source method can be used to resolve profiles up to kilometers while losing resolution in the near-surface. It is possible to overcome the shortcomings by combining active-source and passive-source measurements to take advantage of strengths of each.

For example, Suzuki and Hayashi (2003), in a single joint measurement, used a linear array of 48 geophones for the active-source method, combined with 7 or 10 sensors in triangular arrays and, separately, 11 sensors in “L” shaped arrays for the passive-source method. In the measurement, higher frequency surface waves, 5 to 30 Hz, are generated with a portable source such as a sledgehammer or a weight drop. Low-frequency surface wave data, 2 to 10 Hz, are obtained through the microtremor array measurements. The DCs generated by active-source and passive-source measurements are consistent with each other in the frequency range of overlap (5 to 10 Hz). The integrated use of these two methods proved to be effective for defining the shallow  $V_s$  profile up to 40 m.

Yoon and Rix (2004) used the circular array of 16 sensors described above for passive-source measurement and an irregularly-spaced linear array of 16 sensors for active-source measurements at the same site. Thus, they sampled the frequency ranges 4 to 100 Hz and 1 to 10 Hz in the active-source and passive-source measurements, respectively. The passive-source and active-source measurements overlap in the frequency range of approximately 4 to 10 Hz. The authors observed that the Rayleigh wave phase velocities from the passive-source tests are generally a little bit greater (about 5%) than those from the active-source test over the frequencies where the curves overlap.

Furthermore, the authors noted that the differences decrease as frequency increases. This difference was regarded to be due to the near-field effects. The near-field is the region where the assumption of plane wave propagation is not valid and the near-field effect refers to any adverse effects resulting from the invalid assumption of plane wave propagation in that condition (Yoon and Rix 2004). In the active-source measurement, active sources are often applied relatively close to the sensors and thus the surface wave field can be contaminated by wave scattering and body waves (Yoon and Rix 2004). Consequently, the authors recommended that the composite DC, which is a combination of individual DCs from a group of receiver spacings, be made by using only the passive-source component within the frequency range where active-source and passive-source DCs overlap.

Similarly, a combined measurement of SASW (active source) and ReMi (passive source) methods was performed by Liu et al. (2005). In their study, the sampled frequency range for SASW was from about 3.5 to 500 Hz, while for ReMi it was from about 1 to 40 Hz. In the tests, the DCs from SASW and ReMi overlaid one another in the overlapped frequency range without obvious difference. So, the composite DC was formed by averaging the active-source and passive-source curves within the overlapped frequency range. Thus, the authors noted that the DCs developed by SASW and ReMi methods for the same locations exhibit excellent agreement yet they are supplementary to one another to cover a wider range of wavelengths.

## 2.2 Dispersion Relation Generation

After the field measurement, the next step is to construct an experimental DC. For the active-source measurement, the phase spectral method is used to generate the DC in the two-sensor methods (Stokoe et al. 1994), and more complex dispersion analysis methods such as frequency-wavenumber ( $f-k$ ) spectrum analysis (Gabriels et al. 1987) or frequency-slowness ( $f-p$ ) spectrum analysis (McMechan and Yedlin 1981) are used in multi-channel methods. The slowness is the inverse of phase velocity. For the passive-source measurement, the  $f-k$  spectrum analysis (Capon 1969),  $f-p$  spectrum analysis (Louie 2001) and spatial autocorrelation (SPAC) method (Aki 1957) are used to show the dispersion characteristics of Rayleigh waves.

### 2.2.1 Active-Source Methods

#### One sensor: Multiple filter technique

Most researchers use phase velocity to yield the  $V_s$  profile. Alternatively, some researchers (e.g., Stoll et al. 1994; Long et al. 1999, 2000; Long and Kocaoglu 2001) use group velocity instead. The phase velocity is the rate that an energy peak or wave shape moves across the surface, while the group velocity is the rate of energy propagation along the surface. The advantage of using group velocity over phase velocity is that the group velocities are usually lower and more widely varying. Lower and more widely varying velocities give greater differences in travel times for an anomalous structure. The disadvantages include the need for instrument corrections and the complex computational analysis needed to identify group velocity (Long et al. 1999, 2000).

The multiple filter technique is used to generate the dispersion relations for a one-sensor measurement (Dziewonski and Hales 1972). In this technique, an individual trace is filtered by narrow bandpass filters at a sequence of center frequencies. The wave information is given in terms of narrowband-filtered wave amplitudes as a function of group velocity and frequency, known as a Gabor matrix. Thus, different wave groups are separated in the signal. The filtered time history is then retrieved by an inverse Fourier transform. The maxima of the instantaneous amplitudes of the filtered signal propagate approximately with the group velocity. The multiple filter analysis, therefore, results in the group velocity as a function of frequency. The advantage of this method is that only a single sensor is needed. A comparison of the multiple filter technique and the  $f$ - $k$  method was made in the case reported earlier by Gabriels et al. (1987). Here, the maxima in the multiple filter diagrams were not sharp enough to derive a reliable group velocity curve except for part of the fundamental mode. In contrast, as discussed below, the  $f$ - $k$  spectrum analysis was successful in identifying six modes of propagation for this case.

#### Two sensors: Phase spectral method

In the phase spectral method, the generated signal is recorded by two geophones which are located in line with the source. Using a signal analyzer, as the data are collected, they are translated from time domain into the frequency domain. Calling  $x(t)$  and  $y(t)$  the signals recorded respectively at first and second receiver in time domain,  $X(f)$  and  $Y(f)$  are their Fourier transforms to the frequency domain. The cross-power spectrum is defined as:

$$G_{xy}(f) = X(f) * Y(f) \quad (2.1)$$

where  $*$  denotes the complex conjugate.

The time delay  $\Delta t$  between the arrivals of the wave at the receivers is then calculated using the unwrapped phase angle from the cross-power spectrum:

$$\Delta t(f) = \frac{\tan^{-1} \left\{ \frac{\text{Im}[G_{xy}(f)]}{\text{Re}[G_{xy}(f)]} \right\}}{2\pi f} \quad (2.2)$$

It is important to note that the phase of the cross power spectrum is normally displayed from  $-180$  to  $180$  degrees in what is termed as wrapped phase. By placing each segment end-to-end, the phase is unwrapped. It is the unwrapped phase that is used in the DC calculation.

Because the distance  $d$  between the receivers is known, the phase velocity of the surface wave can be determined as a function of frequency:

$$V_R(f) = \frac{d}{\Delta t(f)} \quad (2.3)$$

Consequently the corresponding wavelength is:

$$\lambda_R = \frac{V_R}{f} \quad (2.4)$$

The coherence function is defined as:

$$\gamma_{xy}^2 = \frac{G_{xy}^* G_{xy}}{G_{xx} G_{yy}} \quad (2.5)$$

where  $G_{xx}, G_{yy}$  are auto-power spectrums:

$$G_{xx}(f) = X(f)^* X(f) \quad (2.6)$$

$$G_{yy}(f) = Y(f)^* Y(f) \quad (2.7)$$

The coherence function is a real-valued function with a value between zero and one, corresponding to the ratio of the measured output power caused by the measured input to the total measured output. A coherence value close to one indicates good correlation between the input and the output signals. The coherence function is used in SASW testing to identify the frequency range having good signal-to-noise ratio. It aids in correctly unwrapping the phase data.

The steps outlined in Eqs. 2.4 through 2.7 are performed for the full test spectrum, and the results are plotted in the form of a DC.

The construction of the DC is affected by operator's experience, because the selection of a valid frequency range, masking and phase unwrapping process are subjective. The masking procedure is required to edit out the data with low-quality phase information and the data in the near-field. Some automated methods for these steps have been proposed (Nazarian and Desai 1993). However, errors can occur when low resolution masks true jumps in the wrapped phase. Noise can induce fictitious phase jumps (Al-Hunaidi 1992, 1993). Due primarily to this difficulty in phase unwrapping, these automated methods, though useful for some applications, are not universally adopted.

A potential limitation in the SASW data analysis arises when one assumes that the measured phase is governed by the fundamental mode of the Rayleigh wave. As mentioned above, this assumption is not valid in some cases. The generated DC is in fact an "effective" (Lai 1998) DC which arises from the superposition of multiple surface wave modes and other wave types. As a result, complications might be introduced for DC generation in a heterogeneous medium, where the presence of wave scattering can have a

significant effect on the measured phase. This situation can also be a problem for other surface wave methods.

Different methods have been used to address this problem. Joh (1996) and Joh et al. (1997) used a technique called Impulse Response Filtration (IRF) to isolate the surface wave energy from the interference of other wave groups and background noise. This technique would help in determining the unwrapped phase. The authors used it successfully to separate body waves and surface waves recorded on a soft seafloor where the surface and shear waves travel much slower than the compression waves. Tsarev (2003) tried to use this technique with a terrestrial dataset for cavity detection but was not successful. The reason would be that compression waves travel much slower on the ground surface than on a soft seafloor, making them more difficult to distinguish from other, slower-moving wave types. Tsarev concluded that the IRF would not work in this situation without significant subjective input.

Professor James Bay of Utah State University uses three receivers in the SASW test for the purpose of efficiency (Gilbert 2004). The use of three receivers allows two different spacings to be measured simultaneously. Receivers R1 and R2 are used to measure the spacing  $d_1$ , while receivers R2 and R3 are used to measure the spacing  $d_2$  which is twice  $d_1$ . This three-receiver method also provides some redundant measurements which would be useful for statistical study. It was used by Gilbert (2004) at 44 sites in and around the Salt Lake City metropolitan area. It is noted that standard “common midpoint” geometry is not strictly observed in this test.

With respect to the traditional phase spectral method, Bay introduced an improved phase spectral method that can be applied to generate the DC (Gilbert 2004, Liu et al.

2005). This method uses information from both the source, which is recorded by the analyzer on one channel, and the receivers. The recorded forcing function applied to the ground by the source is used to correlate the response of each receiver to the source signal before calculating phase shift between receivers, to reduce effects of uncorrelated noise. A transfer function (H), which represents the ratio of the cross-power spectrum and the auto-power spectrum of two records, is introduced to take into account the source function.

For a given receiver pair, records of the source and both receivers in the time domain ( $s(t)$ ,  $x(t)$ , and  $y(t)$  respectively) are converted to the frequency domain ( $S(f)$ ,  $X(f)$  and  $Y(f)$  respectively) respectively using Fast Fourier Transform (FFT). The transfer functions between the source and the two receivers are described by:

$$H_{sx} = \frac{S(f)^* X(f)}{S(f)^* S(f)} \quad (2.8)$$

$$H_{sy} = \frac{S(f)^* Y(f)}{S(f)^* S(f)} \quad (2.9)$$

where  $H_{sx}$  is the transfer function between the source and the first receiver and

$H_{sy}$  is the transfer function between the source and the second receiver. The transfer function between the two receivers  $H_{xy}$  is then defined as:

$$H_{xy} = \frac{H_{sy}}{H_{sx}} \quad (2.10)$$

The time delay  $\Delta t$  and coherence function  $\gamma_{xy}^2$  between the two receivers are calculated as follows:



$$\Delta t(f) = \frac{\tan^{-1} \left\{ \frac{\text{Im}[H_{xy}(f)]}{\text{Re}[H_{xy}(f)]} \right\}}{2\pi f} \quad (2.11)$$

$$\gamma_{xy}^2 = H_{sx} H_{sy} \quad (2.12)$$

## Multiple sensors

Separation of different modes of surface wave propagation is possible only through a multi-channel recording method combined with an appropriate multi-channel data processing technique (Gucunski and Woods 1991b; Tokimatsu et al. 1992c). Several methods have been developed for obtaining DCs from multi-channel recordings.

- Phase spectral method

The phase spectral method has been extended to multi-channel arrays by Phillips et al. (2003, 2004). The method termed Distance Analysis of Surface Waves (DASW) involves the use of a 24-geophone array, and computes the change in phase of a single frequency with respect to distance. Data collected for the same geophone array from different source locations can be processed with the same algorithm as that used in the SASW method to generate the DC. Compared with the SASW method, the possibility of statistical analysis is a clear advantage of the DASW method. The use of multiple receivers to calculate the phase velocity enhances the statistical validity of the DASW results because linear regression analysis can be used in the calculation of phase velocities along the array. However, the data processing is time consuming since each receiver pair is analyzed independently to calculate phase velocity.

- Frequency-wavenumber ( $f$ - $k$ ) spectrum method

Several investigators have employed the frequency-wavenumber ( $f$ - $k$ ) method to generate surface wave dispersion panels (Gabriels et al. 1987; Tokimatsu 1995; Tselentis and Delis 1998; Beaty 2000; Foti 2000). These methods typically utilize multiple receivers arranged in a linear array for active-source measurements or a two-dimensional array for passive-source measurements. The record is translated from the time-space ( $t$ - $x$ ) domain to the frequency-wavenumber ( $f$ - $k$ ) domain by two successive applications of a one-dimensional FFT algorithm: the first application in time takes the raw data from the  $t$ - $x$  domain to the  $f$ - $x$  domain, and the second application in space leads to the  $f$ - $k$  domain.

The data processing approach of the  $f$ - $k$  spectrum method works on the principle that a point in the  $f$ - $k$  domain can be related directly to a phase velocity through the relation  $V = \frac{2\pi f}{k}$ . Commonly, multiple wavenumber peaks are present at a given frequency, indicating the presence of multiple Rayleigh modes. Fundamental- and higher-mode dispersion information can be obtained by locating peaks manually in the  $f$ - $k$  spectrum of the experimental data. Thus, a dispersion panel with fundamental and higher mode DCs is generated.

One application of this procedure to shallow soil characterization was reported by Gabriels et al. (1987) on a tidal flat in the Southwest Netherlands. The walkaway method, which is described in Chapter 7, was applied to acquire the data. Twenty-four sensors at a spacing of 1 m with a 30-kg weight drop source hitting at 12 offsets were used. The authors were able to identify the DCs of the first six modes of propagation as a function of frequency from 5 to 30 Hz. The observed phase velocities were inverted with a

linearized method described by Nolet (1981) to resolve a  $V_S$  profile to a depth of 50 m. Further, the authors also showed how to improve the resolution by zero-padding the traces before inversion.

With respect to the phase spectral method, working in the  $f-k$  domain makes it possible to isolate DCs for different modes, instead of resolving a single effective DC. Besides, the resulting DCs are smoother than the one from the phase spectral method. This certainly facilitates the inversion procedure (Tselentis and Delis 1998), although it might also be a shortcoming for understanding a complex profile. Using a numerically simulated wavefield composed of both Rayleigh and body waves, Tokimatsu (1995) showed that the undesired distortions produced by body waves on the computed DC are minimized by  $f-k$  spectrum analysis by observing that the Rayleigh wave has the maximum wavenumber for any given frequency. Thus, the  $f-k$  spectrum analysis is less sensitive to near-field effects when compared to the phase spectral approach in that the interference of body waves can be reduced.

- Frequency-slowness ( $f-p$ ) transformation method

Another multi-station approach that can be used for geotechnical applications is based on the phase slowness-time intercept ( $p-\tau$ ) transform. This method has been used by researchers McMechan and Yedlin (1981), Foti (2000), Beaty (2000), Forbriger (2003a, 2003b) and O'Neill (2003; 2004a; 2004b).

The procedure consists of two linear transformations: first a slant stack (a process to stack traces by shifting them in time proportional to physical offsets of the sensors on the ground surface) of the raw data produces a wave field in the  $p-\tau$  plane such that phase

slownesses are separated. The time intercept  $\tau$  is equal to  $t - px$  where  $x$  is offset. The spectral peak of the one-dimensional Fourier transform of the  $p - \tau$  wave field then gives the frequency associated with each phase velocity. Thus, the data wavefield is linearly transformed from the time-distance  $t-x$  domain into the phase slowness-frequency  $f-p$  domain, where DCs are imaged. The discrete  $p - \tau$  transform is strictly described by the equation (Turner 1990)

$$\hat{F}(p, \tau) = \sum_{i=1}^N F(x_i, \tau + px_i) \quad (2.13)$$

where

$N$  = the number of seismic traces used in the transform;

$x_i$  = position of the  $i^{th}$  seismic trace;

$\tau$  = zero offset intercept;

$p$  = slowness;

$F(x, t)$  = amplitude at  $(x, t)$  in the seismic section; and

$\hat{F}(p, \tau)$  = amplitude at  $(p, \tau)$  in the  $p - \tau$  domain.

Park et al. (1998b, 1999b) presented a wavefield transformation method to separate different modes at high resolution with a relatively small number of traces collected over a limited offset range. In this method, the Fourier transform is first applied to the time axis of the  $t-x$  domain to obtain datasets in frequency-offset ( $f - x$ ) domain and then a slant stack is applied to produce a wave field in the  $f-p$  domain. This technique yields better results than those from transformation to  $p - \tau$  domain first and then  $f-p$  domain (Park et al. 1998b, Beaty 2000).

In comparison to analysis in the  $f$ - $k$  domain, the localization of peaks in the  $f$ - $p$  domain is directly informative about the shape of the DC. In the  $f$ - $k$  technique, the data are required to be evenly sampled in both space and time for the FFT algorithm. In the  $f$ - $p$  technique, the data are not required to be evenly spaced; thus the technique is not sensitive to dead traces in the experimental dataset. Comparisons of the  $f$ - $p$  and  $f$ - $k$  techniques were made by Beaty (2000) and Foti (2000). They both chose to use  $f$ - $p$  because it provides a cleaner, more realistic representation of the DC.

Because both the  $f$ - $k$  and  $f$ - $p$  methods require manually picking the discrete dispersion data from the dispersion panel, which involves subjective interpretation, it can be possible to misinterpret the mode shapes or order of modes (e.g., taking all or part of the 3<sup>rd</sup> mode as 2<sup>nd</sup> mode). In addition, peaks in the dispersion panels are always broad at low frequencies. This adds difficulty to DC picking.

Despite the fact that many researchers have used  $f$ - $k$  and/or  $f$ - $p$  transformation methods to generate surface-wave dispersion panels, no such studies are known on systems having large stiffness contrasts, such as those caused by carbonate-cemented inclusions.

### 2.2.2 Passive-Source Methods

- Spatial autocorrelation method

The spatial auto-correlation (SPAC) method was first developed by Aki (1957), and recently reviewed by Tokimatsu (1995) and Okada (2003). In this method, a circular array of geophones placed equidistant from a single, central geophone is deployed to

obtain Rayleigh wave data propagating from a wide range of azimuthal angles. By the SPAC method, the configuration of the array is limited to a circle. Only 4 to 7 sensors are needed. No higher modes are considered in this method. Roberts and Asten (2004) reported a field test in which a velocity reversal resulting from the presence of a hard, 12-m-thick basalt flow, which is a HVL, overlying 25 m of softer alluvial sediments and weathered mudstone was successfully resolved by the SPAC technique. The velocities of the HVL and lower layer are approximately 1800 and 700 m/s respectively. This velocity contrast is comparable to that of a carbonate-cemented-layer inclusion in a sediment profile; however, the thickness is much greater. Due to the lower resolution of the passive-source method with respect to the active-source method, it is not expected that the SPAC technique would resolve a thin carbonate-cemented-layer inclusion better than an active-source method would.

- Frequency-wavenumber ( $f$ - $k$ ) spectrum method

Another approach to extract a Rayleigh wave DC from microtremor array records is based on the frequency-wavenumber ( $f$ - $k$ ) spectrum analysis. This method has been used by researchers including Capon (1969), Tokimatsu et al. (1992a), Liu et al. (2000) and Zywicki and Rix (1999). A summary of two dimensional array  $f$ - $k$  spectrum methods, used for passive-source measurements, is presented by Zywicki (1999).

The configuration of the array in the  $f$ - $k$  method is flexible, but more sensors are needed with respect to the SPAC method and the frequency range resolved using the same array is narrower (Zywicki 1999).

The  $f$ - $k$  spectrum is drawn for each frequency on a two-dimensional wave number ( $k_x - k_y$ ) space. This spectrum provides information concerning the power and the vector velocities of propagating waves. A spectrum pick at each frequency at location ( $k_x, k_y$ ) has a distance of  $|k|$  from the origin point (0,0). The corresponding phase velocity  $V_R$  and the wavelength  $\lambda$  can be determined from

$$V_R = \frac{2\pi f}{|k|} \quad (2.14)$$

$$\lambda = \frac{2\pi}{|k|} \quad (2.15)$$

By repeating the above computation over the frequency range of interest, a single DC, assumed to be fundamental mode, can be obtained.

Tokimatsu et al. (1992a) reported a case study using both the  $f$ - $k$  spectrum analysis and SPAC analysis of microtremor data at the same sites. According to their study, the two methods can yield almost the same DCs: they agree reasonably well for wavelengths up to 180 m. Furthermore, the  $V_s$  profiles developed through the inversion analysis using the observed DCs both showed fairly good agreement with those obtained by the conventional downhole method.

- Frequency-slowness ( $f$ - $p$ ) transformation method

Louie (2001) uses the refraction microtremor (ReMi) method to collect data in a linear geometry with ambient noise source energy. The ReMi technique is based on the same  $f$ - $p$  transformation method used in active-source multi-channel methods. The ReMi

analysis adds a spectral power-ratio calculation to McMechan and Yedlin's (1981) technique for spectral normalization of the noise records. Because the ReMi method uses a linear receiver array, true noise-arrival azimuth is unknown. Therefore, velocities generated by picking spectral peaks in the  $f$ - $p$  domain image will be higher than the true Rayleigh-wave phase velocity. Hence, dispersion-curve picking along a "lowest-velocity envelope" bounding the energy appearing in the  $f$ - $p$  image is recommended by the developer. In a study of combined measurements of SASW and ReMi mentioned previously, conducted in an urban environment (Liu et al. 2005), the two measurements provided complementary data and overlaid one another in the overlapped frequencies without obvious difference, with few non-systematic exceptions.

Stephenson et al. (2005) conducted a blind comparison of  $V_s$  data from ReMi, MASW and 200-m deep borehole logs using the P-S suspension technique at four sites in Santa Clara Valley, California. A 250-kg drop weight source was used for the MASW measurement. The  $V_s$  averaged to depths of 30 m, 50 m and 100 m from the MASW and ReMi methods compare favorably with those from borehole data at three sites. However, agreement is poor in the 100-m depth-averaged  $V_s$  at one site due to the existence of a low velocity layer (LVL) between 52 and 75 m which appeared in the suspension borehole log, but neither the ReMi nor the MASW method located. The  $V_s$  of the LVL and the layers above and underneath are about 320, 450 and 600 m/s respectively. Given the limitation of the source used for the MASW measurements, it didn't generally image as deep as ReMi at two sites. The maximum depths resolved by MASW and ReMi are about 70 and 100 m respectively at one site, and 60 and 100 m respectively at the other



site. At the other two sites, both of the MASW and ReMi measurements reached the maximum depth greater than 100 m.

### 2.3 Inversion and Interpretation

After the experimental DC or panel is obtained, the  $V_s$  profile is sought through inversion of the DC. The inversion procedure contains two fundamental components. One is to construct a set of theoretical DCs or bands/fields based on the assumed soil properties and numerical simulation of wave propagation. This procedure is called forward modeling. The other is to exercise the forward model within an optimization algorithm in which model parameters are iteratively adjusted to minimize the difference (error) between the experimental and theoretical dispersion datasets. This procedure is called optimization or inversion analysis.

#### 2.3.1 Forward Modeling Methods

For the surface wave method, the forward modeling develops the theoretical DC or panel for a given layered soil system using wave propagation theories. Various methods have been developed for the analysis of wave propagation in layered media. All the methods discussed here assume that the profile consists of a set of homogeneous, isotropic layers extending infinitely in the horizontal direction. The last layer is considered a homogeneous half-space.

##### Plane wave model

Many of the forward models for surface wave propagation in use today are based on plane wave propagation theory. The most commonly used approach is the transfer matrix

approach presented by Haskell (1953). Most subsequent researchers have maintained the ideas of Haskell in reformulating the problem. The main difference between Haskell's method and the methods of others lies in the algebraic manipulation of the matrices to improve numerical stability. A detailed review of seven different methods is presented by Buchen and Ben-Hador (1996). Carlo Lai (1998) and Glenn Rix at Georgia Tech used the Green's function as described by Hisada (1994) to calculate particle displacement due to a harmonic unit point source. They programmed this calculation method in the code "SWAMI" using FORTRAN 95.

The transfer matrix approach works well when the profile is normal, that is, the velocity increases gradually with depth. However, where anomalous inclusions exist in the profile, especially where impedance contrasts are high, forward modeling is more challenging to accomplish, due to the factors discussed in the problem statement of this dissertation. Advanced forward models should be considered. Two such types of advanced forward models exist: cylindrical wave model and full waveform model.

#### Cylindrical wave model

When there are abrupt changes in  $V_s$ , the wave field, including possible reflections or refractions of body waves, is simulated more realistically by the cylindrical wave model than by the plane wave model (Kausel and Roësset 1981; Roësset et al. 1991). In the cylindrical wave model, waves are assumed to propagate along curved wave fronts and cylindrical coordinates are used. The model simulates the dynamic response of a soil profile to a vertical disk load. Displacements and stresses on a horizontal surface are expanded in Fourier series in the circumferential direction and in terms of cylindrical functions in the radial direction (Foinquinos 1991). An effective DC is yielded using the

cylindrical wave model. The cylindrical wave model has been used by Stokoe et al. (1994) and other researchers. The model is programmed in the code “SASWFI” which was developed at University of Texas at Austin by Rafael Foinquinos (1991) and José Roësset using FORTRAN 77. Plane wave and cylindrical wave models are both simulated in the code.

Using the cylindrical wave model approach, Ganji and Gucunski (1998) were able to successfully model irregular synthetic profiles, including a profile with a softer layer trapped between two HVLs, one with a HVL sandwiched between two softer layers, and a third with softer layers at larger depths, and two experimental pavement profiles. Of the synthetic models studied by these researchers, the one with the largest velocity contrast is a two-layer system, having equal layer thicknesses of 5 m, over a half space. The  $V_s$  of the upper layer, middle layer and half space are 200, 400 and 300 m/s respectively. These velocity contrasts are low with respect to a cemented-layer-included system in an arid soil profile (recall Figure 1.1). Moreover, the thickness of the cemented zones is typically less than 3 m and they can occur at multiple depths (Stone and Luke 2001). Thus, the current study is more challenging than those which have been presented previously.

Rix et al (2001) and Lai et al. (2002) developed an approach to modeling multi-mode surface wave propagation that combines the simplicity of a plane wave analysis with the accuracy of a cylindrical wave analysis. They derived an explicit, analytical expression for the so-called “effective” Rayleigh phase velocity as a function of the homogeneous Rayleigh eigenproblem. Because this effective Rayleigh wave phase velocity can be entirely determined from the solution of the homogeneous Rayleigh eigenproblem, it requires no additional effort compared to a plane wave analysis. The energy partition for

each mode is defined as a function of the first Rayleigh energy integral associated with the propagation mode and horizontal and vertical displacement eigenfunctions. Lai (1998) has supplied detailed information on this process. Use of this effective Rayleigh phase velocity achieves many of the advantages of a cylindrical analysis because it includes contributions from multiple surface wave modes. Moreover, partial derivatives of the effective Rayleigh phase velocity with respect to the  $V_s$  of the medium, needed for the optimization process, are efficiently and accurately calculated using closed-form analytical expressions.

This writer tested this approach for challenging velocity profiles like the one described in Figure 1.1 and encountered some numerical instability problems. Possible influencing factors would include the use of the asymptotic approximation of the Hankel function, the integration range (the limit of the wave number domain used for the numerical integration) and large exponents in the exponential functions in the stiffness matrix (Lee 1996). Lee (1996) has provided detailed information in this respect.

#### Full waveform model

The full waveform model in which interaction of all waves is modeled gives an exact solution to the wave equation for horizontally stratified media (Alterman and Karal 1968). It is one of the most accurate ways to model the wave equation. However, the computational demands for full waveform inversion are great. O'Neill (2003; 2004a; 2004b) presented a full waveform  $P$ - $SV$  reflectivity method to take the place of the wave propagation matrix method. According to O'Neill, velocity reversals are modeled better with this method than with conventional inversion methods considering fundamental mode only. O'Neill found that an LVL directly under a surface caprock or pavement

layer is inverted with more accuracy than one below a buried HVL. The author suggested that the decreased resolution with depth would be one reason for the difficulty of detecting the buried HVL.

OASES (Schmidt 1999) is a general purpose computer code for full waveform modeling of seismo-acoustic propagation in horizontally-stratified waveguides using wavenumber integration in combination with what is called the Direct Global Matrix solution technique. It can be used to generate synthetic seismograms. This technique was developed for acoustic modeling in the ocean. To date, no practical applications to exploit  $V_s$  profiles have been reported. But we have no reason to believe that it would not work for terrestrial surface wave modeling.

Based on the literature reviewed by the author, no comparison was reported of those two forward models, the cylindrical wave forward model and the full waveform model, applied to the same datasets.

#### Other methods

Other forward modeling methods used in surface wave measurements include the finite difference method (Hossain and Drnevich 1989, Tsarev 2003), direct numerical integration method (Aki and Richards 1980) and finite element method (Ganji and Gucunski 1998, Zerwer et al. 2002, Hadidi and Gucunski 2003). Those methods are not the main trend in the field of surface wave study today. This writer suggests that the reason for this might be due to the difficulty in simulating the boundary conditions and embedding them into optimization methods. Besides, the processing is relatively time-consuming.

### 2.3.2 Optimization Methods

In the inversion process, model parameters of concern are  $V_s$ , Poisson's ratio or compression wave velocity ( $V_p$ ), density and their geometric distributions. By comparing the partial derivatives of the phase velocity with respect to  $V_s$ ,  $V_p$  and density, Xia et al. (1999) showed that the dispersion characteristic is most sensitive to  $V_s$ . Fortuitously the  $V_s$  is the parameter in which we are most interested and for which the inversion is sought. Rayleigh inverse problems are non-linear and therefore have the potential for nonuniqueness (Luke et al. 2003a). From a mathematical point of view, nonuniqueness in the solution of an inverse problem is caused either by a lack of information to constrain its solution or because the available information content is not independent (Lai 1998).

Several methods exist for obtaining the  $V_s$  profile from the dispersion relations: simple empirical relationships, iterative forward modeling and inversion analysis.

A simple empirical method of inversion is to assume that the  $V_s$  is equal to 110% of the Rayleigh phase velocity, due to the closed-form relationship that exists between them in a homogenous half space (e.g., Richart et al. 1970), and the effective sampling depth for each wavelength is equal to one-third of that wavelength because it is here that the maximum displacements take place (Stokoe and Nazarian 1983). Stokoe and Nazarian (1985) indicated that the use of this simple inversion method would cause some degree of error in the  $V_s$  profiles. In the Engineering Geophysics Laboratory (EGL) at the University of Nevada, Las Vegas (UNLV), a similar method, differing in that  $V_s$  is assumed equal to Rayleigh phase velocity, is used to generate the initial guess, termed starting model, for automated inversion (Liu et al. 2002; Luke and Calderón-Macías in press; Calderón-Macías and Luke in press).

The iterative forward modeling analysis is a trial-and-error curve-fitting procedure (Stokoe and Nazarian 1985). In this procedure, a theoretical DC is calculated for an assumed site profile with initial assigned model parameters using forward modeling theory. The theoretical DC is then visually compared with the experimental DC. If the match is not good enough, the initial guess of the  $V_s$  profile is adjusted to generate a new theoretical DC. The comparison is again made between the new theoretical DC and the experimental DC. The trial-and-error procedure is continued until satisfactory agreement is achieved between the theoretical DC and the experimental DC. The resulting site profile is then considered to represent actual site conditions. The advantage of this method is that it is straightforward and allows direct investigation of suspected solutions. However, it is slow and subjective. This method is used in ReMi data interpretation (Louie 2001).

Inversion analysis is an automated iterative forward modeling process. The iterative changes in the stiffness profile are made using an optimization technique. Most researchers have employed linearized inversion (LI) (e.g., Menke 1989, Ganji 1996, Ganji and Gucunski 1998) or else a combination of linear and nonlinear methods (Xia et al. 1999) or neural networks methods (e.g., Williams and Gucunski 1995).

Recently, the simulated annealing (SA) method (e.g., Sen and Stoffa 1995, Corona et al. 1987), which is a directed Monte Carlo optimization method, has been investigated by researchers such as Beaty (2000), Martinez et al. (2000), Beaty et al. (2002), Hadidi and Gucunski (2003) and Calderón-Macías and Luke (in press); Luke et al. (2003a, 2003b). This method permits “uphill” moves in error space, which means that the error, defined as the difference between experimental and synthetic DCs, is permitted to increase under

the control of a probabilistic criterion, thus tending to avoid becoming trapped at local minima in the error space, which could occur if inversion was used with a starting model that differs significantly from the correct solution.

Luke, Calderón-Macías and colleagues (Luke and Calderón-Macías in press; Calderón-Macías and Luke in press; Luke et al. 2003a, 2003b) showed that the SA inversion could be used to improve resolution of HVLs in soil profiles because it makes it possible to guide the solution within expected boundaries based upon prior knowledge of site layer geometry or  $V_s$  profile. For the SA inversion, the inverted  $V_s$  profile is composed from a background profile overprinted with one or more HVLs. However, it might take an enormous amount of time and unrealistic computer precision (to keep sampling at low “temperatures”) to find the global error minimum. So once a satisfactory degree of error reduction is found through SA, a following process of linearized inversion can be used to speed up the convergence upon a best-fit solution (Calderón-Macías and Luke in press). In this SA-LI processing, the final  $V_s$  profile from SA serves as the starting model for the final LI process. Because the SA method has a stochastic component, the outcomes of optimization with the same input parameters can be different. Thus, three SA-LI runs are performed for each inversion with identical parameters and search range (SR) (Luke and Calderón-Macías in press). The velocity-averaged profile of the three SA-LI solutions is then considered as the final inverted profile and the outer bound of the three solutions would be presented to illustrate credible ranges. The authors demonstrated that this process tends to envelop the solution within credible ranges.

Liu (2002) tested LI and SA-LI inversion methods with two synthetic datasets and two experimental datasets from two-channel SASW measurements, one of each pair



being normally dispersive and the other having one or more HVLs. The LI method, used alone, always generated  $V_s$  profiles that match the overall velocity trend with respect to the true profiles, but the HVLs are not well defined. The SA-LI method, configured to take into account extensive prior information (e.g., borehole logs and refraction results), yielded very good  $V_s$  matches for the complex profile. The forward model embedded in the inversion algorithm was the plane-wave fundamental-mode Rayleigh wave.

To mitigate the impact of non-uniqueness in inversion of seismic surface wave data, some improvements have been investigated. (1) As mentioned earlier, simultaneous measurement and inversion of dispersion and attenuation functions has been studied by Rix et al. (2001) and Lai et al. (2002). The coupled approach considers the effect produced by material dispersion and improves the “well-posedness” (existence and uniqueness of solutions) of the inverse problem. (2) Xia et al. (2000, 2003) and Beaty (2000) used a multi-channel data acquisition method to explore dispersion panels containing up to three modes and then invert for the three modes simultaneously. (3) Ivanov et al. (2000a) and Ivanov (2002) used the Joint Analysis of Surface Wave and Refractions (JASR) method. In this method, a two-dimensional vertical  $V_s$  slice generated using the MASW method serves as prior information and initial model to generate a two-dimensional  $V_P$  model by refraction tomography. (4) Safani et al. (2005) and Joh et al. (2006) employed Love-wave jointly with Rayleigh-wave dispersion characteristics in the inversion process. The difference between the approaches used by the two research teams is that Safani et al. (2005) used the fundamental-mode Rayleigh wave while Joh et al. (2006) used the effective Rayleigh wave. In contrast to Rayleigh waves, which comprise coupled P-SV particle motion, Love waves comprise SH particle

motion. Safani et al. observed that the Love wave sensitivity and inversion stability is higher than for Rayleigh wave dispersion. Furthermore, they noted that the difference between inverted Rayleigh wave and Love wave velocity profiles could be attributed to transverse isotropy of horizontal ( $V_{SH}$ ) and vertical ( $V_{SV}$ )  $V_s$  of soil deposits. Joh et al. observed that the effective Love wave DC might have significant discontinuities due to multiple reflections of SH waves and mode conversions of Rayleigh waves. Those adverse effects make Rayleigh waves more beneficial than Love waves in the inversion analysis.

#### 2.4 Detection of Anomalous Layers with Surface Wave Methods

Surface-wave methods have been used by some researchers to investigate anomalous layers and inclusions. Most publications address cavities and pavement systems. A few researchers have addressed embedded LVLs or HVLs.

One anomalous feature that is highly studied is cavities (e.g., Tsarev 2003). A cavity may be dry, soft-sediment filled or filled with water; this can significantly affect Rayleigh wave dispersion. Both SASW methods (e.g., Avar and Luke 1999) and MASW methods (e.g., Park et al. 1999a) have been used in cavity detection. Phillips et al. (2004) used the DASW method to detect cavities by measuring lateral velocity variations. By numerical simulations and field measurements, Gucunski et al. (1996) found that cavities can significantly affect the results of SASW tests by causing a decrease in the phase velocities of surface waves over a broad frequency range. Moreover, the existence of the cavity causes fluctuations in the DC which are induced by wave scattering. Recently, Gucunski and Shokouhi (2005) provided a potential method to detect and characterize

cavities using continuous wavelet transforms of surface waves. They illustrated their results with finite element simulation. No field dataset analysis was provided with this method. The attenuation analysis of Rayleigh waves (AARW) to detect the voids has been presented by Nasser-Moghaddam et al. (2005). In the method, two parameters, normalized energy distance parameter and normalized amplified logarithmic decrement values, were introduced to identify the location and depth respectively of a void. The numerical simulations show the promise of the AARW for detecting voids in the real world. Consideration of the research reviewed here leads to the conclusion that difficulties remain in defining the position, size and shape of the cavities, especially when they are deeply buried.

With respect to anomalous layers, the pavement system is special in that the stiffest layer is at the surface. Both the SASW method (e.g., Hossain and Drnevich (1989), Hiltunen (1991), Haegeman and Van Impe (1997), Ganji and Gucunski (1998)) and the MASW method (e.g., Park et al. (2001b) and Rydén (2001, 2002a, 2002b)) have been used in pavement estimation. For example, Rydén (2004) reports great success and accuracy in the evaluation of the thickness and stiffness of the top pavement layer using surface waves. However, the author states that the inversion of a deeper, embedded HVL remains the most challenging part in pavement surface wave measurements. Similarly, also as mentioned previously, O'Neill (2003) found that an LVL directly beneath a surface caprock or pavement layer is inverted with more accuracy than one below a buried HVL.

As mentioned earlier, an embedded LVL or HVL is known to give rise to higher-mode energy (Gucunski and Woods 1991a). Asten and Boore (2005) reported a blind

comparison of fourteen surface wave methods at a single site in the city of San Jose, California. This site was one of four in the study reported by Stephenson et al. (2005) mentioned earlier. Two LVLs were detected by the in-hole shear wave suspension log, one at a depth of 7 to 16 m and another more distinct one at a depth of 55 to 75 m. The velocity contrasts for the two LVLs are both small, less than a factor of 2. Although the averaged  $V_s$  to a depth of 30 m from all the techniques agree well, only three of the non-invasive seismic methods resolved the upper LVL: high-resolution reflection-refraction, SASW with harmonic source and OYO's WAVE-EQ software and a multi-channel surface wave method using a harmonic source with  $f - k$  analysis and direct inversion of the DC. None of the methods resolved the deeper LVL.

As mentioned earlier, Ganji and Gucunski (1998) reported success in modeling a system with an HVL. With respect to their case, however, the HVL system with carbonate-cemented-layer inclusion poses greater difficulties for inversion due to the higher velocity contrast.

Sedighi-Manesh (1991) studied the potential of using the SASW method to detect gas hydrate (an ice-like crystalline solid formed from a mixture of water and natural gas, which has a high  $V_s$ ) offshore. The author developed theoretical formulations from both plane wave and cylindrical wave models for propagation of waves along the interface between a solid and water. Results calculated from the plane wave model solution were compared with experimental data. Changing dominance among surface wave modes was observed when the underwater profile was not ND. (In a ND profile the velocities of soil layers increase monotonically with increasing depth.) Sedighi-Manesh (1991) also compared theoretical solutions from plane wave and cylindrical wave models.

Disagreement in the dispersion relation occurred at wavelengths greater than twice the depth of the water when the  $V_s$  of the underwater half-space is as high as 3,000 m/sec. The author's finding supported the same conclusion described above that soil systems having high-velocity inclusions are particularly difficult to resolve. The cylindrical wave model should be more appropriate than plane wave model for profiles at those cases.

Jin et al. (2006) performed one SASW and one MASW measurement at a site known to have a carbonate cemented layer. For the MASW analysis, commercial software, SurfSeis (Kansas Geological Survey), was used. In the program, the plane wave propagation is modeled and a combined linear and nonlinear optimization methods (Xia et al. 1999) is used to build the  $V_s$  profile. For the SASW analysis, the cylindrical wave propagation model of Roësset et al. (1991) is used and a linearized inversion method is used to build the  $V_s$  profile (Luke et al. 2003b). Even though the fit between the experimental DC and theoretical DC was good in both cases, neither of them resolved the HVL.

By introducing the two-step inversion process of SA-LI as mentioned previously, Luke et al. (2003a, 2003b) have improved the ability to resolve stiff, carbonate-cemented layers using SASW data. The forward model that the authors used is fundamental-mode energy from the plane wave model. As mentioned previously, the DC generated from the SASW method is in fact an effective DC and so can be represented more accurately with a cylindrical wave propagation model.

Consideration of the research reviewed here leads to the conclusion that soil systems with HVLs and/or LVLs are particularly difficult to resolve. The purpose of this research is to find a way using surface wave methods to better resolve the HVL.

## 2.5 Methodology of this Study

Because active-source methods have higher resolution than the passive-source methods within the shallow depths of interest, only active-source methods will be used for this study.

To address the issue of wave scattering in a complex-layered system such as that of a carbonate-cemented inclusion, two possible solutions can be considered, as Tokimatsu et al. (1992c) summarized: either separate a dominant mode and other contributing modes or use a so-called “apparent” (i.e., “effective”) DC to consider all contributing modes simultaneously.

The first solution calls for multi-channel methods and sophisticated signal processing procedures. According to the literature review, the  $f$ - $p$  transformation method is preferred for dispersion panel generation. To perform the  $f$ - $p$  transform, a code in MATLAB written by Mauricio Sacchi of University of Alberta is used with permission. Beaty (2000) incorporated this tool in analyses to examine seasonal variability of near-surface elastic properties. Because different modes can be distinguished from each other, a multi-mode plane wave propagation model can be used as the forward model. In the inversion of multi-mode DC with plane wave forward model, this research includes two analyses: fundamental-mode alone (MDC/PF) and first two modes (MDC/PM). This research will test the hypothesis that the MDC/PM analysis is better than the MDC/PF analysis for complex sites.

In the second case, where a single effective DC is generated, as with the two-channel phase-spectral method, the cylindrical wave model can be used as the forward model to generate one effective DC. This solution is inversion of effective DC with cylindrical

wave forward model (EDC/CM). This research will test the hypothesis that the EDC/CM analysis is better than the EDC/PF analysis for complex sites.

The full waveform model shows promise for embedding into the inversion code; however, that investigation is outside the scope of this research project. Because no clear favorite is reported between the remaining two approaches, they are both tested in this research. Because the SA-LI method is preferred to LI alone especially for the complex profiles, it is used to generate the  $V_s$  profile for both approaches for this research. The SA-LI method has been coded in FORTRAN77 for the UNLV Engineering Geophysics Laboratory (EGL) by Carlos Calderón-Macías (Calderón-Macías and Luke, in press). LI alone will not be considered in this research.

The author embedded the SASWFI and SWAMI codes into the SA-LI optimization code. The two codes are used under permission from their respective developers. UNLV graduate research assistant Bagathbabu Dumpala helped with extracting the cylindrical wave forward model part from the SASWFI code.

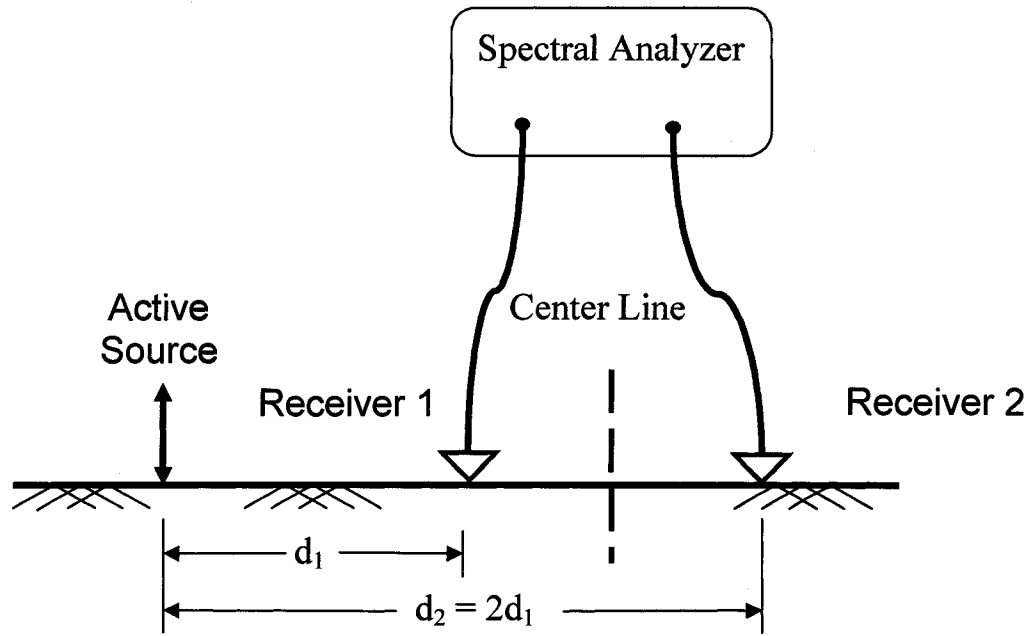
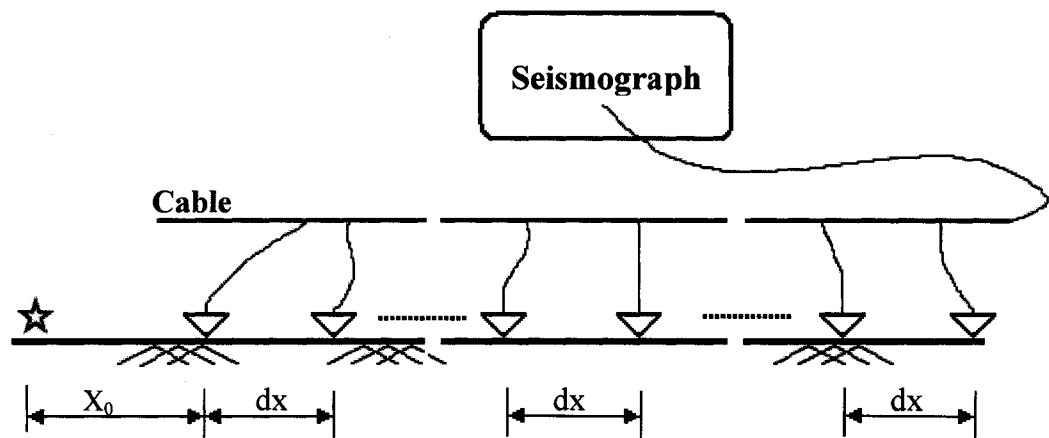


Figure 2.1. Basic configuration for SASW testing.



☆ : Source

▽ : Geophone

$X_0$ : distance from source to the closest geophone

$dx$ : receiver spacing

Figure 2.2. Basic configuration for MASW testing.



## CHAPTER 3

### IMPLEMENTATION OF THE TWO APPROACHES

#### 3.1 Introduction

In this chapter, two synthetic profiles are used to test and verify the newly implemented approaches. They correspond to a ND system and a HVL system. For each profile, two inversion approaches are applied. One is EDC/CM. The other includes two analyses: MDC/PF and MDC/PM. The complete inversion procedures including theoretical DC generation, starting model generation and the inversion implementation are illustrated. An instruction manual for the starting model generation and inversion analyses is included in Appendix A. The ND system is selected to serve as a simple case to test the applicability of the approaches. It is also used to test the applicability of the approaches with incorrect expectation of a HVL. The parameters used to describe the quality of the results are also introduced and discussed.

#### 3.2 Model and Parameter Description

The ND and HVL profiles have the characteristics shown in Tables 3.1 and 3.2 respectively. The profiles are loosely based on sediment properties typical in Las Vegas Valley, Nevada, and more specifically around conditions existing at the UNLV Engineering Geophysics Test Site (EGTS) (<http://www.ce.unlv.edu/egl>). This is the site of the experimental study presented in Chapter 7. Parameters of the target profiles include

the density, Poisson's ratio ( $\nu$ ), thickness,  $V_S$  and compression wave velocity ( $V_P$ ) of the layers. The  $V_P$  is calculated by

$$V_P = V_S \sqrt{\frac{1-\nu}{0.5-\nu}} \quad (3.1)$$

The ND profile is a two-layer normally-dispersive system. The assigned values of  $V_S$  fall within published ranges (e.g., Sharma 1997) for dense sand and stiff clay, which are sediment types common to the Las Vegas Valley. The density of the uncemented layers was selected as  $1700 \text{ kg/m}^3$  which is also within published ranges for stiff clay and dense sand (e.g., Coduto 1994).

As mentioned previously, Rayleigh wave dispersion curves are fairly insensitive to the value of density and Poisson's ratio (e.g., Xia et al., 1999). However, Foti and Strobbia (2002) reported that the wrong hypothesis on the position of the water table, which affects the values of both density and Poisson's ratio, could lead to a misleading result. The authors reported that an incorrect hypothesis of absence of a water table is strongly misleading and can lead to severe errors (as high as 100%) in the final velocities. Teclé et al. (2003) calculated Poisson's ratio at the EGTS from  $V_P$  and  $V_S$  measured with a 7-m deep downhole test. The water table at the site was at 2.7 m depth. The Poisson's ratio of materials above the water table was found to be between 0.26 and 0.3, whereas the Poisson's ratio of materials below the water table was between 0.4 and 0.5. In the synthetic study described here, the water tables are set at 2 m and 3.5 m depth for ND and HVL profiles respectively. The Poisson's ratio for uncemented layers above the water table is set to be 0.3. The  $V_P$  below the water table is 1500 m/s, thus the Poisson's ratio for uncemented layers below the water table is back-calculated to be 0.46 according to Eq. 3.1.

The HVL profile is similar to the ND profile except a thin HVL has been inserted. The HVL represents a carbonate-cemented layer typical of those encountered in Las Vegas. Even though carbonate-cemented layers are ubiquitous in the Las Vegas Valley, there is limited documentation about their thickness, embedment depth and  $V_s$ . The thickness of the carbonate-cemented layer might vary from a few centimeters to 3 m (Wyman et al. 1993). Tecle et al. (2003) measured  $V_s$  of 400 – 900 m/s at about 2 m depth for dry, partially cemented sand and gravel and 1400-2000 m/s at about 4.5 m depth for fully cemented sand and gravel below the water table, in crosshole and downhole tests at the EGTS. Here, the thickness and  $V_s$  of the HVL are assigned 1.5 m and 1500 m/s respectively. Those values fall within ranges of the limited database.

A few studies of density and Poisson's ratio of carbonate-cemented soils have been conducted. Stone and Luke (2001) tested the density and Poisson's ratio of cemented material cored at the EGTS. The density was found to be 2500 kg/m<sup>3</sup> and the Poisson's ratio was 0.23. In their seismic downhole measurement at the EGTS, Tecle et al. (2003) found the Poisson's ratio for a carbonate-cemented layer (at 3.25 m depth) to be 0.33. The difference between these two outcomes can be attributed to the fact that the sample tested in the lab is intact and very well cemented, while field measurements are affected by discontinuities, variable degree of cementation, and other heterogeneities occurring at the macro scale. The density and Poisson's ratio of cemented soils for this study are set to 2200 kg/m<sup>3</sup> and 0.25 respectively.

### 3.3 Theoretical Dispersion Curve Generation

The EDC and the MDC are generated for the ND and HVL profiles (Figures 3.1a and 3.2a, respectively). The effective velocity is always higher than that from the fundamental-mode Rayleigh wave. For the HVL profile, the fundamental mode and first higher mode DCs nearly intersect at 41 Hz. The corresponding velocity ratio, which is defined as the ratio between effective and fundamental-mode velocity, is shown in Figures 3.1b and 3.2b. The difference is larger at lower frequencies and reaches a constant value, very close to 1, with increasing frequency. For the ND profile, the ratio is greater than 1.1 for 4 out of 50 points, with a highest value of 1.12. For the HVL profile, the ratio is greater than 1.1 for 10 out of 50 points, with a highest value of 1.32. However, for the HVL profile, the points with the greatest ratio are concentrated within a much narrower frequency band.

### 3.4 Starting Model Generation

To start the inversion process, the first step is to have a starting model. A good starting model can improve the degree of convergence of the inversion algorithm and favor the correct solution when the solution is nonunique. An algorithm to generate a high-quality starting model based on the work of Liu et al. (2002) has been developed in the EGL (Luke and Calderón-Macías in press).

Density and Poisson's ratio are assumed known with constant values of  $1700 \text{ kg/m}^3$  and 0.3 respectively. Thickness and  $V_S$  of the layers are assumed unknown and generated using the following process. Before solving for the unknown parameters, the preferred number of layers should be decided. Having an insufficient number of layers will not

capture important features in the data. Having more layers gives more flexibility to the profile and thus increases the chances of matching with the true layer interfaces. However, having too many layers may result in unrealistic too-thin upper layers. Hiltunen et al. (2006) reported that uncertainty in  $V_S$  is a function of the number of layers and the uncertainty increases with the increasing number of layers. In this research, based on experience and engineering practicality, it is required that the layers be greater than 0.15 m thick (Jin et al. 2003).

Once the number of layers is decided, several different potential layer geometries are obtained by using a family of exponential functions such that layer thickness increases exponentially with depth (Luke and Calderón-Macías in press):

$$h_i = Z_{hs} \left[ \frac{x_i - x_{i-1}}{1 - x_0} \right] \quad (3.2)$$

where

$h_i$  is the thickness of the  $i$ th layer;

$x_i = e^{\frac{c(i-n)}{n}}$ ,  $i = 1 \cdots n$ ,  $n$  is the number of layers;

$x_0 = e^{-c}$ ;

$Z_{hs}$  is the depth to the top of the halfspace and is normally set as one third of the maximum wavelength (Gazetas 1992); and  $c$  is the decay factor, normally in the range of 1 to 6.

The  $V_S$  of each layer is set equal to the Rayleigh wave velocity from the experimental dataset that corresponds to a wavelength that is three times the depth to the center of the layer. Once all the parameters in the model are set up, the appropriate corresponding forward model (SWAMI or SASWFI) is applied to generate the theoretical DCs for a

family of starting models having different decay factors. For multimode inversion, only the fundamental mode is considered in creating the starting model. The selection of a starting model from the family of candidates is based on the best fit between the target dispersion dataset and that generated from candidate starting models. The quality of the fit is quantified using the data difference (DD), which is defined as the root-square sum of the squared difference between dispersion datasets. The DD compares the theoretical (inverted) and target curve. It is calculated as follows:

$$DD = \sqrt{\sum_{j=1}^{NM} \sum_{i=1}^{NP} W_{ij} (T_i - E_i)^2} \quad (3.3)$$

where

$NP$  is the number of data points in the dispersion curve;

$NM$  is the total number of modes used in inversion;

$W_{ij}$  is the weight for the  $i^{\text{th}}$  data point of the  $j^{\text{th}}$  mode; and

$T_i$  and  $E_i$  are the theoretical and experimental wave velocity respectively at the  $i^{\text{th}}$  point.

The process can be repeated for different numbers of layers. Normally, the model with the lowest DD value that still satisfies the criterion for minimum layer thickness is selected as the starting model. However, based on experience, the author noted that the fit of the DCs at the low wavelength/high frequency limit is important for a good starting model. Thus, the DC with the best fit at low wavelength/high frequency band and reasonable fit overall might be favored over the one with the lowest DD value. The selection of the starting models for the ND and HVL profiles is illustrated in Figures 3.3 to 3.6. The numbers of layers for both profiles are selected as 3. The starting model for the MDC approaches for the ND profile is selected based on the best fit at low

wavelengths (Figure 3.4) while others are selected based strictly on the lowest DD values.

### 3.5 Inversion

The generated theoretical DCs serve as the target DCs for inversion. As mentioned in Chapter 2, the inverted  $V_S$  profile is composed from a background profile overprinted with one or more HVLs for the SA inversion (Luke and Calderón-Macías in press). For the background profile, the  $V_S$  is perturbed randomly within a user-specified range which is normally defined as between half and twice the  $V_S$  of the corresponding layer in the starting model. The search parameters for the HVL include depth, thickness and  $V_S$ . The ranges for them are set based on prior information available. The probability of encountering the HVL in the inversion can be specified based on the reliability of the prior information. This specification is achieved by allowing the SR for thickness to vary from a negative value to a positive one. If the solution gives a negative layer thickness, the HVL is considered not to exist and is omitted. The more negative the value, the lower the probability that a HVL will result (i.e., the lower the reliability of the prior information (Huynh et al. 2003)). Density and Poisson's ratio are specified based on prior information and engineering judgment.

LI follows the SA method. The LI model parameters, density, Poisson's ratio and thickness of each layer, are the output from SA. The  $V_S$  is the only parameter updated for each iteration. The LI method has an unconstrained search, so it is possible that the final solution falls outside the boundaries imposed during SA.

As mentioned in Chapter 2, three SA-LI runs are performed for each inversion with identical parameters and SR and the velocity-averaged profile of the three SA-LI

solutions is then considered as the final inverted profile. The average profile tends to give some too-thin layers due to the different geometries from three runs. The location of those too-thin layers is within the SR of the HVL. To address those unrealistic too-thin layers, two alternative averaging methods can be used. The first method has been used for all the cases when the problem occurs. The second method is tested and compared to the first method for the case of the HVL profile in Chapter 5.

1. If the layer is less than 0.15 m thick, it is combined into the layer above or underneath that has the smaller velocity difference. The velocity of the combined layer is calculated as below:

$$v = \frac{v_{i-1}h_{i-1} + v_i h_i}{h_{i-1} + h_i} \quad (3.4)$$

where  $i$  is the layer number and  $h$  its thickness.

If the thin layer is at the surface, it is combined into the layer underneath.

2. The inverted  $V_S$  profile is composed from a background profile overprinted with one or more HVLs, consequently the background model can first be averaged as-is. Then for the HVL, its depth, velocity and thickness are averaged independently as follows:

$$H_{HVL} = \frac{h_1 + h_2 + h_3}{3} \quad (3.5)$$

$$V_{HVL} = \frac{v_1 h_1 + v_2 h_2 + v_3 h_3}{3H_{HVL}} \quad (3.6)$$

$$D_{HVL} = \frac{v_1 h_1 d_1 + v_2 h_2 d_2 + v_3 h_3 d_3}{v_1 h_1 + v_2 h_2 + v_3 h_3} \quad (3.7)$$

where  $D_{HVL}$ ,  $H_{HVL}$ , and  $V_{HVL}$  are the averaged depth, thickness and velocity respectively of the HVL;  $d_i$ ,  $h_i$  and  $v_i$  ( $i=1\cdots 3$ ) are the depth, thickness and velocity



respectively of the HVL from the  $i^{\text{th}}$  run.

Thus, the average profile would be the average background profile overprinted with the average HVL.

For the MDC approach, the inversion process is performed on (1) fundamental mode DC alone (MDC/PF analysis) and (2) fundamental and first higher mode DC simultaneously (MDC/PM analysis). When more than one mode is considered in the inversion, weights are assigned to each mode. The rationale behind choosing the weight was that the value of the weight for the mode is proportional to its energy content. Thus, theoretically, the weight for each mode at each frequency should be assigned based on its energy contribution at that frequency. Based on the literature review the author performed, no researchers have used this procedure. The selection of weights here is quite subjective. Beaty (2002) inverted the first three modes simultaneously using weights for the fundamental, first higher and second higher modes of 0.5, 0.25 and 0.25 respectively. The fundamental mode shows more dominance in ND cases. As displayed in Figure 3.1, the EDC follows the shape of the fundamental mode DC and does not jump to the higher-mode DC. Thus, weights for fundamental and first higher mode are set 0.9 and 0.1 respectively for the MDC/PM analysis. For the HVL profile, weights for fundamental and first higher mode are set 0.75 and 0.25 respectively, giving heavier contribution to the first higher mode than in the case of the ND profile. Better ways to assign the weights should be sought in future research.

No prior information is considered for the ND profile. For the HVL profile, the range of depths bounding the possible HVL is set from 1 to 5 m, the range of thickness from (-0.5) to 2 m and the range of  $V_s$  from 1000 to 2000 m/s. The search range for the

thickness corresponds to a probability (P) of finding a HVL of 0.8.

### 3.6 Interpretation of Results

The quality of the results from inversion can be evaluated by DD, and the model resolution matrix (RM) and posteriori covariance matrix (CM) (Calderón-Macías and Luke 2002). For a synthetic study where the true model is known, the quality of the results can be easily evaluated using the profile difference (PD). To simplify both visual and numerical comparisons between  $V_S$  profiles having different layer geometries, the concept of equivalent mean (EM) profile is introduced. The EM is a best-fit profile to the target constrained by a different geometry (Calderón-Macías and Luke 2002). It is generated by weighting velocities of the target profile with the layer geometry of the alternate profile. The PD indicates how close the two profiles are. It is defined as:

$$PD = \frac{S}{Z_{hs}} \quad (3.8)$$

where  $S$  is total area between EM and the  $V_S$  profile from inversion processing over the depth from the surface to the top of the half-space and  $Z_{hs}$  is the depth to the top of the halfspace. It is noted that a difference between EM and  $V_S$  profiles at the halfspace will not affect the PD.

The RM and CM are  $n \times n$  matrices, where  $n$  is the number of layers in the model plus one for the halfspace. If the estimated model is equal to the true model, the RM is an identity matrix. The farther the resolution matrix is from the identity matrix, the lower the resolution is and the more a layer velocity becomes dependent on other layers' velocities. The RM depends on the forward modeling and the starting model, not the measured data (target). Thus, it is possible to have a perfectly resolved RM when the solution is not

representative of the true model (Luke and Calderón-Macías in press). In this dissertation, each RM matrix is normalized independently so that the highest value is always unity.

The diagonal elements in the CM give the square root of the standard deviation of the velocity of the layer. The off-diagonal elements in the CM give a measurement of the tendency for layer velocities to vary with respect to one another. If  $CM(i,j) > 0$ , the velocities of the  $i^{th}$  and  $j^{th}$  layers increase or decrease together. If  $CM(i,j) < 0$ , the velocity of one layer increases while that of the other layer decreases or vice versa. The further the off-diagonal element is from zero, the stronger the velocities of the two layers are interdependent. Low interdependence implies high resolution. In this dissertation, each CM matrix is presented using the same scale, from  $(-100)$  to  $100$ .

### 3.6.1 Results for the ND Profile

Resulting DD and PD from three inversion runs for the ND profile using the EDC/CM, MDC/PF and MDC/PM analyses are presented in Table 3.3 and Figure 3.7. Results among the three runs were consistent except for one DD value for the EDC approach. Excepting that anomaly, both the DD and PD for the EDC approach are approximately half that for the MDC approaches.

Figures 3.8 to 3.10 show the results from the EDC/CM analysis. Results include the model fits to the target DC (Figure 3.8), the final  $V_S$  profiles for three runs compared against the target and the starting model and the search range (Figure 3.9a), the average  $V_S$  profile from the three runs compared against the target and EM profiles (Figure 3.9b), and the three RMs and CMs (Figure 3.10) from the three inversion runs.

Two inverted profiles have virtually identical results that nearly match the EM.

However, run 1, the one that has the anomalously high DD, overestimates the velocity of the halfspace. The PDs of the three runs are close because the mismatch of the halfspace is not taken into account in the calculation. The average profile matches well with the EM profile. The RMs display near-perfect resolution for all three runs. The CMs from runs 2 and 3 are similar, showing little to moderate dependence between layers with a higher standard deviation for the halfspace, despite the fact that the  $V_S$  of the halfspace is perfectly resolved. Despite the worse fit from run 1, its CM shows less dependence between layers and lower standard deviation of the layers except the halfspace with respect to the CMs from the other two runs.

Figures 3.11 to 3.14 show the results from the MDC approach following the same format presented for the EDC approach. The numbers on the image to the right of each mode indicate the mode order. The six inverted profiles are virtually identical. They fit the first and third layers but overestimate the velocities of the second layer and halfspace. The uniformity of the outcome improves confidence in the results. For both the MDC/PF and MDC/PM analyses, the RMs and CMs for the three runs are consistent. Although the inverted profiles are similar to each other, the RMs for the MDC/PF analyses show much better resolution. For the MDC/PF analysis, all the CMs show a higher standard deviation for the second layer and halfspace. For the MDC/PM analysis, the CMs show much lower values for standard deviation and interdependence, though patterns are similar.

In summary, all inverted  $V_S$  profiles are adequate. Incorporation of the first higher mode into the inversion does not improve the results at all. The reason is due to the dominance of the fundamental mode in the ND system.

### 3.6.2 Results for the HVL Profile

Following the same format laid out for the ND profile, resulting DD and PD from three inversion runs for the HVL profiles using the EDC/CM, MDC/PF and MDC/PM analyses are presented in Table 3.4 and Figure 3.15. Both DD and PD from MDC/PM are consistently lowest. Most values, but not all, are much higher than those for the ND profile. Results are more variable than they were for the ND profile.

Figures 3.16 to 3.18 show the results from the EDC/CM analysis. The target DC exhibits scatter from 30 to 40 Hz. In that range, none of the theoretical DCs match the target. The DD value from run 2 is slightly greater than the rest because of the DC mismatch at high frequency range in addition to the above frequency band. They all yield a solution that contains an HVL: the third layer from runs 1 and 3 and the fourth layer from run 2. The three inverted profiles fit well with the background of the target profile but show variation in the depth, thickness, and velocity of the HVL. The average profile matches well with the EM profile. All the RMs display high resolution with relatively lower resolution for the HVL. All the CMs show a higher standard deviation for the HVL. The RMs and CMs are virtually identical for runs 1 and 3, despite very different solutions for the HVL.

Figures 3.19 to 3.22 show the results from the MDC analysis. For the MDC/PF analysis, the DD and PD values of runs 1 and 2 are much greater than those of run 3. The theoretical DCs from the two runs having high DD and PD fit poorly with the target DC. Correspondingly for those two runs, the HVL was not located. It is important to note that the RMs for those two solutions still display good resolution. This may lead to misleading evaluation if RM is used alone to evaluate the result quality. Further, the CM

for run 1 shows far lower standard deviation than the rest; this too is misleading. Run 3 found the HVL and thus greatly reduced the DD and PD values. The RM and CM from this run yield no clue that this is the best of the three outcomes. Due to the poor results from two runs, however, the average profile from the three SA-LI solutions fits poorly with the target EM.

For the MDC/PM analysis, the DD and PD are significantly reduced. All the theoretical DCs fit well with the target DCs. It is important to note that the DC fit of the fundamental mode from the MDC/PM analysis is greatly improved with respect to the MDC/PF analysis. All the three runs yield a solution that contains a HVL: the third layer. Though the inverted profiles fit excellently with the target, the RMs are not perfect, having lower resolutions for the HVL and the layer underlying it. The CMs display relatively higher standard deviations for the HVL and the halfspace. The average profile from the three SA-LI solutions fits excellently with the target.

In summary, for the HVL profile, the EDC/CM analysis provides acceptable results. The HVL is acceptably resolved with variation in the depth, thickness, and velocity from three runs. For the MDC/PF analysis, some poor results are encountered with obvious misfit of DCs. The HVL is well resolved when the fit of DCs is good. The MDC/PM analysis provides excellent results; the HVL is excellently resolved. The significant improvement with respect to the MDC/PF analysis is attributed to the influence of the higher mode or modes for this case.

### 3.6.3 Results for the ND Profile with Incorrect HVL Expectation

The ND profile with prior information incorrectly anticipating a HVL is used to test the applicability of the two approaches in the case of incorrect prior information. The prior information used here is the same as that used for the HVL system.

Resulting DD and PD from three inversion runs using the EDC/CM, MDC/PF and MDC/PM analyses are presented in Table 3.5 and Figure 3.23. All the DD are as low as for the ND profile (Figure 3.7). The DD among the three runs were consistent from the EDC/CM and MDC/PM analyses. The MDC/PM analysis has consistently lowest PD and the EDC/CM analysis has consistently highest PD. For the MDC/PF analysis, inverse results between DD and PD are noted. The better DD from runs 1 and 3 correspond to worse PD values with respect to that from run 2.

Figures 3.24 to 3.26 show the results from the EDC/CM analysis. The theoretical DCs fit well to the target DC, though all the inverted profiles yield a profile that contains a HVL. Due to the existence of the HVL generated from the inversion, the average profile matches poorly with the EM profile. The RM for run 1, whose HVL has the greatest thickness of the three runs, shows poor resolution. However, the RMs for runs 2 and 3 display good resolution except for the HVL. The CMs show little to moderate dependence between layers and the layer having greatest standard deviation is inconsistent among the three runs.

Figures 3.27 to 3.30 show the results from the MDC approach. The theoretical and target DCs fit well. For the MDC/PF analysis, two runs yield a profile that contains a HVL. For the MDC/PM analysis, results are consistent and none of the three inverted profiles yield a profile that contains a HVL. The three inverted profiles, average profile

and their corresponding RMs and CMs except RM for run 2 are all similar to those from inversion of the MDC/PM for the ND profile without prior information (Figures 3.9 and 3.10). The  $V_S$  of the second layer and halfspace are also consistently overestimated. It is interesting to note that the RM for run 2 is different from the others despite the nearly identical results.

In summary, for an ND profile with incorrect expectation of an HVL, all solutions yield good DC fits but some erroneously identified an HVL. The EDC/CM analysis always found a solution that incorrectly yielded a profile with a HVL, but still had a good match with the theoretical DC. One solution that has the greatest thickness for the HVL of the three runs shows poor resolution, while the other two display good resolution. Similarly, the MDC/PF analysis might accept the incorrect prior information. The MDC/PM analysis is quite immune to the incorrect prior information. It yields good results, despite the RM showing poor resolution.

### 3.7 Discussion

The quality of the inversion results can be evaluated by a combination of values of DD, image of RM and CM, observed error between the DC fits and repeatability of results. For the synthetic study where the true model is known, the results can be readily evaluated by evaluating the PD and comparing the inverted profile to the EM profile.

The RM and CM are closely related; low interdependence of the velocity of one layer to another implies higher resolution. A perfect result has perfect RM and CM, but perfect RM and CM do not guarantee a perfect result. Sometimes, poor RM and CM might not refer to a poor result either. Thus, it is important to note that RM and CM considered



alone can lead to a misleading evaluation.

Another simple, but not foolproof, way to evaluate the results is by visually inspecting the fit between the DCs. The repeatability of the results also helps to build confidence in the results. If great variability is displayed in the three runs, the average profile might not be very accurate. More runs are recommended to look for trends.

For the ND profile, all inversion analyses provide good results. The incorporation of the first higher mode into inversion does not improve the results at all, due to the dominance of the fundamental mode for this case.

For the HVL profile, the EDC/CM analysis provides acceptable results. For the MDC/PF analysis, poor results are encountered with obvious misfit of DCs. For the MDC/PM analysis, the results and the goodness-of-fit between the theoretical and target fundamental-mode DC are significantly improved from the MDC/PF analysis. The improvement is attributed to the influence of the higher mode or modes for this case.

Given the opportunity, the EDC/CM analysis tends to yield a profile with a HVL when none is present. The MDC/PF analysis sometimes responds similarly, but the MDC/PM analysis is quite immune to the incorrect prior information.

Overall, for an HVL system, inversion following MDC/PM analysis provides the best results of the three inversion analyses. Less reliable is the EDC/CM analysis and the least accurate is the MDC/PF analysis.

Table 3.1. Layer properties of the ND profile. Water table assumed to be at 2 m depth.

Layer number	Thickness (m)	Shear wave velocity $V_S$ (m/s)	Compression wave velocity $V_P$ (m/s)	Poisson's ratio $\nu$	Density (kg/m <sup>3</sup> )
1	2.0	200	370	0.30	1700
2	5.5	400	1500	0.46	1700
Half-space		600	2200	0.46	1700

Table 3.2. Layer properties of the HVL profile. Water table assumed to be at 3.5 m depth.

Layer number	Thickness (m)	Shear wave velocity $V_S$ (m/s)	Compression wave velocity $V_P$ (m/s)	Poisson's ratio $\nu$	Density (kg/m <sup>3</sup> )
1	2.0	200	370	0.30	1700
2	1.5	1500	2600	0.25	2200
3	4.0	400	1500	0.46	1700
Half-space		600	2200	0.46	1700

Table 3.3. Summary of the results for the ND profile.

Run number	EDC/CM		MDC			
			PF		PM	
	DD	PD	DD	PD	DD	PD
1	68	14	27	38	32	31
2	12	15	27	38	32	31
3	12	15	27	38	31	32
Avg.		8		38		31

Table 3.4. Summary of the results for the HVL profile.

Run number	EDC/CM		MDC			
			PF		PM	
	DD	PD	DD	PD	DD	PD
1	112	111	119	443	5	25
2	134	340	119	443	23	117
3	117	94	17	116	10	34
Avg.		128		334		52

Table 3.5. Summary of the results for the ND profile with incorrect HVL expectation.

Run number	EDC/CM		MDC			
			PF		PM	
	DD	PD	DD	PD	DD	PD
1	31	199	11	118	32	32
2	31	91	27	38	32	32
3	30	112	12	204	32	32
Avg.		126		107		32

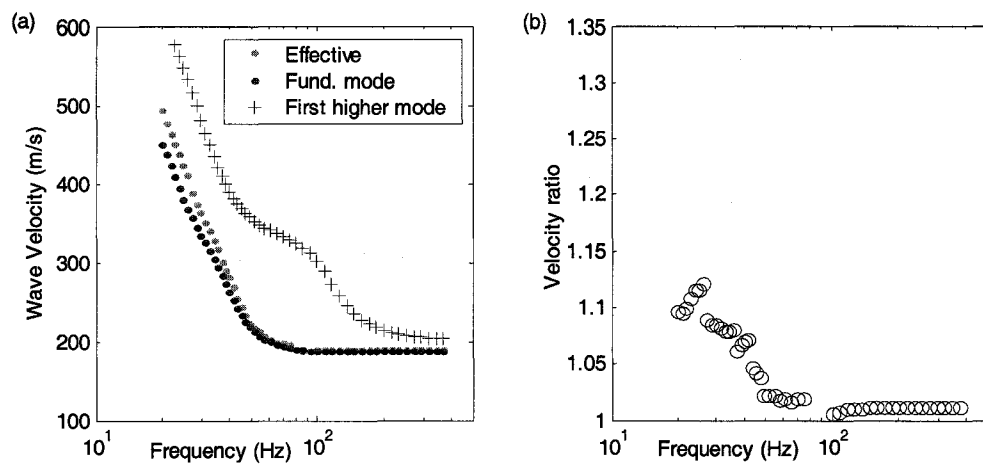


Figure 3.1. ND profile: (a) DCs; (b) velocity ratio between EDC and fundamental mode

DC.

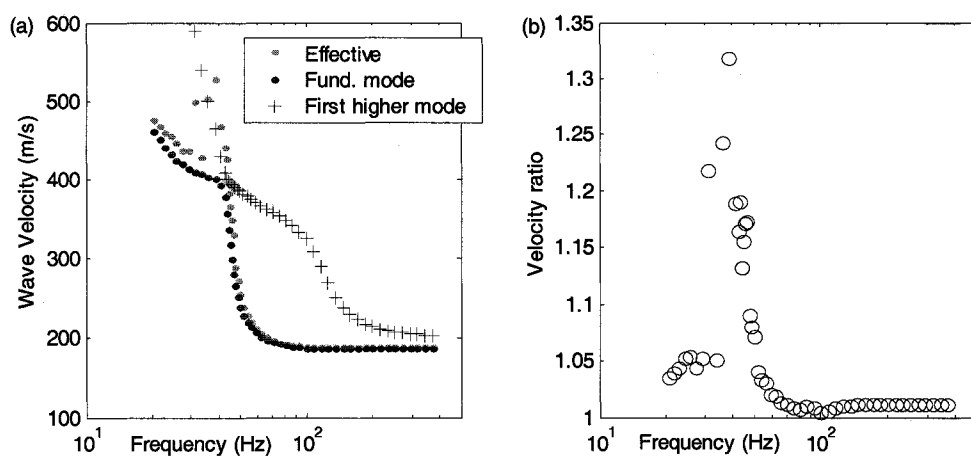


Figure 3.2. HVL profile: (a) DCs; (b) velocity ratio between EDC and fundamental mode

DC.

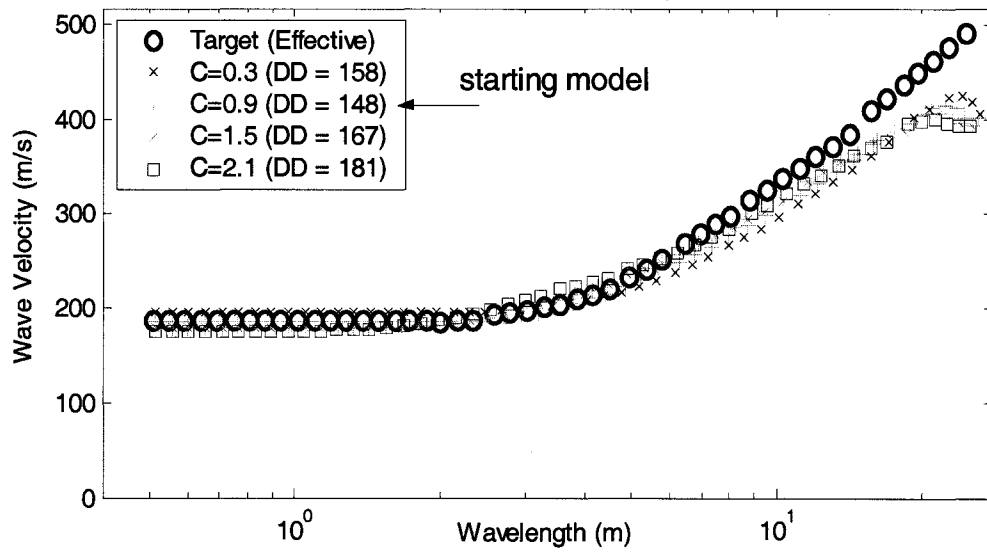


Figure 3.3. ND profile: starting model for the EDC approach.

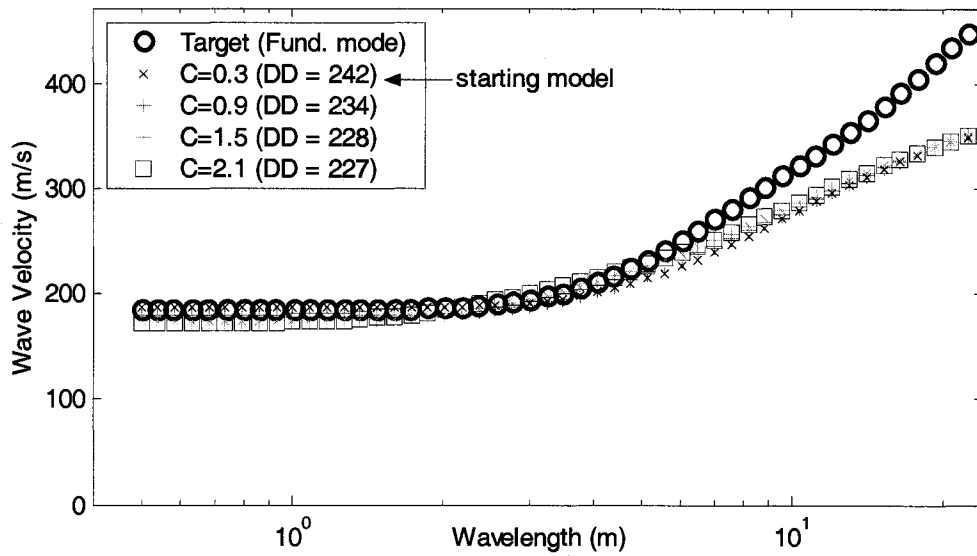


Figure 3.4. ND profile: starting model for the MDC approach.

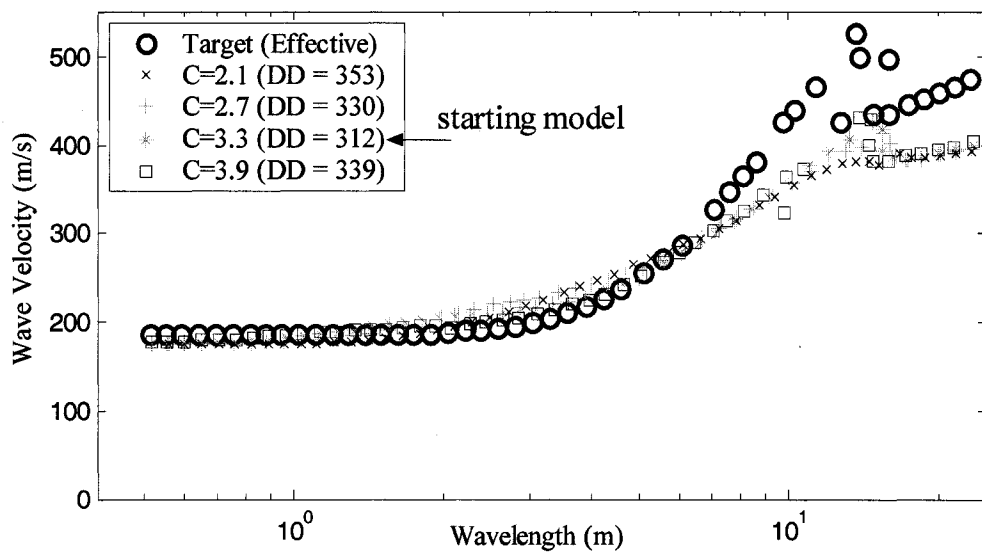


Figure 3.5. HVL profile: starting model for the EDC approach.

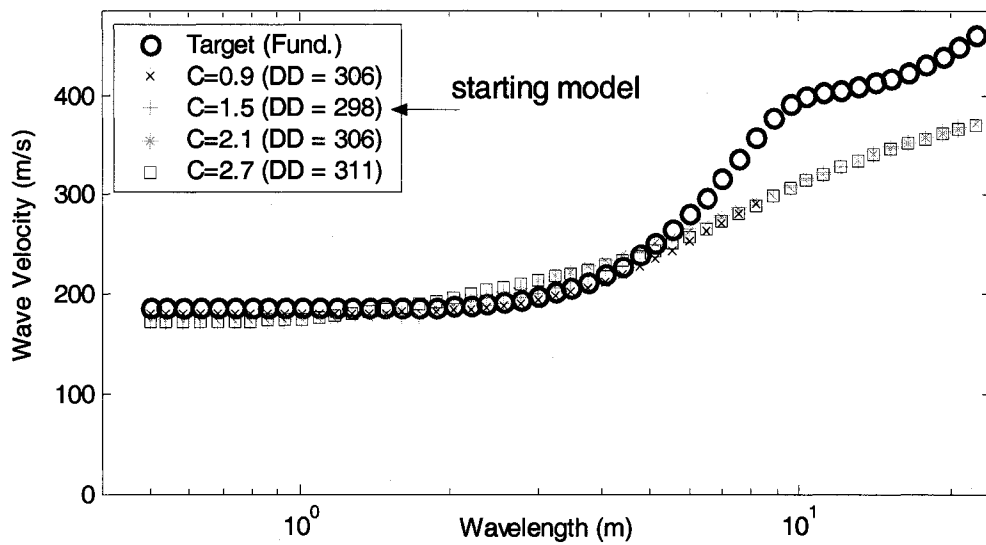


Figure 3.6. HVL profile: starting model for the MDC approach.

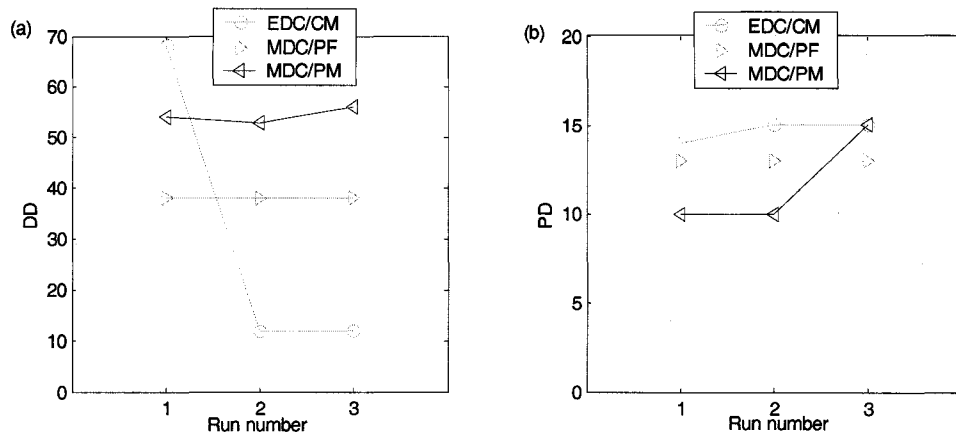


Figure 3.7. ND profile: comparison of (a) DD values, (b) PD values.

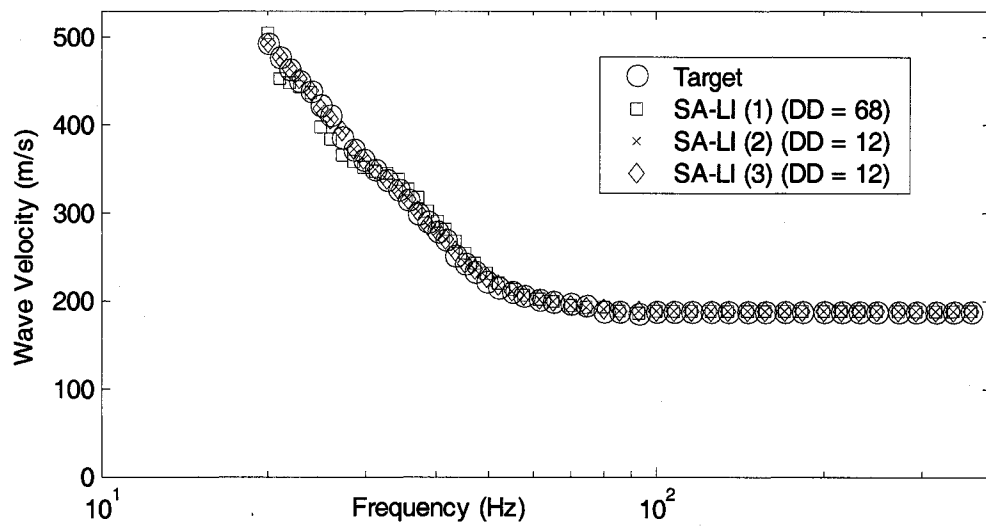


Figure 3.8. ND profile, EDC/CM: comparison of DCs.



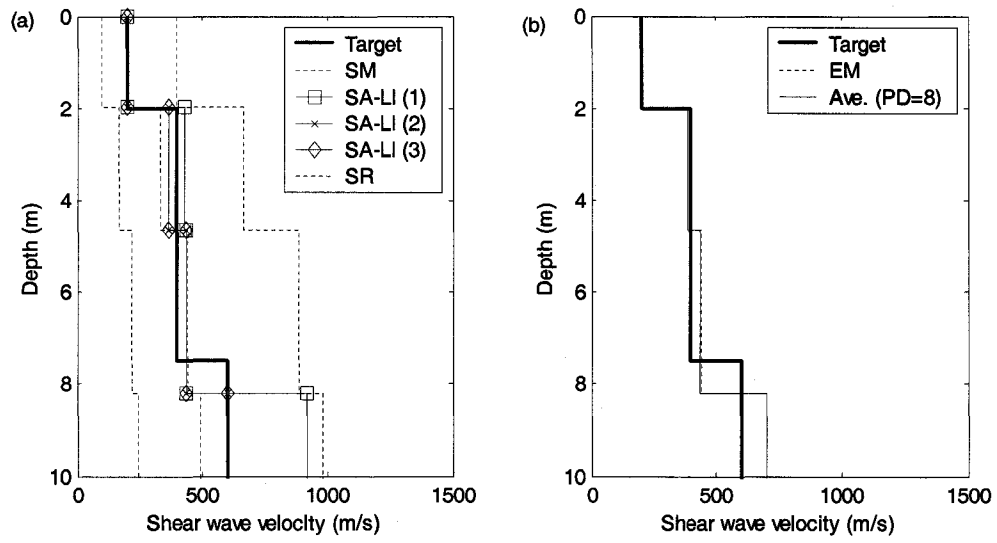


Figure 3.9. ND profile, EDC/CM:  $V_s$  profiles for (a) three runs (b) average.

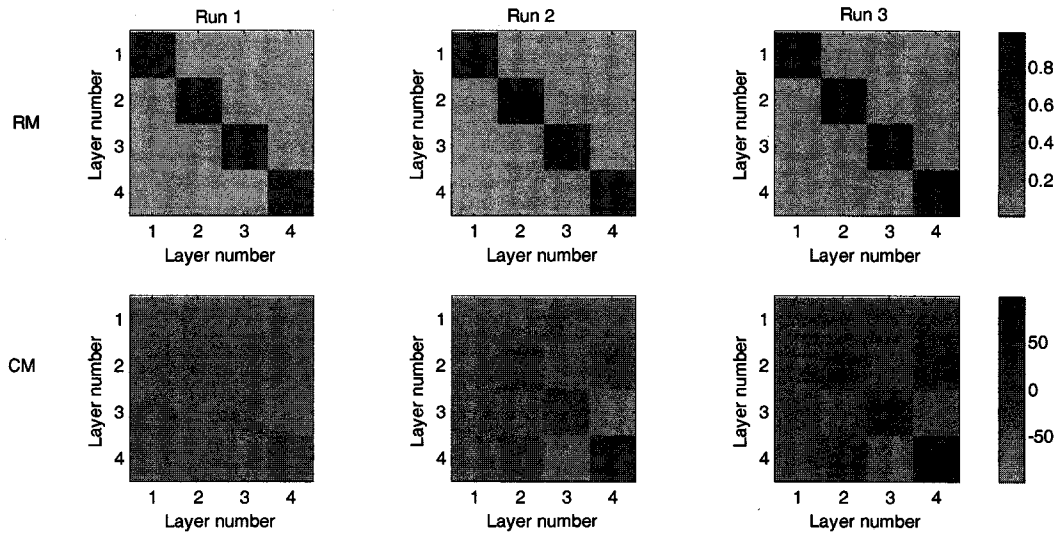


Figure 3.10. ND profile, EDC/CM: RMs and CMs.

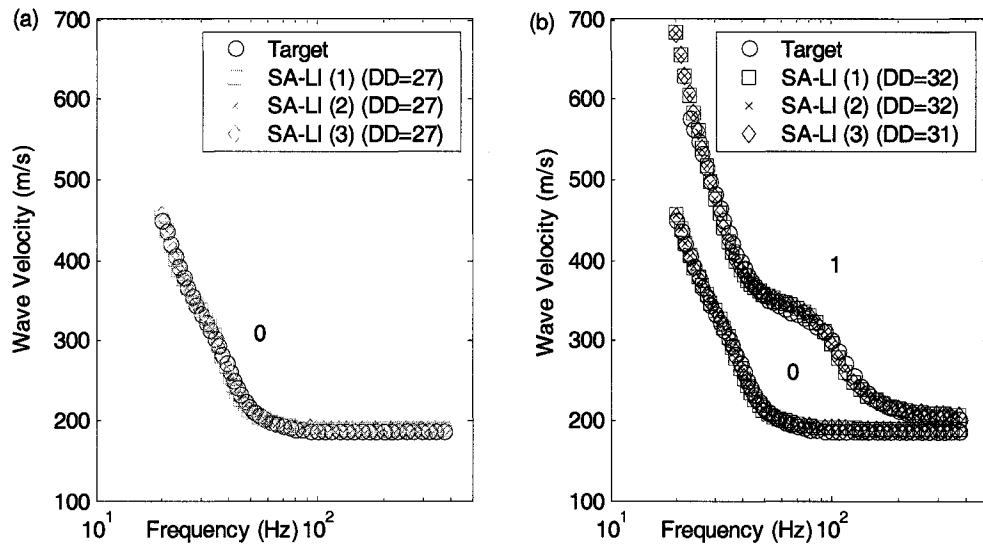


Figure 3.11. ND profile: comparison of DCs for (a) MDC/PF, (b) MDC/PM.

(The numbers on the image to the right of each mode indicate the mode order.)

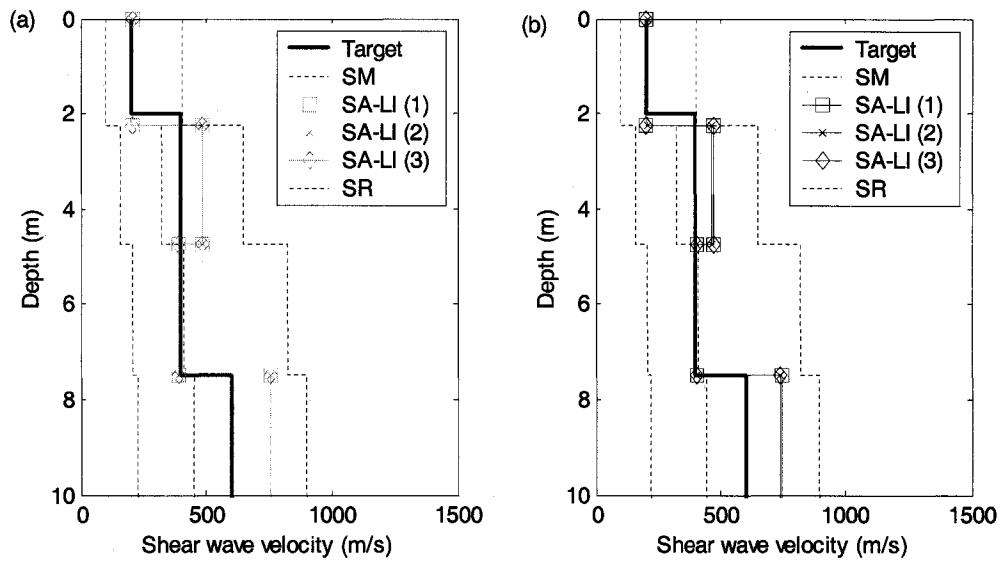


Figure 3.12. ND profile:  $V_S$  profiles from three runs (a) MDC/PF, (b) MDC/PM.

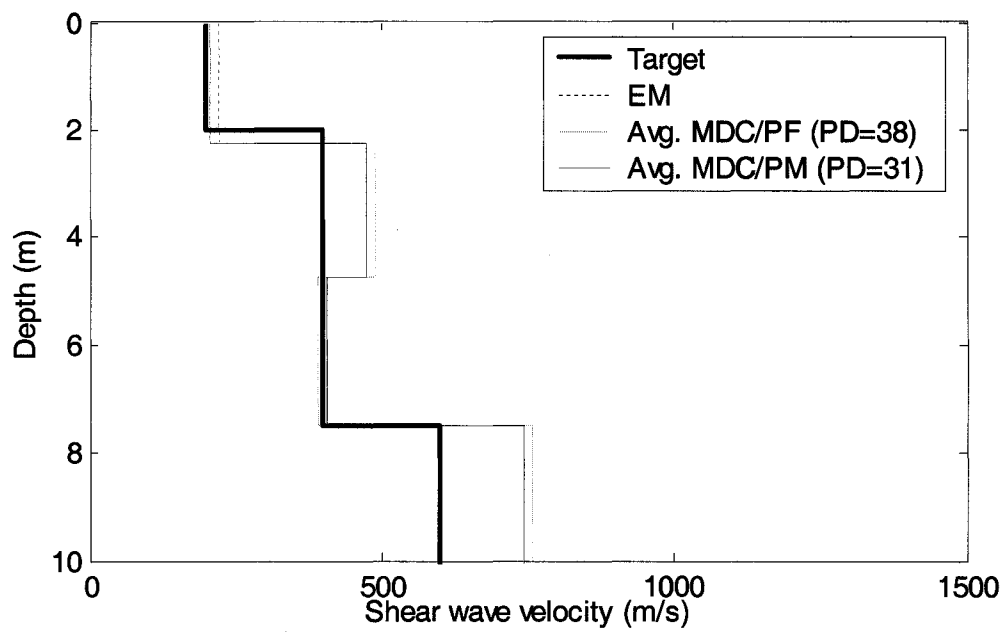


Figure 3.13. ND profile: average  $V_s$  profiles from MDC approach.

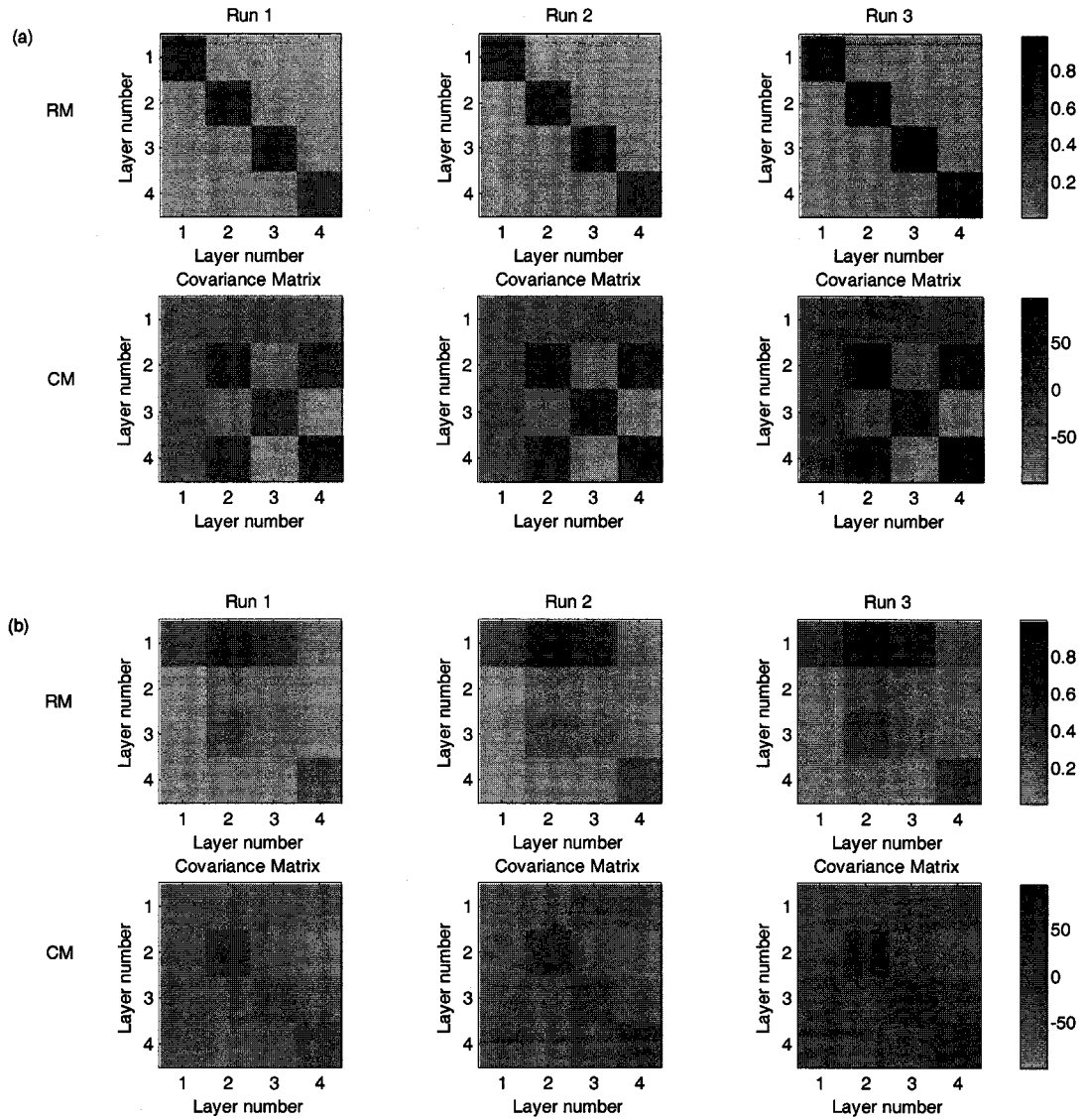


Figure 3.14. ND profile: RMs and CMs from (a) MDC/PF, (b) MDC/PM.

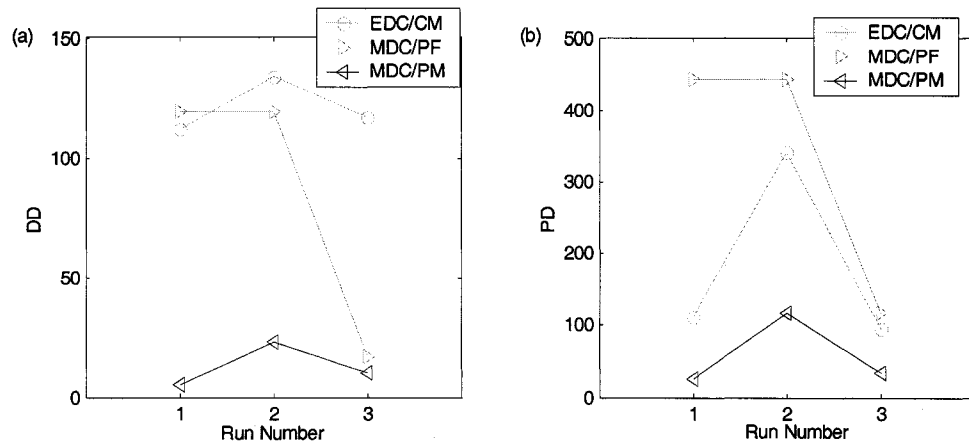


Figure 3.15. HVL profile: comparison of (a) DD values, (b) PD values.

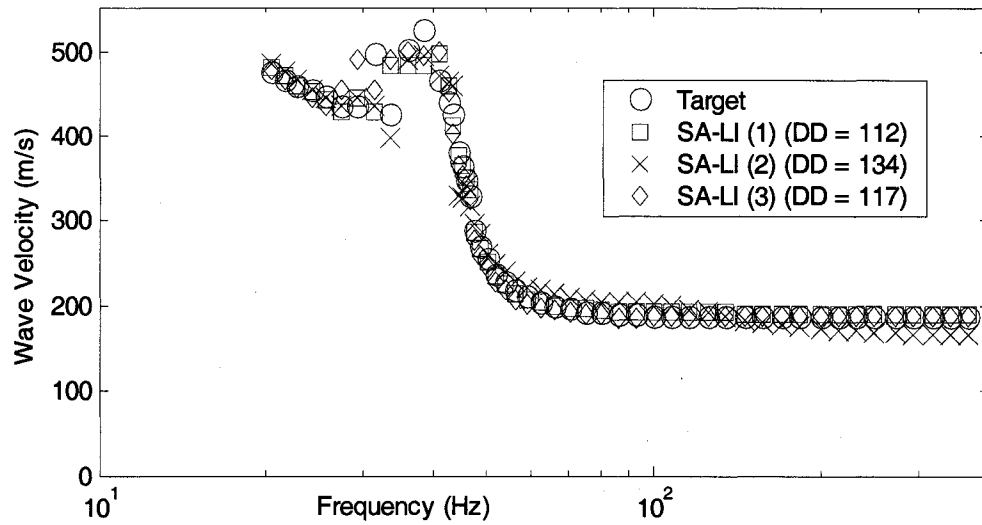


Figure 3.16. HVL profile, EDC/CM: comparison of DCs.

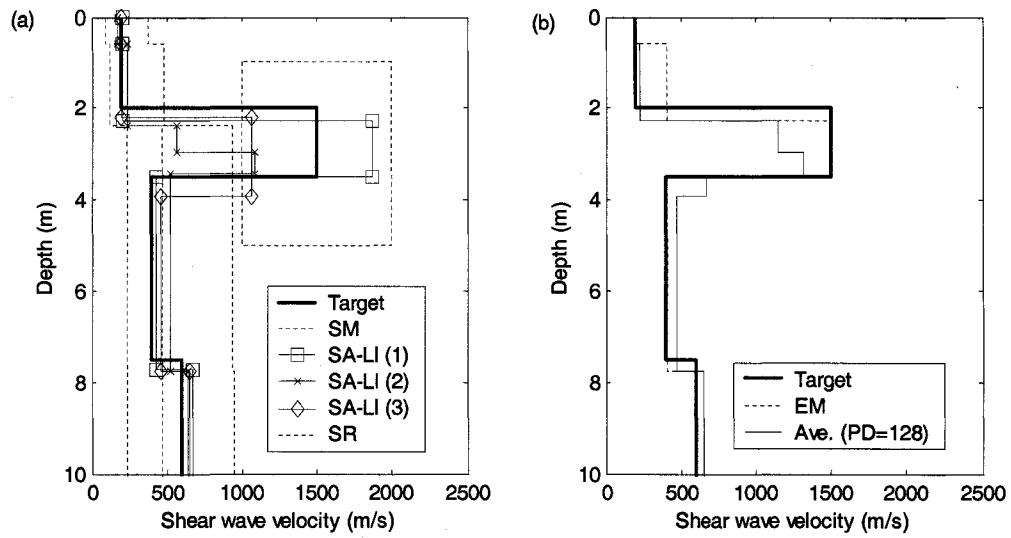


Figure 3.17. HVL profile, EDC/CM:  $V_S$  profile from (a) three runs (b) average.

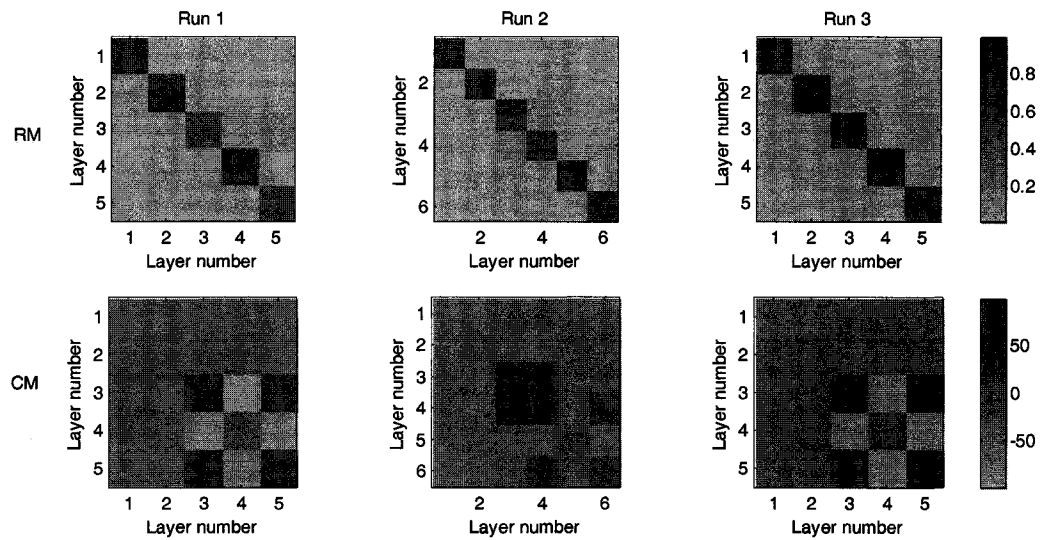


Figure 3.18. HVL profile, EDC/CM: RMs and CMs.

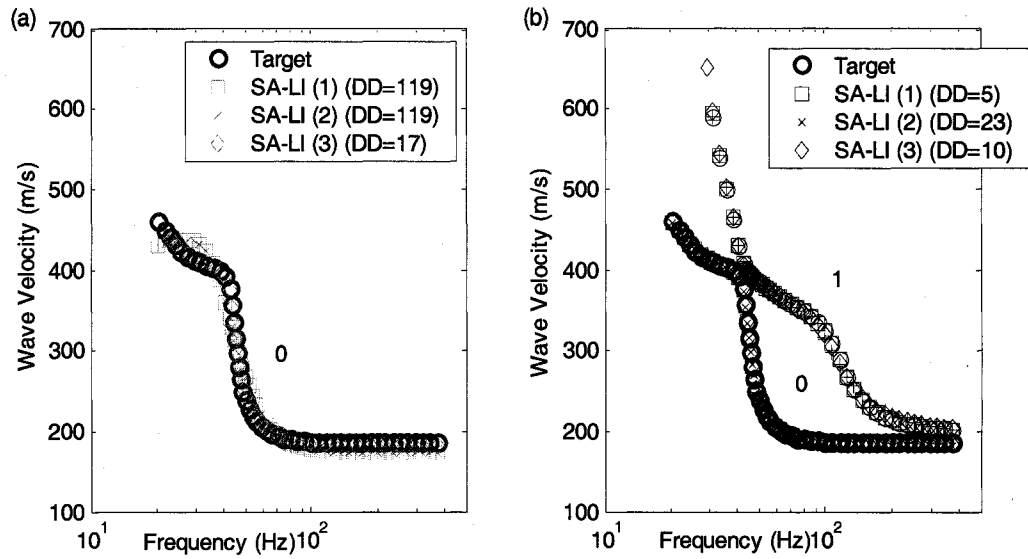


Figure 3.19. HVL profile: comparison of DCs for (a) MDC/PF, (b) MDC/PM.

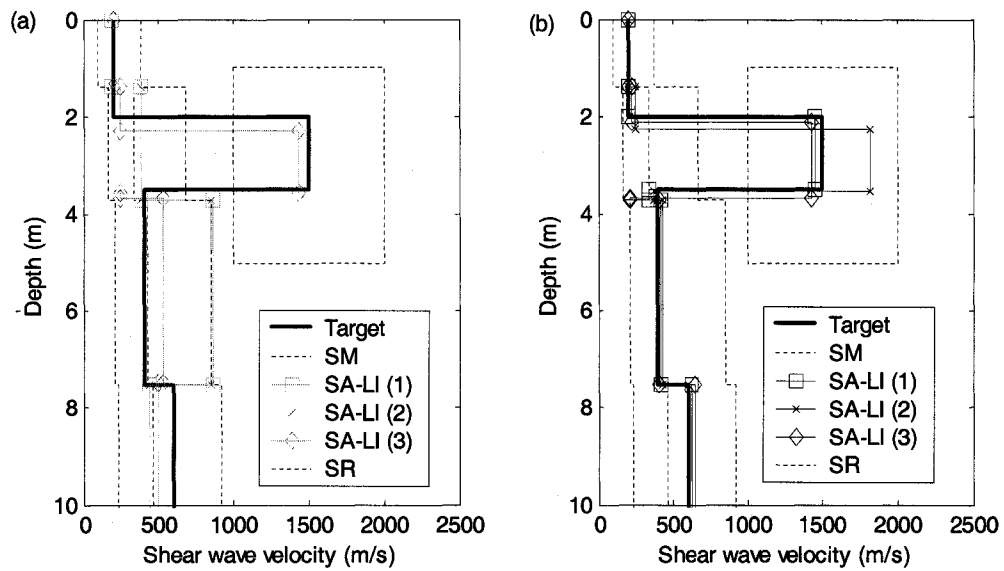


Figure 3.20. HVL profile:  $V_s$  profile from three runs for (a) MDC/PF, (b) MDC/PM.

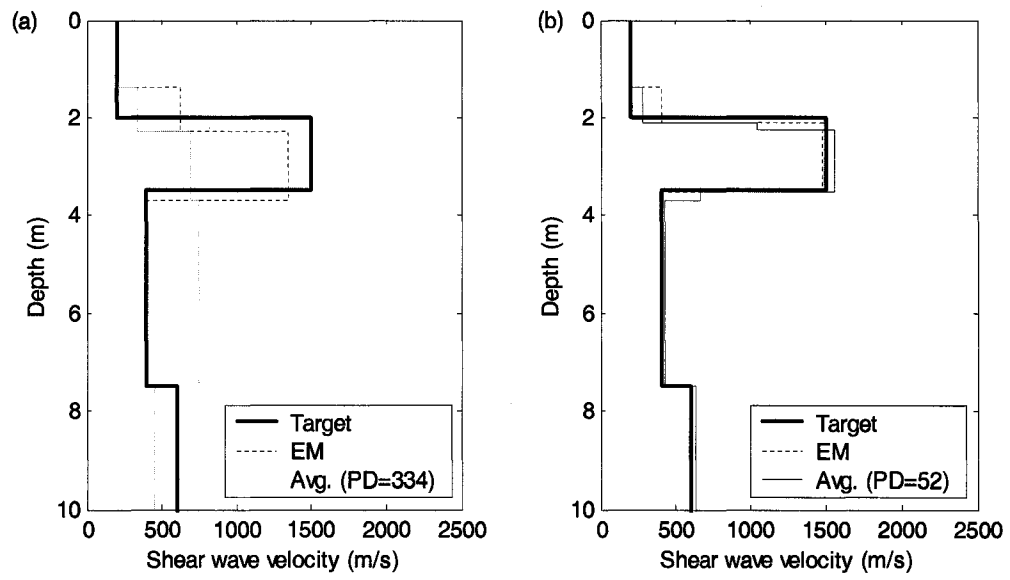


Figure 3.21. HVL profile: average  $V_S$  profile (a) MDC/PF, (b) MDC/PM.





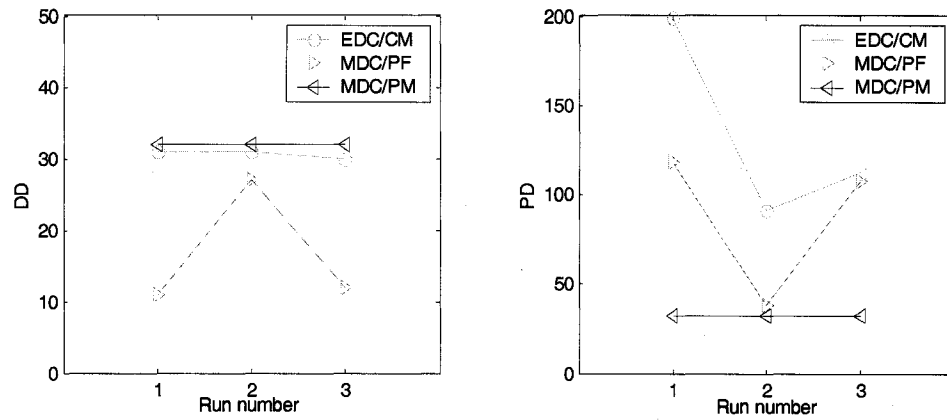


Figure 3.23. ND profile with incorrect HVL expectation: comparison of  
(a) DD values, (b) PD values.

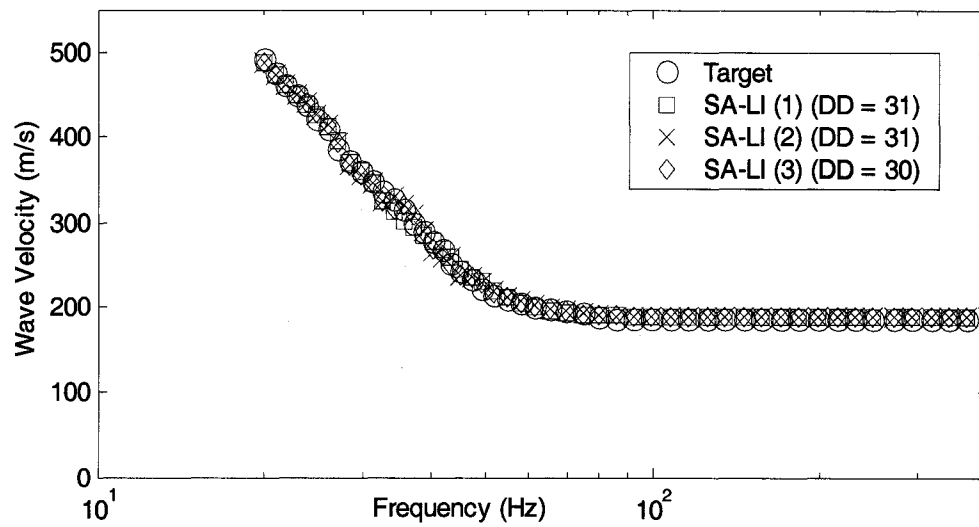


Figure 3.24. ND profile with incorrect HVL expectation, EDC/CM: comparison of DCs.

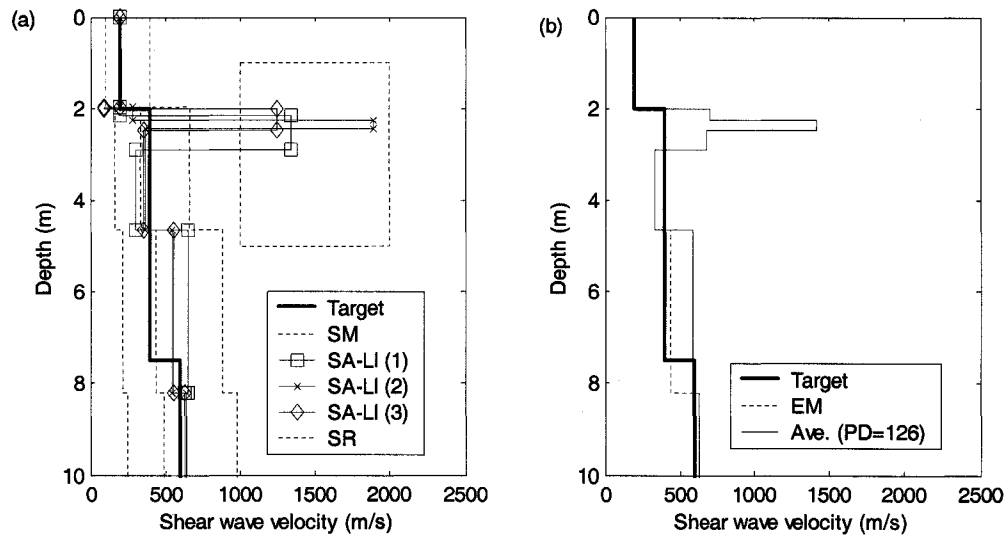


Figure 3.25. ND profile with incorrect HVL expectation, EDC/CM:  $V_S$  profiles for (a) three runs (b) average.

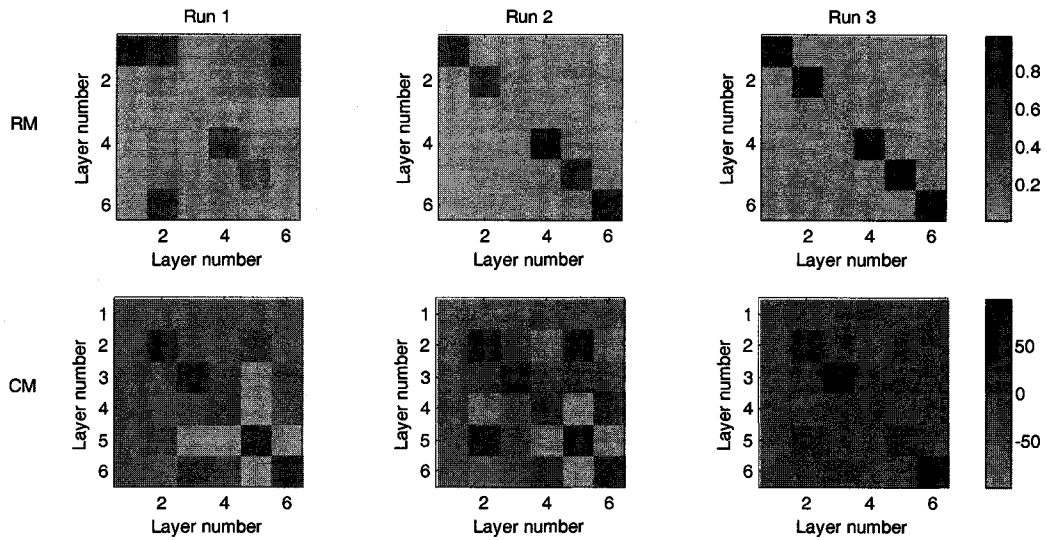


Figure 3.26. ND profile with incorrect HVL expectation, EDC/CM: RMs and CMs.

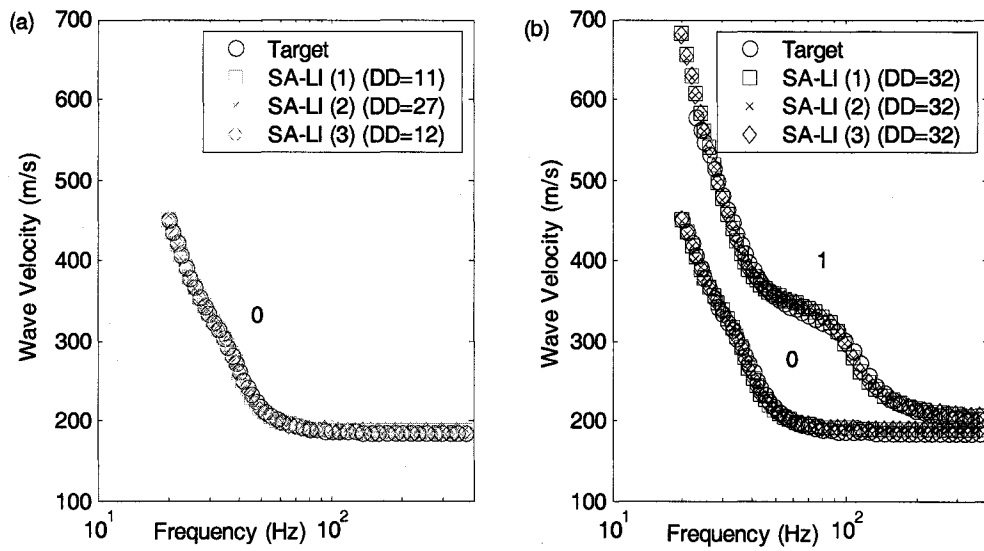


Figure 3.27. ND profile with incorrect HVL expectation: comparison of DCs for (a) MDC/PF, (b) MDC/PF.

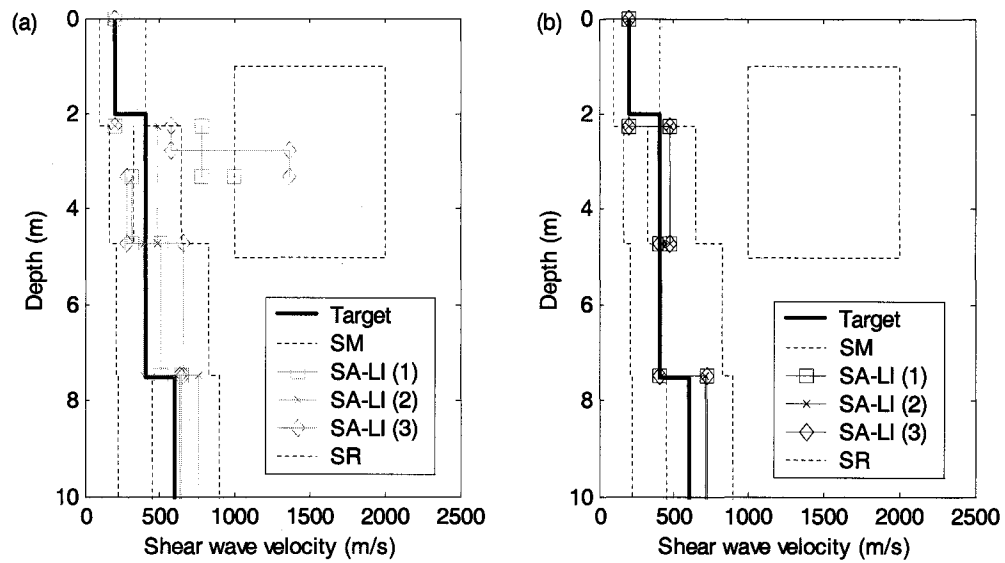


Figure 3.28. ND profile with incorrect HVL expectation:  $V_S$  profiles for three runs from (a) MDC/PF, (b) MDC/PF.

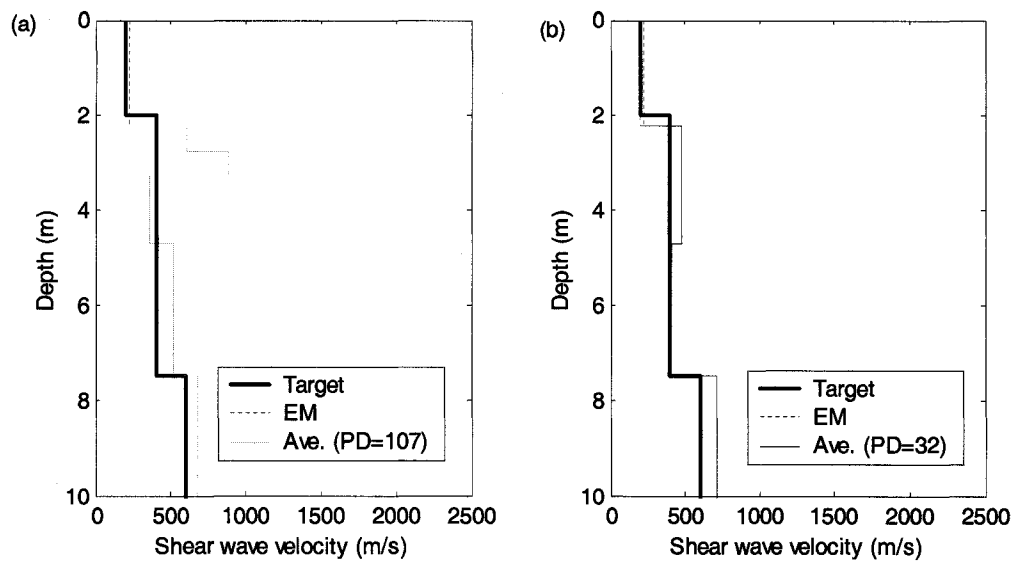


Figure 3.29. ND profile with incorrect HVL expectation: average profiles from (a) MDC/PF, (b) MDC/PM.

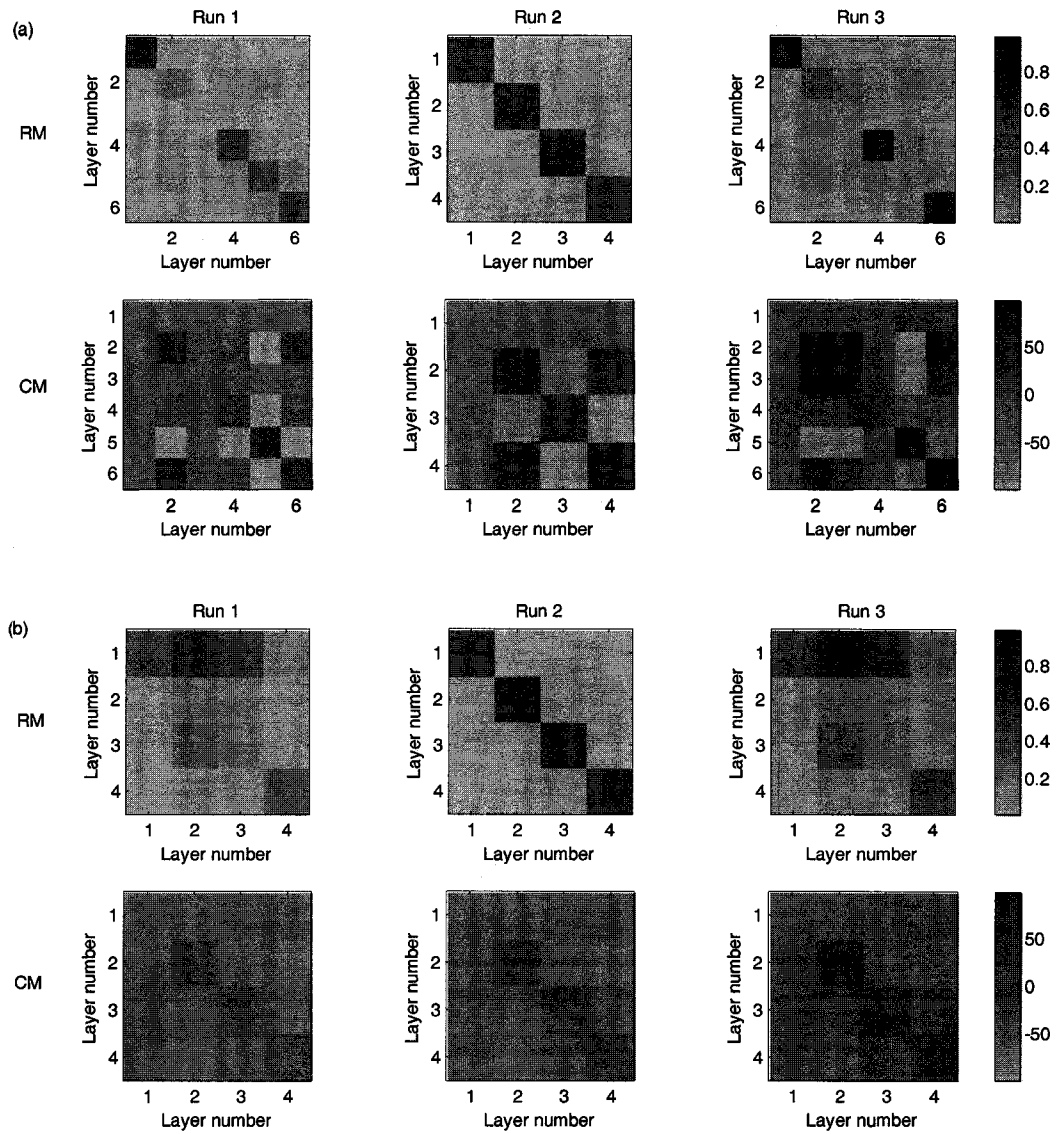


Figure 3.30. ND profile with incorrect HVL expectation: RMs and CMs for (a) MDC/PF, (b) MDC/PM.

## CHAPTER 4

### PRACTICAL STUDIES ON DELINEATING THE HVL SYSTEM

#### 4.1 Introduction

The focus of this chapter is a practical investigation of the HVL system to enhance the ability to identify the HVL. The same HVL profile used in Chapter 3 is used here. Two cases are studied. First, a sensitivity study was designed to examine the effects of depth of a HVL, thickness of the layer, and degree of velocity contrast on the surface-wave DC. Then, incorporation of prior information from a seismic body wave refraction measurement into the inversion analyses is tested. The inversion outcomes are compared to those from Chapter 3.

#### 4.2 Effect of HVL in Soil Profiles on DCs

Information about depth, thickness and velocity of the HVL are all significant in engineering. Variation of any of these three parameters will induce some variation on the dispersion relation, which is a “signature” of the site. To examine the effects of these parameters on the dispersion relation, four profile models designated as RP, DP, HP and VP were created. The geometry and velocities for each profile are shown in Table 4.1. The RP is the reference profile and is identical to the HVL profile in Chapter 3. With respect to the RP, the three other profiles had one parameter modified, while other layer

properties remain unchanged. In the DP, HP, and VP, the depth, thickness and velocity, respectively, of the HVL was increased by 10% (Figure 4.1).

Feng et al. (2005) proposed simple equations to describe the sensitivity of  $V_S$  derived from multi-mode inversion of plane wave propagation to the variation of the velocity and thickness of profile layers as a function of frequency. Here, the equations are applied only to the HVL. Further, this author extends the idea to define the sensitivity of  $V_S$  to the variation of the depth of the HVL in a like manner. The equations are defined as follows:

$$S_D = \frac{|V_R(f, D_{HVL} + \alpha D_{HVL}) - V_R(f, D_{HVL})|}{V_R(f, D_{HVL})} * 100\% \quad (4.1)$$

$$S_H = \frac{|V_R(f, H_{HVL} + \alpha H_{HVL}) - V_R(f, H_{HVL})|}{V_R(f, H_{HVL})} * 100\% \quad (4.2)$$

$$S_V = \frac{|V_R(f, V_{HVL} + \alpha V_{HVL}) - V_R(f, V_{HVL})|}{V_R(f, V_{HVL})} * 100\% \quad (4.3)$$

where  $D_{HVL}$ ,  $H_{HVL}$ , and  $V_{HVL}$  are the depth, thickness and velocity of the HVL respectively;  $S_D$ ,  $S_H$  and  $S_V$  are the sensitivities, in percent, of  $V_R$  to variation of the depth, thickness and velocity of the HVL respectively; and  $\alpha$  is the perturbation factor, set at 10% in this study.

For each profile, both EDC and MDC are generated. Figure 4.2 indicates the EDC and MDC from the RP, plotted as both velocity versus frequency and velocity versus wavelength. The EDC coincides with the fundamental-mode DC over most of the wavelength range, but increases by as much as 30% in the frequency range 30 to 45 Hz (wavelength range 9 to 15 m). Assuming that the effective sampling depth is equal to one-third of that wavelength, the corresponding depth is from about 3 to 5 m. This overestimates the depth and thickness of the HVL. However, it is adequate for a rough estimation (Figure 4.2).



The sensitivities of  $V_S$  to the depth, thickness and velocity of the HVL are shown in Figure 4.3. They are all displayed in terms of frequency and wavelength. The sensitivity function is quite irregular for the EDC while much smoother for the MDC.

Peak values of sensitivity are summarized in Figure 4.4. For both the EDC and MDC cases, the  $V_S$  shows the greatest sensitivity to the depth of the HVL and the sensitivities to the velocity and thickness are similar. For the three parameters, the EDC consistently has the greatest peak sensitivity and the first higher mode consistently has the least peak sensitivity. The peak sensitivity of the fundamental mode is intermediate.

For the variation of the depth, the peak sensitivities of EDC and fundamental mode DC occur at close frequency/wavelength. For the variation of the thickness and velocity, the peak sensitivity of EDC reaches its peak at lower frequency/higher wavelength than that of the fundamental mode DC.

The less sensitive the  $V_S$  is to the variation of the parameter, the more difficult it is for the inversion process to locate the real solution for that parameter. The more similar are the sensitivities to the variation of different parameters, the harder it is to distinguish the contributing parameter. The more sensitive is the  $V_S$  to the variation of the parameter, the greater is the effect of the parameter. Thus, for inversion of both EDC and MDC, it would be easiest to resolve the depth. Furthermore, due to the greatest effect of depth on the DCs, the DC fit could be most significantly improved if prior information of depth were known. This deduction is tested in the second half of this chapter. The effects of variation of thickness and velocity on the DC are similar and would be hard to distinguish from each other: the same effects on the DC might be caused by the variation of thickness alone, velocity alone or a combination of both. Due to the ambiguity of these two

parameters, if one parameter were restricted, one would expect the other one to be better resolved. In practice, the thickness of the HVL might be restricted based on prior information from a borehole log and its velocity can be restricted based on a refraction measurement.

#### 4.3 Inversion with Prior Information from Refraction Measurement

Because the carbonate-cemented HVL can be present at relatively shallow depths, it is feasible to use a refraction measurement to determine the depth to the HVL and the velocities of the upper layers and HVL. With respect to the P-wave refraction measurement, the result from a S-wave refraction measurement is more desirable. However, it is especially convenient to perform a P-wave refraction measurement when collecting surface wave data with multi-channel methods. The same datasets collected can be used for both refraction and surface wave analysis. As mentioned in Chapter 2, Ivanov et al. (2000a, 2000b; Ivanov 2002) used the Joint Analysis of Surface Wave and Refractions (JASR) method, whereby a two-dimensional vertical  $V_S$  slice generated from the MASW method serves as prior information and initial model for refraction tomography inversion. Here, oppositely, I use the information from refraction analysis as prior information for the surface-wave inversion process.

To incorporate the prior information from refraction analysis for the inversion processing, the starting model generation technique is first refined. Except that Eq. (3.2) is not used to generate the layer geometry for the upper one or more layers, other procedures for the starting model generation are the same as specified in Chapter 3. Here, the upper 2-m thick layer is assumed as known from the refraction measurement for the

starting model generation.

Using the technique presented in Chapter 3, the generated starting models for EDC and MDC approaches are shown in Figures 4.5 and 4.6. It is noted that excellent fit of the dispersion curves with the target was achieved at short wavelength.

Considering the uncertainty from the refraction measurement, in the SA inversion, the thickness and velocity of the first layer are allowed to vary within only  $\pm 25\%$  of the prior information from the refraction measurement. Thus, for the first layer, the SR for thickness was from 1.5 to 2.5 m and for velocity, 150 to 250 m/s. For the HVL, thickness ranged from 1 to 2 m and velocity ranged from 1000 to 2000 m/s. Thus, the range of depths bounding the possible HVL is from 1.5 to 4.5 m. The SR for the thickness corresponds to a probability of 1 of finding a HVL. Thus, the SR for the HVL is more restricted than that defined in Chapter 3. The LI inversion procedure is the same as specified in Chapter 3.

Resulting DD and PD from three inversion runs using the EDC/CM, MDC/PF and MDC/PM analyses are presented in Table 4.2 and Figure 4.7. Results from the MDC approach are more variable than those from the EDC approach.

Figures 4.8 to 4.10 show the results from the EDC/CM analysis. Visually, all the theoretical DCs fit well with the target DC except in the range of 30 to 45 Hz where the target DC exhibits scatter. The  $V_S$  of the top layer is perfectly resolved. For all runs, the depth of the HVL is overestimated. The thickness of the HVL is best resolved in this case, not the depth, which is opposite to the conclusion of the sensitivity study. The  $V_S$  of the resolved HVL for the three runs are within 10% of that of the target HVL. The average profile fits well with the EM profile and it is interesting to note that the fit looks better

than the EM. That is because the EM is calculated using the geometry of the average profile. The EM should be more representative mathematically, while the average profile might be more meaningful for engineering purposes. The higher  $V_S$  of the top layer from the EM is due to the contribution of the  $V_S$  of the HVL. With respect to the results in Chapter 3, the HVL is better resolved. The RM of run 3 shows poor resolution for the HVL despite that the HVL was resolved equally well in all runs. The CM from run 2 shows less dependence between layers and lower standard deviation of all layers except the HVL with respect to the CMs from the other two runs. However, its corresponding  $V_S$  profile is not noticeably better than that from the other two runs.

With respect to the results from the EDC/CM analysis observed in Chapter 3 (Figures 3.16 and 3.17), the depth of the HVL is also overestimated and the thickness and velocity of the HVL are better resolved.

Figures 4.11 to 4.14 show the results from the MDC approach. For both MDC/PF and MDC/PM analyses, one solution has a much smaller DD value than the other two in the three runs. It is noted that the depth of the HVL is best resolved in these two runs. The RMs of those two solutions show the best resolution of the three runs: good resolution overall with relatively lower resolution for the HVL. The other four solutions all overestimated the  $V_S$  of the half space and their RMs show low resolution for the half space. The average profiles from both MDC/PF and MDC/PM analyses fit well with the target. The velocity of the HVL is better resolved from MDC/PM. All the CMs display relatively higher standard deviation for the HVL.

Referring to the poor results from the MDC/PF analysis observed in Chapter 3 (Figures 3.20a and 3.21a), all three solutions are good here. This can be attributed to the

prior information from refraction that is stricter. With respect to the results from the MDC/PM analysis observed in Chapter 3 (Figures 3.20b and 3.21b), the HVLs are equally well resolved while the  $V_S$  of the half space tends to be overestimated here.

With respect to the outcomes for the same HVL profile with relatively less restrictive prior information observed in Chapter 3, the outcomes from the EDC/CM and MDC/PF analyses are better and the outcomes from the MDC/PM analysis are equally good. Still the MDC/PM analysis has the best results of the three inversion analyses.

The HVL is better resolved for all inversion analyses. For the MDC analysis, it is noted that for the cases where the depth is best resolved, run 3 from the MDC/PF analysis and run 2 from the MDC/PM analysis, the lowest DD and PD values occur. That is to say, the more accurately the depth is resolved, the closer is the solution to the target profile.

Table 4.1. Sensitivity study: layer properties of four target profiles.

			RP		HP		TP		VP	
Layer No.	Poisson's ratio	Density (kg/m <sup>3</sup> )	Thickness (m)	$V_s$ (m/s)	Thickness (m)	$V_s$ (m/s)	Thickness (m)	$V_s$ (m/s)	Thickness (m)	$V_s$ (m/s)
1	0.30	1700	2.0	200	2.275	200	2.00	200	2.0	200
2	0.25	2200	1.5	1500	1.5	1500	1.65	1500	1.5	1650
3	0.46	1700	4.0	400	3.725	400	3.85	400	4.0	400
Half-space	0.46	1700		600		600		600		600

Table 4.2. Summary of the results for HVL study incorporating refraction data.

Run number	EDC/CM		MDC			
			PF		PM	
	DD	PD	DD	PD	DD	PD
1	88	142	96	82	95	142
2	103	119	172	254	9	29
3	119	154	5	82	73	97
Avg.		124		129		75

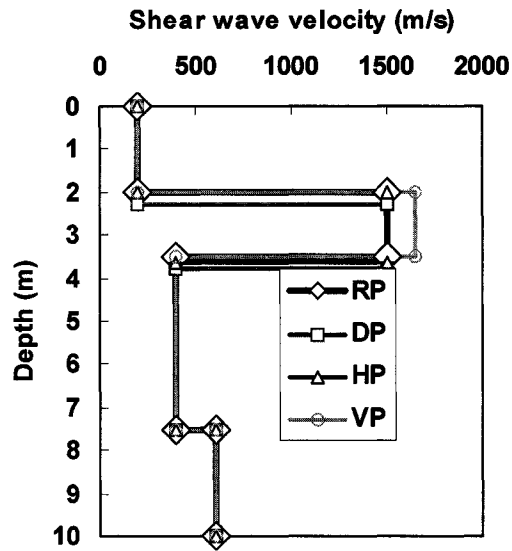


Figure 4.1. Four target profiles.

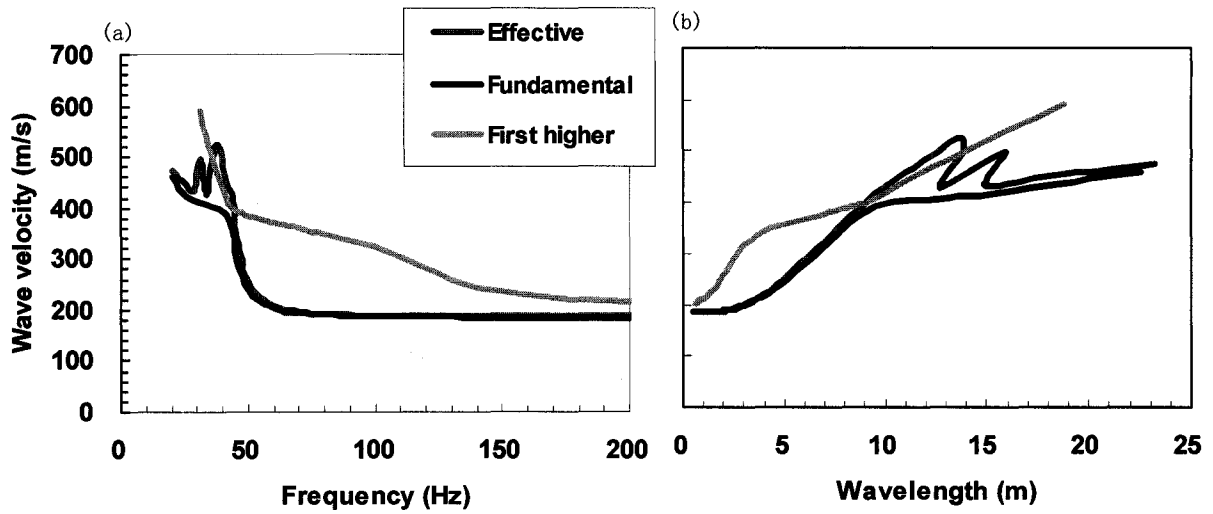


Figure 4.2. Dispersion curves of the RP in terms of a) frequency, b) wavelength.

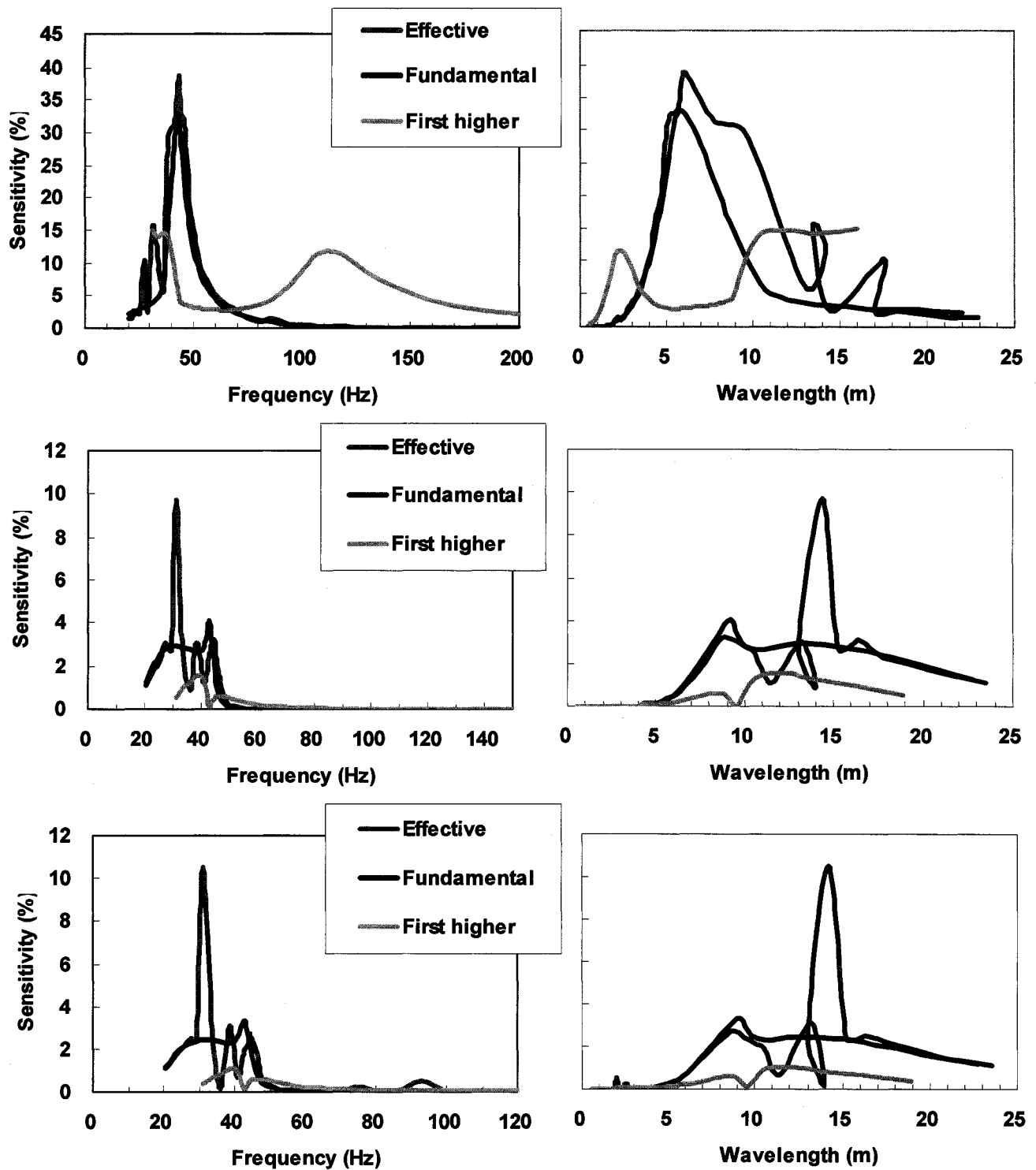


Figure 4.3. Sensitivity of wave velocity to perturbations of depth (top), thickness (middle) and velocity (bottom) in the HVL.



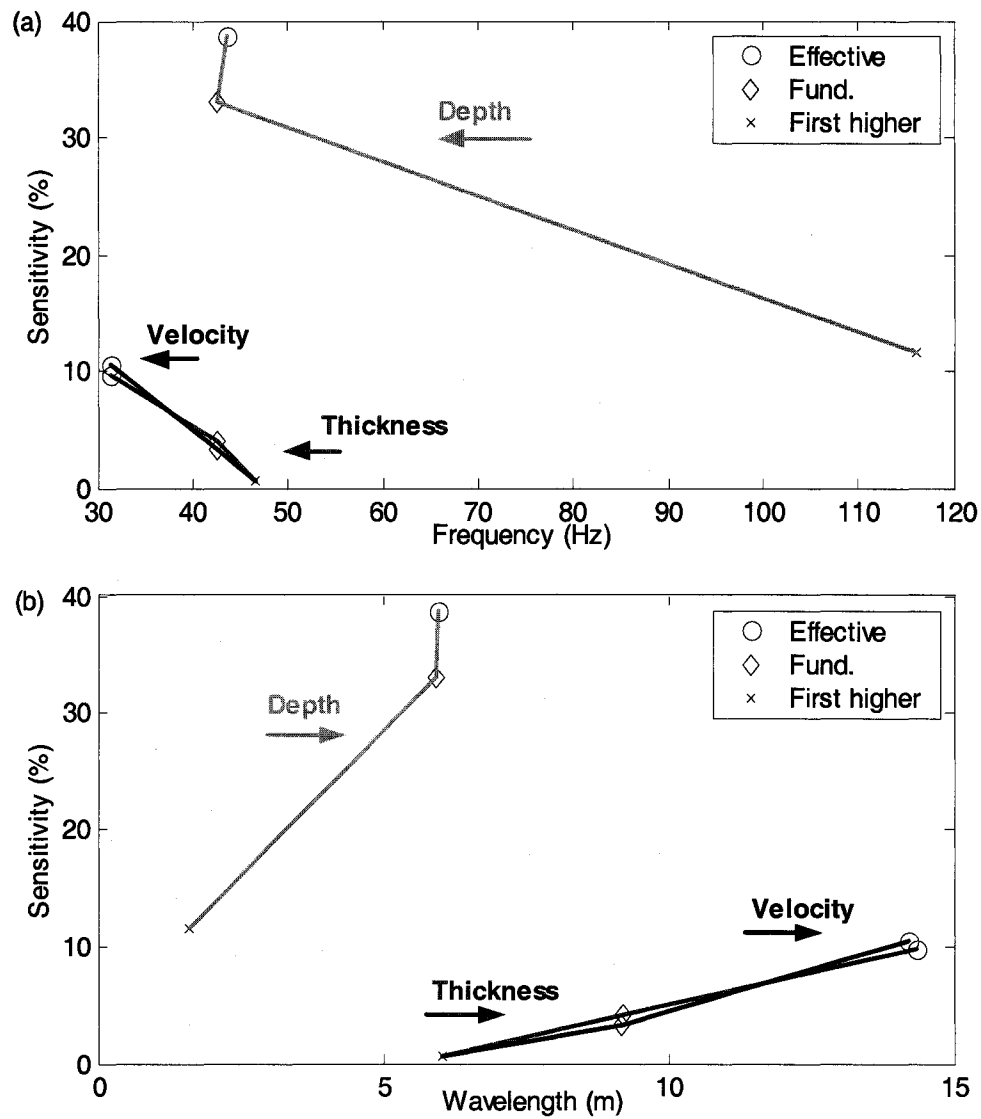


Figure 4.4. Maximum values of sensitivity for EDC, fundamental and first higher mode to perturbations in HVL.

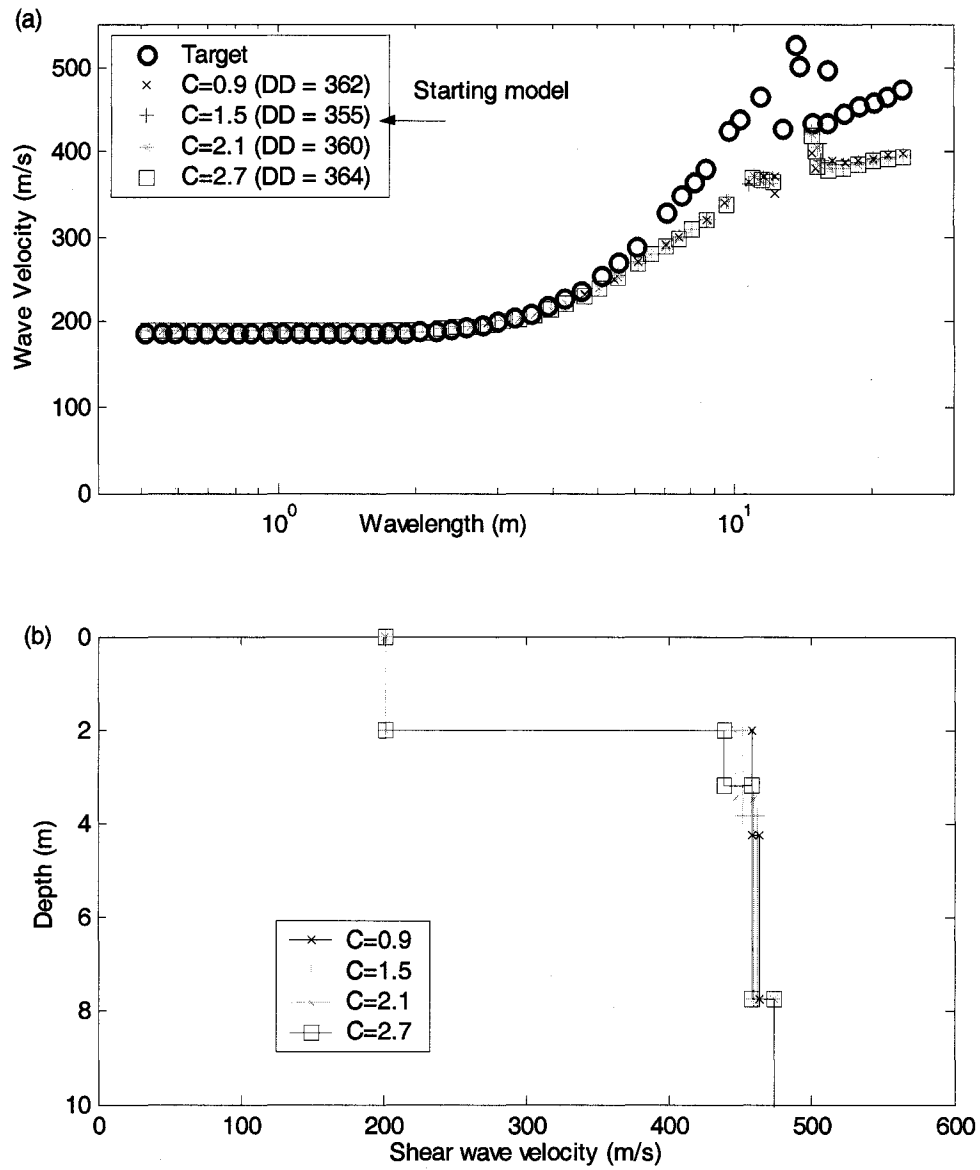


Figure 4.5. Incorporating refraction data, starting model for EDC approach: comparison of (a) DCs and (b)  $V_S$  profiles.

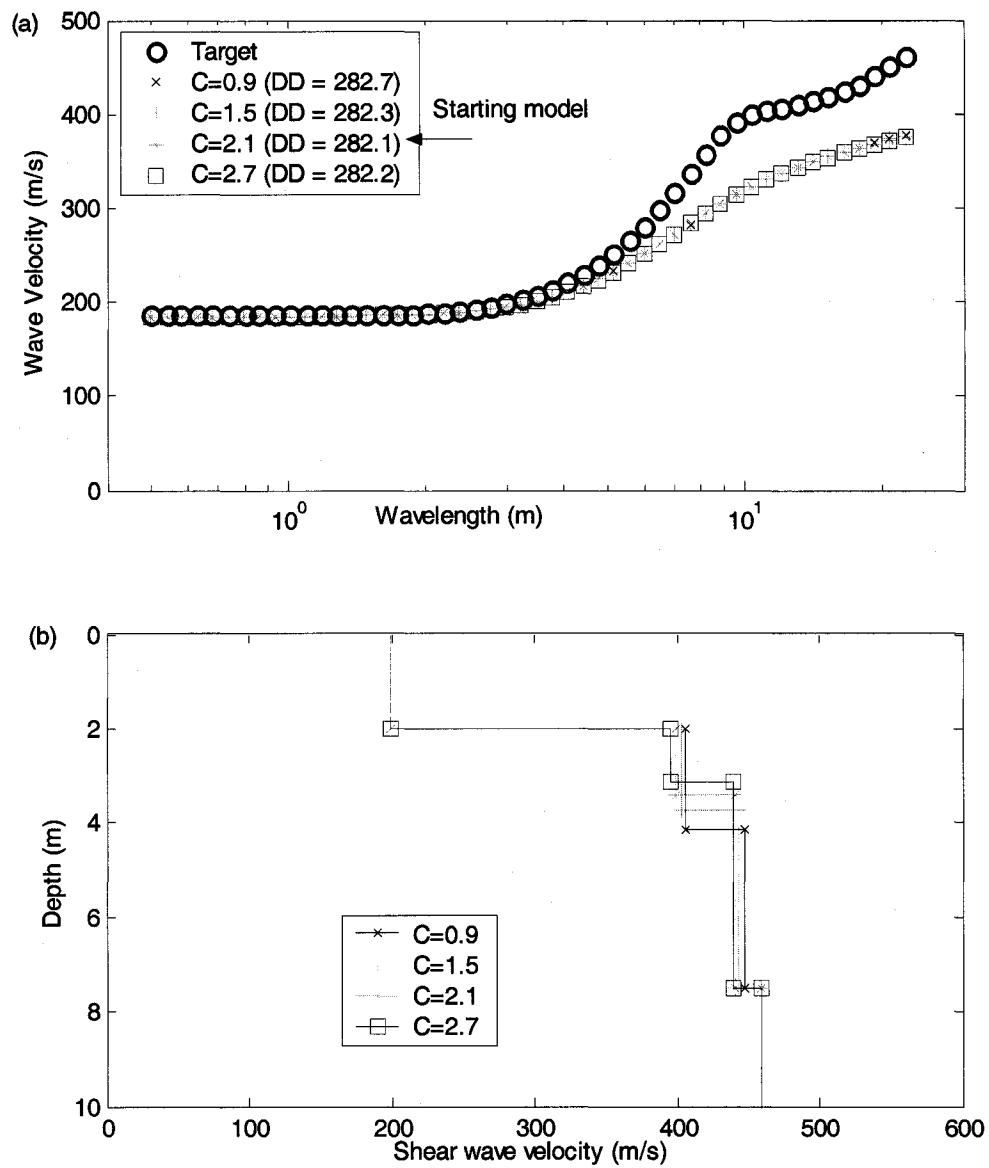


Figure 4.6. Incorporating refraction data, starting model for MDC approach: comparison of (a) DCs and (b)  $V_S$  profiles.

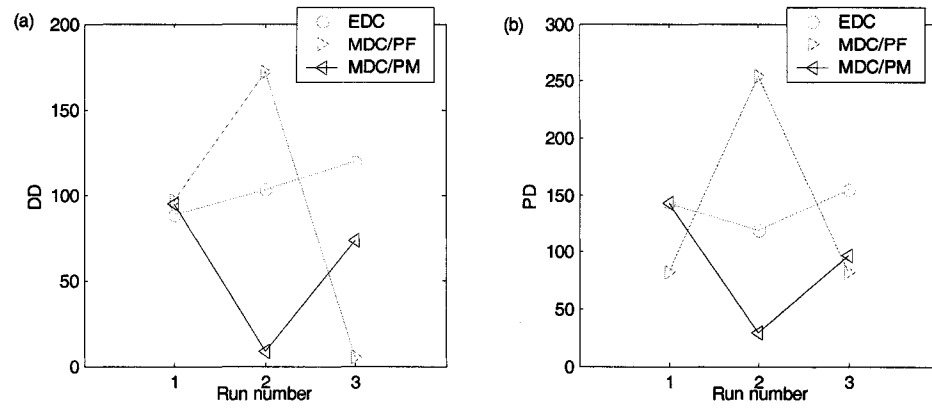


Figure 4.7. Incorporating refraction data: comparison of (a) DD values, (b) PD values.

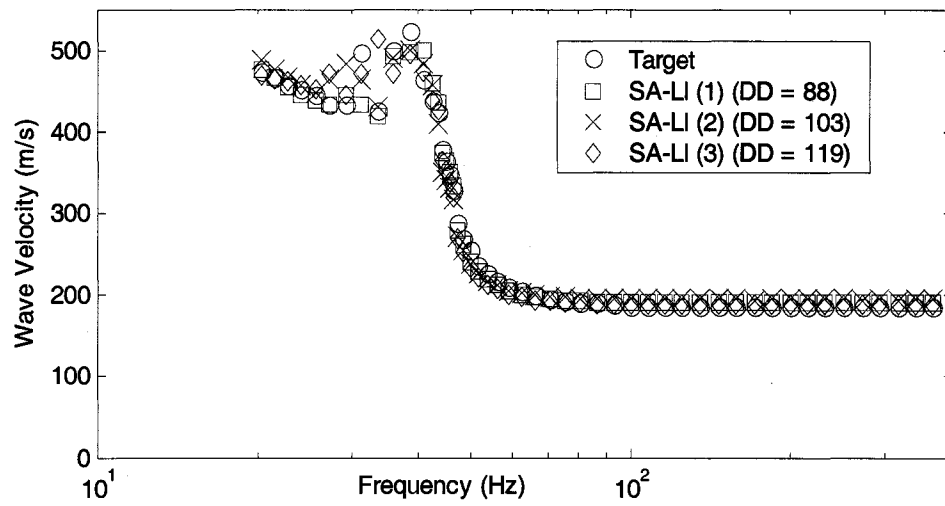


Figure 4.8. Incorporating refraction data, EDC/CM: comparison of DCs.

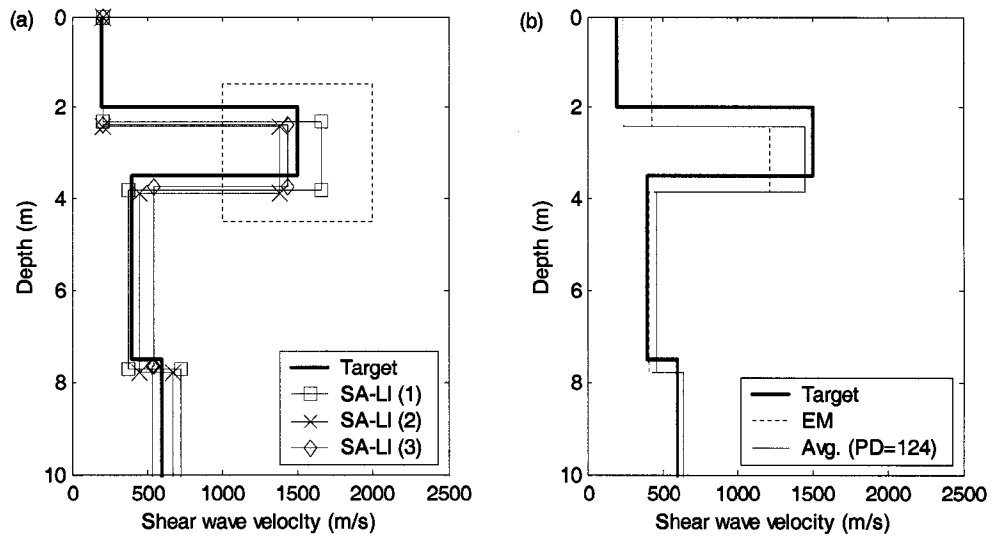


Figure 4.9. Incorporating refraction data, EDC/CM:  $V_s$  profile from (a) three runs (b) average (black dashed line is the SR for the HVL).

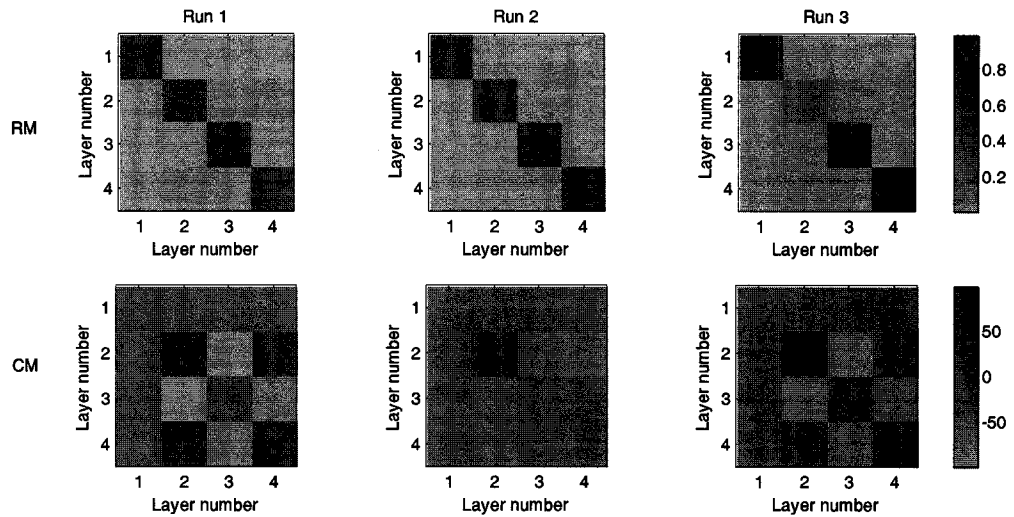


Figure 4.10. Incorporating refraction data, EDC/CM: RMs and CMs.

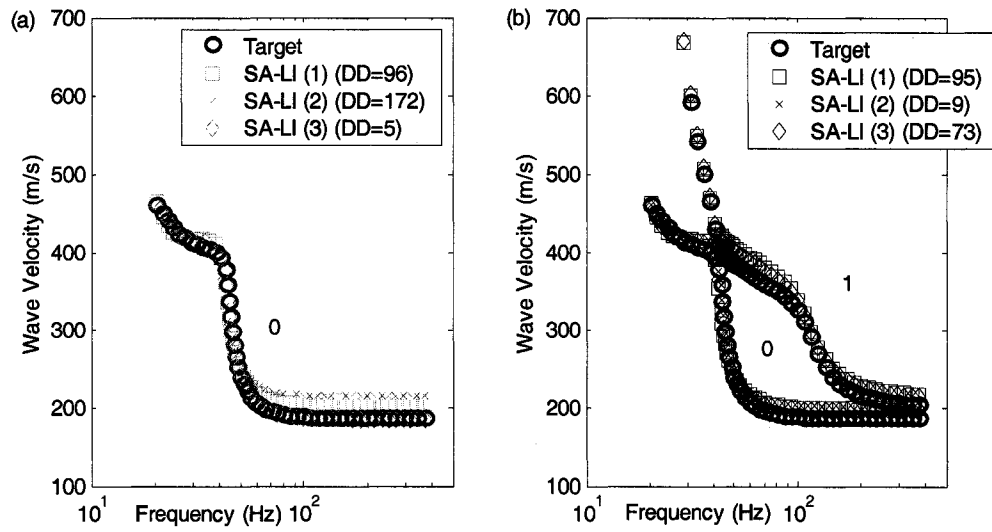


Figure 4.11. Incorporating refraction data: comparison of DCs for (a) MDC/PF and (b) MDC/PM.

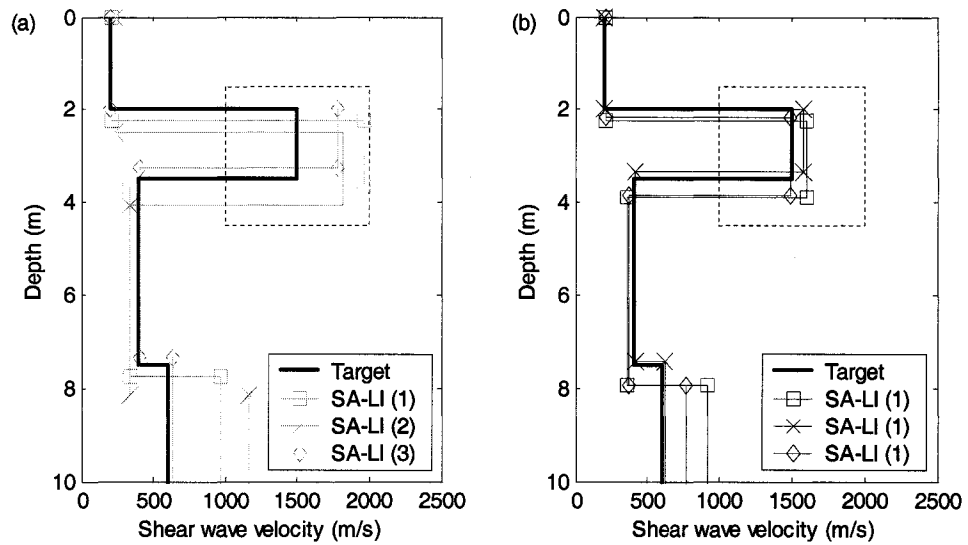


Figure 4.12. Incorporating refraction data:  $V_S$  profile from three runs for (a) MDC/PF (b) MDC/PM.

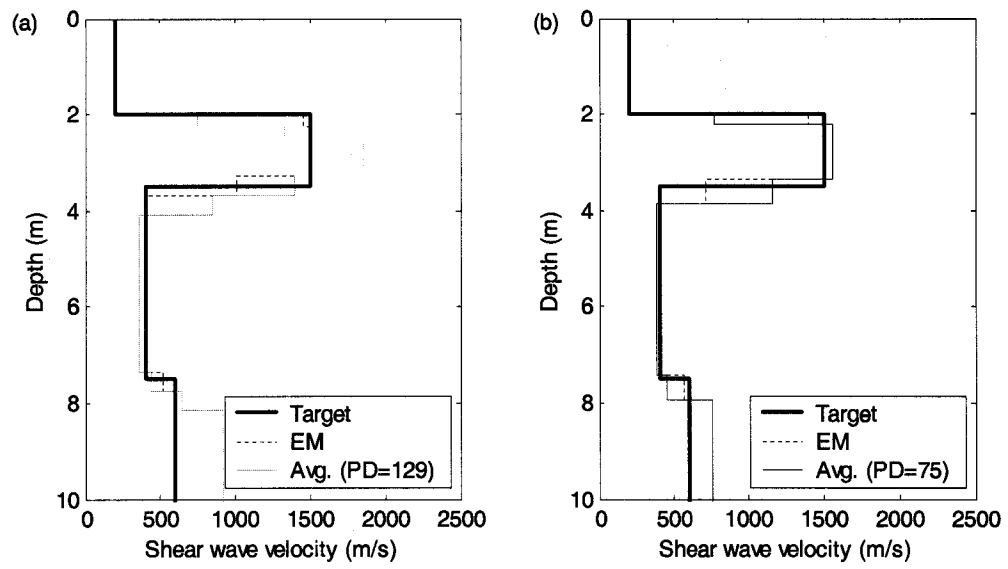


Figure 4.13. Incorporating refraction data: average  $V_s$  profile (a) MDC/PF (b) MDC/PM.





## CHAPTER 5

### FINITE DIFFERENCE SIMULATION OF MULTI-CHANNEL $f$ - $p$ METHOD

#### 5.1 Introduction

The finite-difference method can be used to simulate wave propagation in the near-surface. This technique provides a valuable tool for understanding the characteristics of Rayleigh waves in various geological settings and verifying the results from forward modeling. Compared to the synthetic study (Chapters 3 and 4), this process is more realistic. Here, E3D, which is an explicit 2D/3D elastic finite-difference wave propagation code (Larsen and Schultz 1995; Larsen and Grieger 1998), is used for the modeling of seismic waves. The E3D code is available upon request from Dr. Shawn Larsen at Lawrence Livermore National Laboratory (LLNL). Heath et al. (2006) used it to generate synthetics to investigate the applicability of the ReMi method. Xia et al. (2006) have also used the FD method to model Rayleigh wave propagation.

Here, in this chapter, the E3D code is used to generate synthetic time histories for both the ND and HVL profiles. The multi-channel  $f$ - $p$  method is applied to the time-history data to simulate the multi-channel measurement. The numerical  $f$ - $p$  image is compared to the result from the plane wave forward model. Data acquisition parameters, including the numbers of receivers, spacing of receivers and array ranges, are investigated. The MDC approach is applied and the results are compared to those

generated in the synthetic study in Chapter 3. In Chapter 6, the phase-spectral method is applied to the synthetic time-history data to simulate the two-channel measurement.

## 5.2 E3D Model and Parameter Description

The same ND and HVL model profiles presented in Chapter 3 were used as the target profiles. A two-dimensional grid 150 m wide and 50 m deep, with a grid spacing ( $d_h$ ) of 0.125 m, was used. The grid dimension is selected to be sufficiently larger than the ND and HVL model layer geometries to minimize boundary effects. The time step ( $d_t$ ) is 0.025 ms and the simulation lasts for 0.5 seconds. The time-step increment is determined to satisfy the Courant condition ( $c_t$ ):

$$d_t < c_t = \frac{\text{factor} \times d_h}{V_{\max}} \quad (5.1)$$

Where  $V_{\max}$  is the  $V_p$  in the grid. The "factor" constant is 0.606 for two-dimensional problems and 0.494 for three-dimensional problems (Larsen and Schultz, 1995). The factors are calculated from the nature of the finite-difference numerical approximation used by E3D. If  $d_t$  is greater than  $c_t$ , then the solution quickly becomes unstable. According to Larsen and Schultz (1995), for most applications, it is best to set  $d_t$  as close to the Courant limit as possible. This improves the run-time, and it improves the accuracy. In this case, the  $c_t$  is about 0.03 ms. The data were later downsampled to 1 ms sampling rate which is normally used in real surface wave measurement to decrease processing time for the  $f$ - $p$  method. Thus, a Nyquist frequency of 500 Hz was maintained.

The parameters that describe the source include type, location, orientation, amplitude, frequency, and start-time.

A seismic source ideally produces a single wave or wavelet. A common shape for testing is the Ricker wavelet (e.g., Dobrin and Savit 1988, Sheriff 2002), which is defined as

$$S_R(t) = (1 - 2\pi^2 f_M^2 t^2) e^{-\pi^2 f_M^2 t^2} \quad (5.2)$$

where  $f_M$  is the central frequency in the spectrum of the wavelet.

The start time  $t_0$  equals to zero.

The source force is applied downward at the center of the grid surface. In a two-dimensional modeling problem, the absolute amplitude value of the source does not have true physical significance, because it is a line source in three-dimensional space, which has no area. Changing this value would result in changing of the results by the proportional amount.

Multiple wavelets can be superimposed. Here, two Ricker wavelet sources with central frequencies of 100 Hz and 25 Hz were used to simulate the multi-channel data recording. The higher central frequency, 100 Hz, is set to retain information at higher frequencies where higher modes are expected to appear. The lower central frequency, 25 Hz, is set to reach greater depths of interest. Figure 5.1 indicates the time domain and frequency domain representations of the combined Ricker wavelet source.

### 5.3 Multi-Channel $f$ - $p$ Method Simulation

The signals were “recorded” with 81 receivers at 0.5 m spacing. The time histories from all receivers for the ND and HVL profiles are displayed in Figure 5.2 (a) and (b) respectively. The time history image for the ND profile is clearer and the wave train is

more complex for the HVL profile. The complexity is due to the scattering of seismic energy caused by the presence of the HVL.

The maximum frequency to avoid aliasing can be calculated using the equation below (Levander, 1988):

$$f_{\max} = \frac{V_{\min}}{d_h \times \text{grid points per wavelength}} \quad (5.3)$$

Approximately 10 grid points per wavelength are recommended by Larsen and Schultz (1995) to avoid numerical dispersion. The minimum velocity is 200 m/s and the grid spacing is 0.125 m. Theoretically, using 10 grid points per wavelength, the maximum frequency avoiding aliasing should be 160 Hz. Here, the author set the cut-off frequency as 200 Hz which corresponds to 8 grid points per wavelength. Their  $f$ - $p$  images are exactly the same. Using the  $f$ - $p$  method, the  $p$ - $\tau$  and  $f$ - $p$  images are generated for the ND and HVL profiles (Figure 5.3). Both fundamental and higher modes can be distinguished from the  $f$ - $p$  images for both cases.

#### 5.4 Effects of Some Factors on the $f$ - $p$ Image

In this section, the effects of a real source with respect to the Ricker wavelet source are studied using both the ND and HVL profiles. Then, the ND profile is used to study the effects of the number of receivers and the spacing of receivers on the  $f$ - $p$  image.

##### 5.4.1 Real Source Effect

To investigate the effect of the source, a real dataset was used instead of the default Ricker wavelet. The source was a PCB instrumented sledgehammer struck upon a metal plate and recorded by a dynamic signal analyzer. The sampling interval is 2 ms. Figure

5.4 indicates the real source data in time and frequency domain. The frequency band of the source is up to 250 Hz. To incorporate it into the E3D model, the dataset is resampled at 40 times the original sample rate to satisfy the Courant condition. The  $f$ - $p$  images of the two sources for both the ND and HVL profiles are displayed in Figure 5.5. The discontinuity at frequency 50 Hz in the fundamental mode of the Ricker wavelet source is caused by the destructive interference of the two Ricker wavelets (100 Hz and 25 Hz central frequencies) which yields a relatively low spectral amplitude at 50 Hz (Figure 5.1b). For the ND profile, the first higher mode from 50 to 80 Hz (in the rectangular window) is clearer with real source data. For the HVL, what will be shown to be the fundamental mode below 40 Hz (in the rectangular window) is clearer with the Ricker wavelet source.

#### 5.4.2 Effect of Numbers and Spacing of Receivers

Seven different array setups are investigated to study the effects of varying the number and spacing of receivers on the quality of the  $f$ - $p$  images with the ND profile (Table 5.1). Array setups A, B, C and D share the same 0.5 m spacing, but have different numbers of receivers. This results in different overall array lengths. Array setups E and F both have 1 m spacing, and 24 and 36 receivers, respectively. Array setup G has 1.5 m spacing with 24 receivers.

Figure 5.6 displays the  $f$ - $p$  images of these array setups. The image labeled as “reference” has 0.5 m spacing with all the 81 receivers and is used for comparison. For the array setups A, B, C and D, the quality of images improves with increasing number of receivers. The qualities of images A through D, assigned subjectively, are designated in

Table 5.1. The images of array setups A and B are blurred with respect to array setups C and D. The same trend can be seen from the  $f$ - $p$  images of array setups E and F that increased numbers of receivers improves the quality of  $f$ - $p$  images. The quality of the  $f$ - $p$  image for array setup G is good. Array setups F and G cover similar array lengths; though they have different spacing, the  $f$ - $p$  images of the two array setups are of similar quality.

The qualities of the  $f$ - $p$  images are controlled by a combination of two factors: number and spacing of receivers. For the same spacing, the increasing numbers of receivers improves the quality of image. Given a fixed number of receivers, the array length becomes more important. The image with wider spacing has better quality (compare E to A and F to B). Based on this study, for the ND profile, which has a depth of 7.5 m to the halfspace, the maximum acceptable spacing is 1.5 m and the minimum offset range is 29.5 m.

### 5.5 Dispersion Curve Picking

The  $f$ - $p$  images with all 81 receivers are used for the DC generation of the ND and HVL profiles. The DC picks are performed manually. For the ND profile, the fundamental mode is clear, continuous and thus relatively easy to pick. The first higher mode is clear except from 50 to 80 Hz, where it is blurry (Figure 5.7a). Picks are made only along the continuous parts above 80 Hz. For the HVL profile, the fundamental mode is continuous above 40 Hz, but blurred below 40 Hz so experience and knowledge is required to make the picks in this frequency range. The first higher mode is clear but discontinuous or blurred from 50 to 80 Hz (Figure 5.8a). Again, picks are also made only along the continuous parts above 80 Hz.

Based on the picks, a cubic spline data interpolation method is applied to increase the number of points (total number of points less than 100) and smooth the curve (Lancaster and Šalkauskas 1986). Figure 5.7 displays three  $f-p$  images for the ND profile: a)  $f-p$  image alone, b) superposed with picks for the first two mode DCs, and c) superposed with the solutions of the first two mode DCs presented in Chapter 3. Figure 5.8 displays the corresponding  $f-p$  images for the HVL profile. For both the ND and HVL profiles, the solutions fit well with the  $f-p$  images. However, as shown in Figure 5.8 (c), for the HVL profile, the solutions of the first two modes nearly cross at 40 Hz. This illustrates the difficulty in making the accurate DC picks. The difficulty in identification of modes in DC panels has been reported by many researchers (e.g., Wathelet 2005). Zhang and Chan (2003) used a synthetic dataset to illustrate that incorrect or inaccurate DC identification would have a dramatic influence on the final results and usually produce misleading results. Dal Moro et al. (2006) used numerical simulation to demonstrate that reflection events and their multiples could be misinterpreted as higher-mode DCs because of their similarity. They suggest using synthetic data analysis to guide the DC interpretation of field data.

Figure 5.9 indicates three DCs for the ND profile: 1) manually picked DCs, 2) cubic spline fit of picked DCs and 3) theoretical DCs from the plane-wave forward model. For the fundamental mode DC, the DCs from (1) and (2) match well with that from (3). For the first higher mode DC, the DCs from (1) and (2) match well with that from (3) but do not include the frequencies below 80 Hz because picks were only made along the continuous part. The same comparison of DCs can be made for the HVL profile (Figure 5.10). The DCs from (1) and (2) have lower velocities from 30 to 40 Hz compared to the

solution from the plane-wave forward model. This is due to the extreme difficulty in identifying the fundamental mode below frequency 40 Hz.

## 5.6 Inversion and Interpretation

Using the technique described in Chapter 3, the MDC/PF and MDC/PM analyses are applied for both the ND and HVL profiles. The parameter settings are the same as those presented in Chapter 3.

### 5.6.1 Results for the ND profile

The resulting DD and PD from three inversion runs for the ND profile using the MDC/PF and MDC/PM analyses are presented in Table 5.2 and Figure 5.11. Results among the three runs were consistent.

Figures 5.12 to 5.15 show the results. All the theoretical DCs fit the target well. All the six inverted profiles and the average profiles are nearly identical. Except for the first layer, the  $V_S$  of other layers are about 10% higher compared to the target. All the RMs display nearly perfect resolution and CMs show little dependence between layers with a higher standard deviation for the halfspace.

With respect to the results from MDC approach observed in Chapter 3 (Figures 3.11 to 3.14), the solutions are equally good here.

### 5.6.2 Results for the HVL Profile

Resulting DD and PD from three inversion runs for the HVL profile using the MDC/PF and MDC/PM analyses are presented in Table 5.3 and Figure 5.16. The PD



from the MDC/PF analysis are consistently lower than those from the MDC/PM analysis. The DD are similar except for one value from the MDC/PF analysis, which is much greater.

Figures 5.17 to 5.20 show the results. The theoretical DCs fit well with the target DC. For the MDC/PF analysis, the same trend that occurred with this analysis for the HVL profile in Chapter 3 happened here: the solution with the greatest DD and PD corresponds to one in which the HVL was not located yet its RM showed misleading perfect resolution.

For the MDC/PM analysis, all three runs yield a profile that contains a HVL. However, the thickness and depth of the HVL are not as well resolved as the solutions of runs 1 and 3 from the MDC/PF analysis. The RMs display good resolution with relatively lower resolutions for the HVL and the CMs display relatively higher standard deviations for the HVL. With respect to the results from the MDC/PM analysis observed in Chapter 3 (Figures 3.20b and 3.21b), the HVL is not as well as resolved.

As mentioned in Chapter 3, an alternative averaging method is applied to the  $V_S$  profiles from the MDC/PM analysis. Figure 5.21 indicates the comparison of the final average profiles from the two methods to the target. The second method, in which the background profile and the HVL are averaged separately, overestimates the  $V_S$  at depths 3.5 to 7.5 m. This happens because some layers (the third layer in runs 1 and 2) belonging to the background profile have high velocities. The theoretical DCs from the two average profiles are compared to the target DC in Figure 5.22. They both show higher velocities than the target DC at frequencies above 120 Hz for the first higher mode. The second averaging method has the higher DD value.

## 5.7 Discussion

An accurate DC is essential to determine the  $V_S$  profile. For the ND profile, due to the match between the picked fundamental mode DC and the solution from the plane-wave forward model, the outcomes from the MDC/PF analysis are as good as those observed in Chapter 3. Furthermore, due to the dominance of the fundamental mode in this case, the outcomes from the MDC/PM analysis are almost identical to those from the MDC/PF analysis despite that the first-higher mode is part of the solution from the plane-wave forward model.

For the HVL, the outcomes from the MDC/PF analysis have the same trend as those observed in Chapter 3. However, it is important to note that the determination of the fundamental mode DC below 40 Hz is extremely difficult. For the MDC/PM analysis, the HVL is not resolved as well as that observed in Chapter 3, because the first-higher mode is not complete. This emphasizes the necessity of a continuous and complete first higher mode to significantly improve the outcomes. Unfortunately, it is extremely difficult to completely identify the first higher mode.

In this chapter, the FD simulation demonstrated the difficulty in DC interpretation from the  $f$ - $p$  image even for perfect site conditions, especially for the HVL profile. In practice, many factors (e.g., traffic, wind) may decrease the resolution of the  $f$ - $p$  image, making the accurate DC interpretation even more difficult. Thus, the method of improving the results by incorporating the first higher mode in the inversion may not be dependable for real datasets.

Recall in Chapter 3, it was mentioned that the weight for the mode should be proportional to its energy participation. Here, the amplitude of the point shown in the  $f$ - $p$

image can be interpreted as its energy participation. Assignment of weights for the mode that are proportional to the amplitude is a promising way to reduce the subjectivity in the data analyses and might be able to improve results.

The FD simulation proved to be a powerful tool to simulate surface wave measurement for different profiles. Here, the factor of attenuation is not considered in the cases studied. Its effect should be considered in the future research. In addition, to better simulate the field conditions, random noise should be added to the surface response recorded by the receivers.

Table 5.1. Parameters of seven different array setups.

Array setup	Spacing (m)	Number of receivers	Offset range (m)	Image quality
A	0.5	24	1-12.5	Poor
B	0.5	36	1-18.5	Poor
C	0.5	48	1-24.5	Fair
D	0.5	60	1-30.5	Good
E	1.0	24	1-24.0	Fair
F	1.0	36	1-36.0	Good
G	1.5	24	1-35.5	Good

Table 5.2. Summary of the results for the ND profile with DCs from FD simulation of multi-channel  $f$ - $p$  method.

Run number	MDC/PF		MDC/PM	
	DD	PD	DD	PD
1	31	33	33	33
2	31	33	32	33
3	31	33	32	33
Avg.		33		33

Table 5.3. Summary of the results for the HVL profile with DCs from FD simulation of multi-channel  $f$ - $p$  method.

Run number	MDC/PF		MDC/PM	
	DD	PD	DD	PD
1	37	60	43	136
2	71	98	43	151
3	27	66	33	157
Avg.		113		120

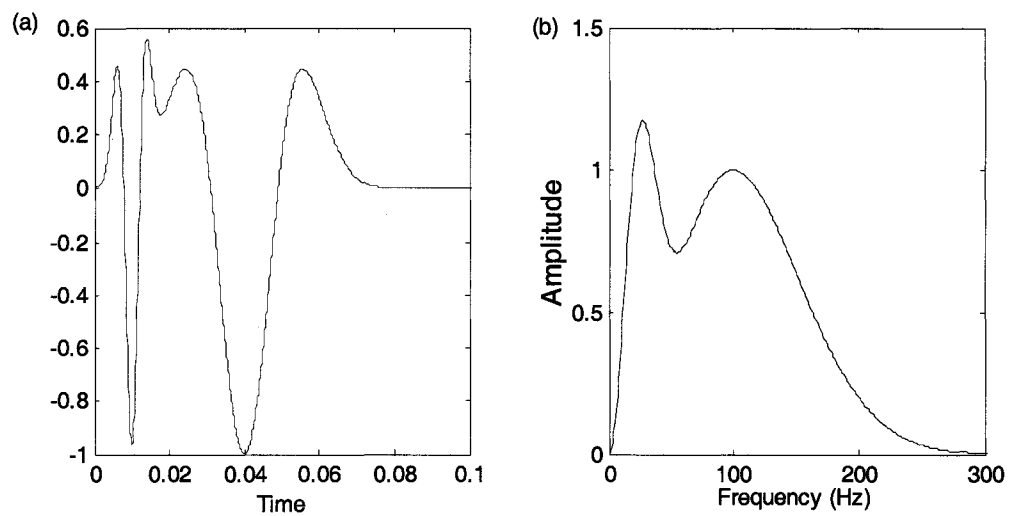


Figure 5.1. Ricker wavelet source with 100 & 25 Hz central frequencies: (a) time- and (b) frequency- domain representations.

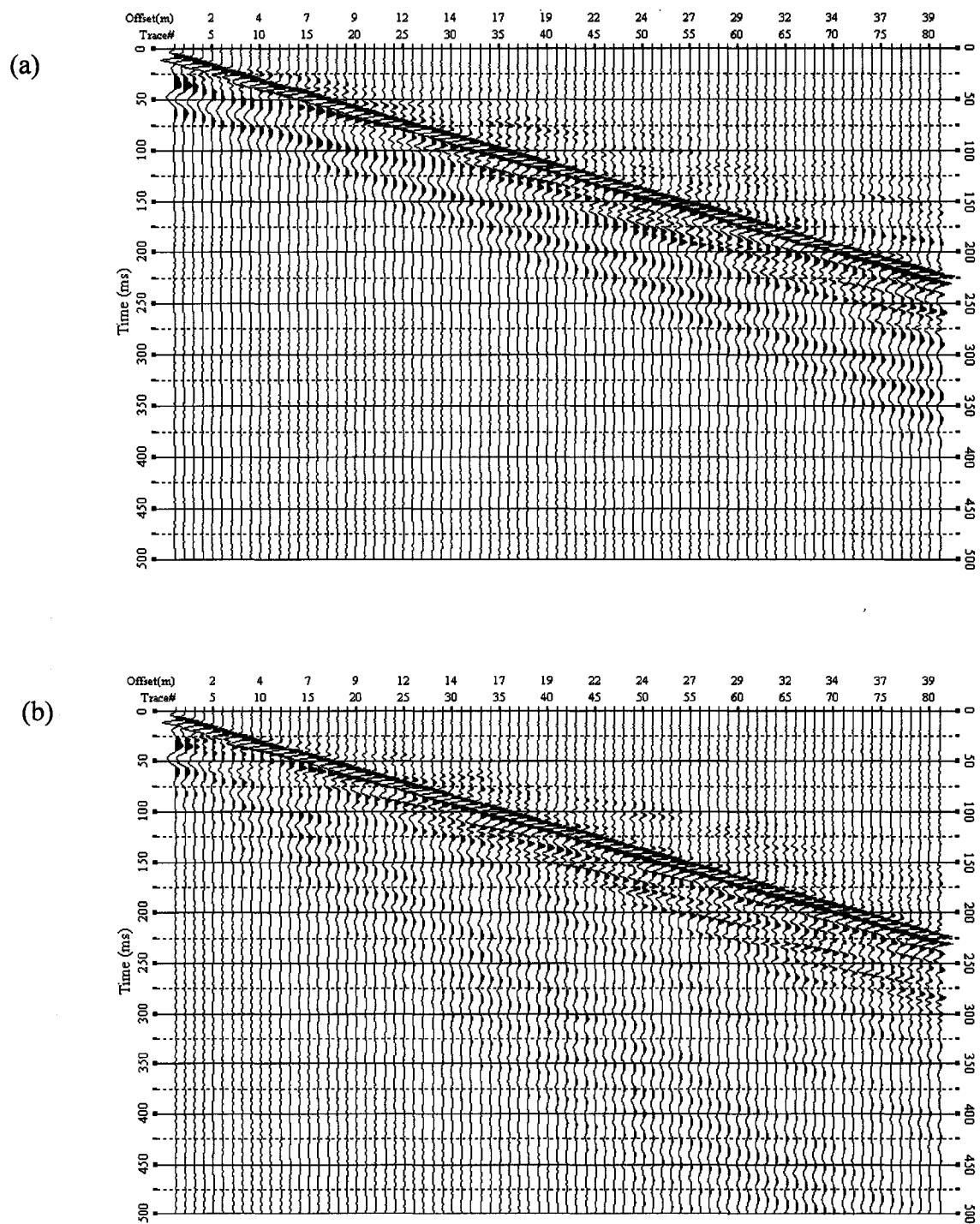


Figure 5.2. Synthetic time histories for 81 receivers, 0.5 m spacing with superposed 25 & 100 Hz Ricker wavelet sources for (a) ND and (b) HVL profiles.

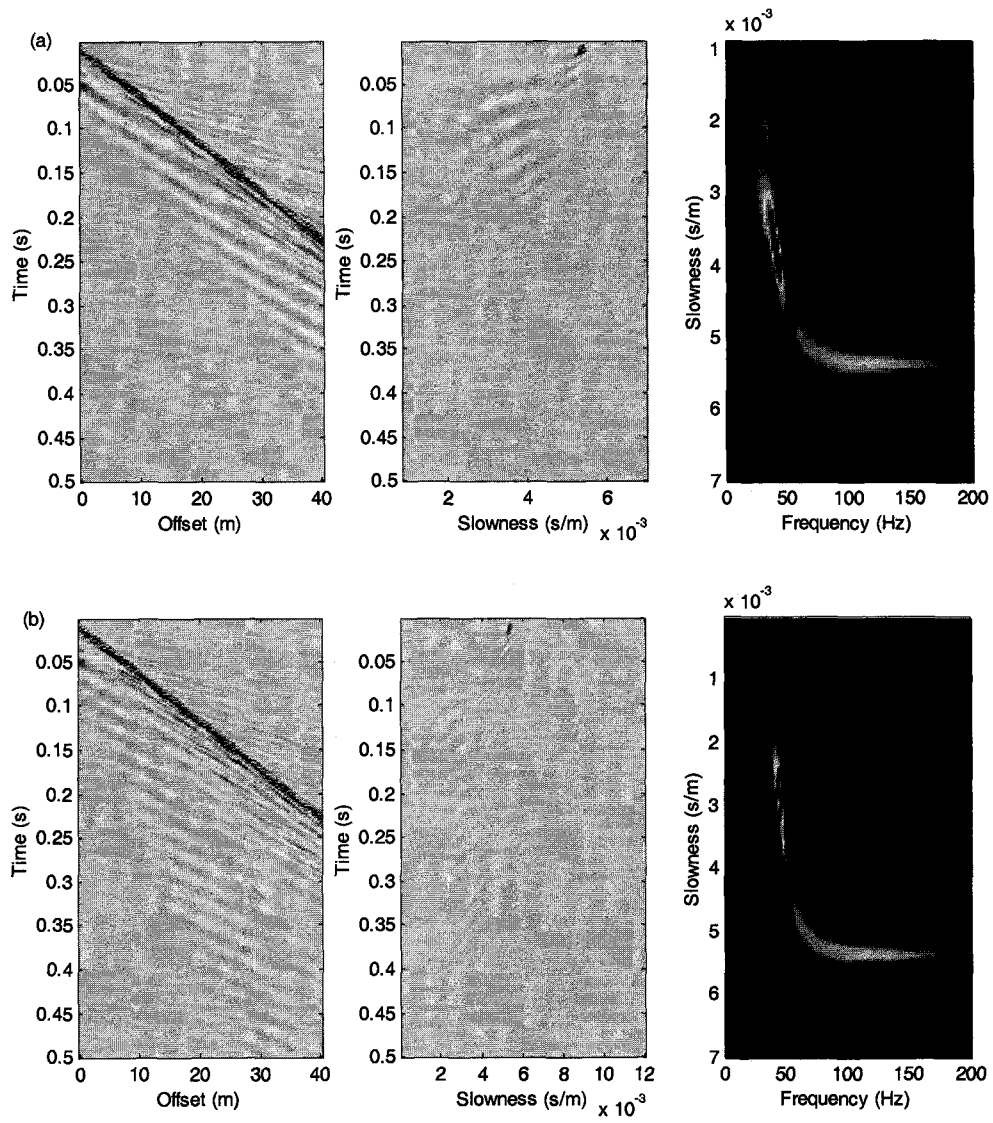


Figure 5.3. Offset-time,  $p-\tau$  and  $f-p$  images of the (a) ND and (b) HVL profiles.

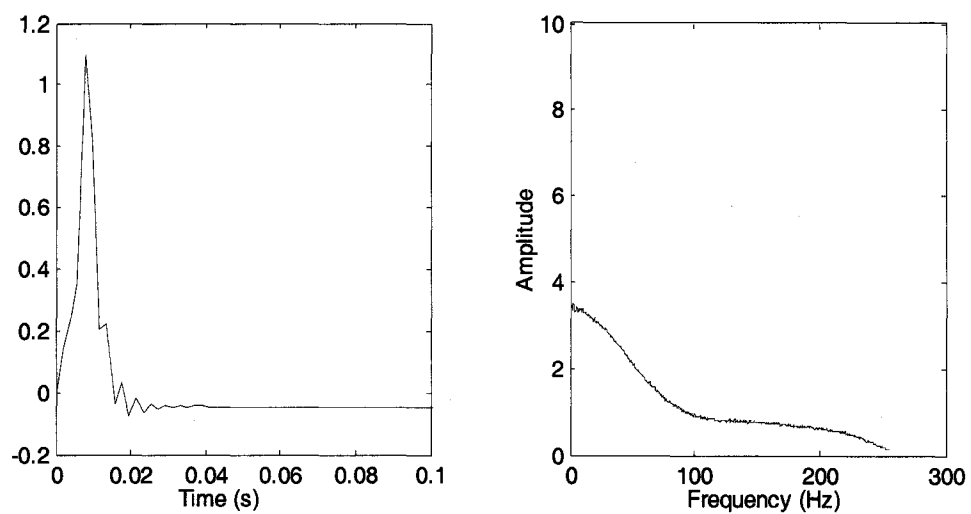


Figure 5.4. Real source time and frequency domain.



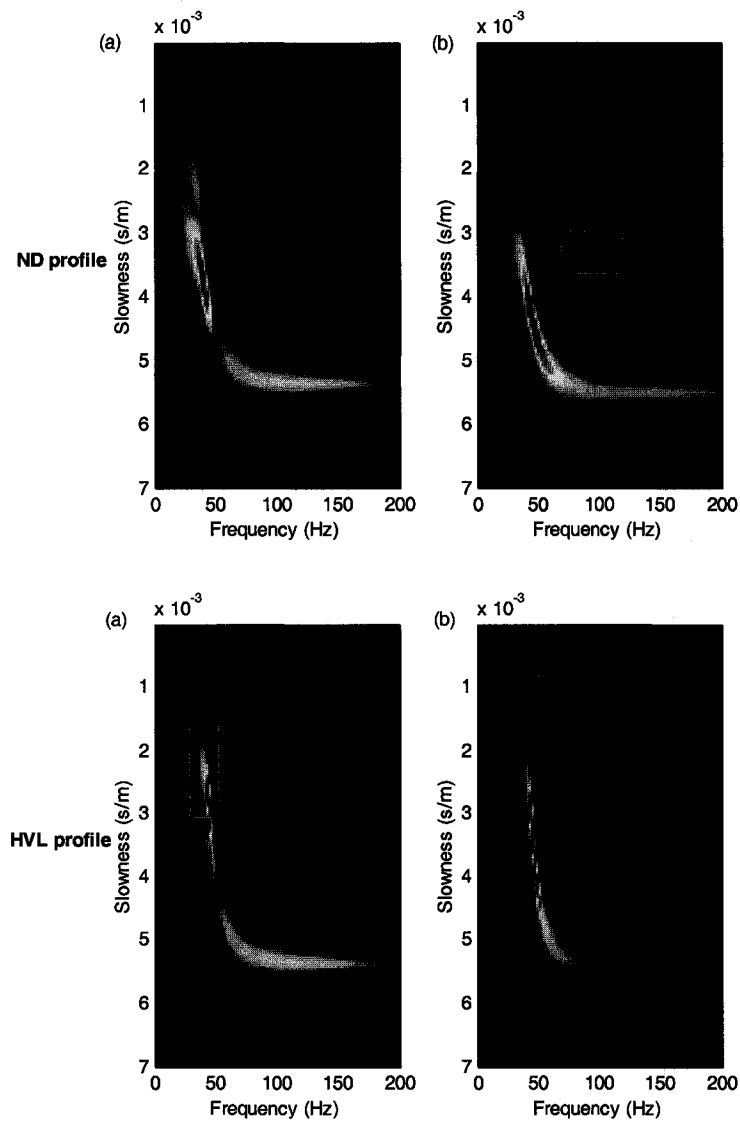


Figure 5.5. Source effect on the  $f$ - $p$  images: (a) superposed 25 & 100 Hz Ricker wavelet sources; (b) real source for the ND (top) and HVL profiles (bottom).

(See text for discussion of highlighted areas)

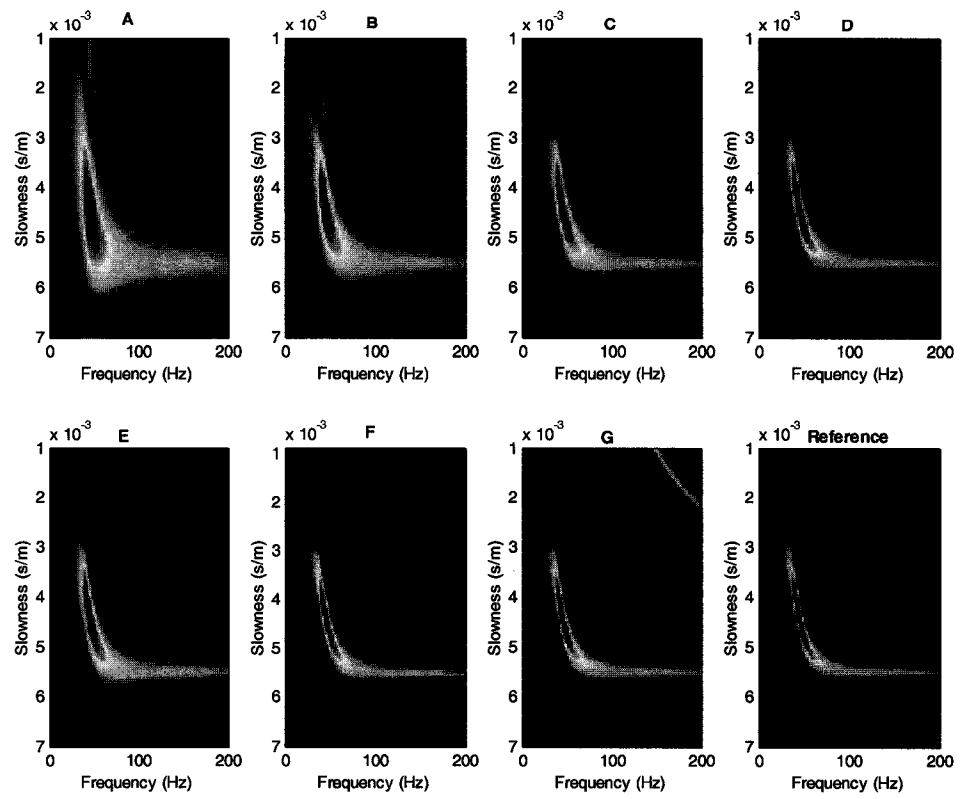


Figure 5.6. Effects of numbers of receivers and spacing of receivers on  $f$ - $p$  images.

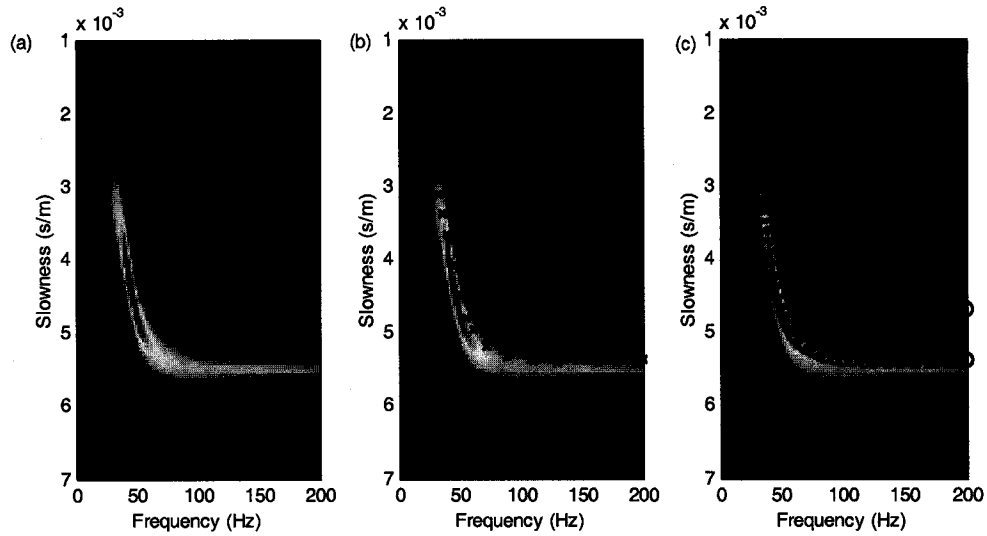


Figure 5.7. ND profile: (a)  $f$ - $p$  image alone, (b) superposed with picks of the first two modes and (c) superposed with the solution from plane wave forward model (black: fundamental mode; red: first higher mode).

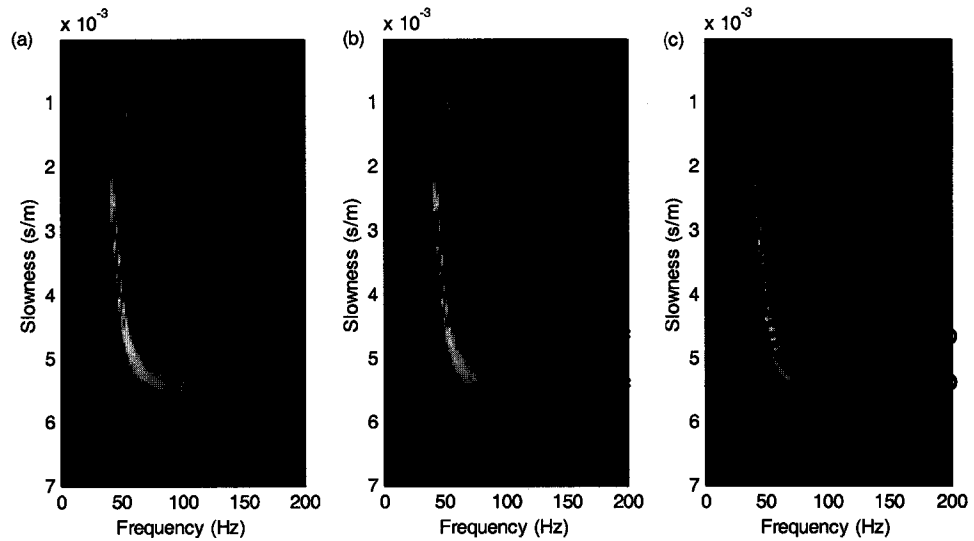


Figure 5.8. HVL profile: (a)  $f$ - $p$  image alone, (b) superposed with picks of the first two modes and (c) superposed with the solution from plane wave forward model (black: fundamental mode; red: first higher mode).

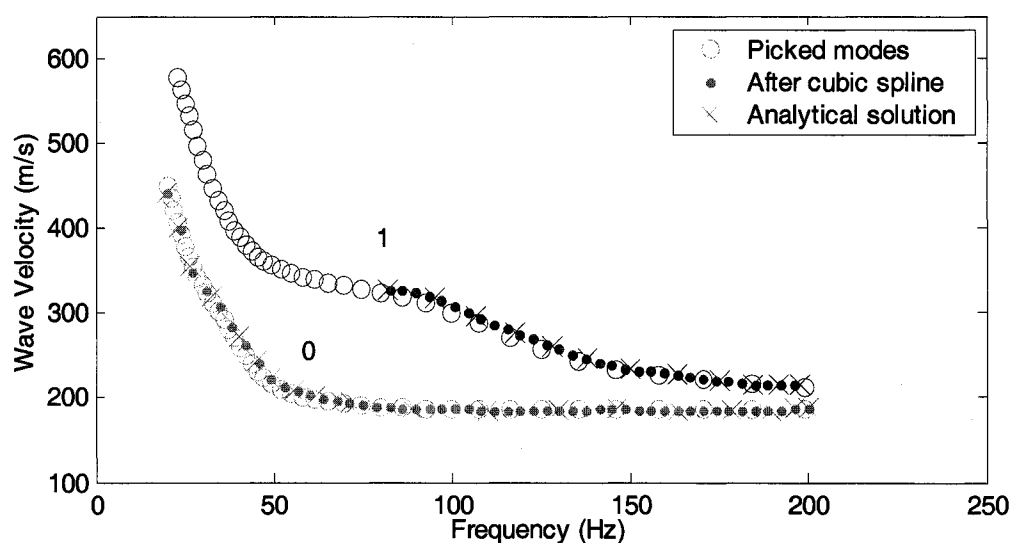


Figure 5.9. FD study, ND profile: comparison of DCs from picked modes, cubic spline fit of picked modes and solution from plane wave forward model.

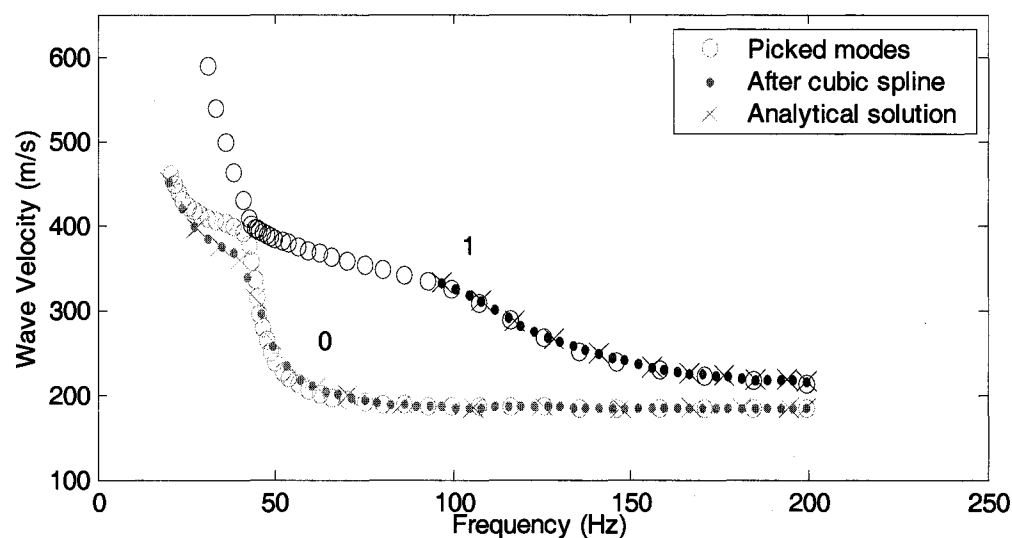


Figure 5.10. FD study, HVL profile: comparison of DCs from picked modes, cubic spline fit of picked modes and solution from plane wave forward model.

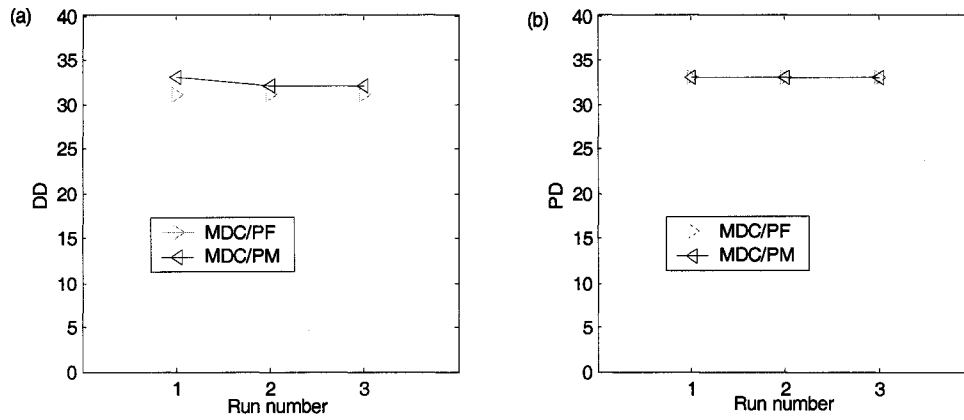


Figure 5.11. FD study, ND profile, MDC approach: comparison of (a) DD values, (b) PD values.

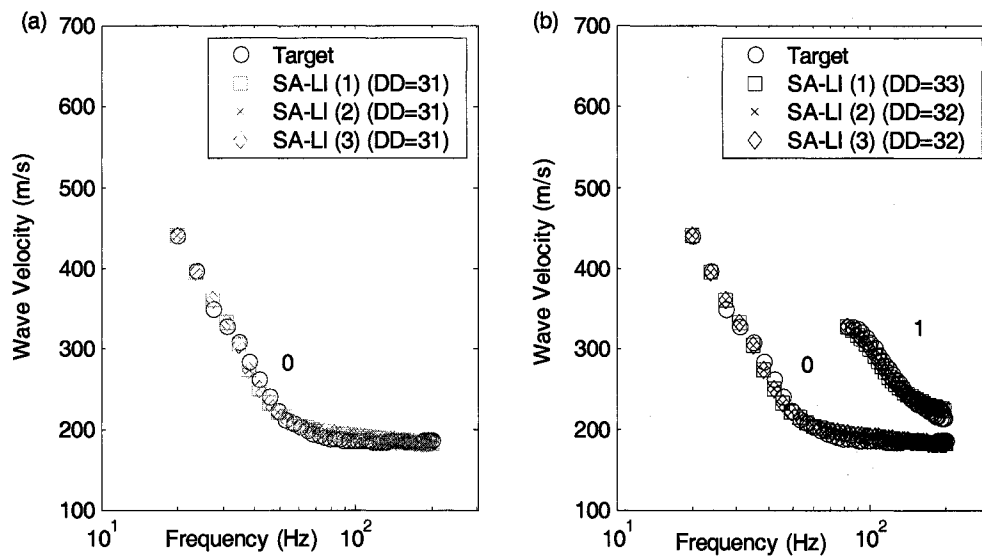


Figure 5.12. FD study, ND profile, MDC approach: comparison of DCs for (a) MDC/PF, (b) MDC/PM.

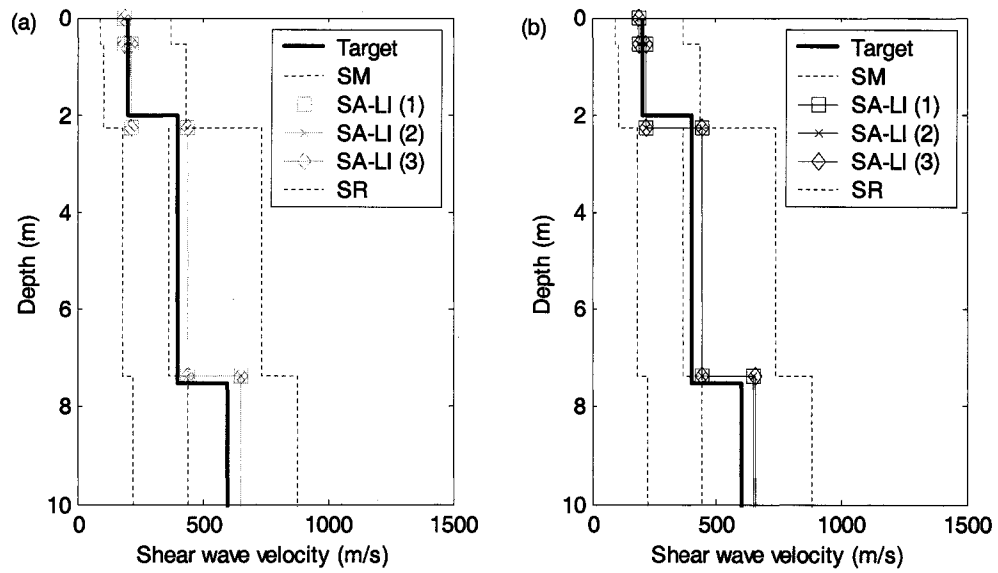


Figure 5.13. FD study, ND profile, MDC approach:  $V_S$  profiles from three runs for (a) MDC/PF, (b) MDC/PM.

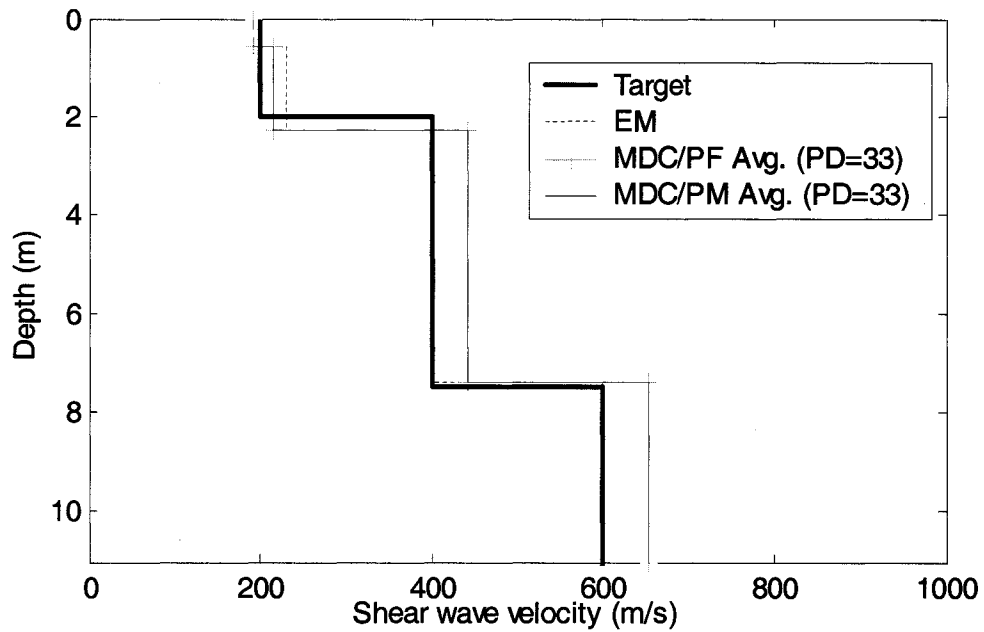


Figure 5.14. FD study, ND profile, MDC approach: average  $V_S$  profiles.

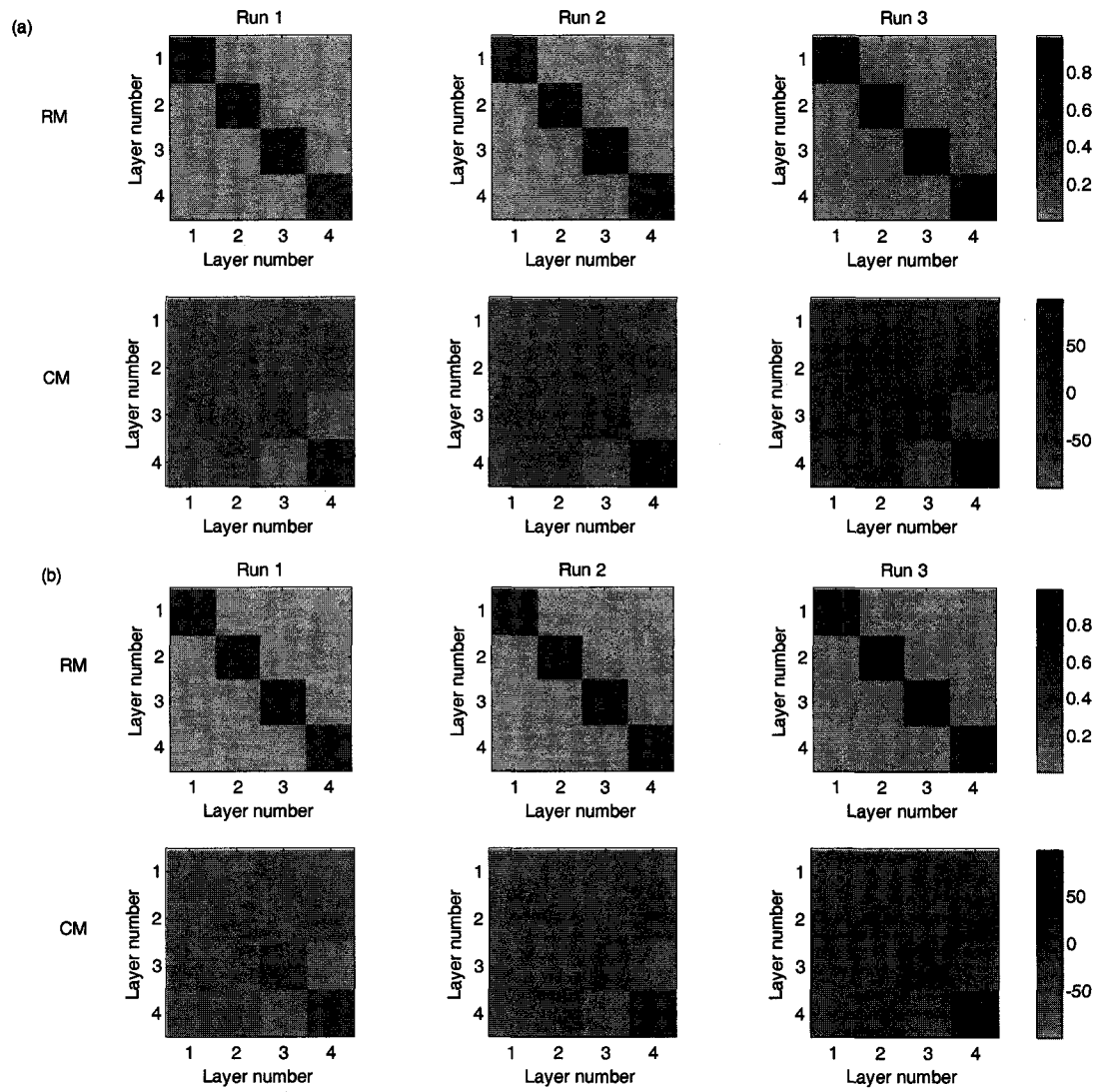


Figure 5.15. FD study, ND profile, MDC approach: RMs and CMs from (a) MDC/PF, (b) MDC/PM.

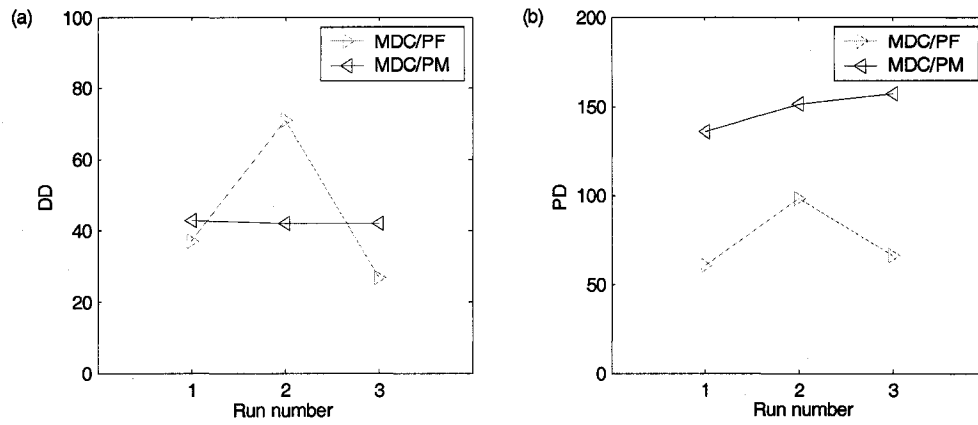


Figure 5.16. FD study, HVL profile, MDC approach: comparison of (a) DD values, (b) PD values.

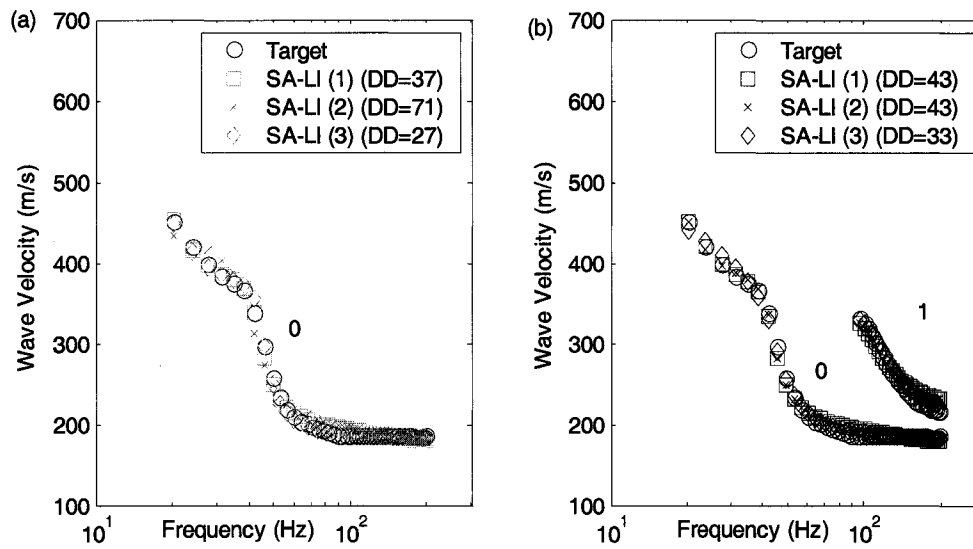


Figure 5.17. FD study, HVL profile, MDC approach: comparison of DCs from (a) MDC/PM, (b) MDC/PF.



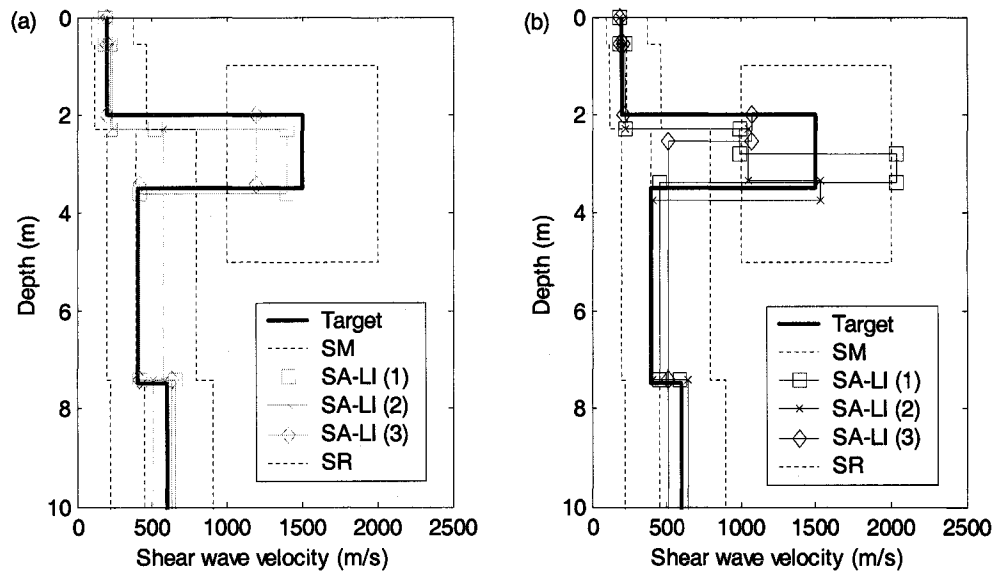


Figure 5.18. FD study, HVL profile, MDC approach:  $V_S$  profiles from three runs

(a) MDC/PF, (b) MDC/PM.

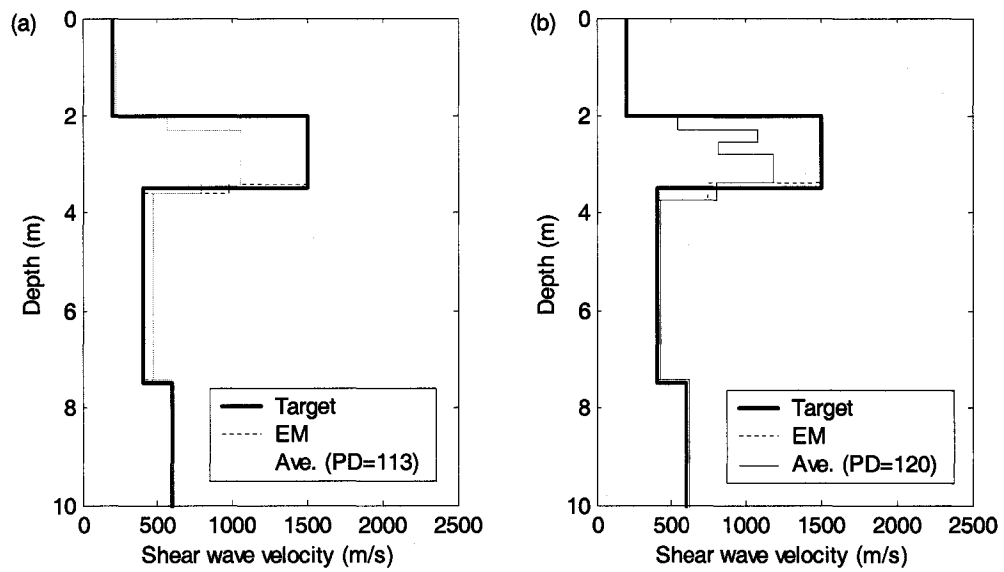


Figure 5.19. FD study, HVL profile, MDC approach: average profiles from (a) MDC/PF,

(b) MDC/PM.

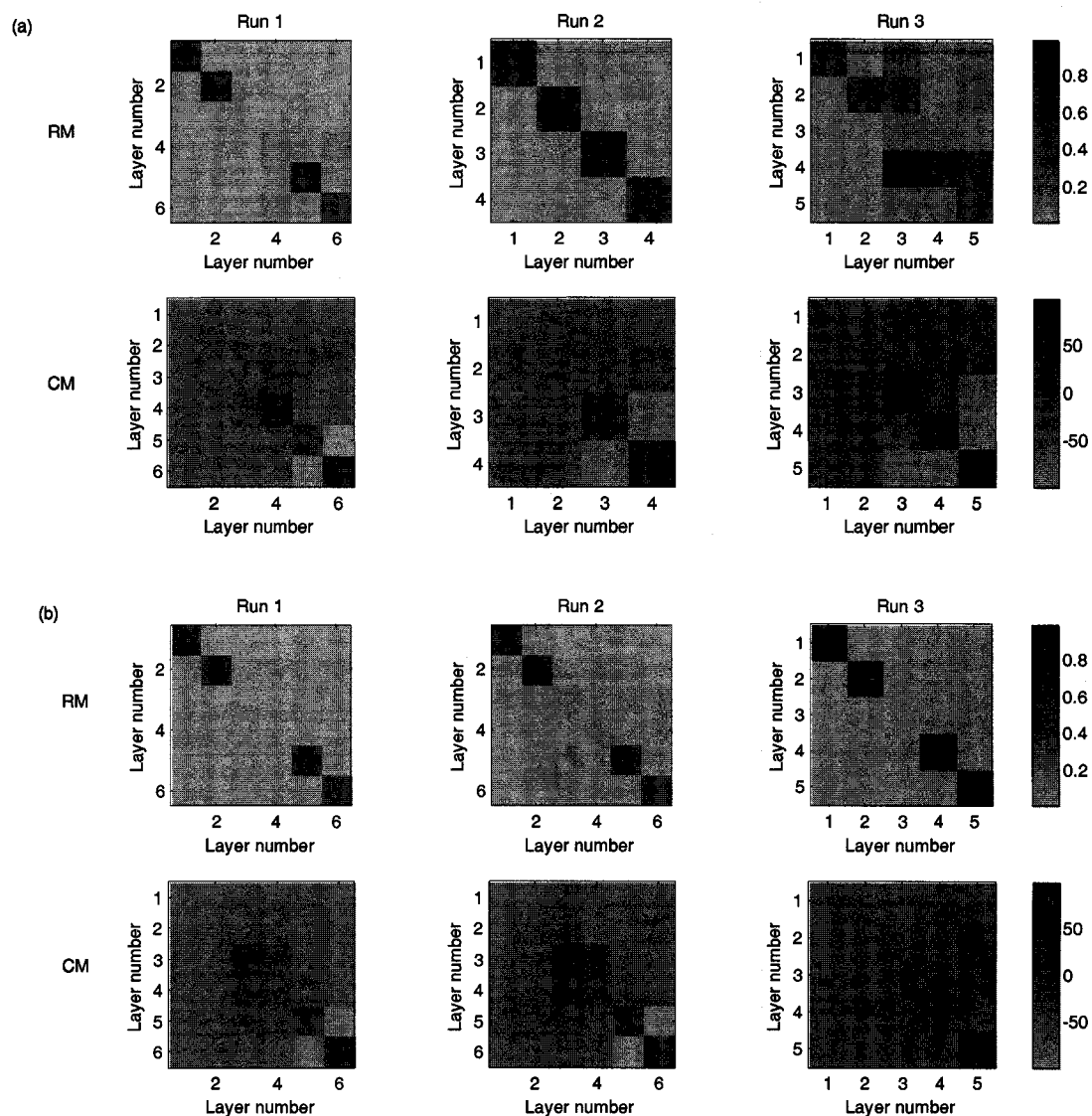


Figure 5.20. FD study, HVL profile, MDC approach: RMs and CMs from  
(a) MDC/PF, (b) MDC/PM.

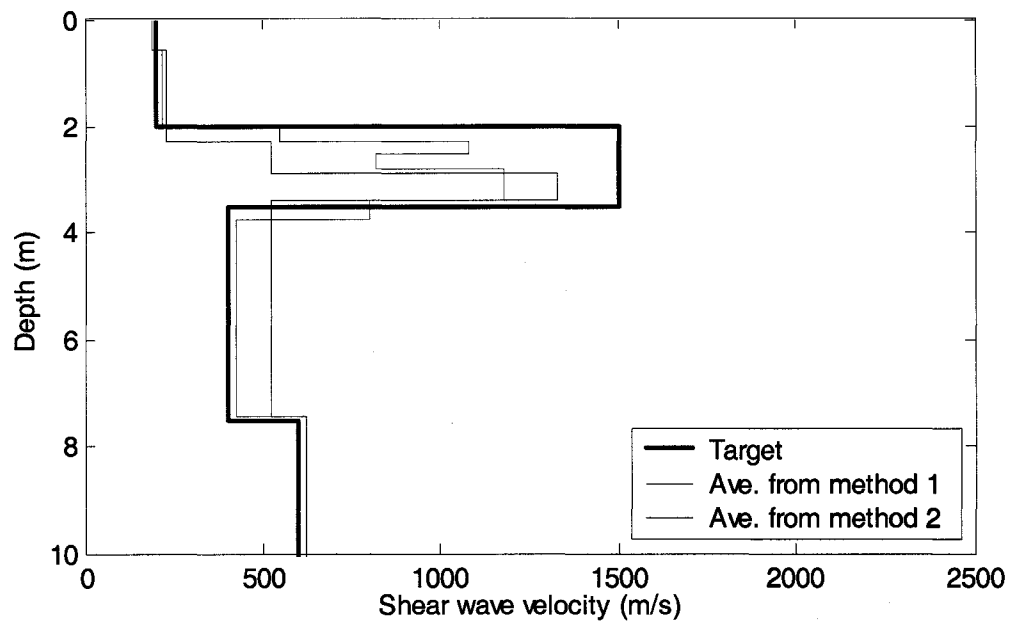


Figure 5.21. Comparison of average  $V_S$  profiles from two averaging methods.

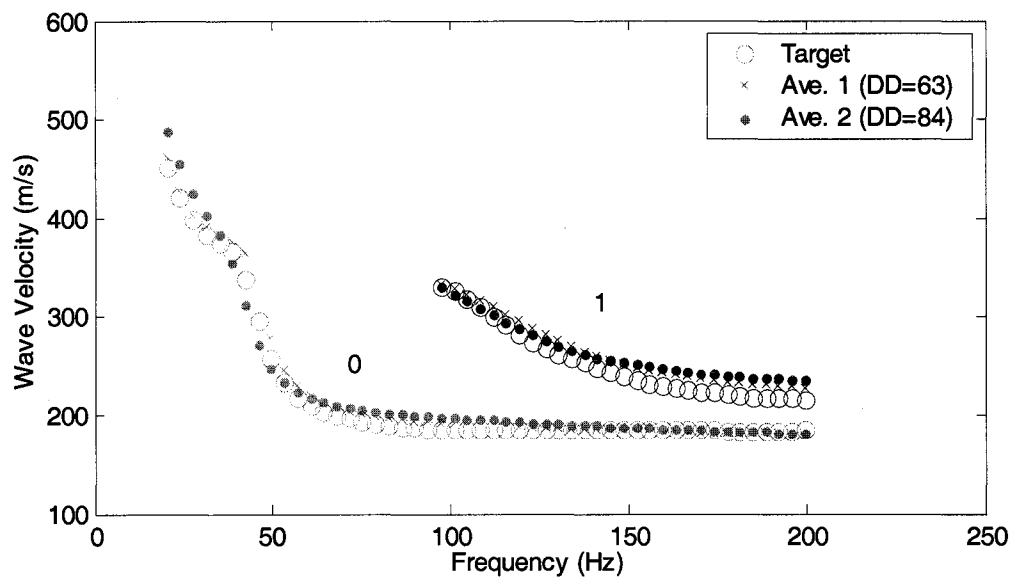


Figure 5.22. Comparison of DCs from two averaging methods.

## CHAPTER 6

### FINITE-DIFFERENCE SIMULATION OF TWO-CHANNEL PHASE SPECTRAL METHOD

#### 6.1 Introduction

As in Chapter 5, the E3D code is used to generate synthetic time histories for both an ND and a HVL profile. In this chapter, the traditional two-channel phase spectral method is applied to the time-history data to simulate the two-channel measurement. Since the cylindrical wave forward model is the appropriate forward model for the two-channel phase spectral method, a three-dimensional model is used here instead of the two-dimensional model used in Chapter 5. The numerical result is compared to the solutions from both the cylindrical forward model and fundamental-mode DC of the plane-wave forward model. The EDC approach is then applied and the results are discussed.

#### 6.2 E3D Model and Parameter Description

Two synthetic profiles, ND (Table 6.1) and HVL (Table 6.2), are modified from those used in Chapter 3. The changes are highlighted in the tables. The layer geometries remain the same, but the water table is not considered. This is because when the water table is introduced to the three-dimensional model, the resulting high ratio of

$V_p/V_s$  causes the program to fail. However, this is not a problem for two-dimensional models.

A three-dimensional grid 150 m wide, 150 m long and 50 m deep was used. A two-dimensional simulation takes several minutes but a three-dimensional simulation may take months. To save simulation time and to satisfy the Courant condition (Eq. 5.1), which is stricter for three-dimensional models, the  $V_s$  of the HVL is decreased from 1500 to 1000 m/s. The grid spacing ( $d_h$ ) and the time step ( $d_t$ ) are increased to 0.25 m and 0.05 ms respectively. As used in Chapter 5, a Ricker wavelet source is applied in the downward direction on the surface at the center of the grid and the simulation lasts for 0.5 seconds. This three-dimensional model takes about 6 hours to run.

As we know, the two-channel surface wave measurement is performed with different receiver spacings. Different sources (e.g., hammer, drop weight) are used to produce signals with different frequency components and normally more than one source is necessary for a measurement. Thus, a Ricker wavelet with different central frequencies might be required to simulate a two-channel surface wave measurement. Since the depth to the halfspace for the ND and HVL profiles is 7.5 m, four spacings are simulated: 2, 4, 8 and 16 m. Various central frequencies were tested. The rationale behind the selection of the proper corresponding central frequency for each spacing was that the frequency response for a longer spacing is lower than that from a shorter spacing. Table 6.3 shows the spacings and corresponding central frequencies for the ND and HVL profiles. For the 8-m spacing, a much lower central frequency is needed for the HVL profile to yield a useful outcome compared to the ND profile. This suggests that the HVL is reached at the 8 m spacing and that the energy dissipation is faster for the HVL profile.

### 6.3 Two-Channel Phase Spectral Method Simulation

The time histories and the development of the DC for the ND and HVL profiles are included in Appendix B. The maximum frequency needed to avoid aliasing is about 80 Hz, given 10 grid points per wavelength (Eq. 5.3). Here, the author set the cut-off frequency as 100 Hz. This corresponds to 8 grid points per wavelength. Figures 6.1 to 6.3 show the results from the two-channel phase spectral method simulation for the ND profile. Results include the phase of the cross power spectrum for each spacing (Figure 6.1), a composite DC (Figure 6.2) and the comparison of the three DCs (Figure 6.3). The three DCs are from E3D simulation, cylindrical-wave forward model and fundamental-mode of plane-wave forward model. The three DCs match well above 40 Hz. Several phenomena are observed below 40 Hz: 1) the DC from the cylindrical-wave model has the highest velocities; 2) the DC from E3D simulation has scatter while the other two DCs are smooth; and 3) the DC from E3D simulation is closer to the DC of the fundamental mode from the plane-wave forward model than to that of the cylindrical-wave forward model.

Figures 6.4 to 6.6 show the corresponding results for the HVL profile. The DCs from E3D simulation and cylindrical-wave forward model agree well and both display a kink from 30 to 45 Hz. No kink is displayed in the fundamental-mode DC. This difference between DCs is attributed to the significant energy partitioning to higher modes induced by the presence of the HVL. It is also noted that the difference is concentrated in a narrow frequency band with few data points as was observed in Chapter 3.

## 6.4 Inversion and Interpretation

### 6.4.1 Results for the ND Profile

As in Chapter 3, no prior information is considered for the ND profile. The resulting DD and PD values from the EDC/CM analysis are presented in Table 6.4 and Figure 6.7. Two runs have the same DD and PD. The third one has a higher DD, but a significantly lower PD.

Figures 6.8 to 6.10 show the results from the EDC/CM analysis. The first layer fits the target for all the runs. Runs 1 and 2 have virtually identical results and they underestimate the  $V_S$  of all layers except the first layer. Their RMs display perfect resolution and CMs show little interdependence between layers with a higher standard deviation for the half space. Run 3, the one with a higher DD, underestimates the  $V_S$  of the second layer and overestimates the  $V_S$  of the halfspace. Its RM displays relatively lower resolution for the halfspace, and its CM shows more dependence between the halfspace and the second and third layers with respect to the CMs from the other two runs. The significantly lower PD value is due to the better fit for the  $V_S$  of the third layer. The average  $V_S$  profile underestimates the  $V_S$  of the second and third layers.

The underestimation of the  $V_S$  at most depths in most runs is due to the difference between the target DC and the theoretical DC generated from the forward model that is used in the inversion. Here, the target DC is from the E3D simulation while the theoretical DC is generated from the cylindrical-wave forward model. As shown in Figure 6.3, the DC from E3D simulation has lower velocities than those of the cylindrical wave model below 40 Hz. The cause of the difference between DCs requires more investigation.

### 6.4.2 Results for the HVL Profile

For the HVL profile, prior information is provided for the HVL. The parameter settings for the HVL are the same as those presented in Chapter 3 except that the SR for  $V_S$  is set from 750 to 1500 m/s.

The EDC/CM analysis is applied. Additionally, inversion of the EDC with fundamental mode DC from plane wave model (EDC/PF) is also considered, because the difference between the DC from the E3D simulation and the fundamental mode DC concentrates in a narrow frequency band with a few data points.

The resulting DD and PD are presented in Table 6.5 and Figure 6.11. The DD of all runs are close. The PD from the EDC/CM analysis are approximately half to one-third that from the EDC/PF analysis.

Figures 6.12 to 6.14 show the results from the EDC/CM analysis. Even though only one run (run 1) yields a profile that contains a HVL, all the theoretical DCs fit well with the target DC. The sole resolved HVL is extremely thin compared to the target HVL and its RM shows poor resolution for this HVL and the layers above and underneath. The three inverted profiles and the average profile match well with the background profile but not for the HVL. The  $V_S$  profiles from runs 2 and 3 are similar except that the  $V_S$  from run 2 is about 10% lower for the fourth layer. However, their RMs show obvious different resolutions which is misleading.

Figures 6.15 to 6.17 show the results from the EDC/PF analysis. It is noted that the data spacing for theoretical and target DCs do not match. The reason is that the theoretical DC in this case is calculated with equal spacing in wavelength (on a logarithmic scale) but plotted by frequency. All three runs yield a profile that contains a



HVL: the second layer. Of the parameters describing the HVL, the depth is best resolved. This agrees with the finding from the sensitivity study presented in Chapter 4. The velocity and thickness are both overestimated. Due to the overestimation of the HVL, the PD from the three inverted profiles and average profile are greater than those from the EDC/CM analysis. Despite the HVL being well resolved, all the RMs show poor resolution.

Surprisingly, none of the runs from the EDC/CM analysis resolved the HVL while all three runs from the EDC/PF analysis resolved the HVL. To investigate the cause, four DCs are plotted and displayed in Figure 6.18: 1) fundamental mode DC for the ND profile, 2) fundamental mode DC for the HVL profile, 3) DC from cylindrical wave forward model for the HVL profile and 4) DC from the E3D simulation of the HVL profile.

The three DCs for the HVL profile, including the fundamental mode DC, all diverge from the fundamental-mode DC for the ND profile below 50 Hz. This difference is induced by the presence of the HVL. That means the shape of the fundamental-mode DC also carries the signature of the HVL. This makes it possible to use the EDC/PF analysis to resolve the HVL.

In theory, the cylindrical-wave forward model is the proper model for the EDC approach. The FD simulation also illustrated that the DCs from the E3D simulation and the solution of the cylindrical-wave forward model match well and both display a kink. Unfortunately, the EDC/CM analysis failed to resolve the HVL. The reason might be that the kink's limited number of data points over a narrow frequency band makes it difficult for the inversion to capture the correct information. Or it can be put another way. The

failure occurs because the influence of the HVL is not enough to make the EDC distinguishable from the fundamental-mode DC. This deficiency may be due to its thinness, and/or depth of embedment, and/or lower velocity contrast. Recall that the velocity of the HVL in this case is 1000 m/s instead of the 1500 m/s used in previous chapters. The reduced velocity contrast could contribute to the failure.

To improve the ability of the EDC/CM analysis to resolve the HVL, one possible solution is to emphasize the difference between 30 and 45 Hz by assigning heavier weights to the points in the DC over the range where the kink occurs. However, in practice, the difference between the EDC and fundamental-mode DC may be overshadowed by many factors as mentioned in Chapter 5. This will make it still more difficult for the EDC/CM analysis to capture the key information for real datasets.

Table 6.1. Layer properties of the ND profile for the three-dimensional model.

(Differences with respect to the profile tested in Chapter 3 are highlighted.)

Layer number	Thickness (m)	$V_P$ (m/s)	$V_S$ (m/s)	Poisson's ratio	Density (kg/m <sup>3</sup> )
1	2.0	374	200	0.3	1700
2	5.5	<b>748</b>	400	<b>0.3</b>	1700
Half-space		<b>1122</b>	600	<b>0.3</b>	1700

Table 6.2. Layer properties of the HVL profile for the three-dimensional model.

(Differences with respect to the profile tested in Chapter 3 are highlighted.)

Layer number	Thickness (m)	$V_P$ (m/s)	$V_S$ (m/s)	Poisson's ratio	Density (kg/m <sup>3</sup> )
1	2.0	374	200	0.30	1700
2	1.5	<b>1732</b>	<b>1000</b>	0.25	2200
3	4.0	<b>748</b>	400	<b>0.30</b>	1700
Half-space		<b>1122</b>	600	<b>0.30</b>	1700

Table 6.3. Spacings and corresponding central frequencies of Ricker wavelet  
for the ND and HVL profiles.

	ND profile	HVL profile
Spacings (m)	Central frequency (Hz)	Central frequency (Hz)
2	100	100
4	100	100
8	100	10
16	10	10

Table 6.4. Summary of results for the ND profiles from FD simulation of two-channel  
phase spectral method.

Run number	DD	PD
1	28	63
2	28	63
3	32	39
Avg.		55

Table 6.5. Summary of results for the HVL profiles from FD simulation of two-channel  
phase spectral method.

	EDC/CM		EDC/PF	
Run number	DD	PD	DD	PD
1	35	71	31	155
2	38	86	36	184
3	38	67	36	187
Avg.		92		165

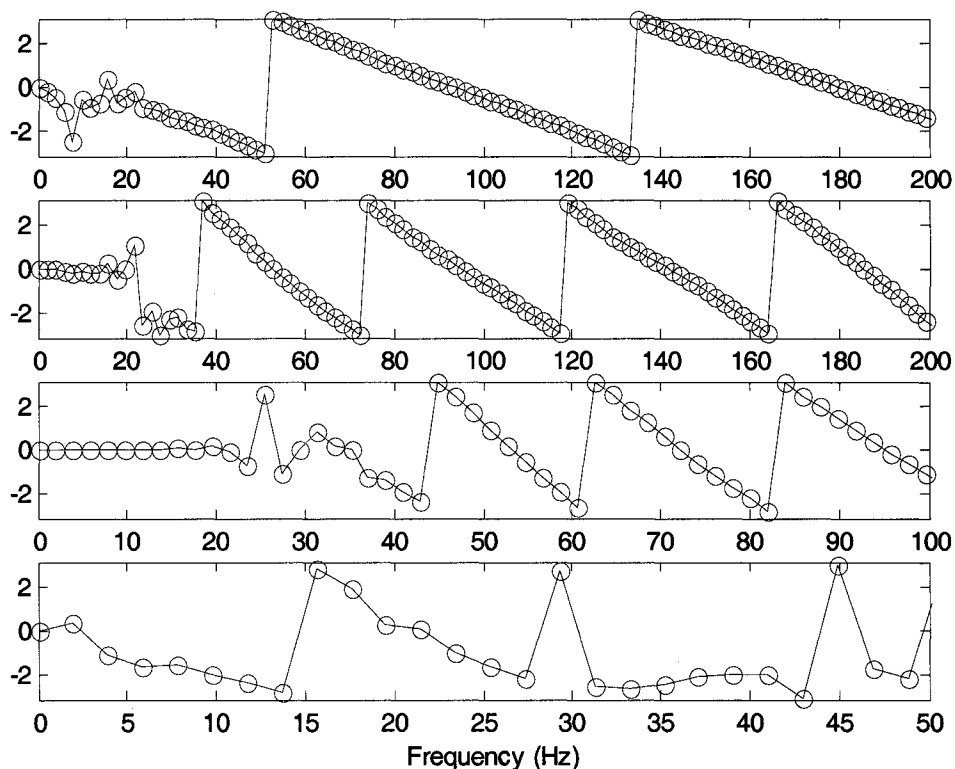


Figure 6.1. ND profile: Phase of the cross power spectrum of each spacing (2, 4, 8  
and 16 m from top to bottom).

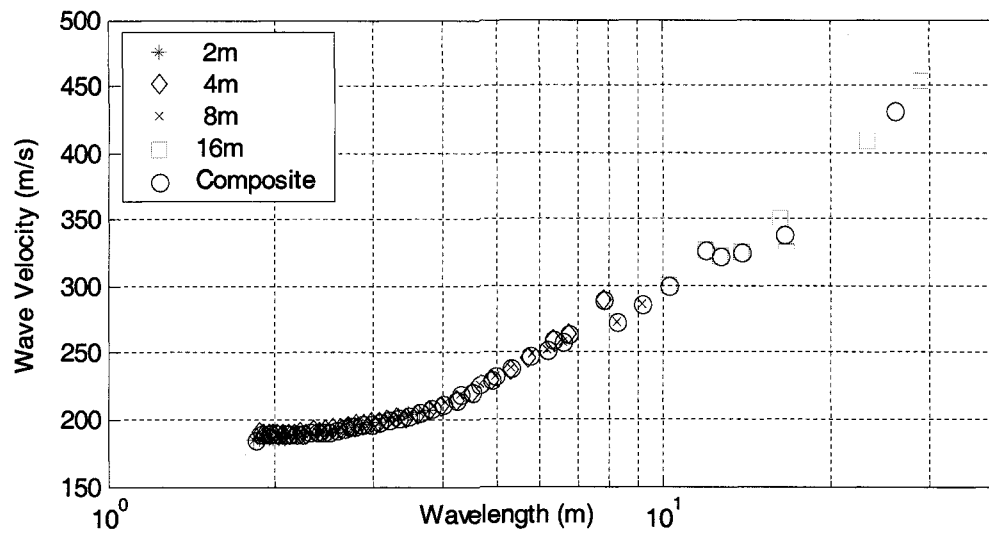


Figure 6.2. ND profile: Composite DC.

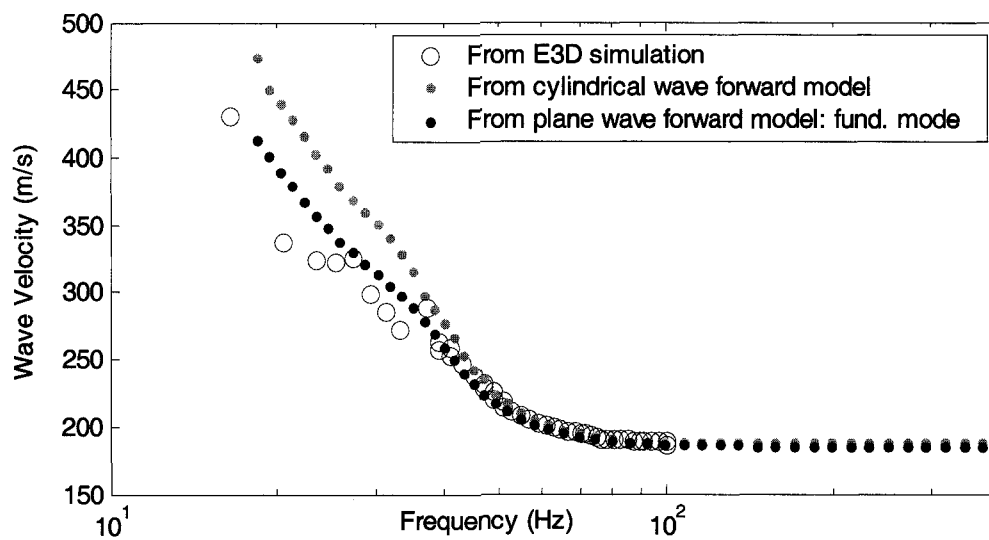


Figure 6.3. ND profile: comparison of DCs from E3D simulation.

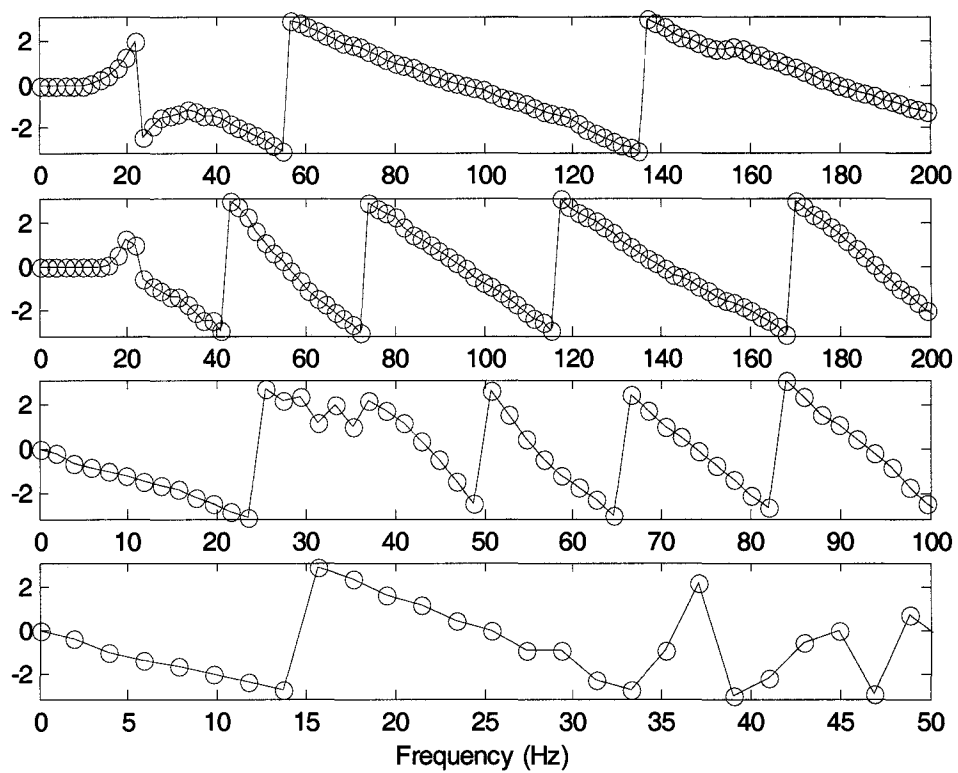


Figure 6.4. HVL profile: phase of the cross power spectrum of each spacing (2, 4, 8 and 16 m from top to bottom).

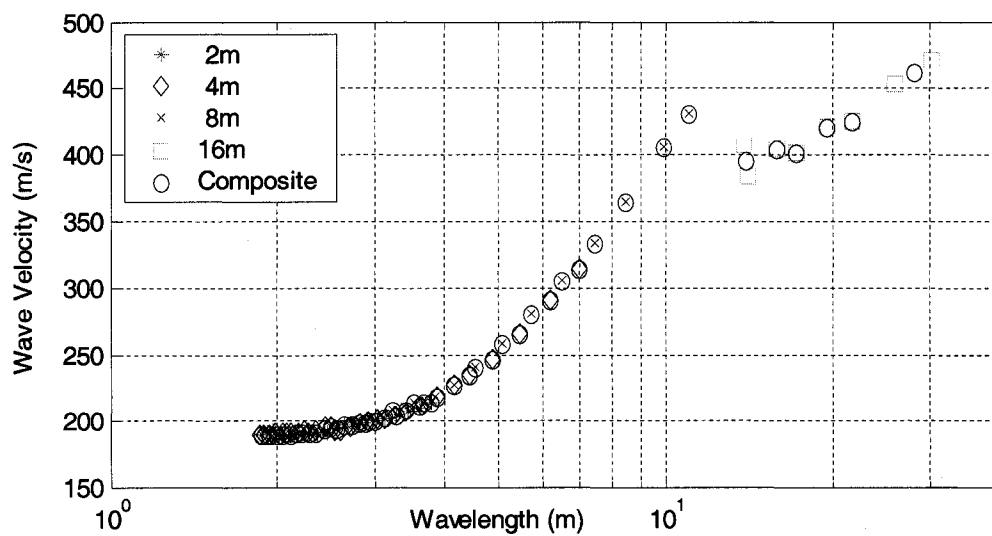


Figure 6.5. HVL profile: composite DC.

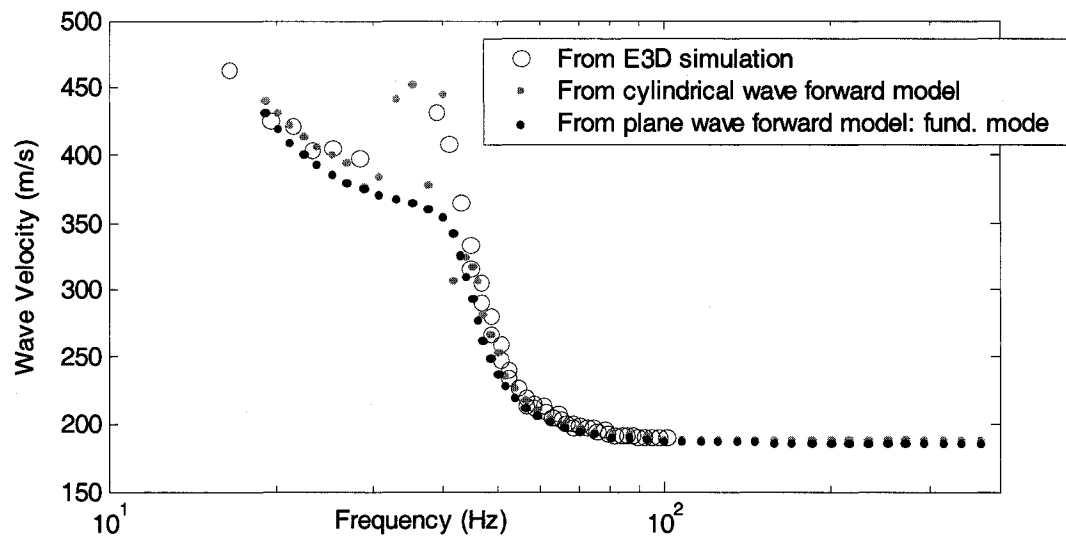


Figure 6.6. HVL profile: comparison of DCs from E3D simulation.

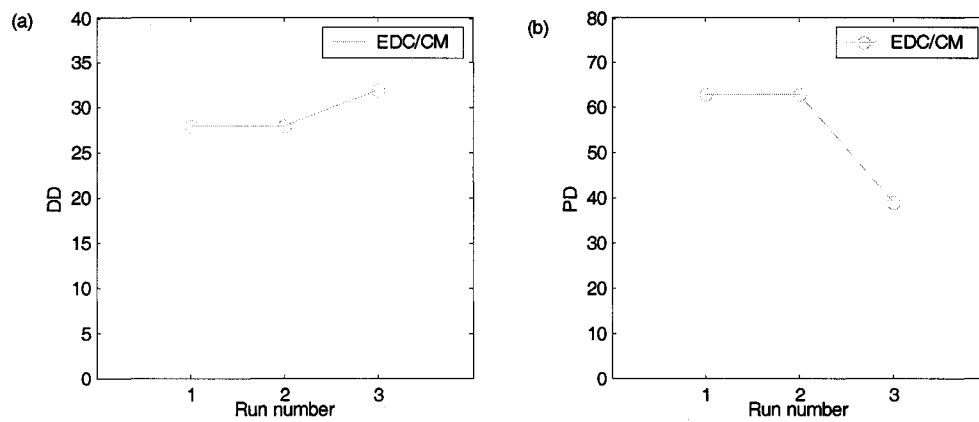


Figure 6.7. FD study, ND profile, EDC/CM: comparison of (a) DD values, (b) PD values.



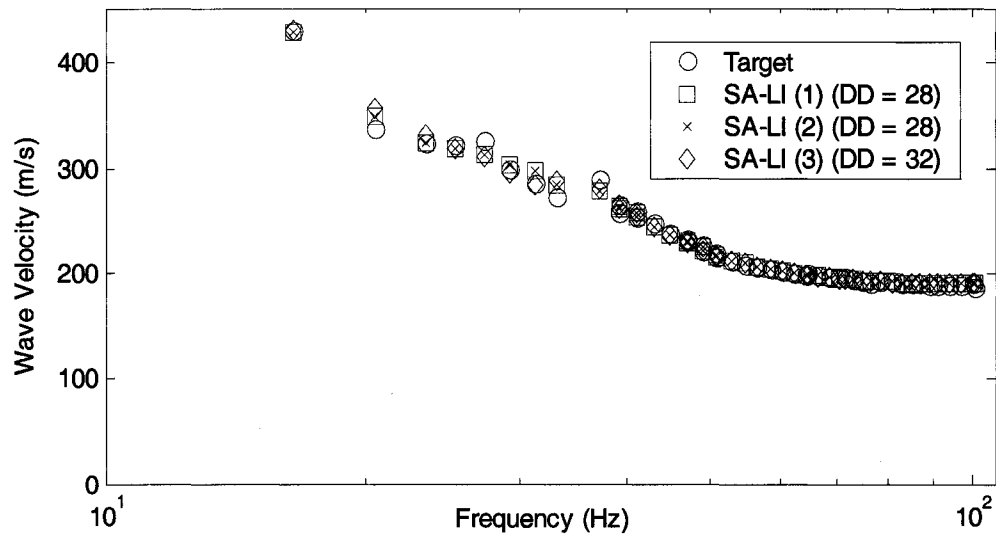


Figure 6.8. FD study, ND profile, EDC/CM: comparison of DCs.

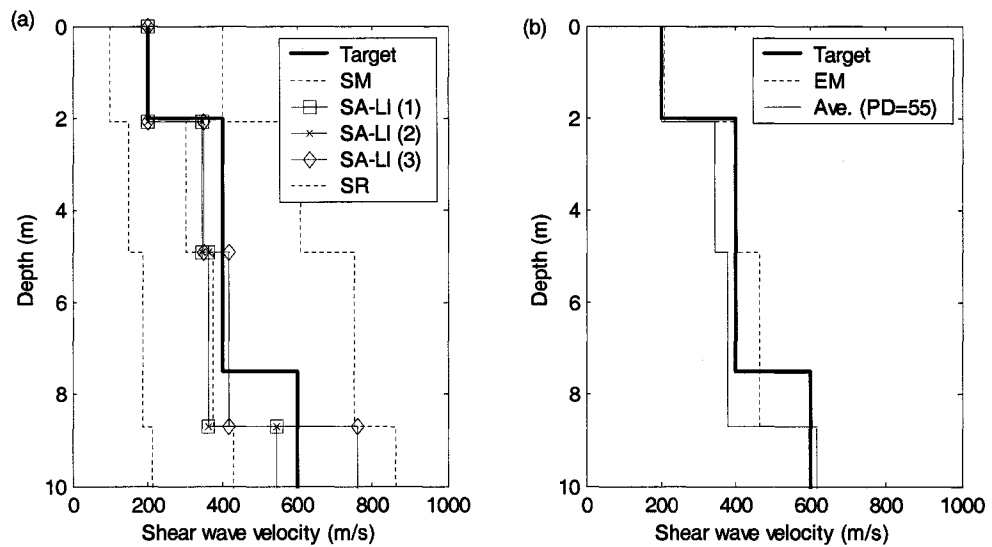


Figure 6.9. FD study, ND profile, EDC/CM:  $V_S$  profile from (a) three runs (b) average.

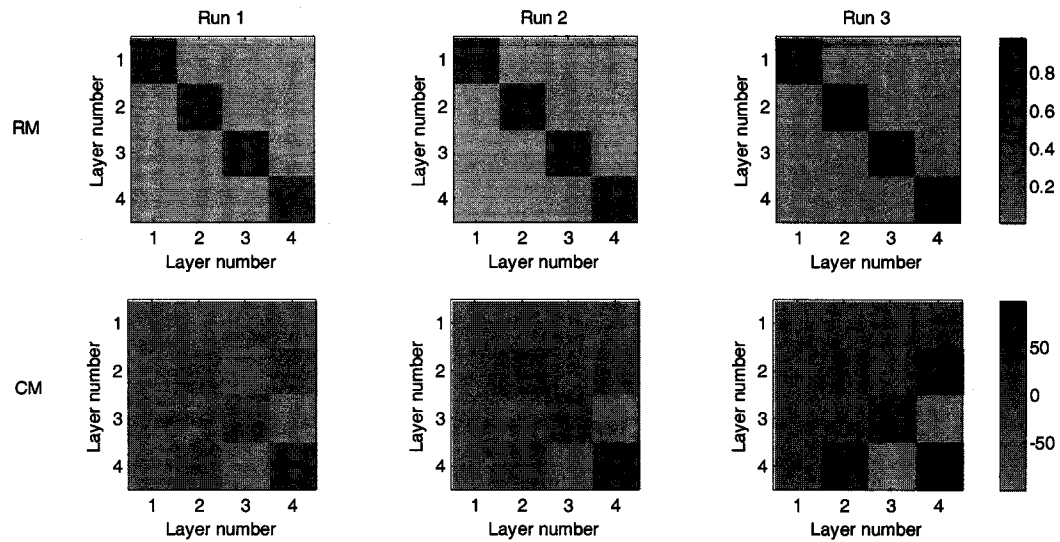


Figure 6.10. FD study, ND profile, EDC/CM: RMs and CMs.

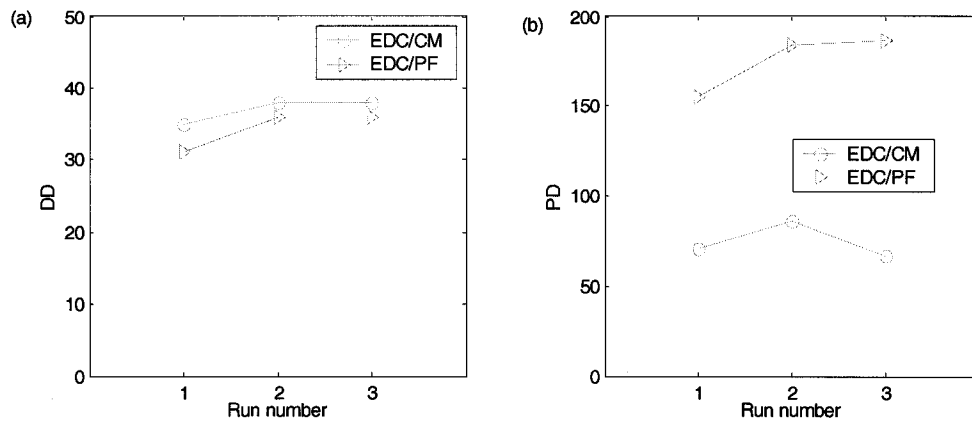


Figure 6.11. FD study, HVL profile, EDC: Comparison of (a) DD values, (b) PD values.

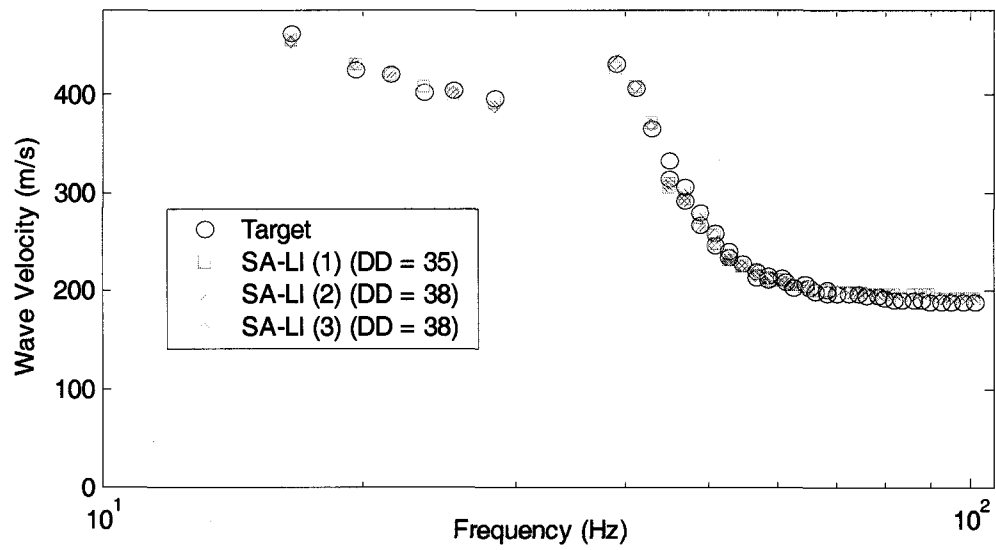


Figure 6.12. FD study, HVL profile, EDC/CM: comparison of DCs.

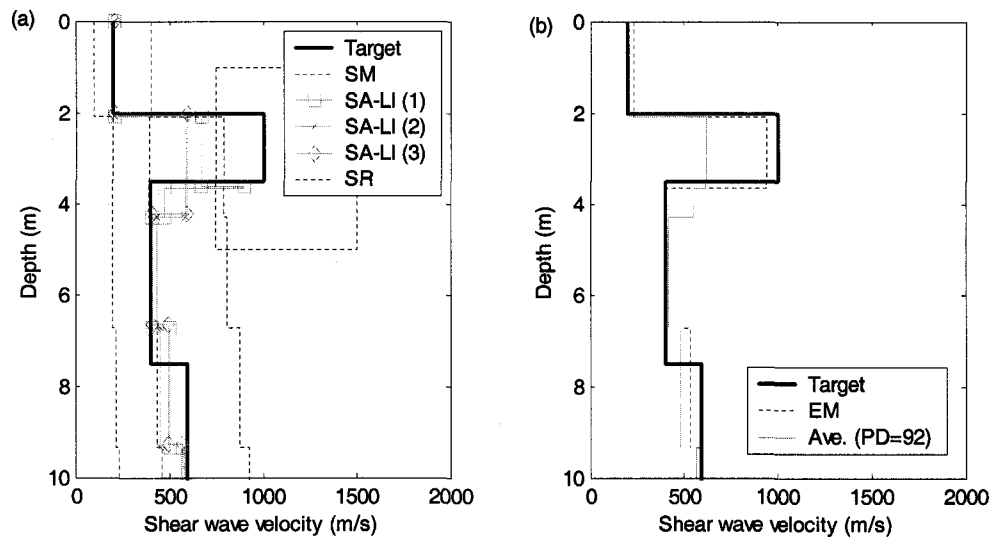


Figure 6.13. FD study, HVL profile, EDC/CM:  $V_S$  profile from (a) three runs (b) average.

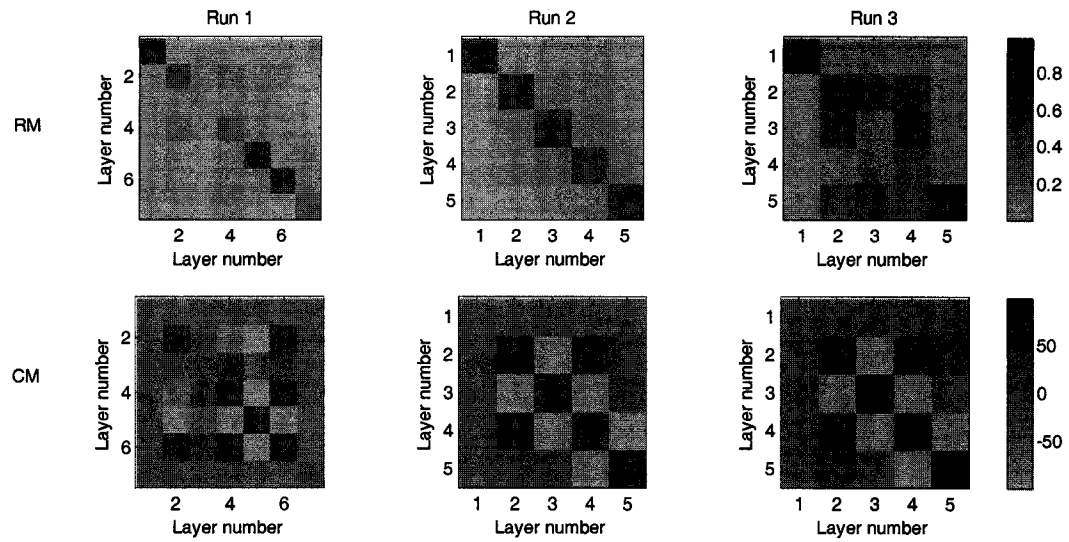


Figure 6.14. FD study, HVL profile, EDC/CM: RMs and CMs.

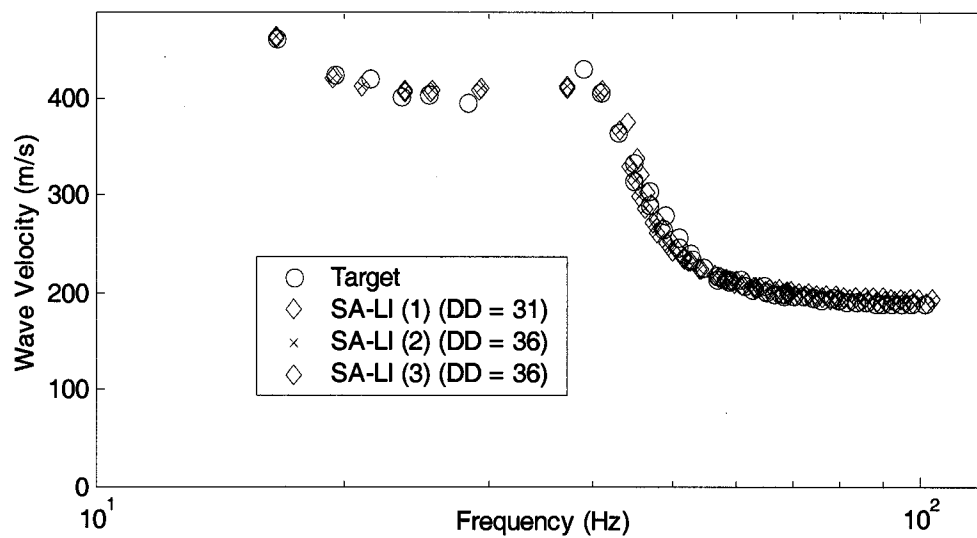


Figure 6.15. FD study, HVL profile, EDC/PF: comparison of DCs.

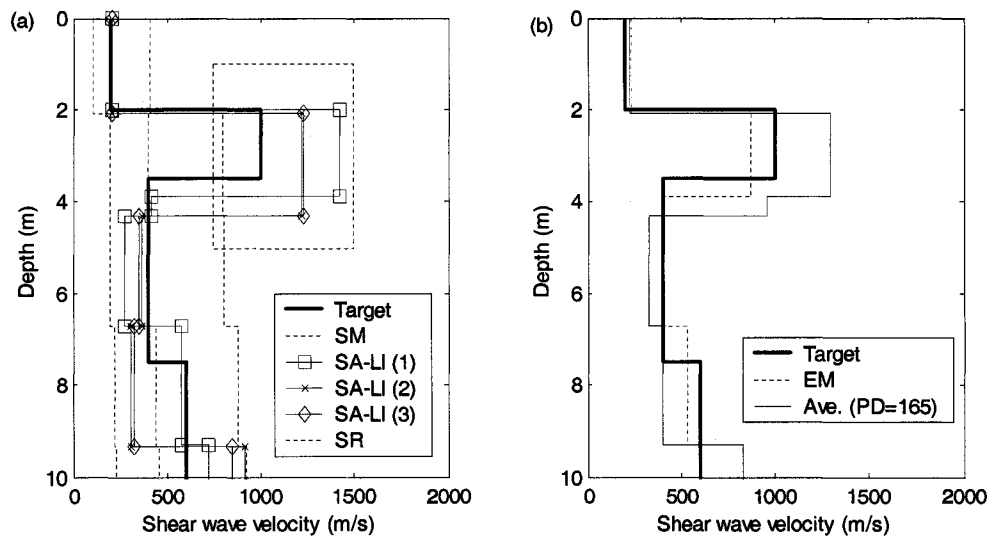


Figure 6.16. FD study, HVL profile, EDC/PF:  $V_s$  profile from (a) three runs (b) average.

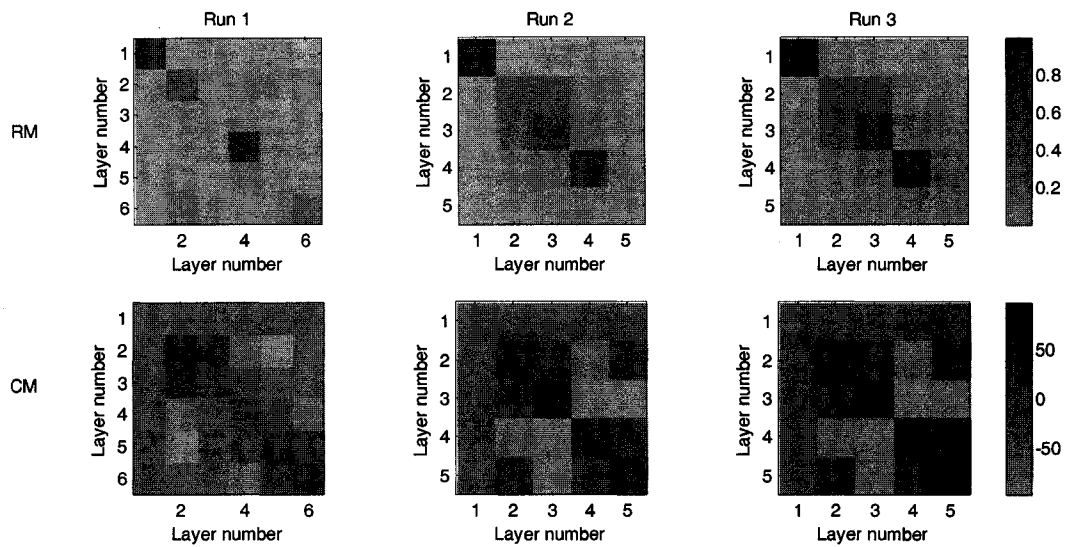


Figure 6.17. FD study, HVL profile, EDC/PF: RMs and CMs.

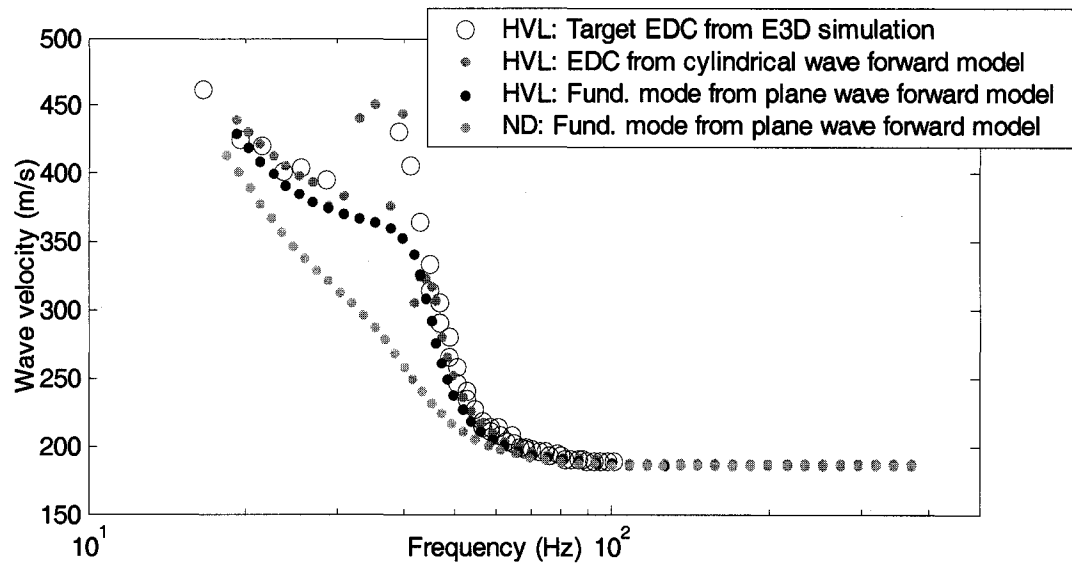


Figure 6.18. Comparison of four DCs.

## CHAPTER 7

### EXPERIMENTAL STUDY

#### 7.1 Introduction

Different surveys have been performed at the UNLV EGTS to measure the seismic wave velocities. Among those, the measurements that are discussed here include a 30-m deep downhole measurement, a  $V_P$  refraction measurement, a SASW measurement and two MASW measurements.

The new approaches are applied to the SASW and MASW measurements. The resulting  $V_S$  profiles are compared to the borehole log and  $V_S$  profile from the downhole measurement, which serves as the reference profile. The outer bounds of the three solutions are presented to illustrate credible ranges (Luke and Calderón-Macías in press). Based on the  $V_S$  profile from the downhole measurement and the borehole lithologic log, two anomalous layers are identified. One is a HVL located at depths 2 to 4 m and the other is a LVL located at depths 12 to 15 m. The  $V_S$  profiles from the new approaches are compared to two factors: 1) ability to resolve the HVL and LVL; and 2) average  $V_{S30}$ . The  $V_{S30}$ , which is the average shear wave velocity in the top 30 m (100 ft), is used in the U. S. National Earthquake Hazard Reduction Program (NEHRP) provisions and the International Building Code to assign site classification for earthquake engineering design. It is computed by arithmetic averaging of slownesses (IBC 2003):

$$V_{s30} = \frac{\sum_{i=1}^n D_i}{\sum_{i=1}^n \frac{D_i}{V_i}} \quad (7.1)$$

Where  $n$  is the number of layers and  $D_i$  and  $V_i$  are the thickness and velocity respectively of the  $i^{th}$  layer over the upper 30 m.

## 7.2 Study Site

The EGTS is located on the campus of University of Nevada, Las Vegas, south of the Engineering Building (Figure 7.1). The site is a grassy, level field, which was chosen as the location to test different surface-based and intrusive seismic and other geophysical methods.

Three boreholes, B-1, B-2 and B-3, were drilled in a line by Western Technologies, Inc., in 1997. They are 10 m deep with 4.5 m center-to-center spacing. A 30 m deep borehole, B-4, was drilled by Kleinfelder, Inc., in 2004. Two already-backfilled boreholes, A-1 and A-2, were 7 m deep and drilled by Western Technologies, Inc., in 1996. The maximum distance between the boreholes is about 18 m. The borehole logs reveal that the subsurface at the EGTS comprises stiff cemented layers interspersed among much softer clays and sands. The cemented layers were encountered in all borehole logs at depths varying from about 2 to 4.5 m. No significant lateral variations were observed. The groundwater table encountered in these boreholes ranged from 2.4 m to 4.0 m. This difference may be due to periodic groundwater fluctuation. Detailed borehole logs are available at the Engineering Geophysics Laboratory website, <http://www.ce.unlv.edu/egl/test-site/boringlogs/>.



The survey locations are marked on Figure 7.2. The downhole measurement was conducted using borehole B-4. This hole was advanced using a hollow-stem auger and cased with 4-inch PVC pipe. The refraction array was laid out with a north-south orientation, parallel to the alignment of the three boreholes, B-1, B-2 and B-3, with the center point located 3 m west of borehole B-2. Due to space limitations, the SASW and MASW measurements were performed at the boundary along the south edge of the EGTS in an east-west orientation.

### 7.3 Seismic Downhole Measurement

#### 7.3.1 Data Acquisition

For the downhole measurement, the P-wave vibrations were generated by vertical sledgehammer blows to a metal plate (20 x 20 x 1.2 cm), while S-wave vibrations were generated by horizontal hammer blows to both ends of a wooden beam (2.4 m x 18.5 cm x 8 cm) with steel end caps, held in place by the weight of a vehicle (Figure 7.3). The vehicle is used to achieve good coupling in that transmission of shear wave energy increases with increasing coupling stress (Areias et al. 1999). A vehicle is commonly used to apply the normal stress. The tires of the vehicle decouple the load from the beam in such a way as to limit the undesirable transmission of shear wave energy to the vehicle. The wooden beam was aligned with magnetic north. The P- and S-wave sources were offset 2 m from the borehole. The hammer has an impact sensor that is attached to the handle near the head. The sensor triggers the recording process upon impact with the plate or beam. Two 4.5 Hz geophones, one vertical and the other horizontal, were placed on the surface, close to the P- and S-wave sources respectively (Figure 7.4). In fact, 40

Hz geophones would be preferred, but the proper type was not available at that time. A three-component, wall-locking geophone package containing 10-Hz geophones, manufactured by Geostuff, was clamped to the borehole casing and lowered to different depths. This geophone package includes a fluxgate compass and servo mechanism which automatically orients the radial geophone to magnetic north. Thus, the radial geophone stays aligned with the S-wave source at each measurement point (Crice 2002).

The water table, according to the log for borehole B-4, is at a depth of 4 m. The water inside the casing was bailed out prior to performing the measurement to combat the interference of tube waves (Crice 2002). The downhole measurement was performed by B. Luke, H. Murvosh, Q. Su and the author on July 15, 2006. The measurements were made every 0.5 m in depth from 0.5 to 20 m and every 1 m from 21 to 29 m. Thus, a total of 49 depths were measured. Data were recorded using a Geometrics Geode seismograph with a sampling rate of 0.0625 ms; that is fast enough to capture a  $V_S$  as high as 4000 m/s.

### 7.3.2 Data Analysis

For each measurement, the travel time is the difference between the first arrivals for the in-hole geophone and the geophone at the surface. All the downhole data are presented in Appendix C. This includes the raw data records of P- and S-waves after adjustment for inconsistent triggering, superposed with picks. The picks were made by the author. In general, the quality of the P-wave data was good to excellent at all depths. It was relatively easy to pick the first arrivals. For the S-wave data, the picks were consistently made before the first peak/trough. The picks were reasonably clear at

shallow depths. The picks below 12 m are suspect due to the increased ambiguity with depth.

Polarity reversals were noted at some depths. Reversals are not due to the equipment in this case. Also they are not due to the heterogeneities of the site because no significant lateral variations were observed from all the boring logs. Possible reasons might be grouting and aging of the borehole. The annulus of the borehole was grouted with cement from bottom to (–10) ft and the remainder was backfilled with pure bentonite to surface, which is improper. In addition, the downhole measurement was performed about two years after the borehole was drilled.

The times were corrected for the horizontal offset,  $h$ , from source to borehole using the following equation:

$$t_{vrt} = t_{slant} \frac{z}{\sqrt{h^2 + z^2}} \quad (7.2)$$

where  $t_{slant}$  is the measured travel time from the offset source to depth  $z$  and

$t_{vrt}$  is the time for the energy to travel from the top of the borehole to depth  $z$ .

Analysis of the P- and S-wave first arrival picks was performed using two techniques. One is the direct method (Kim et al. 2004) and the other is the ray-path method (Boore 2003).

#### 1) Direct method

Figure 7.5 indicates the plots of  $t_{vrt}$  versus depth for both P- and S-waves. They are interpreted into major straight-line segments by curve fitting. The slope of the fitting line segment represents the wave velocity in the covered depths. As shown in Figure 7.5, four layers are identified from the P-wave data and six layers are identified from the S-

wave data. The Poisson's ratio is within reasonable range (0 to 0.5). The value is above 0.4 below 5.5 m depth. This agrees with the finding that the water table is at 4 m depth from the borehole log because the value of Poisson's ratio should be close to 0.5 for soft saturated soil. One LVL is detected from S-wave data at depths 12 to 14.5 m. Comparing to the borehole log, the location fits well with a clayey silt layer.

## 2) Ray-path method

It is important to note that the arrival times for several data points are earlier than those just underneath them (Figure 7.5). This is most likely due to the energy following a refracted ray path instead of the straight ray path assumed in the direct method. In the ray-path method, it is assumed that the wave propagates along the refracted ray path based on Snell's Law (e.g., Boore 2003). Thus, it is more accurate than the direct method. This method is coded in R by Eric M. Thompson at Tufts University and the code is available online at <http://www.tufts.edu/~ethomp04/>. The R is an open source language available online at <http://www.r-project.org/>. Figure 7.6 indicates the  $V_P$ ,  $V_S$  and Poisson's ratio from this method. The Poisson's ratio is again within reasonable range. The value is above 0.4 below 5.5 m, which agrees with the outcome from the direct method. According to the  $V_S$  profile, two anomalous layers are detected. In addition to the LVL, which is also detected at depths 12 to 14.5 m, an HVL is detected at depths 2 to 5.5 m. From the borehole log, two cemented layers, one with cemented sand and gravel and the other logged as caliche, are located at depths 2.3 to 4 m. The depth of the HVL from the ray-path method is close to that from the borehole log but its thickness is greater. Thus, the  $V_S$  profile from the ray-path method serves as reference profile for the

following surface wave measurements.

The comparison of the outcome from the two methods is displayed in Figure 7.7. For most depths, the  $V_P$  from the ray-path method is 10% greater than that from the direct method. A decrease in  $V_P$  is noted from the ray-path method at the corresponding LVL location. The  $V_S$  profiles from the two methods match well except that the HVL is not detected by the direct method. Even though a LVL is identified from both methods, the existence of this layer is suspect due to the ambiguity of picks below 12 m.

#### 7.4 P-wave refraction measurement

Because P-wave refraction and MASW measurement have the same data acquisition methods, it is convenient to collect them at one time. But the two measurements presented here were not collected at the same time or with the same array. However, they are measured at close locations. Thus, the information from refraction can still be used to guide the inversion of surface wave measurement as mentioned in Chapter 4. The P-wave refraction measurement was performed by B. Luke, M. Tecle and R. Stone on March 30, 2002. Twelve, 40 Hz geophones with 1 m spacing were used. Data were recorded using a seismograph with 0.25 ms sampling rate. The source was positioned at 1 m distance from the first geophone. Both forward and reverse measurements were performed. For each direction, records of single hits and multi-hit stacks were stored. The forward stacked measurement has the clearest waveform and thus was used for the analyses. The picks were made using the software Tomtime (<http://www.giscogeo.com/pages/seixgott.html>). The raw data with picks are presented in Appendix D. The refraction analysis was performed using the program Plotrefa from Geometrics. The result is shown in Figure 7.8.

The  $V_p$  from refraction is compared to the results from downhole measurements in Figure 7.7. The  $V_p$  of the top layer is 24% higher than that from the direct method of downhole measurement. The  $V_p$  of the second layer is close to that from the ray-path interpretation of the downhole measurement. The thickness of the first layer varies between 2.1 m and 2.3 m along the test line. This small lateral variation is assumed to have an insignificant effect on the surface wave measurement. The depth to the second layer is in good agreement with the location of the cemented layers from the borehole logs.

## 7.5 SASW measurement

### 7.5.1 Data Acquisition

The SASW data were collected by Y. Liu, B. Luke and J. Gilbert of Utah State University on July 26, 2003. Three 1-Hz vertical geophones and a 4-channel signal analyzer were used. For short spacings, 1, 2, 4, 8 and 16 m, a hammer was used to excite the wave energy. For long spacings, 10, 20, 40 and 80 m, a 2040-kg drop-weight developed by Dr. James Bay at Utah State University was used. The detailed geometry and procedures for this measurement and DC generation are provided by Liu (2006). The DCs generated from all receiver spacings, superposed with the composite DC are shown in Figure 7.9.

### 7.5.2 Inversion

Prior information for the HVL that can be extracted from two sources, borehole log and refraction measurement, is considered. A summary of the prior information settings from the borehole log and refraction data is provided in Table 7.1. Based on the borehole

log, the HVL is at 2.3 m depth and is 1.7 m thick. Thus, the depth of the possible HVL ranges from 1 to 5 m and the thickness ranges from (-0.5) m to 2 m. The SR for thickness corresponds to a probability of 0.8 of finding a HVL. The SR for  $V_S$  ranges from 1000 to 2000 m/s.

Based on the P-wave refraction measurement, the thickness of the top layer is about 2 m and the  $V_P$  of the top and second layers are 400 and 1900 m/s respectively. If Poisson's ratio is assumed to be 0.3, the corresponding  $V_S$  is 210 and 1020 m/s. As in Chapter 4, the thickness and velocity of the top layer are searched within ranges set to correspond with the refraction measurement. For the top layer, thickness ranged from 1.5 to 2.5 m and  $V_S$  ranged from 150 to 250 m/s. For the starting model generation, the thickness of the top layer is fixed at 2 m. For the HVL,  $V_S$  ranged from 900 to 1500 m/s. Since the thickness of the cemented layer is normally from 1 to 2 m, the thickness range is set from 1 to 2 m. The SR for the thickness corresponds to a probability of 1 of finding a HVL. The range of depths bounding the possible HVL is from 1.5 to 4.5 m.

It is important to note that the thickness of the HVL based on prior information from both borehole log and refraction are thinner with respect to the reference profile. Thus, the thickness of the HVL will be underestimated from inversion analyses with respect to the reference profile.

As illustrated in Chapter 6, for the SASW measurement, inversions with both cylindrical-wave forward model (EDC/CM) and fundamental-mode plane-wave forward model (EDC/PF) are performed. The EDC/CM analysis is also performed without prior information to test whether the inversion analysis can detect the HVL without prior information.

Thus, according to the description above, five inversion analyses with the EDC approach are considered: a) EDC/CM analysis with no prior information (EDC/CM/NPI); b) EDC/CM analysis with prior information from borehole log (EDC/CM/BL); c) EDC/PF analysis with prior information from borehole log (EDC/PF/BL); d) EDC/CM analysis with prior information from refraction measurement (EDC/CM/R); and e) EDC/PF analysis with prior information from refraction measurement (EDC/PF/R). For each analysis, three SA-LI runs are performed.

Figure 7.10 indicates the DD from the five inversion analyses. The EDC/PF/BL analysis has the lowest DD for all runs. The DD from the EDC/CM/BL analysis and the EDC/CM/NPI analysis are intermediate. The inversion analyses with prior information from refraction have greater DD values than the rest.

Figures 7.11 to 7.25 show the results from all the inversion analyses, following the same format used in previous chapters. It is important to note that the LVL is beyond the lower boundary of the SR. Thus, it is not possible for the inversion of SA to resolve it. However, as we know that LI is an unconstrained method, it is still possible for the SA-LI analysis to get the correct solution, if layer geometry permits. Overall, the resulting  $V_s$  profiles follow the trend of the reference profile. None of the inversion analyses resolved the LVL. However, a velocity decrease, with larger velocity and thickness, is identified at the depth of the LVL by the EDC/PF/BL and EDC/PF/R analyses.

Without prior information, the EDC/CM analysis does not resolve the HVL. The theoretical DCs from inversions with prior information from refraction fit the target DC poorly above 100 Hz (Figures 7.20 and 7.23). This mismatch induced greater DD values than the rest. The cause of the mismatch is that only a single layer is assumed above the



HVL based on the prior information from refraction. The constant velocity of the single layer forces the theoretical DC to have a constant value above 100 Hz.

For the inversion analyses given prior information, the HVL is detected in most runs. The depth to the top is quite well resolved with respect to the reference  $V_S$  profile. The velocity of the HVL is frequently underestimated. It is not surprising that the thickness of the HVL is consistently underestimated because the SR for the thickness is smaller than the HVL thickness in the reference profile. The thickness is better resolved from inversion analyses with prior information from refraction than with prior information from the borehole log. This can be attributed to the SR for refraction being more restricted. Of the three parameters, the depth of the HVL was most reliably resolved.

Recall in Chapter 6, the numerical simulation illustrated that the HVL is better resolved from the EDC/PF analysis than from the EDC/CM analysis, given the same prior information. Here, the EDC/PF/BL analysis has lower DD than that from the EDC/CM/BL analysis for all runs. The HVL is identified by both inversion analyses with similar quality.

For the real data, the quality of the results can be evaluated by the DD value, qualitative assessment of fit between the DCs and repeatability of results. It is hard to use the RM and CM to guide the evaluation of the solution. As discussed in previous chapters, they are misleading in many cases even for perfect synthetic data. Here, for example, run 1 of the EDC/CM/NPI analysis has good resolution (Figure 7.13), however, both the HVL and LVL are not resolved (Figure 7.12). And run 3 of the EDC/CM/R analysis has poor resolution (Figure 7.22), although it has the lowest DD value in three runs (Figure 7.20) and the HVL is resolved (Figure 7.21).

Figure 7.26 indicates the average  $V_S$  profiles from the five inversion analyses with respect to the reference profile. The EDC/CM/R analysis overestimates the reference  $V_S$  at depths 7.5 to 11 m by 30%. For the EDC/PF/R analysis, the  $V_S$  at depths 28 to 32.5 m is 60% higher than the rest. None of the analyses resolved the suspected LVL. The  $V_S$  profiles from the other three inversion analyses (EDC/CM/NPI, EDC/CM/BL and EDC/PF/BL) show small variance except at the location of the HVL. The EDC/PF/BL analysis has the lowest DD in all inversion analyses. In addition, the  $V_S$  profile fits well with the reference  $V_S$  profile and the HVL is well resolved. Thus, its solution is considered as the best solution from the SASW measurement.

## 7.6 MASW Measurements

### 7.6.1 Data Acquisition

Two MASW measurements were performed along the same line as the SASW survey. One was performed by the author, S. Saldaña and J. O'Donnell on February 5, 2005. Sixty, 4.5-Hz vertical geophones at 0.5 m spacing were used. A sledgehammer was used to generate the source energy and a seismograph was used to record the dataset. That equipment was on loan from the PASCAL Instrument Center IRIS Consortium (<http://www.iris.edu/>). The sampling rate and the recording length were 0.5 ms and 1 s, respectively. Separations between source and nearest geophone varying from 7 to 15 m were tested. Records were stacked to improve signal-to-noise ratio.

The second survey used a “minivib” T-7000W vibroseis manufactured by Industrial Vehicles International, Inc. (IVI) to generate the source energy. The measurements were performed by the author, E. Peters and Q. Su on April 1<sup>st</sup>, 2006. Twenty-four 4.5 Hz

vertical geophones with 1 m spacing were used. The walkaway method (Park et al. 2001a) was applied to acquire the data. In this method, the location of either the source or the receivers is fixed while the other moves to cover wider testing ranges. The record groups are then joined to form a combined dataset. The minivib was fixed at the same location where the drop-weight source was placed for the forward-direction SASW survey. The separation between source and nearest geophone was chosen as 10 m to reduce near-field effects (Park et al. 1999b). Channel 1 was set to save the sweep pilot. Thus, only 23 channels were available for each walkaway setup. A 14-second linear down-sweep from 120 Hz to 5 Hz was applied, and a 16-second record was recorded with 1-ms sampling interval. Geophones were moved four times. Thus a total equivalent number of geophones is 115 (23 times 5) with the offset coverage from 10 to 124 m.

#### 7.6.2 Data processing and DC generation

The vibroseis data that are acquired using the Minivib in sweep mode must be processed to produce a data record equivalent to that of an impulsive source. This processing is accomplished by a cross-correlation of the raw data with the vibroseis sweep (Brittle et al. 2001). A seismic trace can be viewed as the superposition of seismic pulses reflected from seismic interfaces. The basic seismic convolutional model for a vibroseis source is

$$x(t) = r(t) * s(t) \quad (7.3)$$

where  $x(t)$  is the signal recorded at the receiver;

$r(t)$  is the reflection coefficient which is the ratio of the amplitude of the reflected wave and the amplitude of the incident wave;

$s(t)$  is the sweep pilot and  $*$  is the convolution operator.

To remove the sweep, both sides of the equation are cross-correlated ( $\otimes$ ) with the synthetic pilot. The equation becomes

$$c(t) = x(t) \otimes s(t) = r(t) * s(t) \otimes s(t) \quad (7.4)$$

where  $c(t)$  is the signal after cross-correlation.

The autocorrelation of a vibroseis sweep is defined as a Klauder wavelet  $k(t)$ , so the equation is simplified to

$$c(t) = r(t) * k(t) \quad (7.5)$$

Thus, the embedded sweep is removed and a seismic record equivalent to that of an impulsive source is resolved. The Seismic Processing Workshop<sup>TM</sup> (SPW) software package was used to implement the above processing. Figure 7.27 displays the time history images of each single record and the combined record after vibroseis correlation.

After getting the time history records, the next step is to use the  $f$ - $p$  transformation method to generate the dispersion relation. For the hammer source measurements, the one with the 15-m source offset yielded the best outcome and thus is discussed here. The  $f$ - $p$  images from hammer and minivib source surveys are displayed in Figure 7.28 (a) and (b) respectively. The frequency coverage in the  $f$ - $p$  image using the hammer source is approximately from 30 to 80 Hz while that using the Minivib source is approximately from 5 to 50 Hz. Thus, they are complementary to each other. The superimposed  $f$ - $p$  image is displayed in Figure 7.29 (a). Up to three modes can be distinguished in the image. Due to the ambiguity in the mode picking, only two modes are picked manually. The combined  $f$ - $p$  images superposed with the picked points are displayed in figure 7.29 (b). Figure 7.30 indicates the DCs after interpolation by the cubic spline method, which

served as the target for inversion analysis.

### 7.6.3 Inversion

As in previous chapters, the inversion analysis is performed on 1) fundamental-mode DC alone and 2) fundamental and first-higher mode DC with weights 0.75 and 0.25 respectively. As illustrated for the SASW inversions, prior information extracted from both borehole log and refraction is considered. The MDC/PF analysis is also performed without prior information to test whether the inversion analysis can detect the HVL without prior information.

Thus, five inversion analyses with the MDC approach are considered: a) MDC/PF without prior information (MDC/PF/NPI); b) MDC/PF analysis with prior information from borehole log (MDC/PF/BL); c) MDC/PM analysis with prior information from borehole log (MDC/PM/BL); d) MDC/PF analysis with prior information from refraction (MDC/PF/R); and e) MDC/PM analysis with prior information from refraction (MDC/PM/R). The SR for the HVL is the same as described for the SASW inversions.

Figure 7.31 indicates all the DD from the five inversion analyses. The MDC/PF/NPI and MDC/PF/BL analyses have the lowest and second lowest DD respectively for all three runs. The MDC/PM/BL and MDC/PM/R analyses have greater DD than the rest.

Figures 7.32 to 7.45 show the results for all the inversion analysis following the same format used in previous chapters. Overall, the resulting  $V_s$  profiles follow the trend of the reference profile. As in the SASW inversion analyses, none of the inversion analyses resolved the suspected LVL. However, all the inversion analyses showed a velocity decrease, with larger velocity and thickness, at the depth of LVL.

Without prior information, the fundamental-mode DC generated by the hammer source was inverted using commercial software, SurfSeis (Kansas Geological Survey) (Jin and Luke 2006). The HVL was not detected. Here, the MDC/PF/NPI analysis resolved the HVL in all three runs. However, the resolved HVL is of similar thickness but deeper and the velocity is 12% greater with respect to the reference  $V_s$ . Compared to the downhole data, it overestimated the  $V_s$  of the layer at depths 19 to 29 m by as much as 86%.

Recall in Chapter 5, the numerical simulation demonstrated the difficulty in picking the higher modes, especially for the HVL profile. Here, for the MDC/PM/BL and MDC/PM/R analyses, the DC fit of both modes is poor (Figures 7.38 and 7.44) with greater DD. This might imply that great uncertainty exists in the first-higher mode DC picks. However, the solution is not disrupted compared to the reference  $V_s$  profile. This finding can be attributed to the low weights assigned to the first-higher mode DC.

Considering all the inversion analyses given prior information, the HVL is detected in most runs. The depth to the top is quite well resolved with respect to the reference  $V_s$  profile. The velocity of the HVL is frequently underestimated. The thickness of the HVL is also consistently underestimated. Of the three parameters, the depth of the HVL was again most reliably resolved.

Figure 7.47 indicates the average  $V_s$  profiles from the five inversion analyses with respect to the reference profile. The MDC/PF/BL analysis has the second-lowest DD values of all the inversion analyses. In addition, the  $V_s$  profile fits well with the reference  $V_s$  profile and the HVL is well resolved. Thus, it is considered as the best solution for the MASW measurement.

## 7.7 Comparison

### Dispersion curves

The DCs from SASW and MASW measurements are displayed in Figure 7.48. The lowest frequency from both measurements is approximately 5 Hz. The SASW DC matches well with that from the fundamental-mode MASW measurement in the range 5 to 30 Hz. The SASW DC starts a gradual transition from the fundamental to the first-higher mode at approximately 30 Hz. At frequencies above 56 Hz, it falls back below the first-higher mode response. However, it does not fall back to the fundamental mode DC. A similar trend was seen in a comparison of SASW and MASW data generated by hammer source (Jin et al. 2006). This phenomenon does not agree with the observations from both the synthetic data study and the numerical simulation, that the EDC falls back to the fundamental mode at high frequencies (Figures 3.2 and 6.6). This disagreement requires more investigation.

### $V_S$ profiles

Figure 7.49 indicates the best  $V_S$  profiles from SASW and MASW measurements compared to the reference profile. They fit reasonably well with each other but show variance at the depth of HVL. The HVL is better resolved by the MASW method. The suspected LVL is not accurately resolved, but both show a velocity decrease at that depth.

For the HVL, both inversion analyses consistently underestimate the thickness. This is because the thickness based on the prior information is less than that from the downhole measurement. The depth is slightly overestimated and velocity is consistently underestimated. Of the three parameters, depth is the most reliably resolved. These outcomes agree with a recent study by Luke et al. (2006) in which, using a HVL system

as target profile, twenty-one runs were conducted for inversions using EDC/CM and EDC/PM analyses. Outcomes were similar over much of the profile, but differed greatly in the vicinity of the HVL and just beneath it. The authors observed that the thickness tends to be underpredicted and the depth is best resolved.

According to the borehole log, the thickness of the suspected LVL is about 2.5 m and it appears at approximately 12 m depth, far below the HVL. In the inversion, no prior information was provided for this layer. Those can be the reasons that make the inversion analyses hard to resolve the LVL.

$$V_{S30}$$

The  $V_{S30}$  from downhole, SASW and MASW measurements are summarized in Table 7.2. Results in all cases would yield an IBC site classification of C, “very dense soil and soft rock”. Had the classification been based solely on lithology, this mostly-clay site would have received a classification of D, “stiff soil”. The  $V_{S30}$  from SASW and MASW measurements are 17% and 23 % higher respectively than that from the downhole measurement. The reason can be that neither of the surface wave measurements resolved the LVL. The  $V_{S30}$  from the SASW and MASW measurements compared very closely, with those from the MASW measurement about 5% higher. In summary, while the resulting  $V_S$  profiles were different, slowness-averaged velocities were comparable.

## 7.8 Discussion

The comparison of DCs from the SASW and MASW measurements confirms the expectation that a profile with a high stiffness contrast will elicit a considerable higher-mode response.



Prior information from the borehole log and P-wave refraction helps the inversion analyses to detect the anomalous layers. Without prior information, the inversion analysis failed to detect the HVL for the SASW measurement and it yielded a deeper HVL for the MASW measurement, and neither detected the suspected LVL. Given prior information, the HVL was resolved in most runs.

For the SASW measurement, the results from the EDC/PF/BL analysis were considered to be the best of the five inversion analyses tested. This finding agrees with the finding observed in the numerical studies (Chapter 6) that the EDC/PF inversion analysis yields better results with respect to the EDC/CM inversion analysis given the same prior information. For the MASW method, the results from the MDC/PF/BL analysis were considered as the best of the five inversion analyses, but the fit of the first-higher mode was poor. This finding supports the findings in the numerical studies (Chapter 5) that accurate DC picking for the first higher mode is difficult and the MDC/PF inversion analysis with prior information is able to yield good solution.

For most inversion analyses, the thickness of the HVL is better resolved from inversion analysis with prior information from refraction with respect to the inversion analysis with prior information from the borehole log. This finding can be due to the higher probability of finding the HVL in the analysis with prior information from refraction. However, the theoretical DCs from inversion analysis with prior information from refraction match the target DC poorly at high frequencies. This mismatch is due to the lower resolution of the refraction measurement with respect to the surface wave measurement close to the surface. In addition, the center point of the refraction array is about 40 m away from the center points of the SASW, MASW arrays. This separation

might have great effect on the  $V_S$  of the upper layers. To overcome this problem, two solutions can be considered. One is to improve the resolution of the refraction measurement (e.g., smaller receiver spacing). The other is to subdivide the layer geometry provided by the refraction measurement for the surface wave inversion analysis.

For the parameters of the HVL, the depth is the most reliably resolved with respect to its velocity and thickness. This agrees with the finding from the sensitivity in Chapter 4 that the  $V_S$  shows the greatest sensitivity to the depth of the HVL. None of the tests resolved the suspected LVL. Due to its deeper location, we expect it is more difficult to detect. Further research might test whether or not prior information would help to resolve this layer.

Table 7.1. Summary of the prior information settings from borehole log and refraction data.

		Borehole Log	Refraction	Anticipated from downhole measurement (ray-path method)
Top Layer	Thickness (m)	N/A	1.5 to 2.5	2
	$V_S$ (m/s)	N/A	150 to 250	174
HVL	Thickness (m)	-0.5 to 2	1 to 2	3.5
	Depth (m)	1 to 5	1.5 to 4.5	2
	$V_S$ (m/s)	1000 to 2000	900 to 1500	1274

Table 7.2. Summary of the  $V_{S30}$  from downhole, SASW and MASW measurements.

	Downhole	SASW					MASW				
		a	b	c	d	e	a	b	c	d	e
$V_{S30}$ (m/s)	368	439	434	435	430	420	457	460	464	437	450





Figure 7.2. Aerial view of the EGTS showing the location of the measurements.



Figure 7.3. Donwhole measurements.

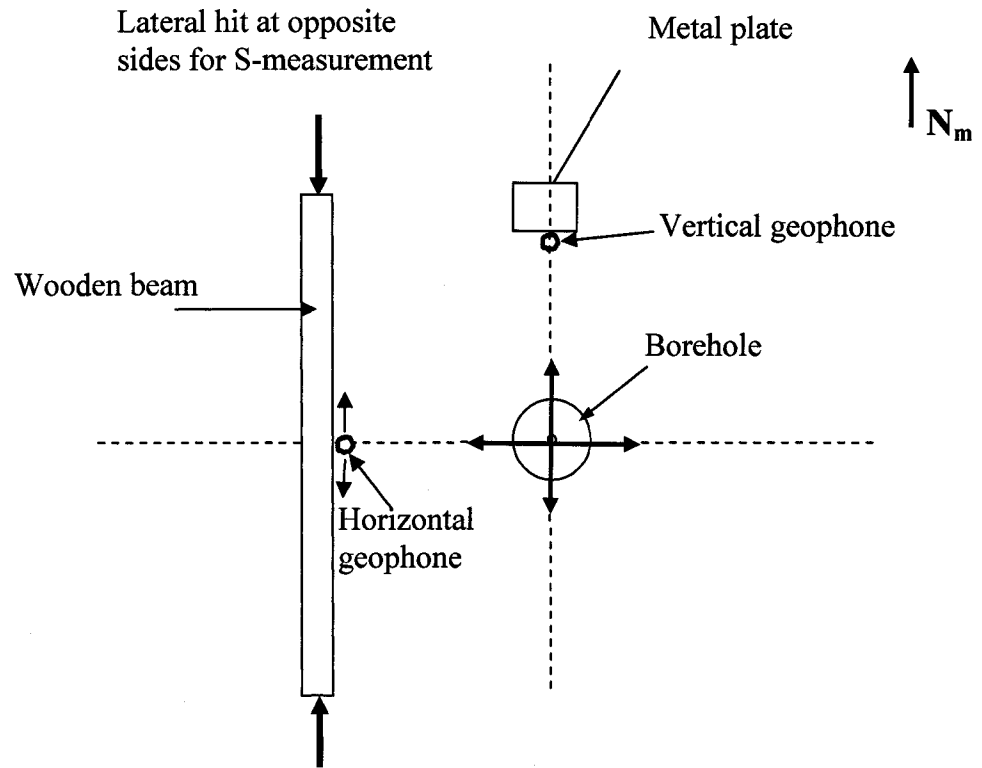


Figure 7.4. Orientation of the three-component geophones in downhole measurement.  
(not to scale)

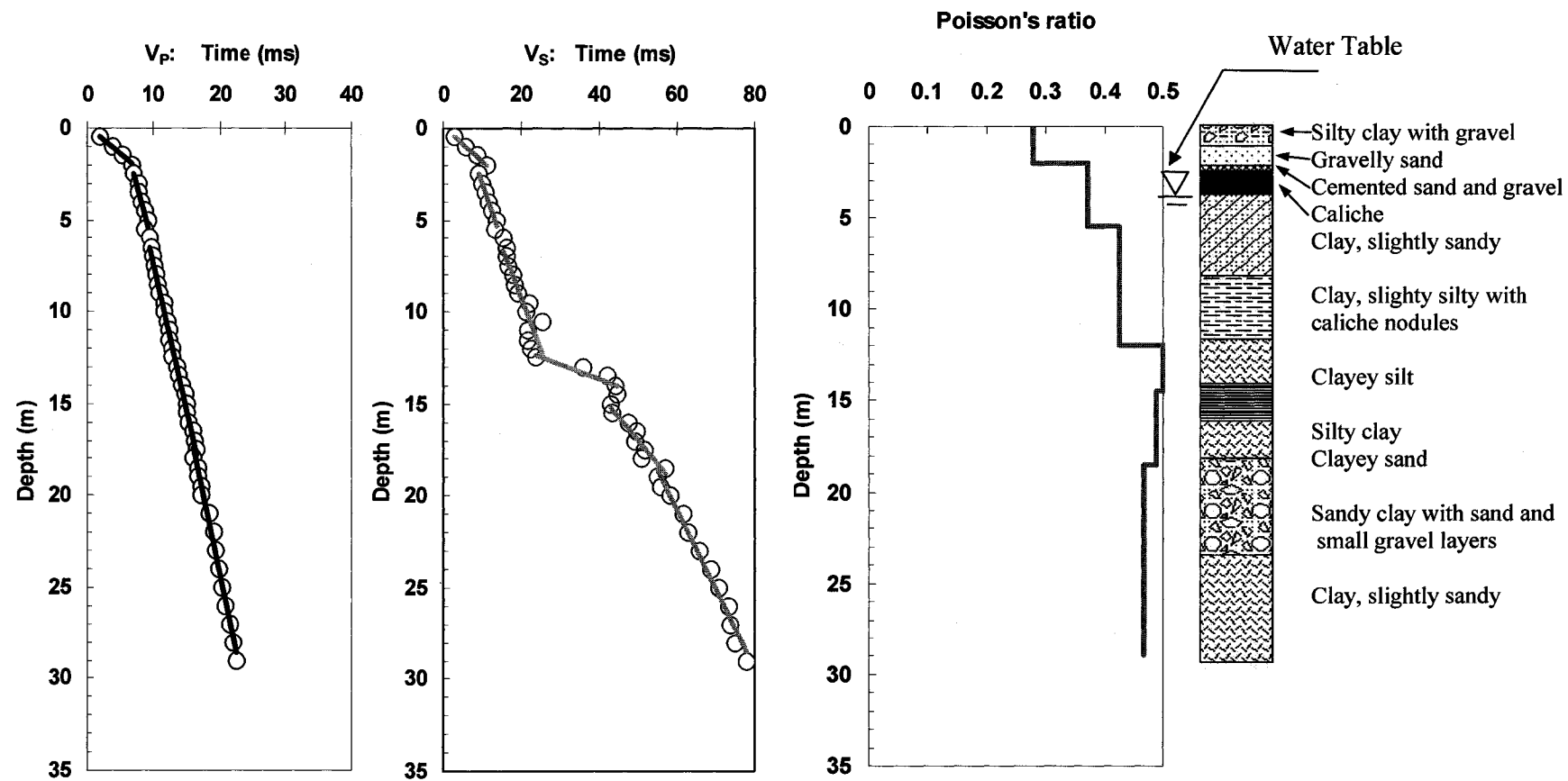


Figure 7.5. The  $V_p$ ,  $V_s$  and Poisson's ratio from the direct method with respect to the borehole log.



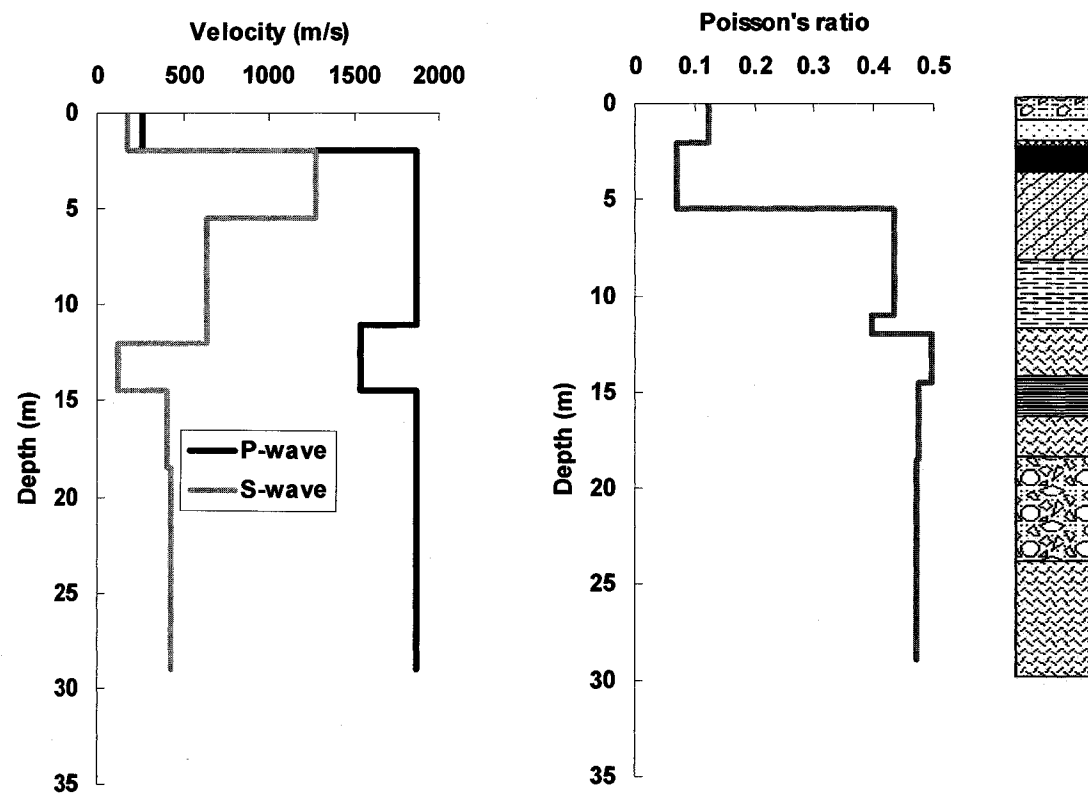


Figure 7.6. The  $V_P$ ,  $V_S$  and Poisson's ratio from the ray-path method with respect to the borehole log.

(The key of the borehole log appears on Figure 7.5.)

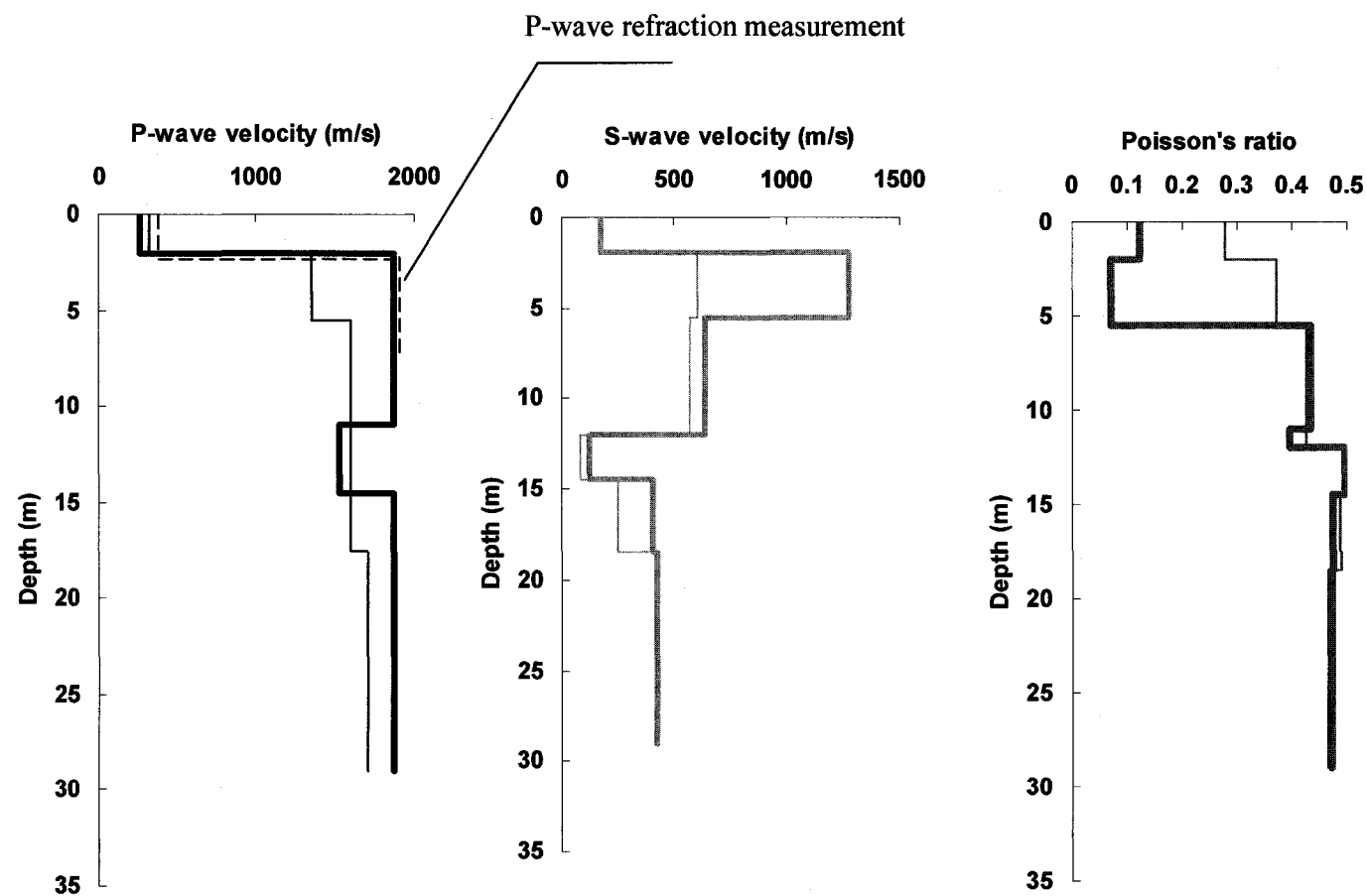


Figure 7.7. Comparison of the  $V_P$ ,  $V_S$  and Poisson's ratio from the direct method (thinner line) and ray-path method.

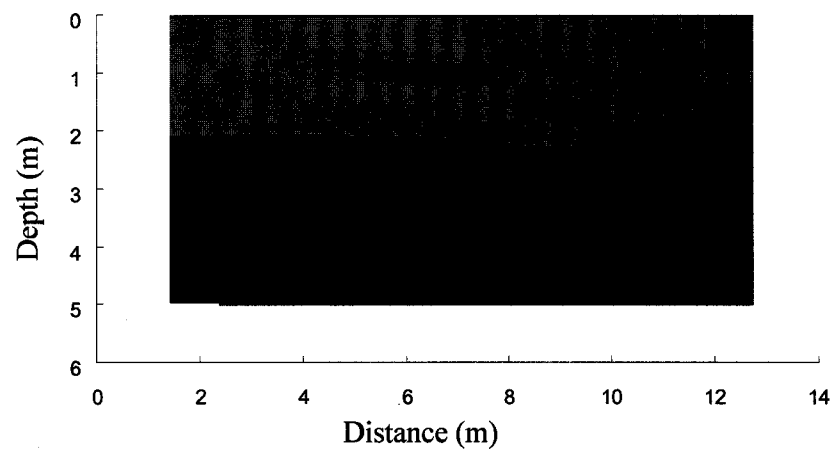


Figure 7.8. The  $V_p$  profile from refraction measurement, unit for velocity is km/s.

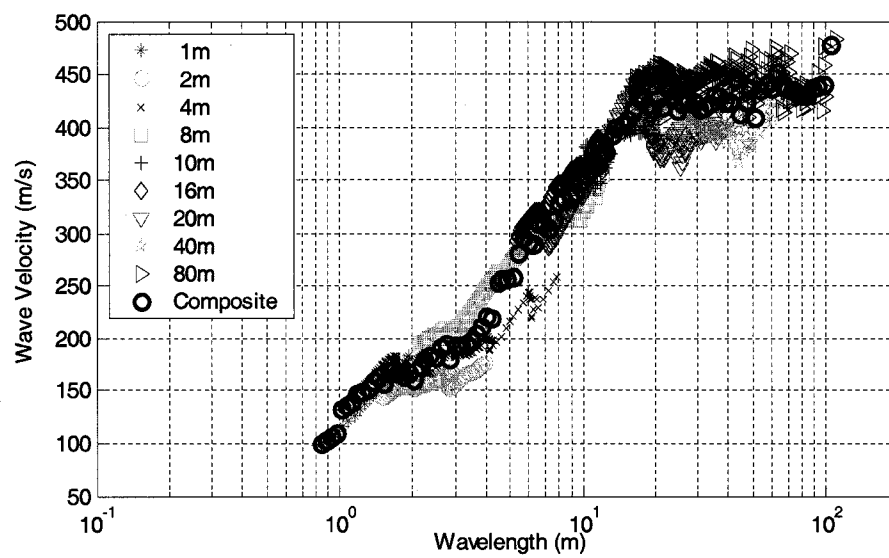


Figure 7.9. SASW: DCs for each receiver spacing and the composite DC.

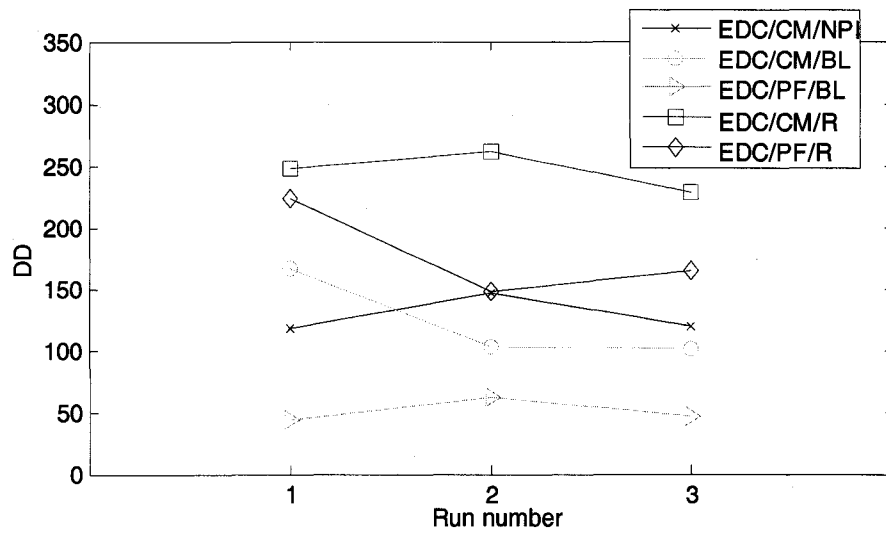


Figure 7.10. SASW: comparison of DD values from inversions.

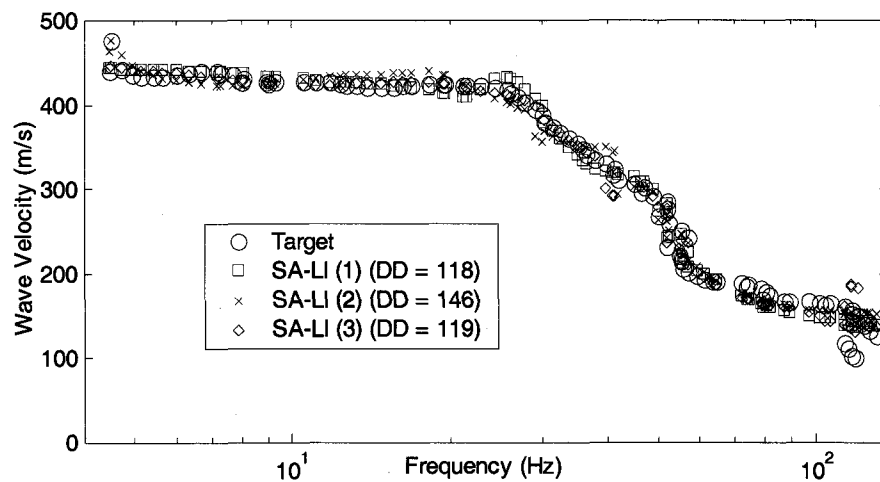


Figure 7.11. SASW, EDC/CM/NPI: comparison of DCs.

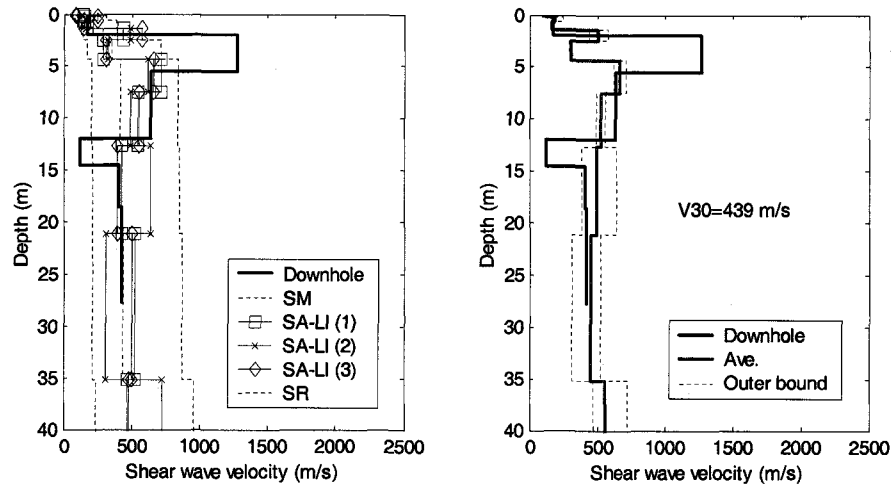


Figure 7.12. SASW, EDC/CM/NPI:  $V_S$  profiles for (a) three runs (b) average.

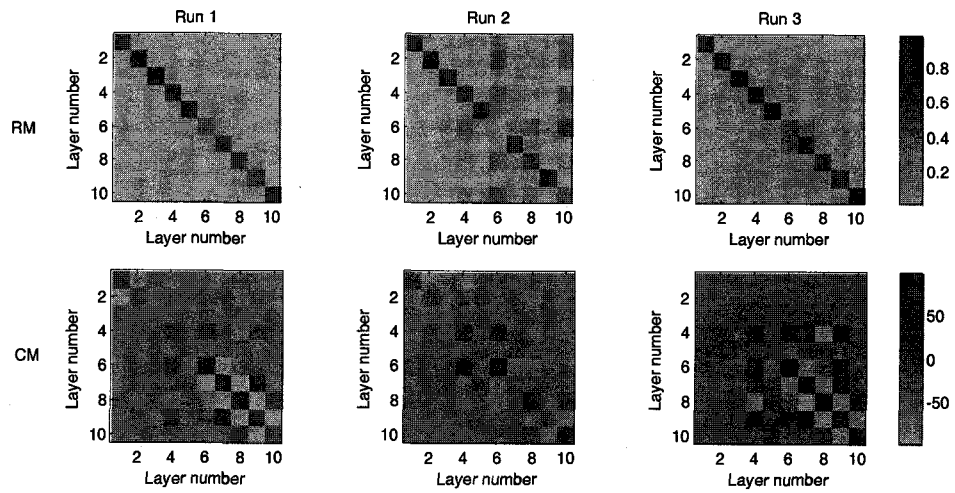


Figure 7.13. SASW, EDC/CM/NPI: RMs and CMs.

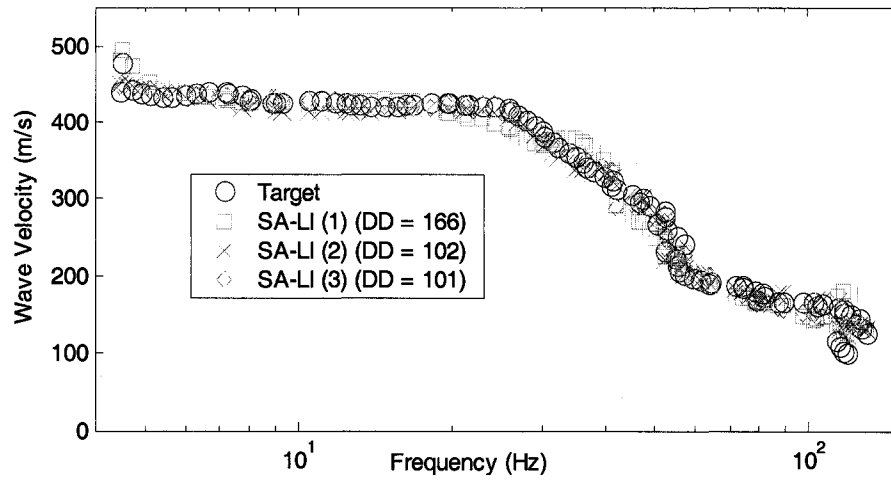


Figure 7.14. SASW, EDC/CM/BL: comparison of DCs.

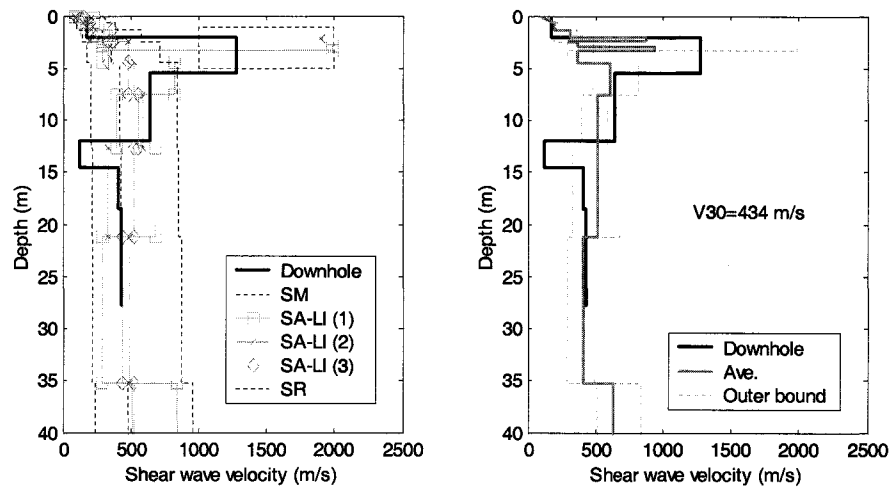


Figure 7.15. SASW, EDC/CM/BL:  $V_s$  profiles for (a) three runs (b) average.

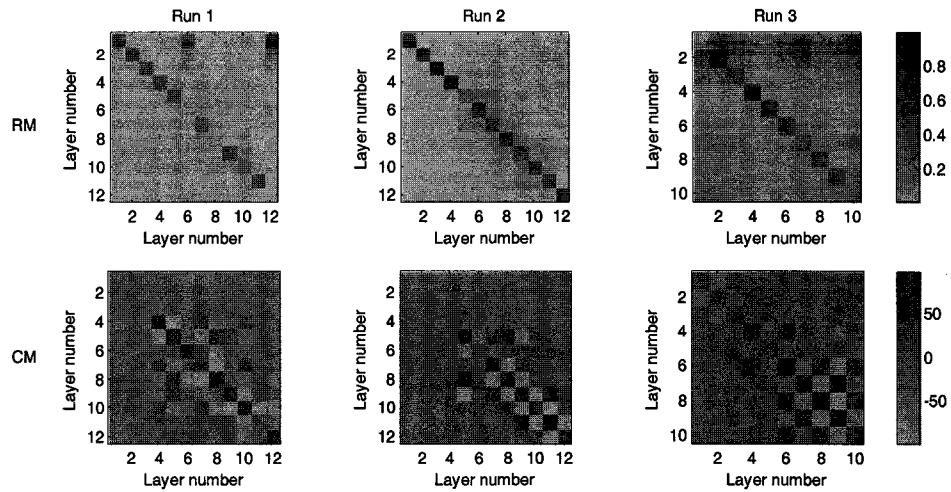


Figure 7.16. SASW, EDC/CM/BL: RMs and CMs.

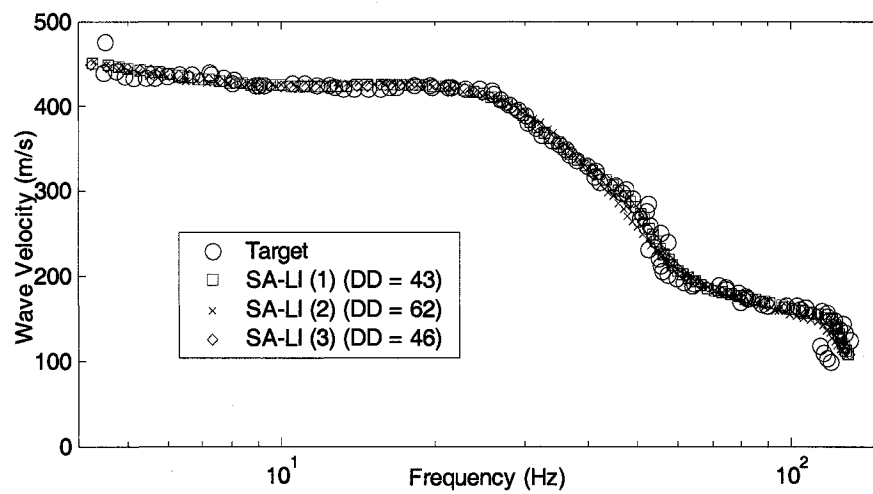


Figure 7.17. SASW, EDC/PF/BL: comparison of DCs.

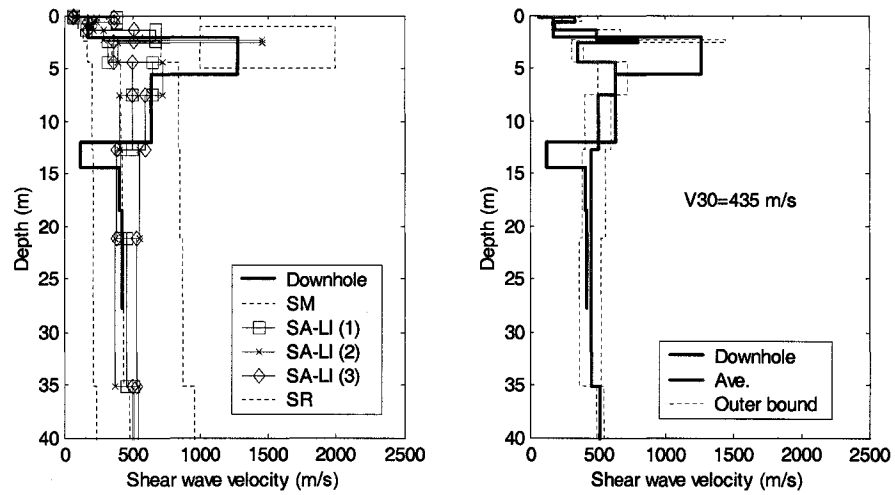


Figure 7.18. SASW, EDC/PF/BL:  $V_S$  profiles for (a) three runs (b) average.

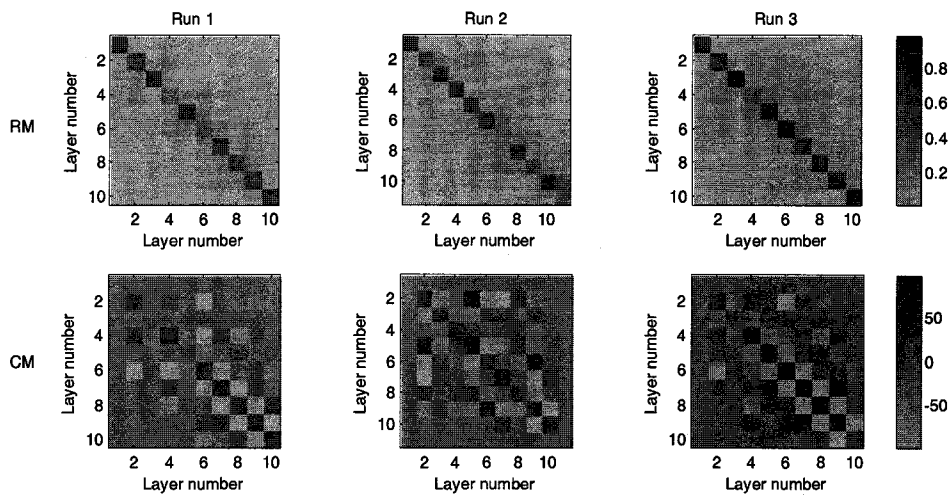


Figure 7.19. SASW, EDC/PF/BL: RMs and CMs.



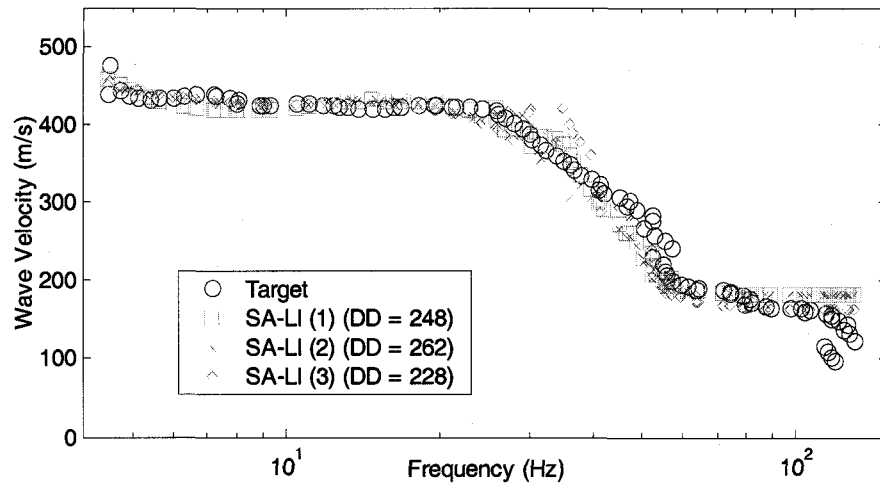


Figure 7.20. SASW, EDC/CM/R: comparison of DCs.

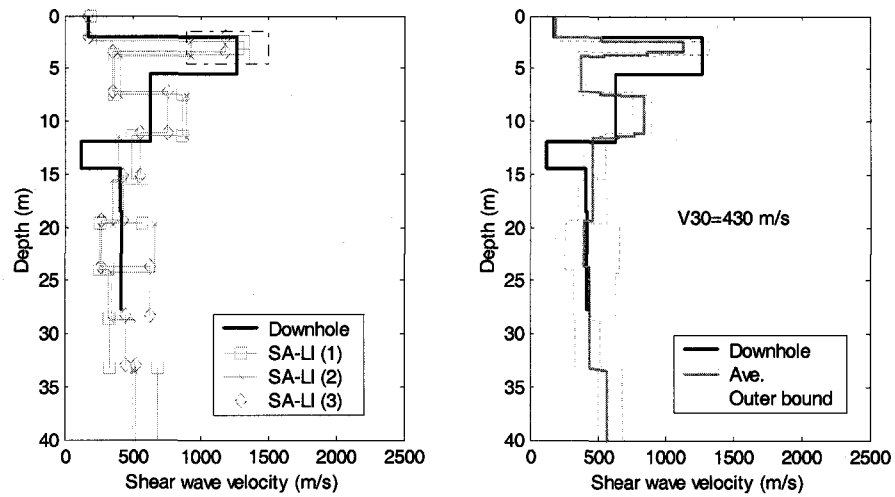


Figure 7.21. SASW, EDC/CM/R:  $V_s$  profiles for (a) three runs (b) average.

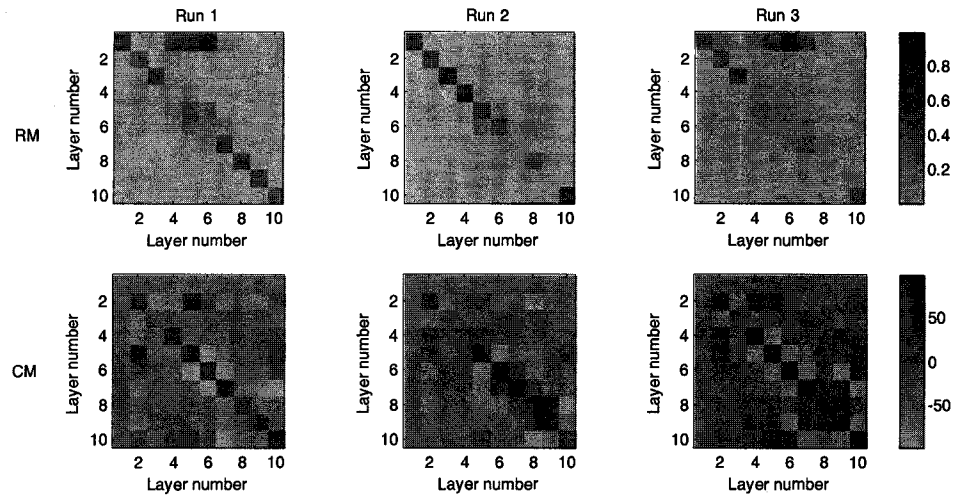


Figure 7.22. SASW, EDC/CM/R: RMs and CMs.

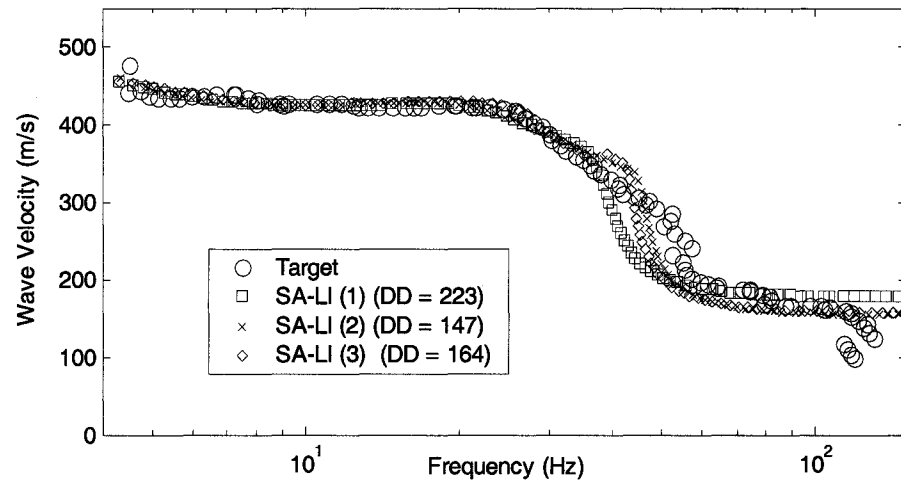


Figure 7.23. SASW, EDC/PF/R: comparison of DCs.

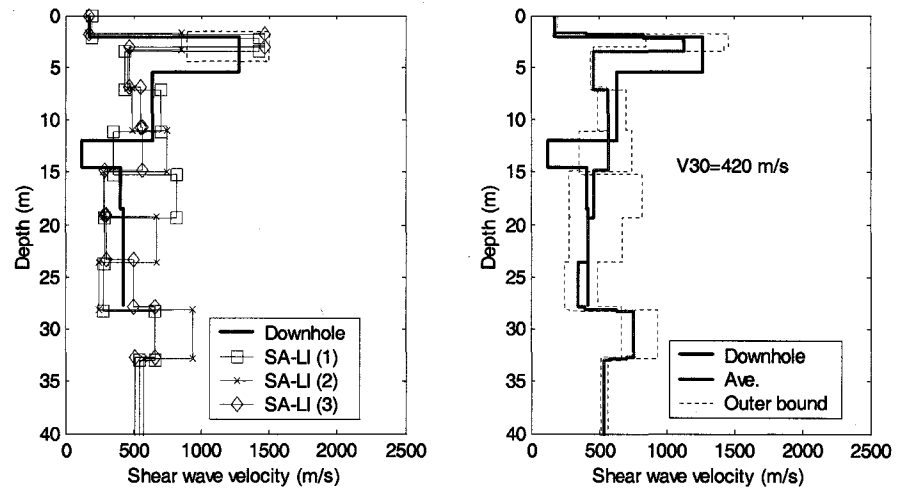


Figure 7.24. SASW, EDC/PF/R:  $V_S$  profiles for (a) three runs (b) average.

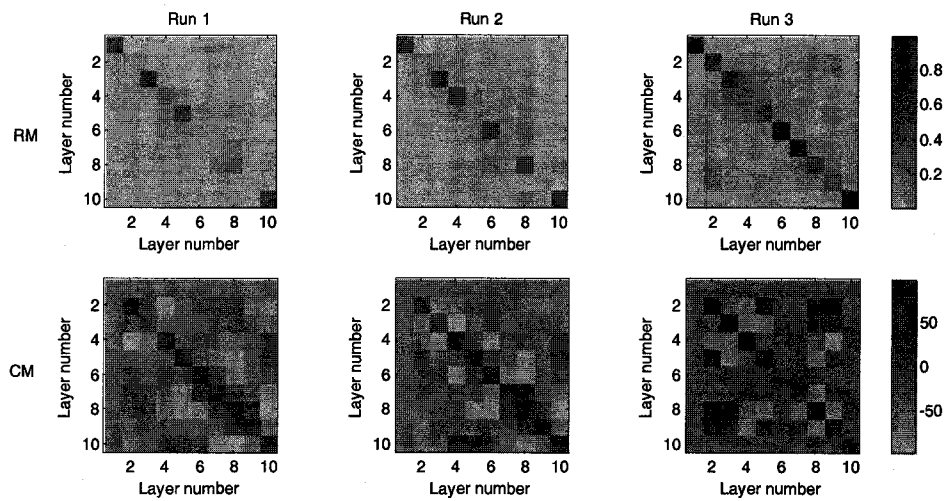


Figure 7.25. SASW, EDC/PF/R: RMs and CMs.

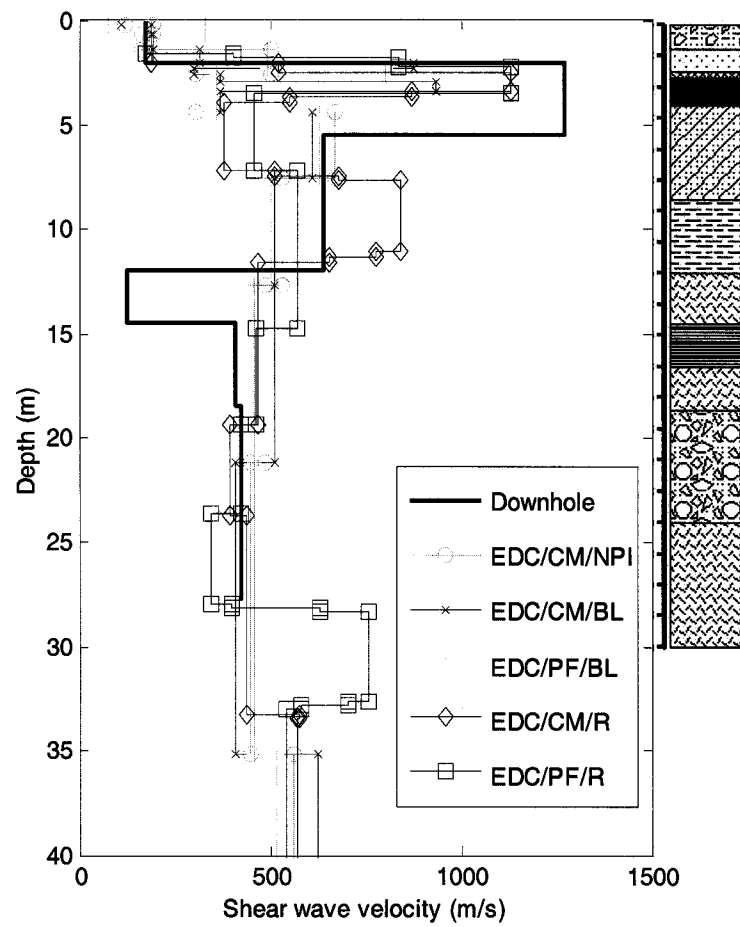


Figure 7.26.  $V_s$  profiles from SASW inversion analyses with respect to the borehole log (The key of the borehole log appears on Figure 7.5.)

(a)

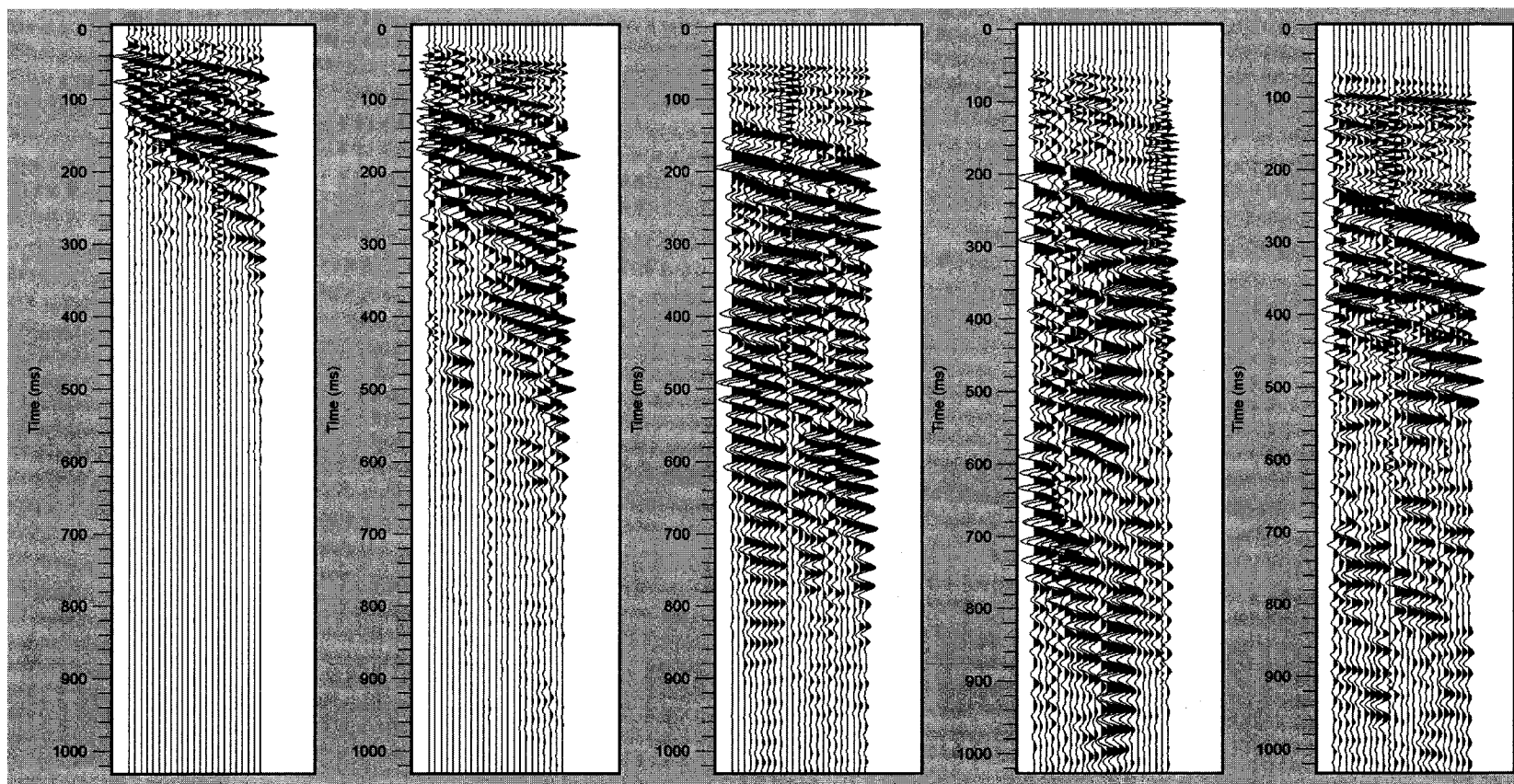


Figure 7.27a. Time history images of each single record after vibroseis correlation.

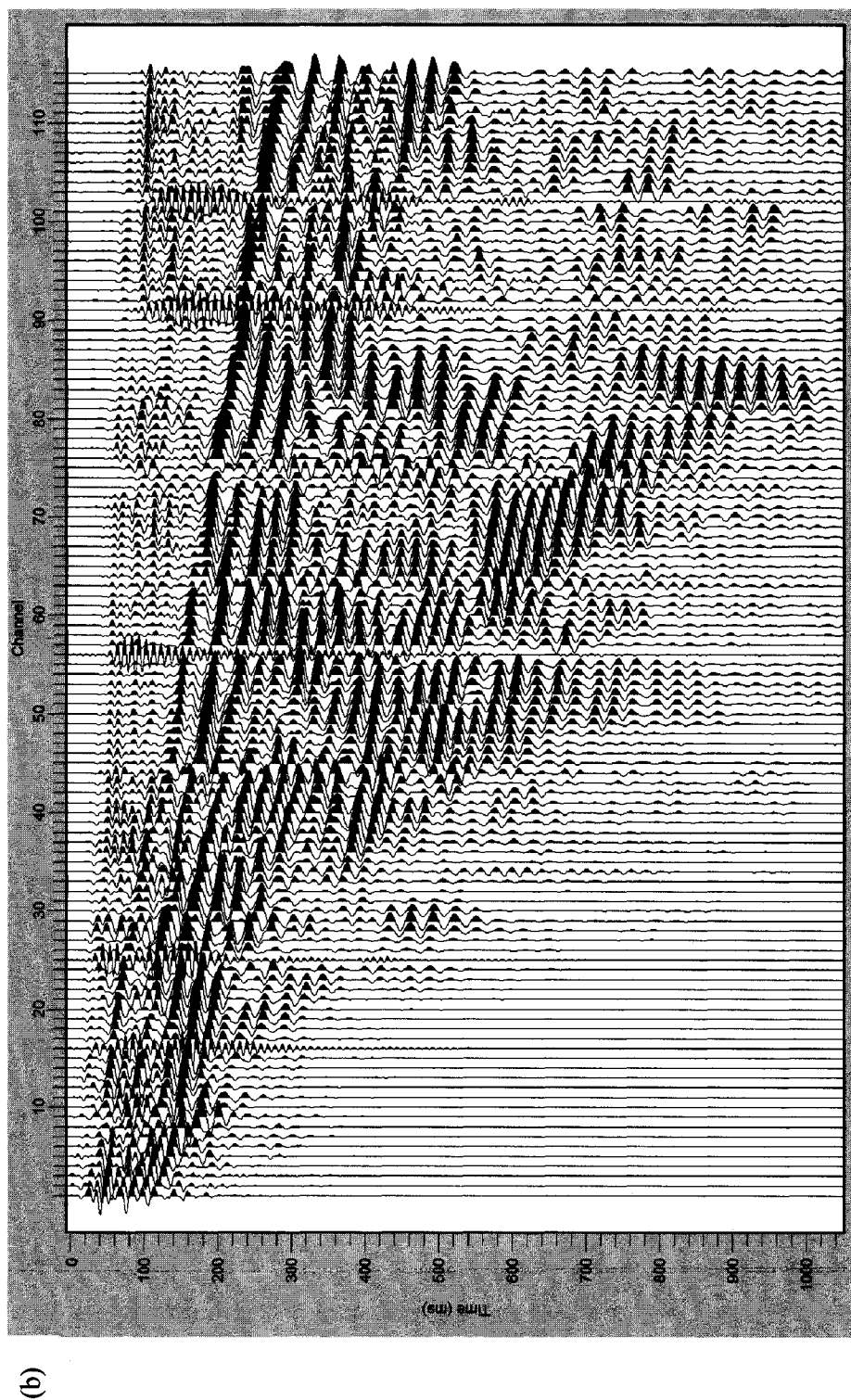


Figure 7.27b. Time history images of the combined record after vibroseis correlation.

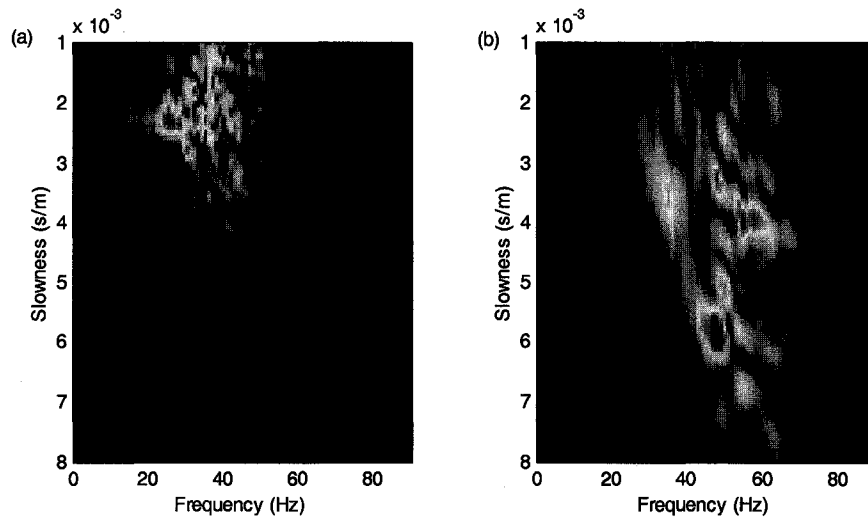


Figure 7.28. The  $f$ - $p$  images from (a) Minivib source and (b) hammer source.

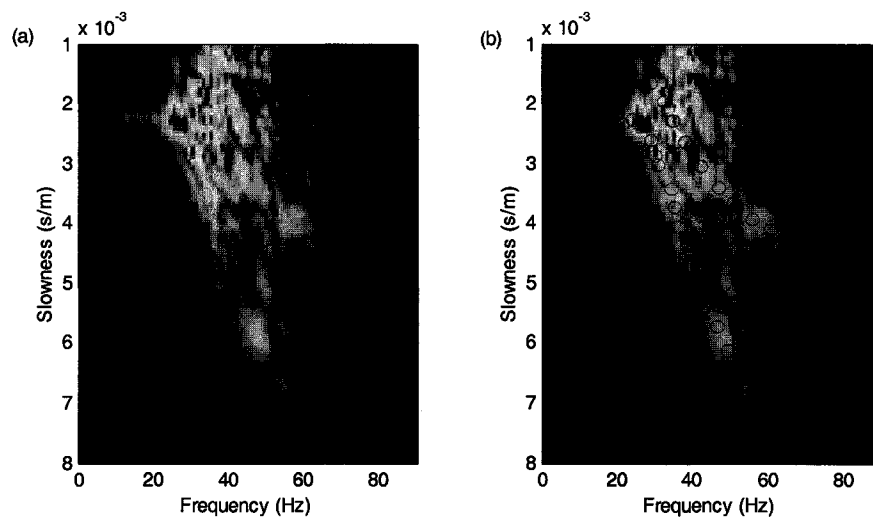


Figure 7.29. (a) The combined  $f$ - $p$  images alone and (b) superposed with picks for two modes.

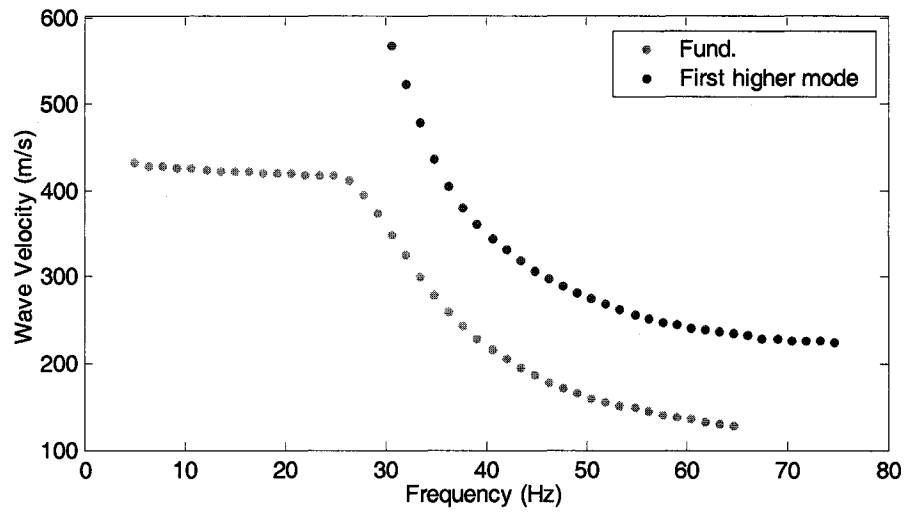


Figure. 7.30 DCs from MASW measurement.

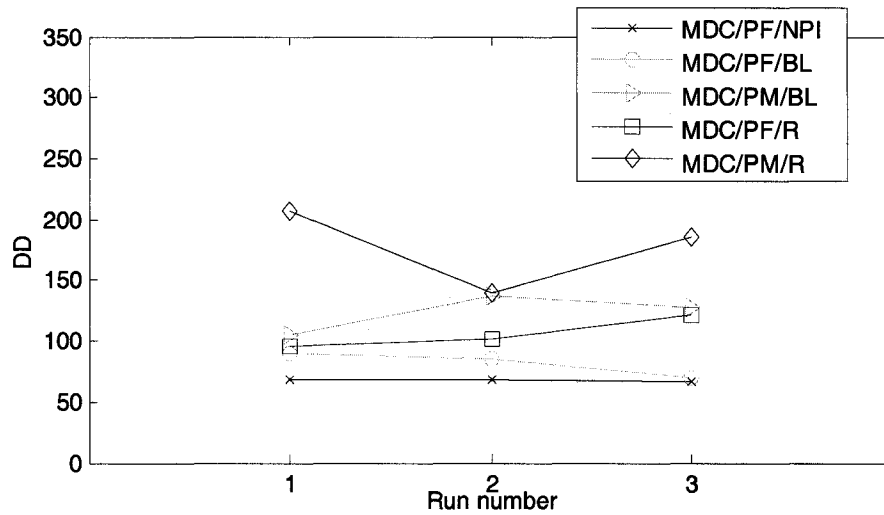


Figure 7.31. MASW: comparison of DD values from inversions.



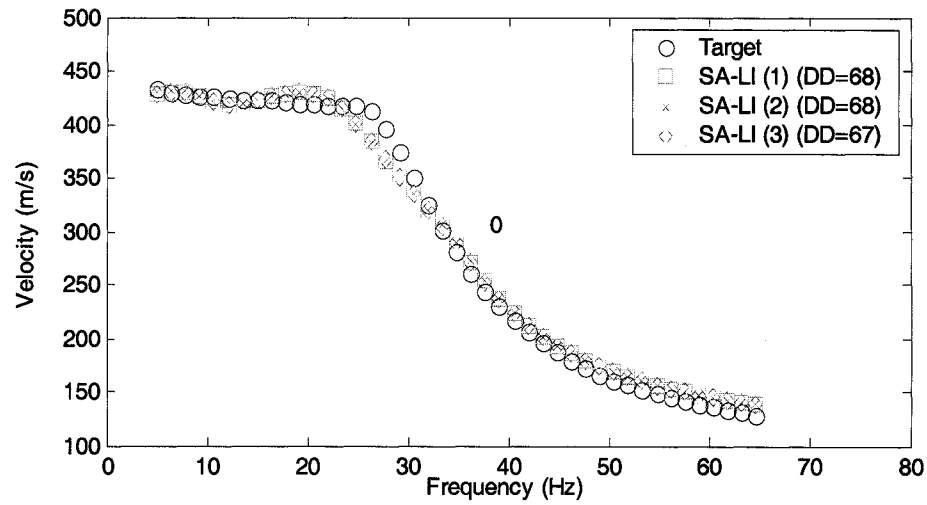


Figure 7.32. MASW, MDC/PF/NPI: comparison of DCs.

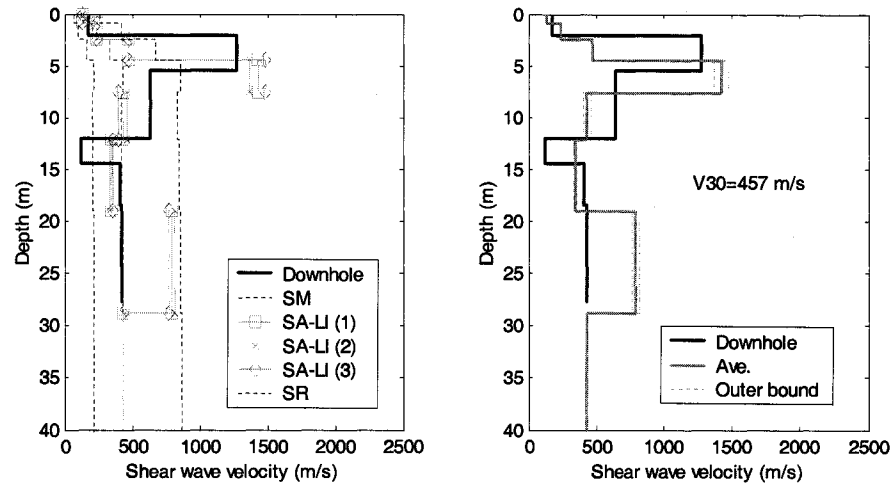


Figure 7.33. MASW, MDC/PF/NPI:  $V_s$  profiles for (a) three runs (b) average.

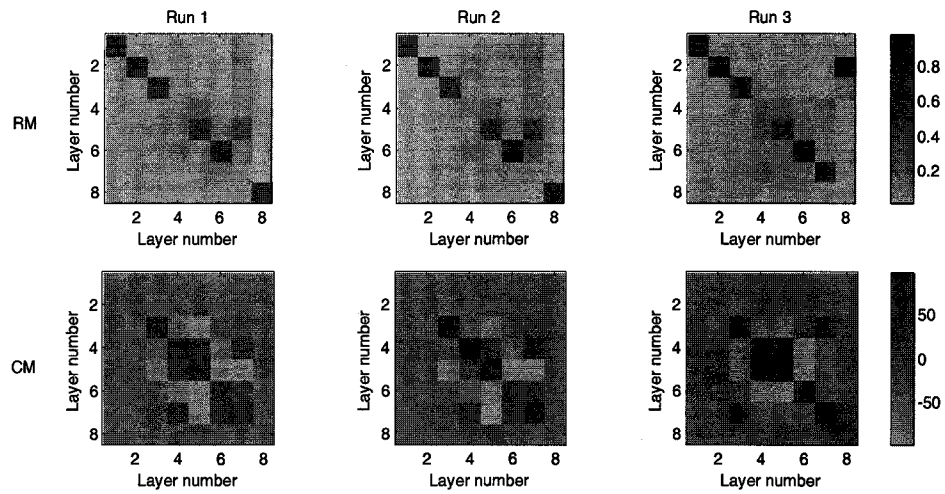


Figure 7.34. MASW, MDC/PF/NPI: RMs and CMs.

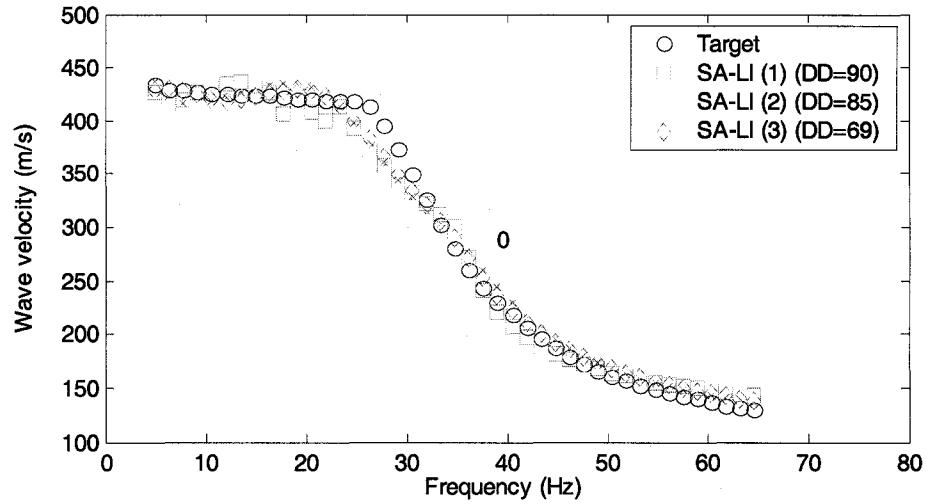


Figure 7.35. MASW, MDC/PF/BL: comparison of DCs.

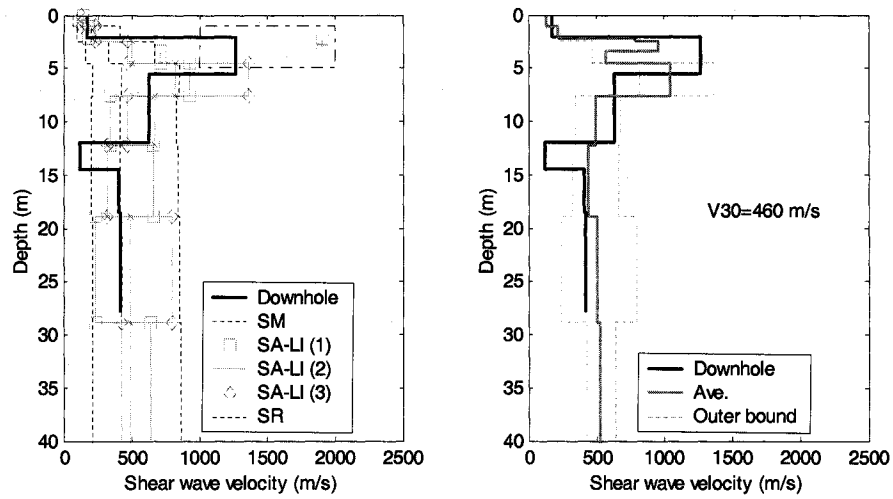


Figure 7.36. MASW, MDC/PF/BL:  $V_S$  profiles for (a) three runs (b) average.

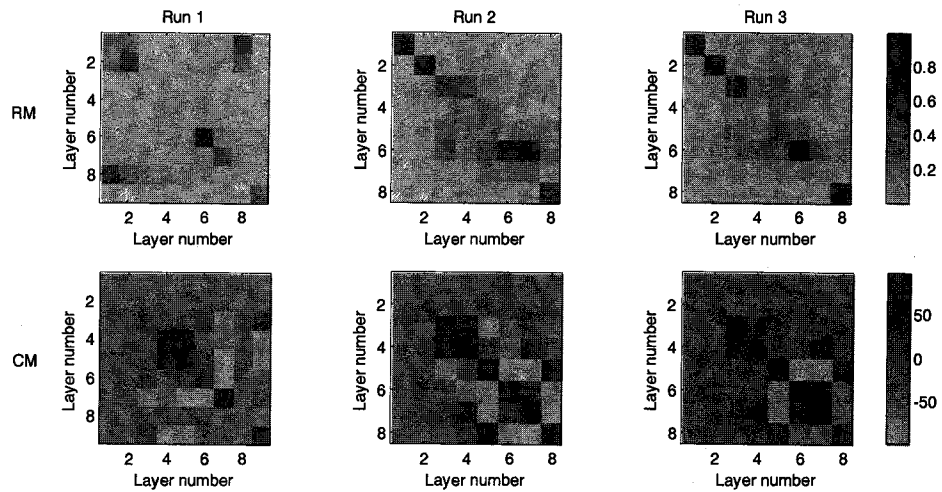


Figure 7.37. MASW, MDC/PF/BL: RMs and CMs.

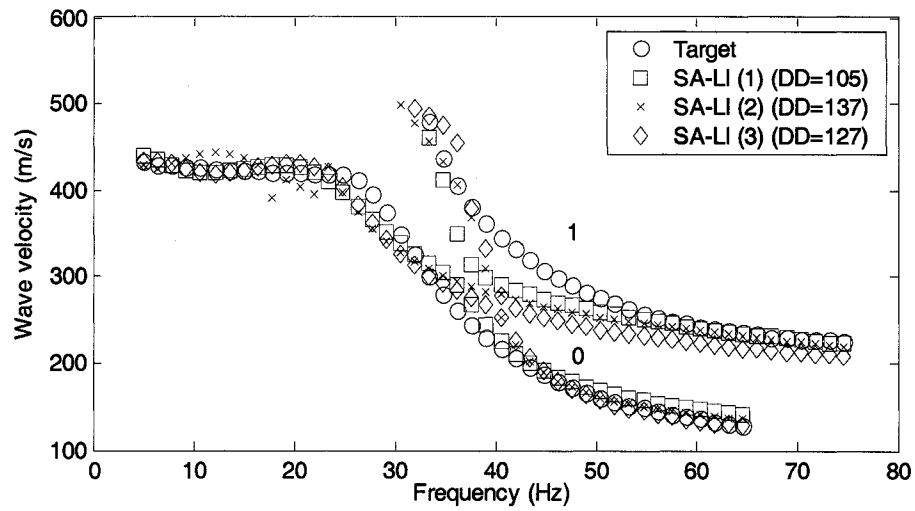


Figure 7.38. MASW, MDC/PM/BL: comparison of DCs.

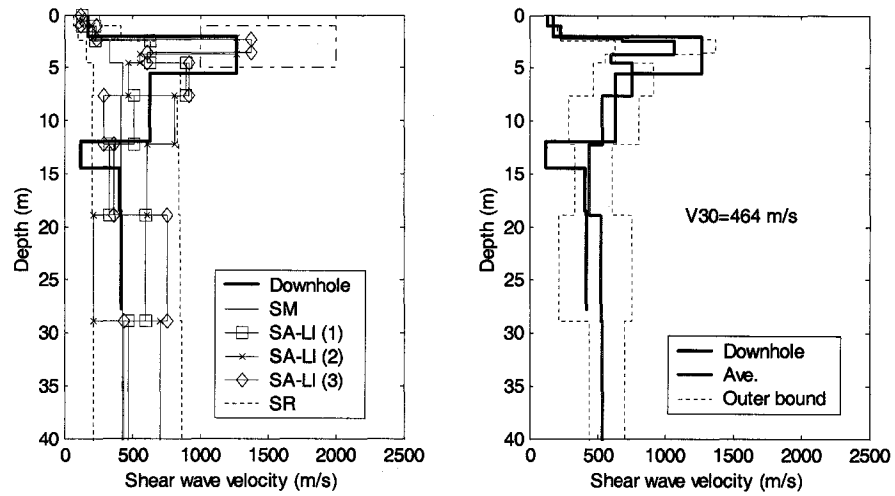


Figure 7.39. MASW, MDC/PM/BL:  $V_S$  profiles for (a) three runs (b) average.

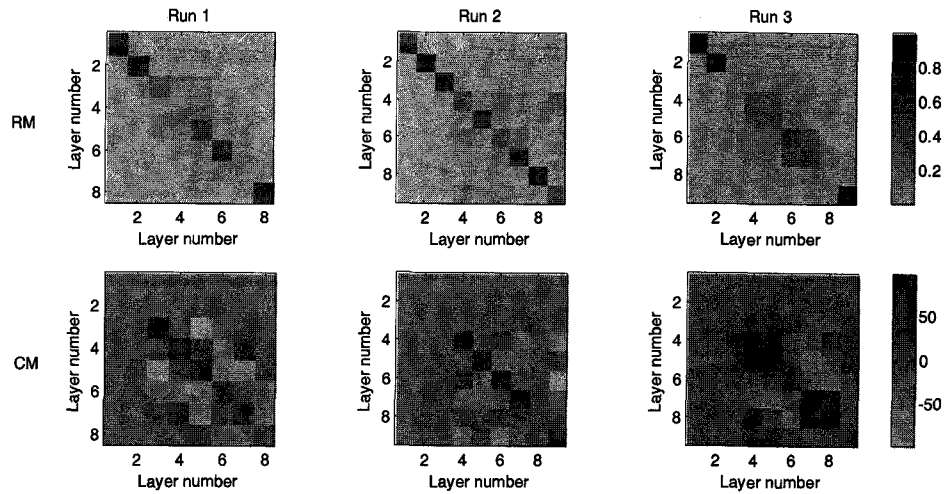


Figure 7.40. MASW, MDC/PM/BL: RMs and CMs.

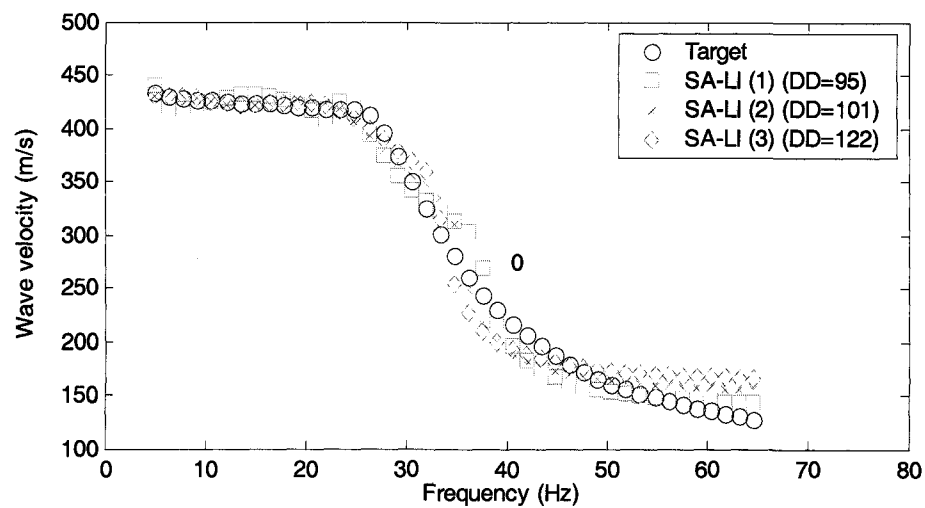


Figure 7.41. MASW, MDC/PF/R: comparison of DCs.

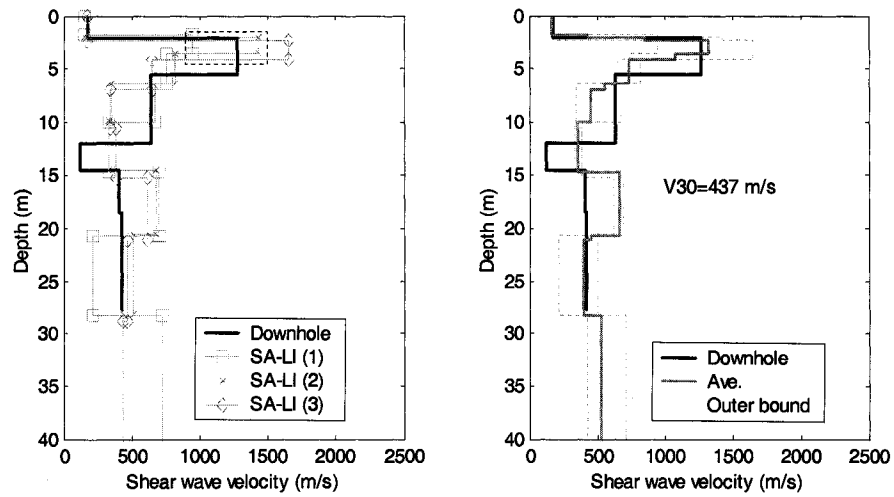


Figure 7.42. MASW, MDC/PF/R:  $V_S$  profiles for (a) three runs (b) average.

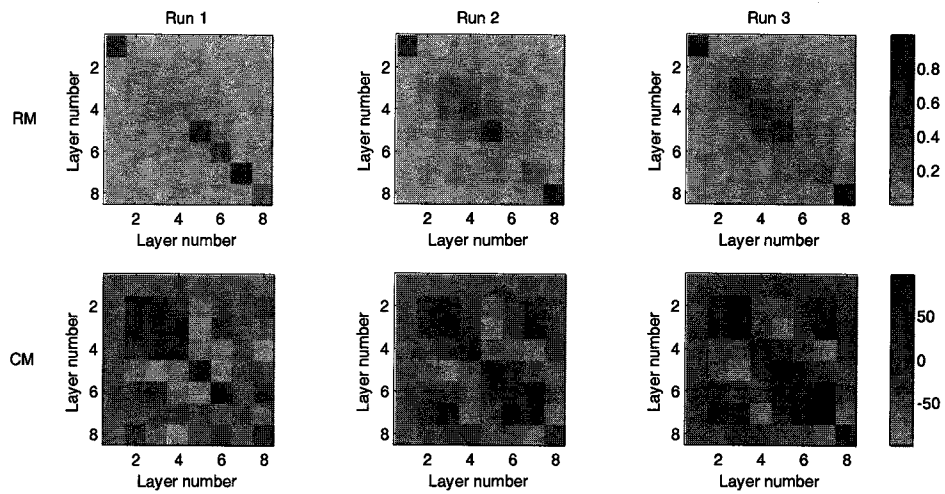


Figure 7.43. MASW, MDC/PF/R: RMs and CMs.

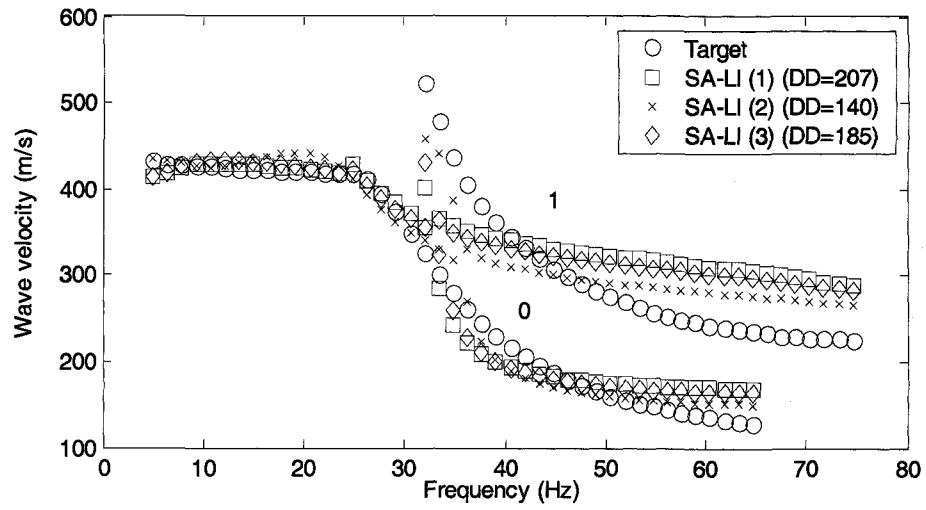


Figure 7.44. MASW, MDC/PM/R: comparison of DCs.

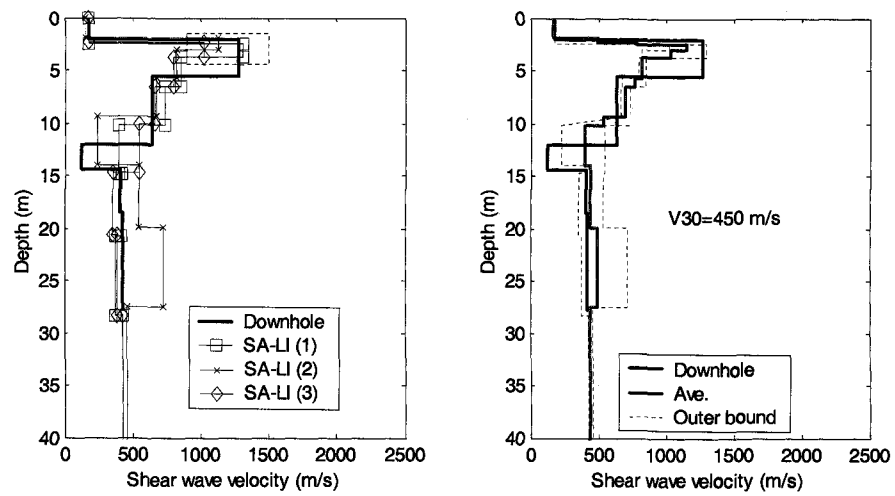


Figure 7.45. MASW, MDC/PM/R:  $V_s$  profiles for (a) three runs (b) average.

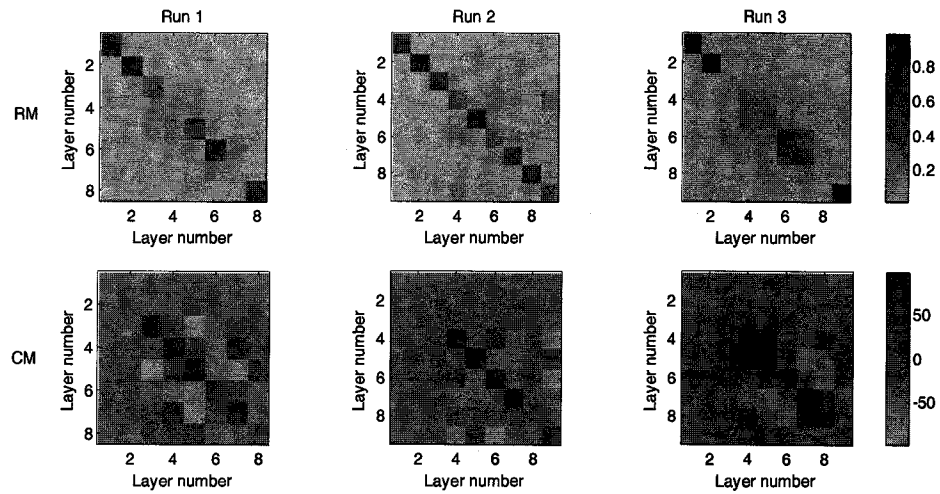


Figure 7.46. MASW, MDC/PM/R: RMs and CMs.

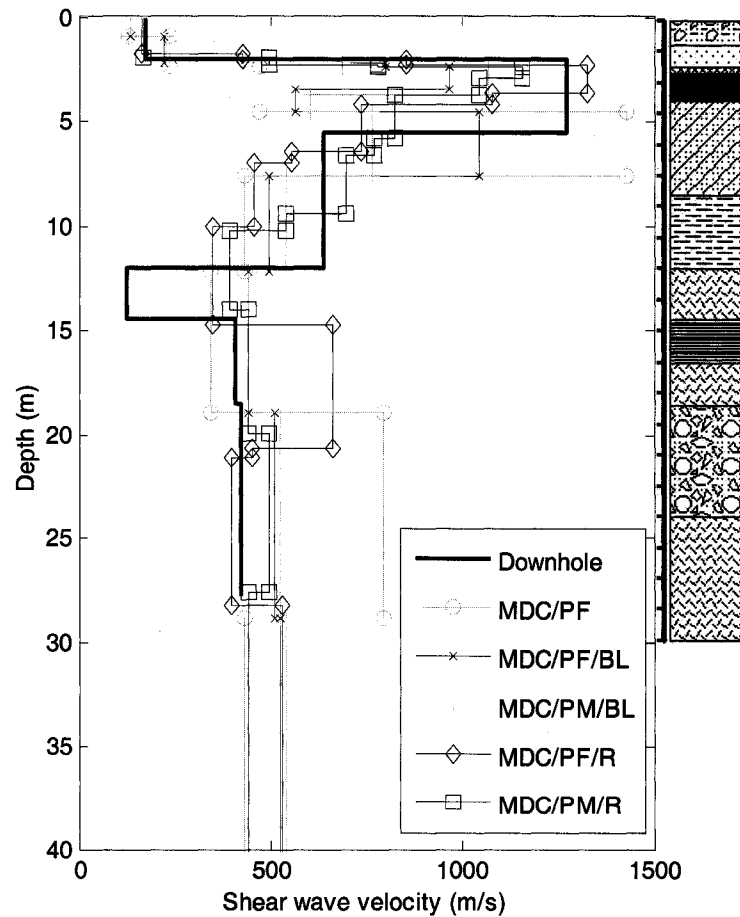


Figure 7.47.  $V_s$  profiles from MASW inversion analyses with respect to the borehole log (The key of the borehole log appears on Figure 7.5.)



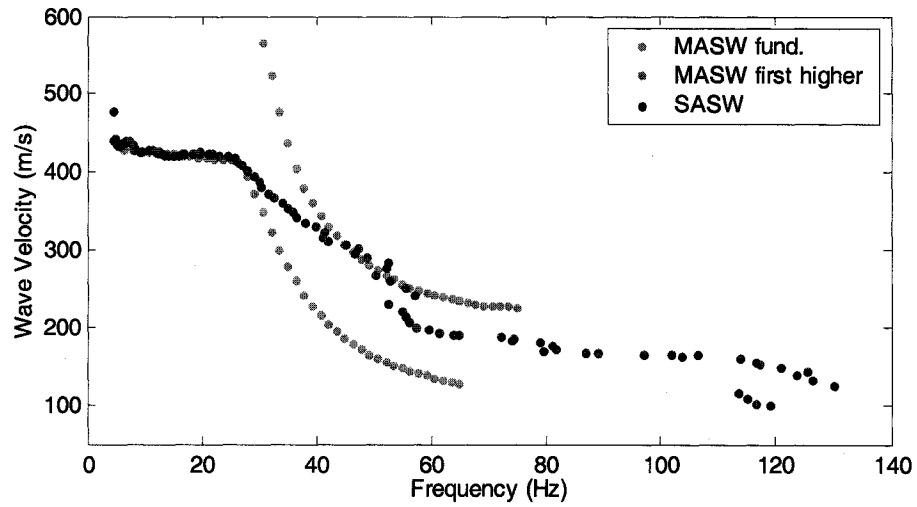


Figure 7.48. Comparison of DCs from MASW and SASW measurements.

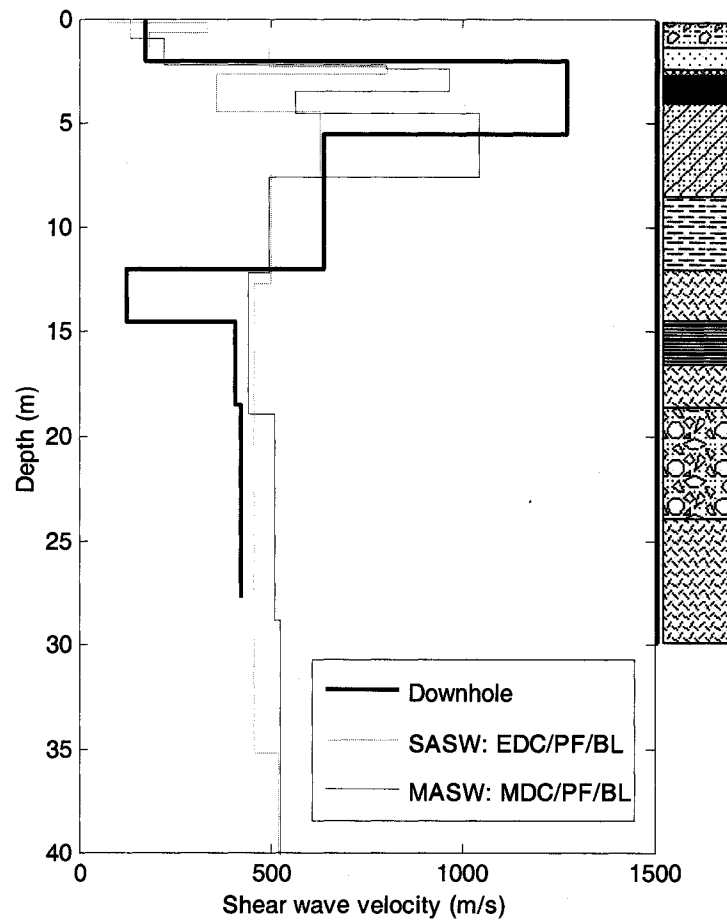


Figure 7.49. Comparison of best  $V_S$  profiles from MASW and SASW measurements with respect to the borehole log (The key of the borehole log appears on Figure 7.5.)

## CHAPTER 8

### SYNTHESIS, CONCLUSIONS AND RECOMMENDATIONS

In this research, two approaches were developed to resolve an HVL modeled after a carbonate-cemented layer that occurs in a sediment column using active-source surface wave measurements. One is the EDC/CM analysis and the other is the MDC/PM analysis. They are expected to be superior to the EDC/PF and MDC/PF analyses respectively for this application. A two-step optimization process of SA-LI is used to generate the  $V_s$  profile. The applicability of the two approaches was first tested with two synthetic datasets, which were solutions from forward models, one being an ND profile and the other being a HVL profile. Then it was tested by datasets from FD simulation, which are more realistic than the solutions from forward models. Last, the approaches were applied to experimental datasets collected at a site known from borehole logs to have a HVL.

#### 8.1 Synthesis

##### 8.1.1 Dispersion Curve

For the HVL profile, the shape of the DC itself presents clues for the presence of the HVL. The difference between the EDC and fundamental-mode DC is concentrated within a narrow frequency/wavelength band. By assuming that the effective sampling

depth is equal to one-third of the wavelength, the expected location can be roughly estimated from the frequency/wavelength band where the EDC and fundamental-mode DC diverge.

Comparison of experimental DCs from the SASW and MASW measurements confirms the expectation that a profile with a HVL will elicit a considerable higher-mode response.

### 8.1.2 Inversion

For both ND and HVL cases, multiple runs are preferred to a single run due to the inherently stochastic nature of the SA inversion process. This research supports the recommendation by Luke and Calderón-Macías (in press) that three runs are sufficient for general applications. The average of the three runs can be taken as the final result. If great variability is displayed in the three runs, the average profile might not be very accurate. In that case, more runs are advisable, to show the trend of the results.

The following discussions address inversion of a ND profile, inversion of an HVL profile, the value of incorporating prior knowledge in the inversion and effects of characteristics of the HVL on results.

#### ND profile

For the ND profile, the synthetic study showed that all the inversion analyses including EDC/CM, MDC/PF and MDC/PM were adequate. Incorporation of the first higher mode into the inversion does not improve (or degrade) the results. The reason is

due to the dominance of the fundamental mode in the ND system. The FD simulation of the MDC approach demonstrated that both the MDC/PF and MDC/PM analyses provided similar, close-to-target results for the ND profile. This supports the conclusion that the participation of higher modes is inconsequential in this case. The FD simulation of the two-channel method yielded an EDC with lower velocities below 40 Hz compared to the solution from the cylindrical-wave forward model. This causes the EDC/CM to underestimate the  $V_S$  at most depths in most runs. The cause of the difference between the DCs requires more study.

#### HVL profile

Here, considering the HVL profile, the multi-channel (MDC) approach is considered first, for all three studies (synthetic, FD simulation and experimental), and then the two-channel (EDC) approach is addressed.

For the MDC approach, both the synthetic study and the FD simulation showed that the MDC/PF analysis yielded some poor results with obvious misfit of DCs. In the cases where the fit of DCs was good, the HVL was well-resolved. The FD simulation demonstrated that the fundamental mode at low frequencies was extremely difficult to identify.

Considering the synthetic study, significant improvement to the results is seen from the MDC/PM analysis compared to the MDC/PF analysis, due to the influence of the higher mode (or modes). The FD simulation showed the value of a continuous and complete first higher mode to significantly improve the outcomes. The improvement of

outcomes by the MDC/PM analysis with respect to the MDC/PF analysis is constrained by the accuracy of the picks of the higher modes.

For the experimental MASW measurement, the best results were from the MDC/PF analysis with prior information from the borehole log. The DC fit was poor especially for the PM analyses. Considering the findings of the FD simulation study, this poor fit might be due to errors in picking the dispersion curve. In practice, many factors would make accurate DC interpretation even harder. Thus, the method of improving the results by incorporating the first higher mode in the inversion may not be dependable for real datasets.

For the EDC approach, the synthetic study demonstrated the applicability of EDC/CM inversion for HVL profiles. However, in the FD simulation the EDC/CM analysis failed to resolve the HVL while the EDC/PF analysis was successful, despite that the DCs from the FD simulation and the solution from the cylindrical-wave forward model matched well, both displaying a kink. The failure is likely because the influence of the HVL on the EDC is insufficient to make it distinguishable from the fundamental-mode DC. The insufficient difference may be due to the thinness, and/or deep embedment, and/or lower velocity contrast of the HVL with respect to the background profile. (Recall that the target profile had to be modified to accommodate limitations of the FD model.) The success of the EDC/PF analysis can be explained by observing that the shape of the fundamental-mode DC also carries the characteristics of the HVL.

For the experimental SASW measurement, the best results were from the EDC/PF analysis with prior information from the borehole log. This is in agreement with the FD simulation study in which the EDC/PF analysis was able to resolve the HVL. This is contrary to prior expectations that the CM analysis would be superior to PF for complex profiles. In practice, the difference between the EDC and fundamental mode DC may be overshadowed by many factors. Thus, the EDC/CM analysis may not be successful for real datasets when profiles are complex.

Thus, with the experimental data, the EDC/CM analysis did not show superiority to the EDC/PF analysis. Nor was the MDC/PM analysis found to be superior to the MDC/PF analysis.

Considering the possibility of the inversion process yielding a “false positive,” namely a profile with a HVL when none is actually present, for the parameterizations studied, the synthetic study with the EDC/CM analysis always indicated the presence of a thin HVL, given the opportunity. The MDC/PF analysis sometimes responded similarly, but the MDC/PM analysis was quite immune to such incorrect prior information. The EDC/PF analysis was not tested for this situation.

#### Prior information

It is known that prior information about a complex site is always helpful in guiding inversion, and even necessary to overcome problems of non-uniqueness of the DC inversion for the HVL profile. The more prior information that can be mustered from other studies and geologic constraints, the better the chance for a fruitful study. The

synthetic data study demonstrated the improvement in identifying the HVL by inversion with prior information as might be obtained from refraction. However, the experimental data study was less successful due to a mismatch at high frequencies.

#### Characteristics of the HVL

For both the EDC and MDC cases, the  $V_S$  shows the greatest sensitivity to the depth of the HVL, and the sensitivities to the velocity and thickness are similar. As a result, the depth of the HVL is the most reliably resolved with respect to its velocity and thickness.

Considering the inversion with prior information from refraction, the thickness of the HVL was better resolved with respect to the inversion with prior information from a borehole log. That is likely due to the difference in search parameterizations: a higher probability of finding the HVL was set in the inversion with prior information from refraction.

### 8.1.3 Evaluating Quality of the Results

The quality of the inversion results can be evaluated by a combination of values of DD, image of RM and CM, observed error between the DC fits and repeatability of results. For both synthetic study and FD simulation where the true model is known, the results can be readily evaluated by evaluating the PD and comparing the inverted profile to the EM profile. The RM and CM are closely related; low interdependence of the velocity of one layer to another implies higher resolution. A perfect result has perfect RM and CM, but perfect RM and CM do not guarantee a perfect result. Sometimes, poor RM

and CM might not correspond to a poor result, either. Thus, it is important to note that RM and CM considered alone can lead to a misleading interpretation.

## 8.2 Conclusions

The main objective of the research was to build a reliable process to resolve an HVL system using surface wave methods. Two approaches were developed and tested. Overall, both approaches were successful in enhancing ability to delineate carbonated cemented layers in soil columns. However, this research showed that it is still challenging to resolve an HVL from surface wave measurements, even with the benefit of prior information about the site.

The synthetic studies supported part of the hypothesis presented in Chapter 2 that the MDC/PM analysis is superior to the MDC/PF analysis for HVL systems. Given optimal parameterization, the MDC/PM analysis was able to clearly resolve a HVL that was 2 m deep and 1.5 m thick, with  $V_S$  of 1500 m/s. The hypothesis that the EDC/CM analysis was superior to the EDC/PF analysis for HVL systems was not tested in the synthetic study, because theoretically, the cylindrical wave forward model is the proper forward model for the EDC inversion. Both EDC/CM and MDC/PM analyses were able to provide close-to-target results for both ND and HVL profiles in the synthetic studies.

The FD simulation demonstrated potential difficulties with both approaches, however. For the MDC approach, accurate picking of the DC can be challenging for HVL systems. For the EDC approach, the EDC/CM analysis failed to resolve an HVL due to the



insufficient difference between the EDC and fundamental mode DC.

The experimental study denied both hypotheses. The best results in both cases came from the less complex analysis approach: MDC/PF analysis for the MASW measurement and EDC/PF analysis for the SASW measurement. The simpler approaches succeed because the shape of the fundamental-mode DC carries the characteristic of the HVL; thus, with an intelligently guided search, the HVL can be resolved. Although  $V_S$  profiles for different inversion analyses were different, slowness-averaged velocities over the upper 30 m were comparable.

Secondary goals were to evaluate the quality of the outcomes from the process and to study its applicability and limitations. The quality of the inversion results can be evaluated by a combination of values of DD, image of RM and CM, observed error between the DC fits and repeatability of results. This research tested a profile with a single, shallowly buried HVL. Performance of the approaches in more complex situations that might be encountered in practice is yet to be explored.

### 8.3 Future Research Recommendations

Recommendations for future research are as follows:

1. To take full advantage of higher modes, means to correctly and completely identify the DC from an  $f - p$  image should be found.
2. Instead of assigning weights to different modes arbitrarily, the weight assigned for each mode should be proportional to its energy participation. It is necessary

to quantitatively evaluate the energy partitioning between different modes.

3. Instead of resolving the profile by fitting picked dispersion curves, one might fit the entire  $f - p$  image.
4. The DC from the FD simulation of the two-channel method had lower velocities with respect to the solution from the plane-wave forward model at low frequencies. The cause of the difference between the DCs requires more study.
5. The differences between EDC and fundamental-mode DC induced by the thickness, embedment depth and velocity of the HVL need further investigation by parametric study.
6. To improve the ability of the EDC/CM analysis to resolve the HVL, a solution that emphasizes the part of the EDC where the kink occurs by assigning heavier weights can be tested.
7. Means to incorporate prior information from a P-wave refraction measurement should be enhanced. Two solutions can be considered. One is to improve the resolution of the refraction measurement (e.g., smaller receiver spacing). The other is to subdivide the layer geometry provided by the refraction measurement for the surface wave inversion analysis.
8. An uncertainty study is a necessary part of geophysical measurements. The uncertainties induced by many different factors (e.g., incoherent noise, error in the placement of geophones) in the DC generation should be considered. Means to map the uncertainties in the DC into the uncertainties in the  $V_S$  profile should

be sought or enhanced.

9. In the FD simulation, the effect of attenuation should be considered.

Furthermore, the FD simulation provides a promising tool for understanding characteristics of Rayleigh waves in various geological settings (e.g., dipping layers and other lateral heterogeneities). More studies of this nature could be designed to investigate the influence of geological variability on the DCs.

10. The inversion method introduced in this research was applied to one-dimensional profiles. Technology now exists to study two- or three-dimensional profiles. Means to incorporate the inversion method into that technology should be sought.

## APPENDIX A

### INSTRUCTION MANUAL FOR STARTING MODEL GENERATION, SA AND SA-LI INVERSION ANALYSES

Process for synthetics: (For experimental data, start from step 2 in A.)

#### A. Starting model

1. Generate a target file (*dct.dat*).

For cylindrical wave model:

- Create a folder named *EDC*.
- Create an input file named *input.dat* and run *revisedsaswtest.exe*. The output file is *curdisp3d.dat*.
- The file *curdisp3d.dat* includes two columns, wavelength and velocity. Change to three columns: wavelength, frequency and velocity. Name the three-column file *dct.dat*
- Create a folder named *sm*. Copy the *dct.dat* file to the folder *sm*.

For multimode inversion:

- Create a folder named *MDC*.
- Create an input file named *input.dat* and run *rixforward.exe*. The output file is *fund.dat* and *out.dat*.
- Create a folder named *sm*. Copy the file *fund.dat* to the folder *sm* and change the name to *dct.dat*.

Note: the formats of the two *input.dat* files are different.

2. Run *LV3.m* using different values of “C” to generate layer geometries. It will output files “ZVxxx” where “xxx” is the multiplier “C” times 1000.
3. Open *inx.m* using Matlab. Change the number of points, min and max wavelength according to the file *dct.dat*. Run *Inx.m* using files “ZVxxx”. The

output file is *inxxx*.

4. The files *inxxx* contain real numbers and the following codes require integers, so use Excel to open files and modify format of all cells to “general.” Save as the same file name.
5. Generate theoretical dispersion curves for each of the *inxxx* files.

For cylindrical wave model:

- Create a folder named *xxx*.
- Copy the file *inxxx* to the folder *xxx* and change name to *input.dat*. Run *revisedsaswtest.exe*. Change the output filename *curdisp3d.dat* to *DCxxx.dat*.
- Copy file *DCxxx.dat* into the folder *sm*.
- Repeat this procedure for each *inxxx* file.

For multimode inversion:

- Create a folder named *xxx*.
- Copy the file *inxxx* to the folder *xxx* and change name to *input.dat*. Run *disp2d.exe*. Change the name of the output file *Graf.d.dat* to *DCxxx.dat*.
- Copy file *DCxxx.dat* into the folder *sm*.
- Repeat this procedure for each *inxxx* file.

6. Run *pltdc.m* to plot dispersion curves and calculate and display DD values.
7. Pick starting model based on DD, thickness of the upper layer and fit at lower wavelength range.
8. Rename files *DCxxx*, *Inxxx*, and *ZVxxx* as *DCsm.dat*, *Insm.dat* and *Vssm.dat*, respectively. Also rename the corresponding folder *xxx* as *xxxbest*.

## B. SA

For cylindrical wave model:

- Under the *EDC* folder, create a folder named as *SA*.
- Copy the *dct.dat* file under *EDC* folder to *SA* folder. Delete the wavelength column and add a weight column with constant value of 1. Save it as *ccedd.dat*.
- Open *inv.dat*. Make sure the number of point is correct.
- Generate the *param.dat* file according to the *Vssm.dat*.
- Double click *sasaswfi.exe*. Type in the names of the input and output files step by step: *inv.dat*, *param.dat*, *ccedd.dat*, *mf.dat*, *cf.dat* and *ef.dat*. It might take hours.

For multimode inversion:

- Under the MDC folder, create a folder named as *SA*.
- Under *SA*, create two folders, *fund* and *2md*. Copy the *out.dat* file to the two folders and change name to *ccedd.dat*. Delete the profile information in the *ccedd.dat* file and keep only the columns. Save as same file name.
- Generate the *param.dat* file according to the *Vssm.dat*.
- Open *inv.dat*. Make sure the number of point is correct. Input the weights for fundamental mode and higher modes.
- Double click *saswami.exe*. Type in the names of the input and output files step by step: *inv.dat*, *param.dat*, *ccedd.dat*, *mf.dat*, *cf.dat* and *ef.dat*. It might take hours.

Note: the *inv.dat* file under EDC and MDC folder is different.

## C. LI

For cylindrical wave model:

- Under the *EDC* folder, create a folder named as *SALI*.
- Copy the *ccedd.dat* file under EDC/SA folder to *SALI*.
- Change the *model.dat* file according to the output *mf.dat* file under *EDC/SA* folder.
- Double click *lisaswfi.exe*. Type in the names of the input and output files step by step: *model.dat*, *ccedd.dat*, *mf.dat* and *cf.dat*. It might take 15 to 30 minutes.

For multimode inversion:

- Under the *MDC* folder, create a folder named as *SALI*.
- Under *SALI*, create two folders, *fund* and *2md*. Copy the *ccedd.dat* file under *MDC/SA* folder to *SALI*.
- Change the *model.dat* file according to the corresponding output *mf.dat* file under *MDC/SA* folder.
- Double click *liswami.exe*. Type in the names of the input and output files step by step: *model.dat*, *ccedd.dat*, *mf.dat* and *cf.dat*. It might take 15 to 30 minutes.

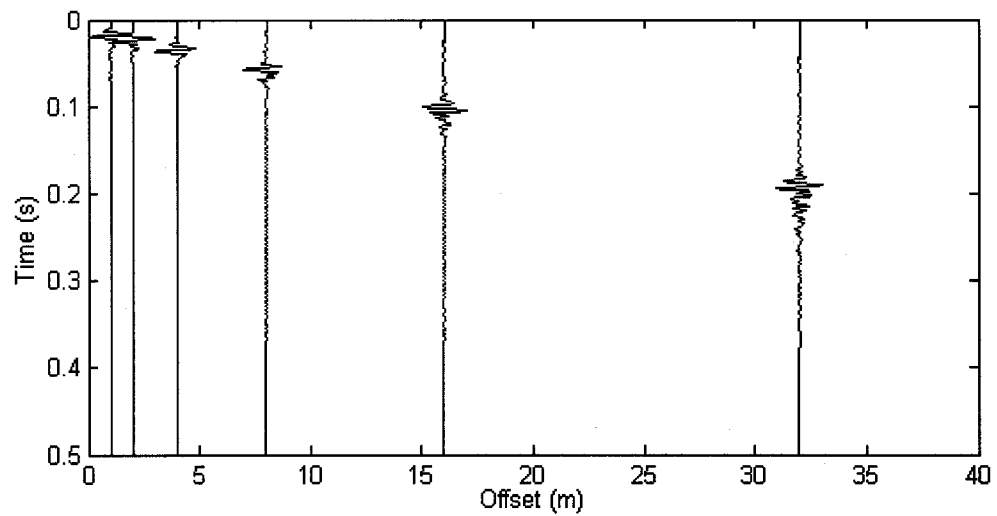
## APPENDIX B

### DEVELOPMENT OF DISPERSION CURVE FOR THE ND AND HVL PROFILES

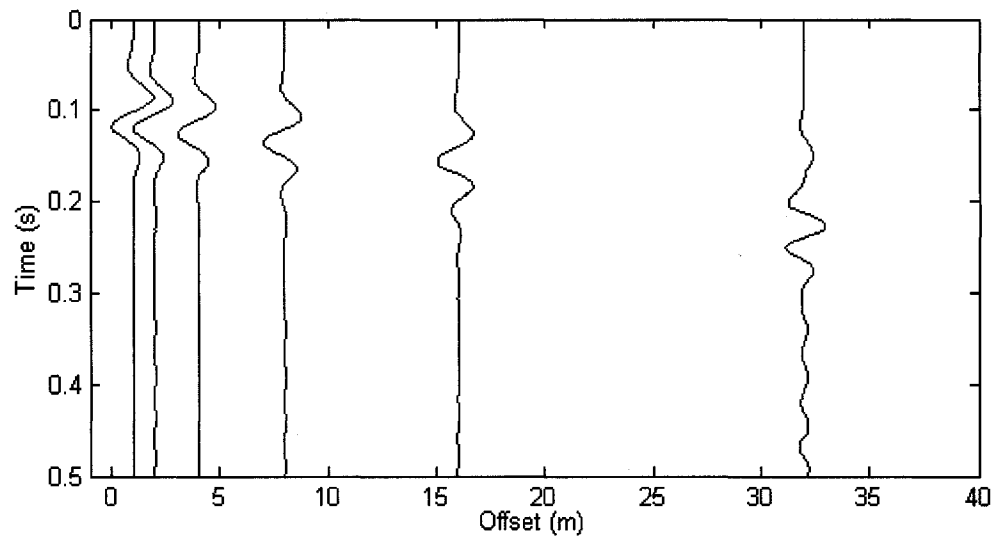
ND profile

1) Time history

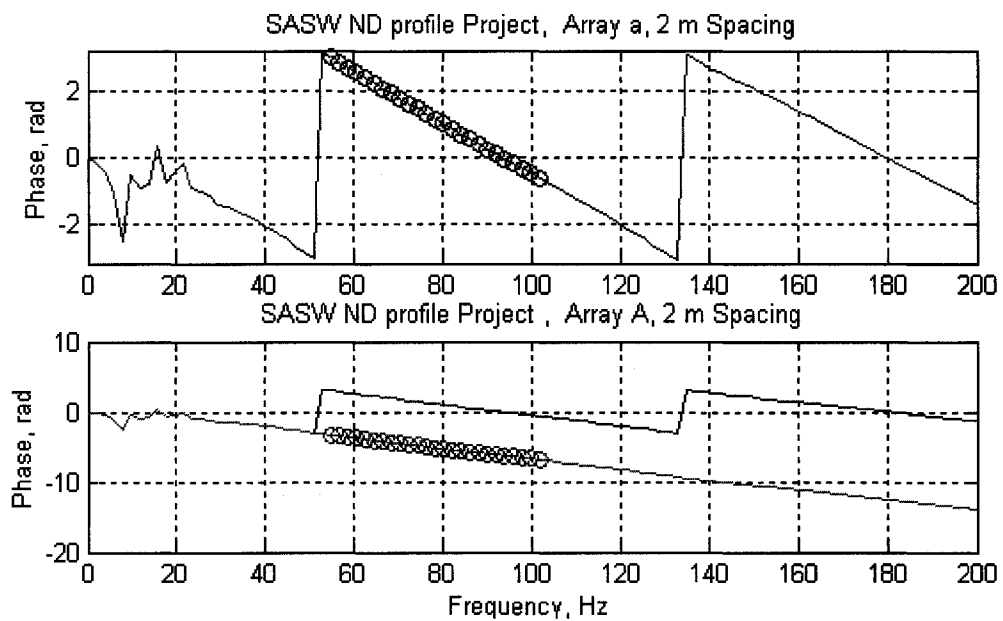
a) Central frequency 100 Hz, receivers at 1, 2, 4, 8, 16 and 32 m



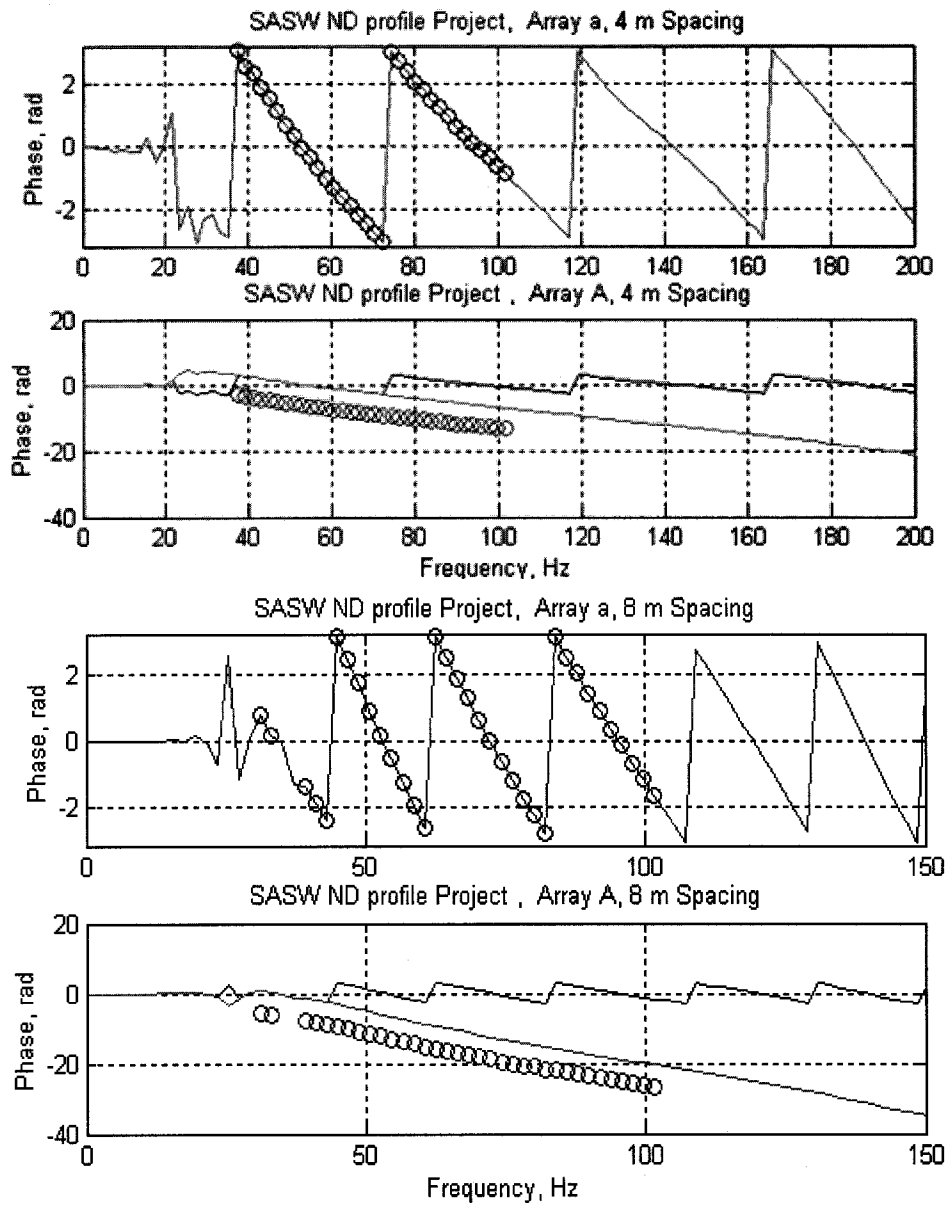
b) Central frequency 10 Hz, receivers at 1, 2, 4, 8, 16 and 32 m

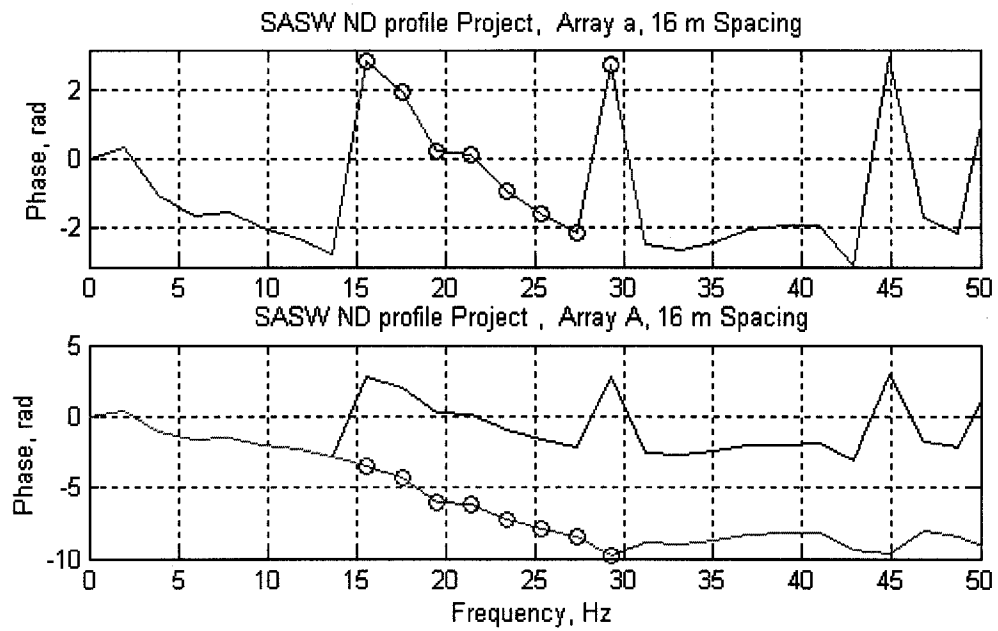


2) Phase plots selected for use

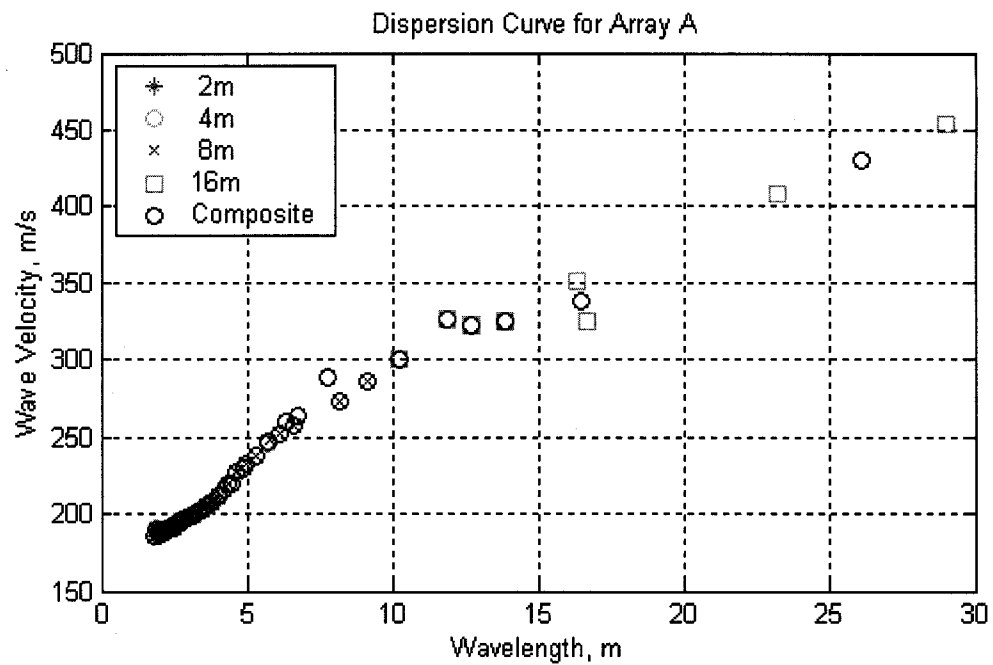


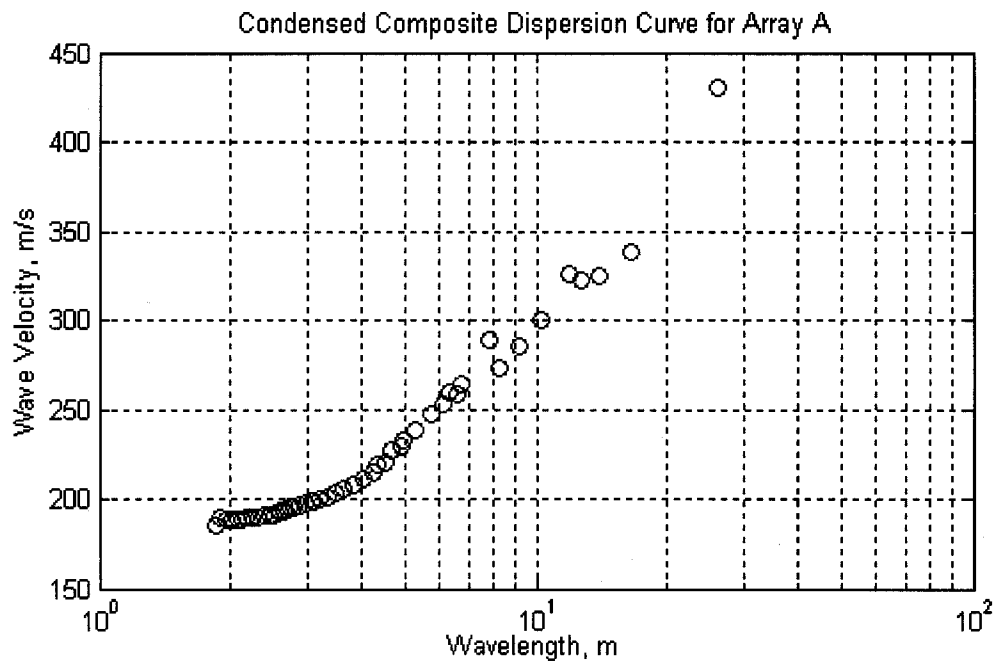






### 3) Dispersion curve

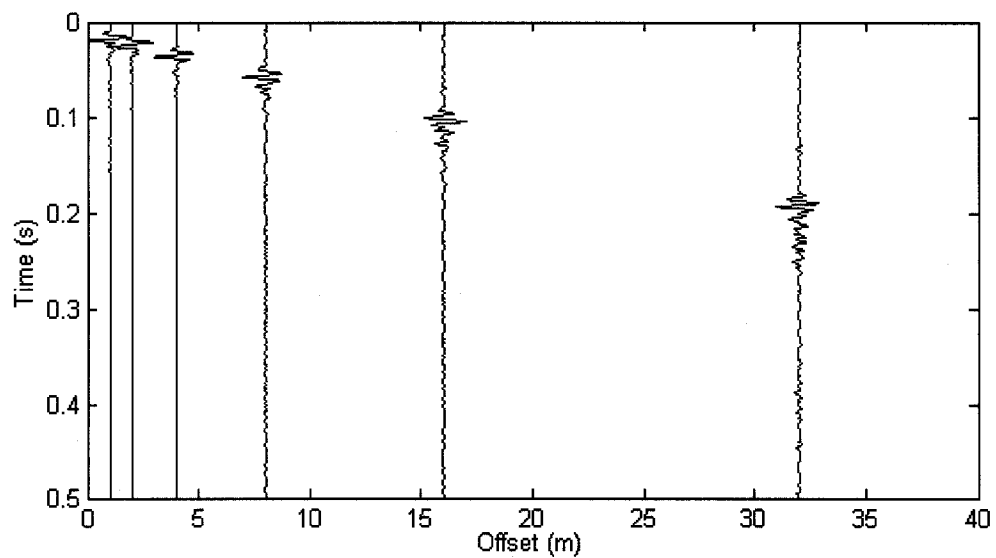




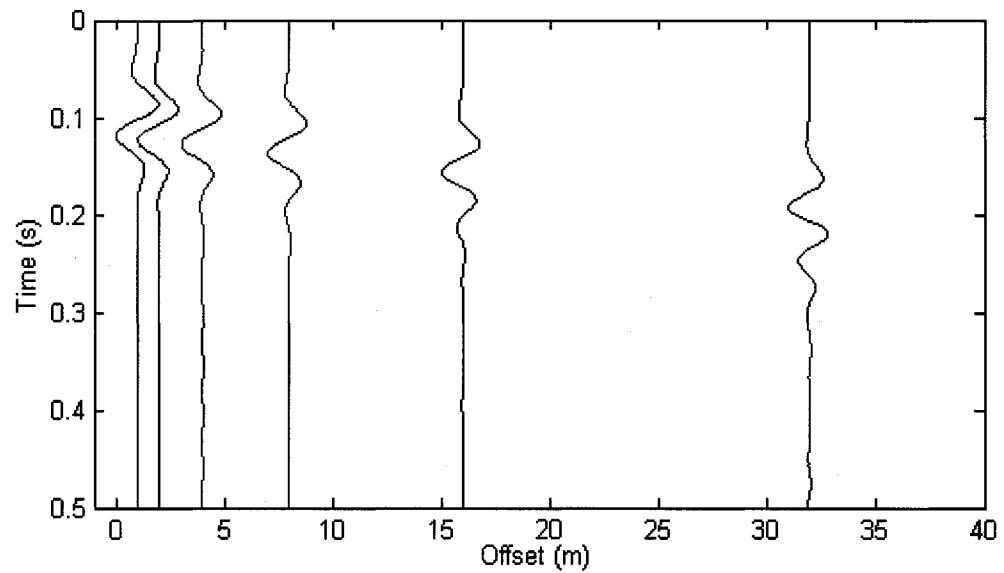
HVL profile

1) Time history

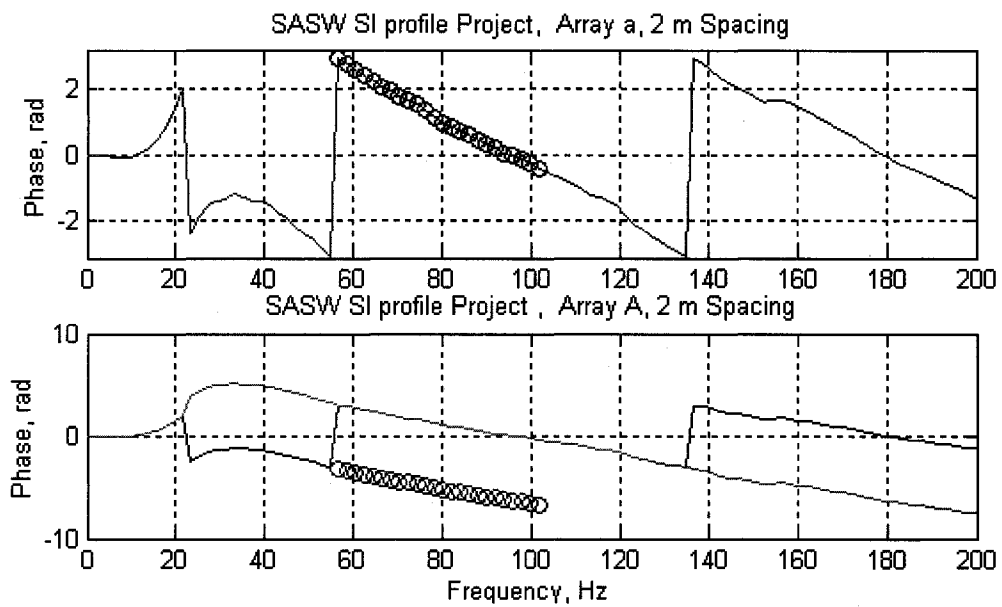
a) Central frequency 100 Hz, receivers at 1, 2, 4, 8, 16 and 32 m

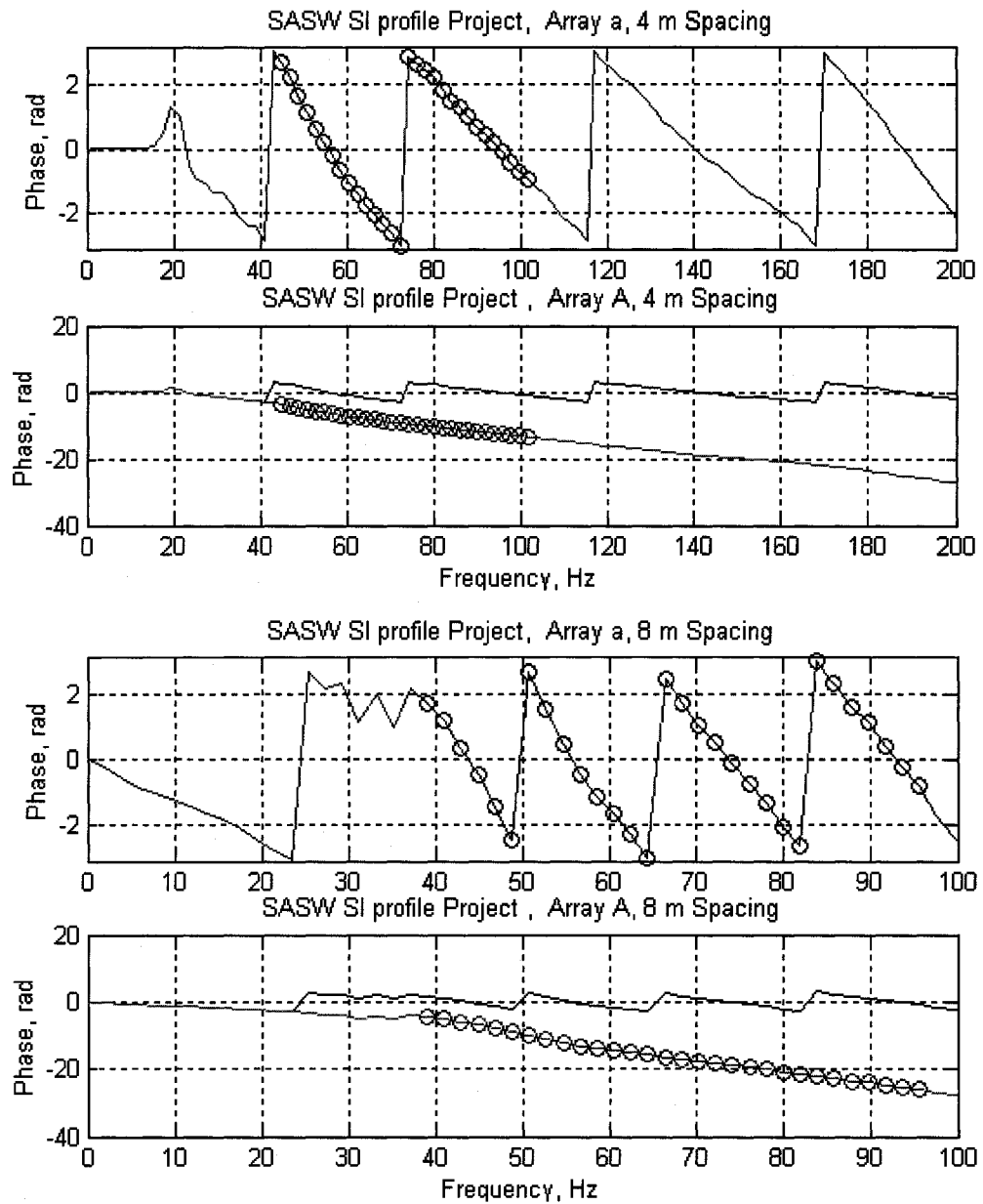


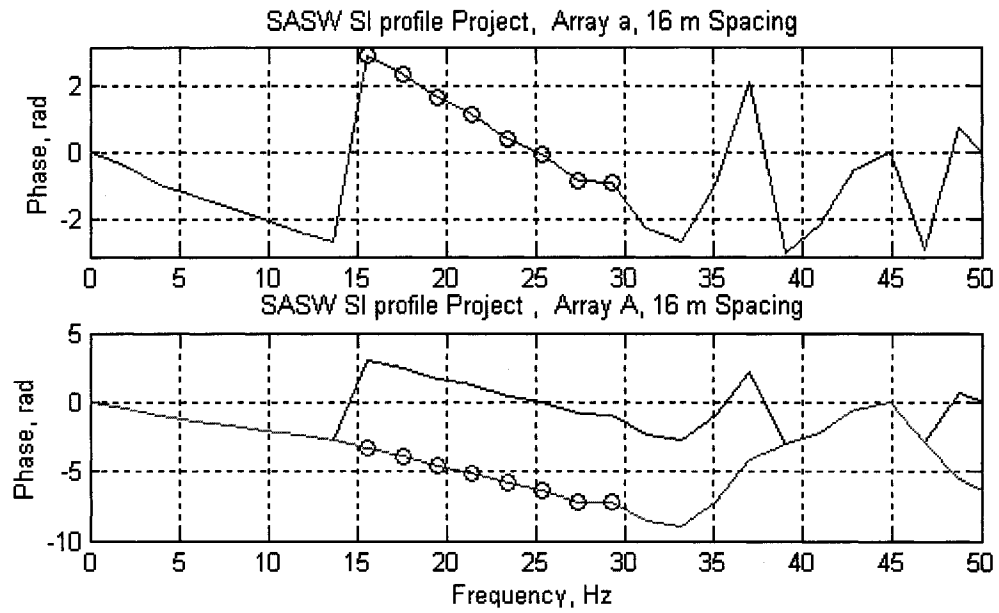
b) Central frequency 10 Hz, receivers at 1, 2, 4, 8, 16 and 32 m



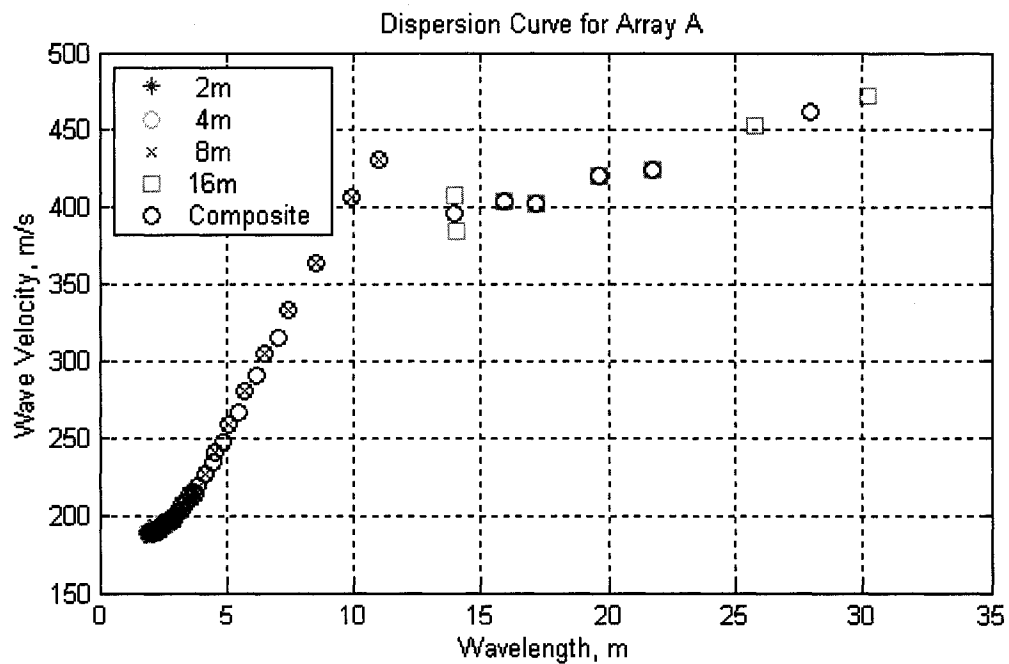
2) Phase plots selected for use

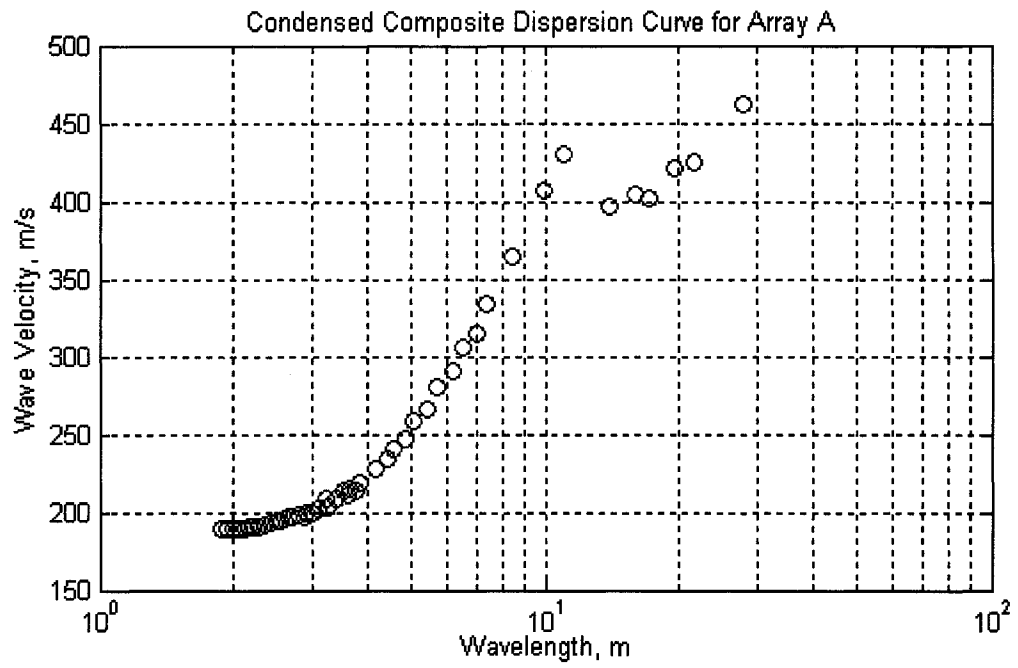






### 3) Dispersion curve

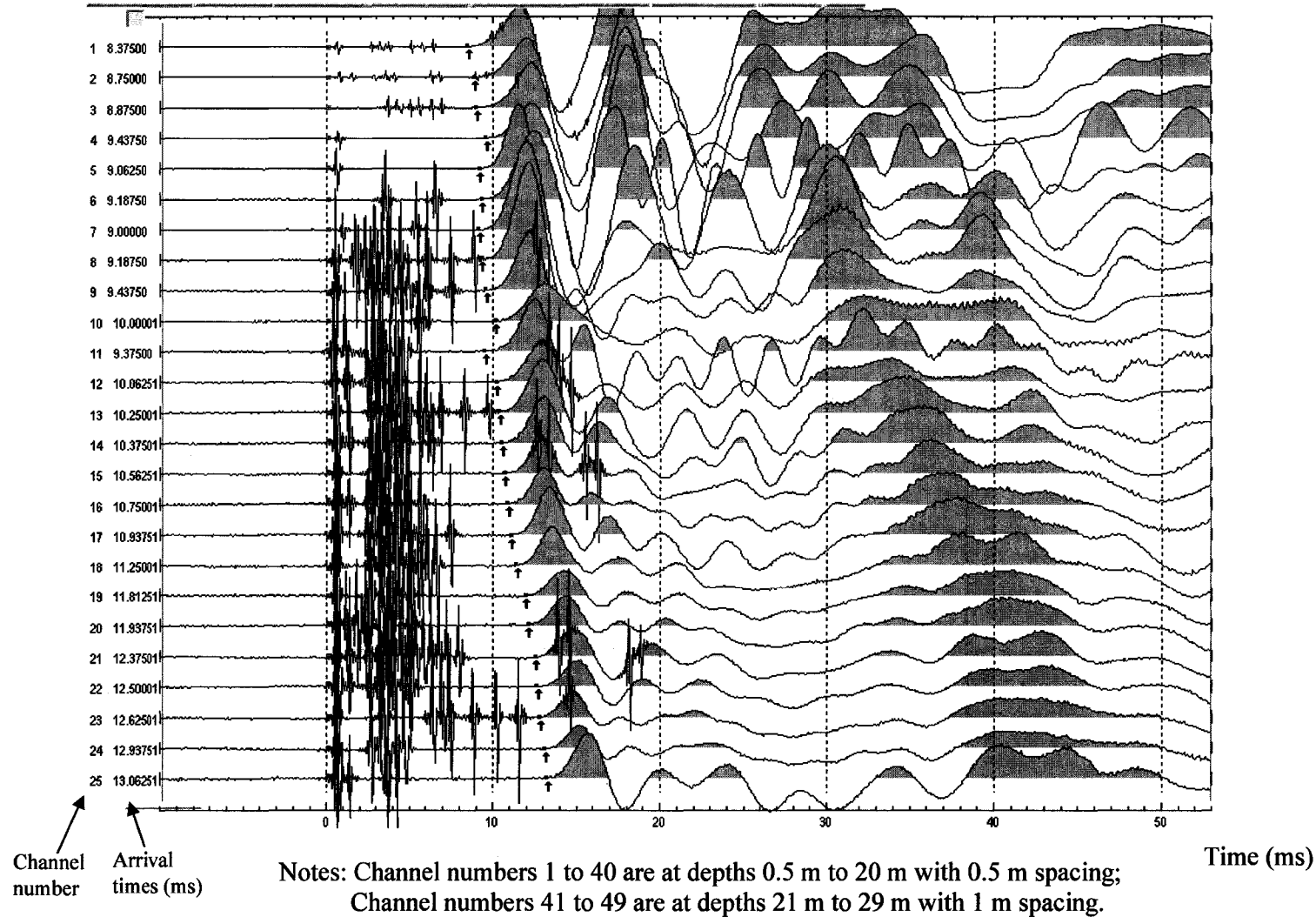


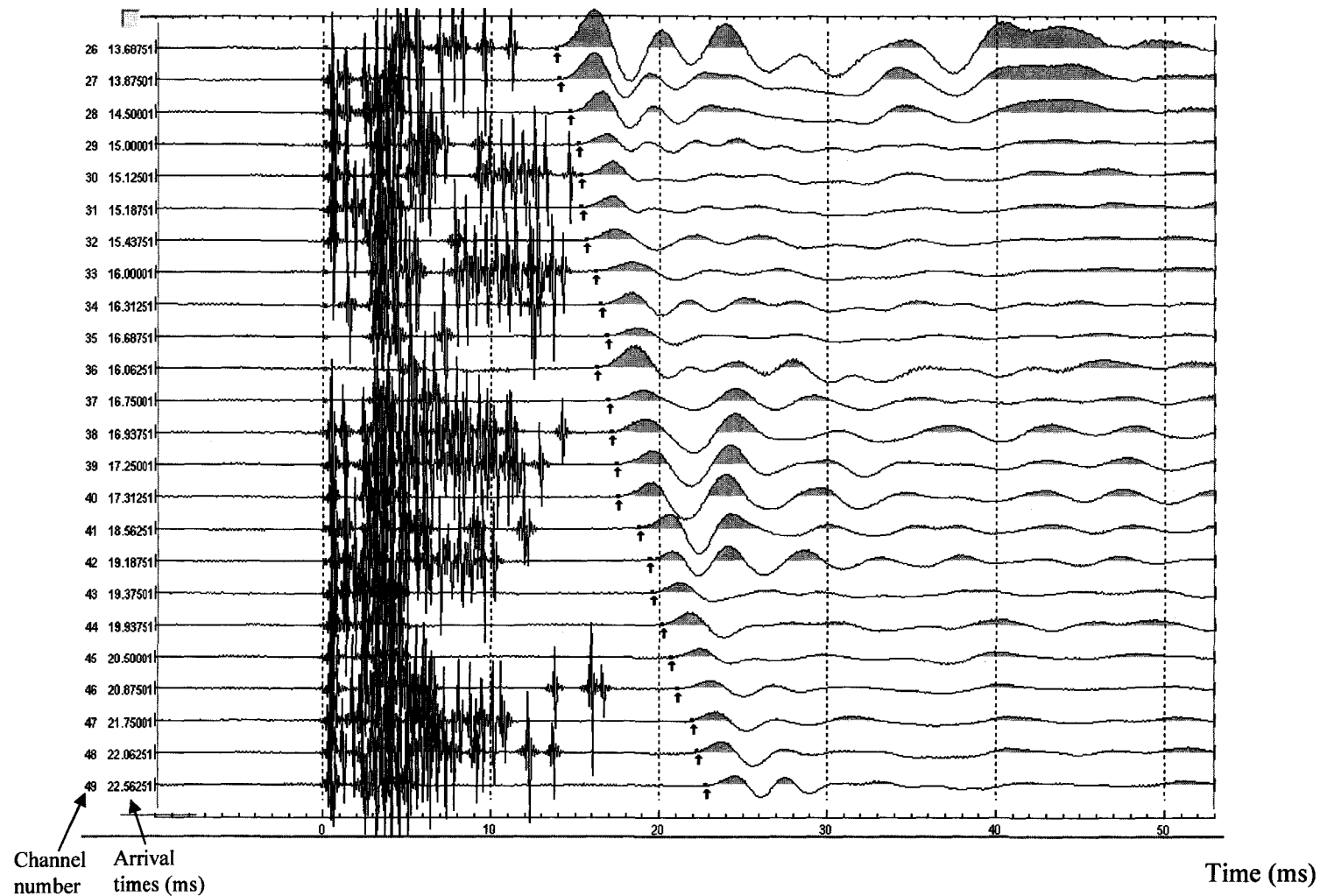


APPENDIX C  
DOWNHOLE MEASUREMENT TIME HISTORIES WITH PICKS



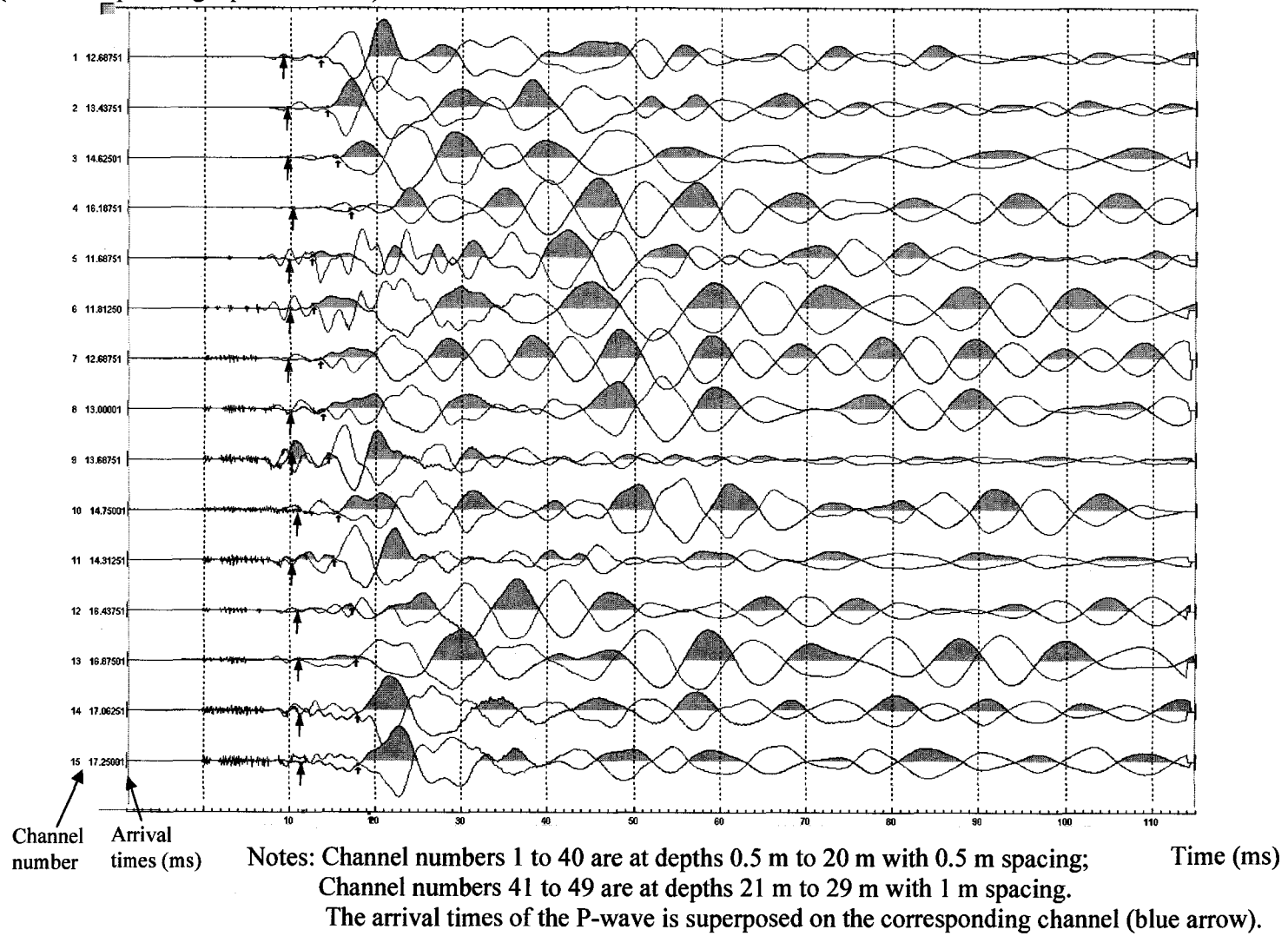
1. P-WAVE

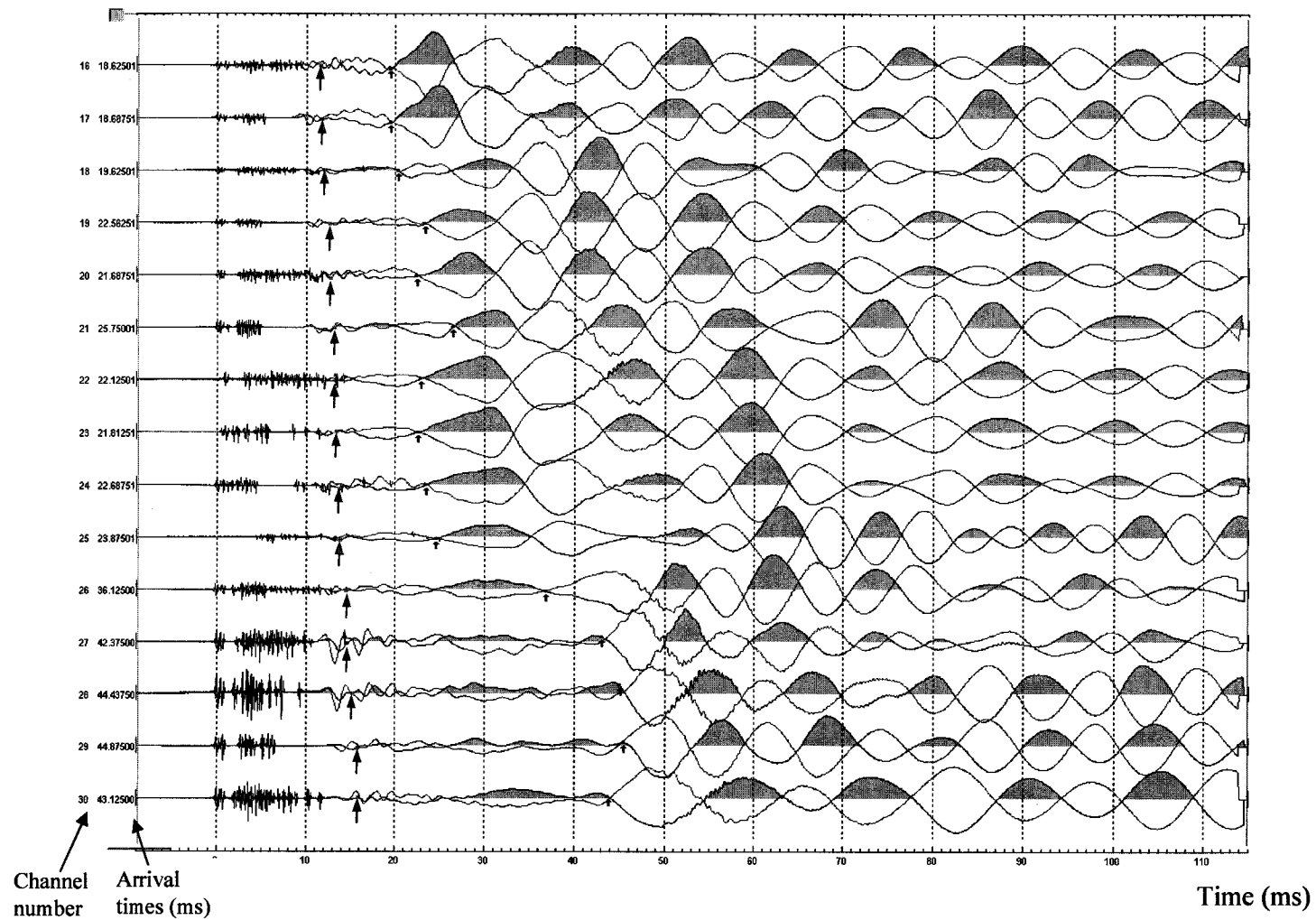




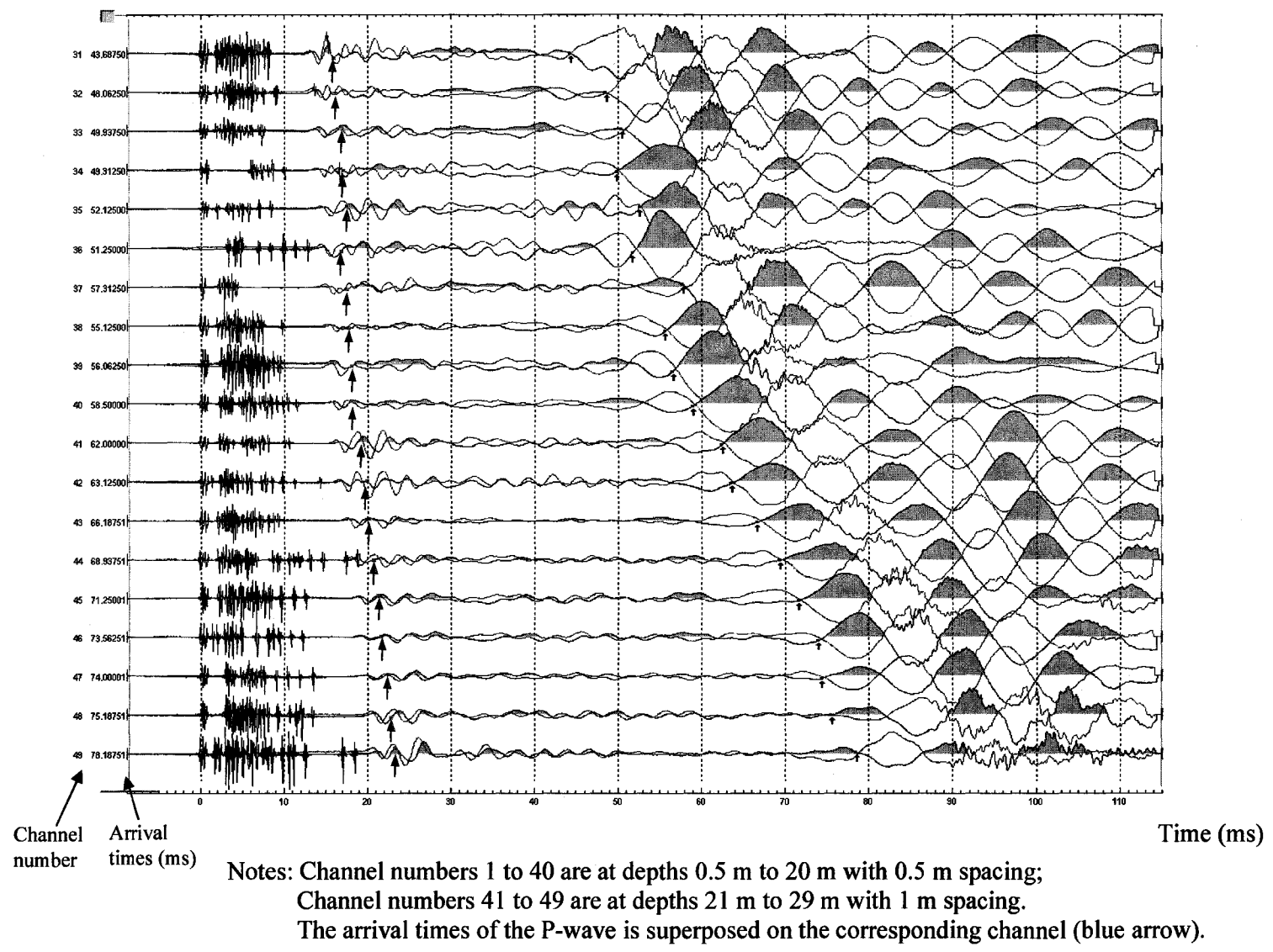
Notes: Channel numbers 1 to 40 are at depths 0.5 m to 20 m with 0.5 m spacing;  
Channel numbers 41 to 49 are at depths 21 m to 29 m with 1 m spacing.

# S-WAVE (radial component geophone is used)



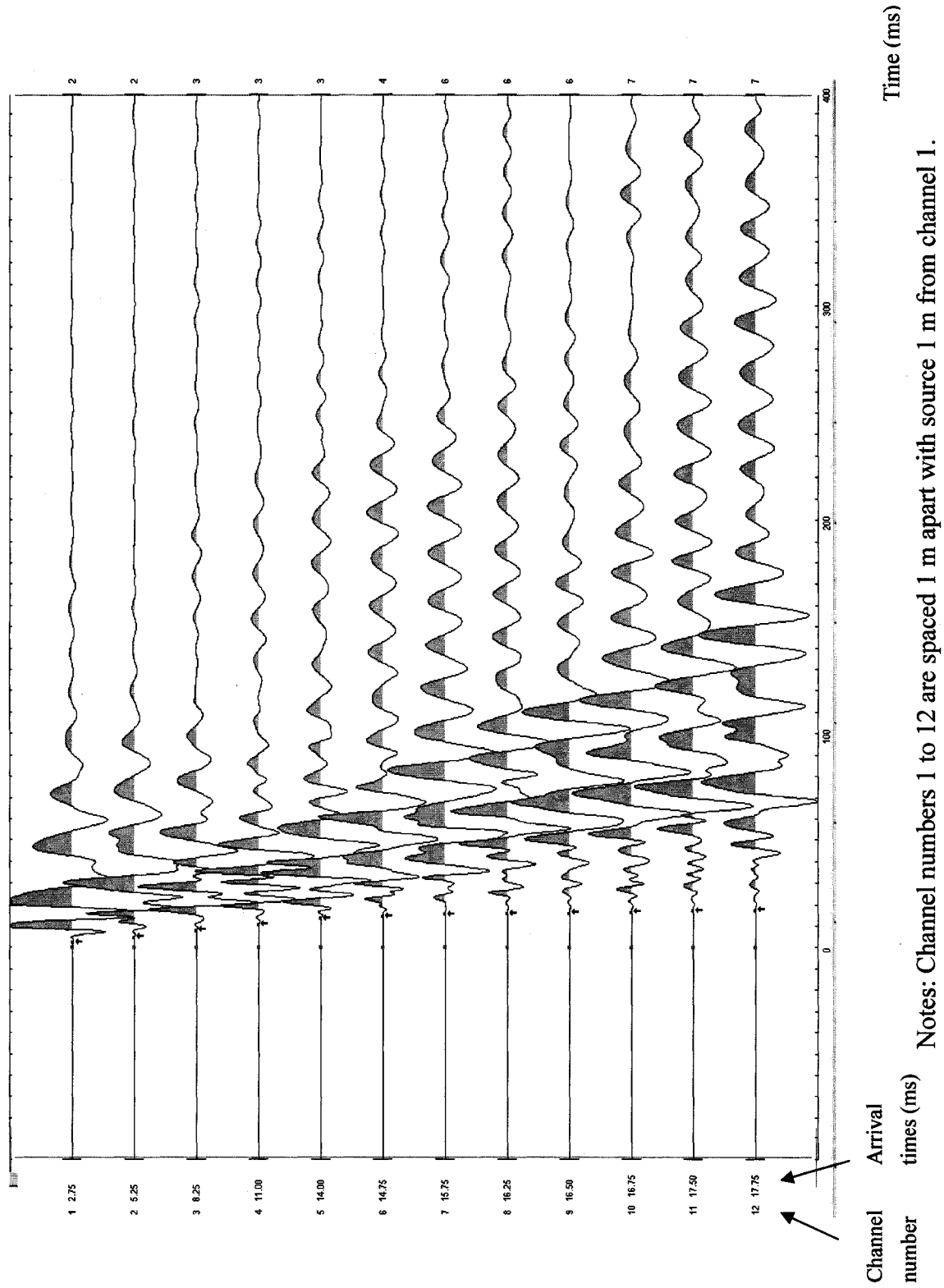


Notes: Channel numbers 1 to 40 are at depths 0.5 m to 20 m with 0.5 m spacing;  
 Channel numbers 41 to 49 are at depths 21 m to 29 m with 1 m spacing.  
 The arrival times of the P-wave is superposed on the corresponding channel (blue arrow).



## APPENDIX D

### P-WAVE REFRACTION DATA WITH PICKS



## REFERENCES

- Aki, K. (1957). "Space and time spectra of stationary stochastic waves, with special reference to microtremors." *Bulletin of the Earthquake Research Institute*, 35, 415-456.
- Aki, K., and Richards, P. G. (1980). *Quantitative Seismology*, Freeman. San Francisco.
- Al-Hunaidi, M. O. (1992). "Difficulties with phase spectrum unwrapping spectral analysis of surface waves nondestructive testing of pavements." *Canadian Geotechnical Journal*, 29, 506-511.
- Al-Hunaidi, M. O. (1993). "Insights on the SASW nondestructive testing method." *Canadian Journal of Civil Engineering*, 20, 940-950.
- Alterman, Z., Karal, F. C. (1968). "Propagation of elastic waves in layered media by finite difference methods." *Bulletin of the Seismological Society of America*, 58, 367-398.
- Areias, L., Van Impe, W. F., and Haegeman, W. (1999). "Variation of shear wave energy with coupling stress in the SCPT method." *European Journal of Environmental and Engineering Geophysics*, 4, 87-95.
- Asten, M. W. and Boore, D. M. (2005). *Blind comparisons of shear-wave velocities at closely spaced sites in San Jose, California*. U. S. Geological Survey open file report 2005-1169. Menlo Park, California.
- Avar, B. B. and Luke, B. (1999). "Roadside application of seismic surface waves over abandoned mines." *Proceedings of the Symposium on the Application of Geophysics to*



- Engineering and Environmental Problems (SAGEEP)*, edited by Powers, M. H., Cramer, L., and Bell, R. S., Environmental and Engineering Geophysical Society, Denver, 31-40.
- Beaty, K. S. (2000). *Determination of Near-Surface Variability Using Rayleigh Waves*. Master's Thesis, University of Alberta.
- Beaty, K. S., Schmitt, D. R., and Sacchi, M. (2002). "Simulated annealing inversion of multi-mode Rayleigh wave dispersion curves for geological structure." *Geophysical Journal International*, 151, 622-631.
- Boore, D. M. (2003). *A compendium of P- and S-wave velocities from surface-to-borehole logging: Summary and reanalysis of previously published data and analysis of unpublished data*. U.S. Geological Survey Open-File Report OFR 03-191.
- Brittle, K. F., Lines, L. R., and Dey, A. K. (2001). "Vibroseis deconvolution: a comparison of cross-correlation and frequency-domain sweep deconvolution." *Geophysical Prospecting*, 49, 675-686.
- Buchen, P. W., and Ben-Hador, R. (1996). "Free-mode surface-wave computations." *Geophysical Journal International*, 124, 869-887.
- Calderón-Macías, C., and Luke, B. (2002). "Inversion of Rayleigh wave data for shallow profiles containing stiff layers." *SEG International Exposition and Seventy-Second Annual Meeting*, Salt Lake City, Utah. CD-ROM Publication, NEG 1.1, 1-4.
- Calderón-Macías, C., and Luke, B. (in press). "Addressing nonuniqueness in inversion of Rayleigh-wave data for shallow profiles containing stiff layers." *Geophysics*.
- Capon, J. (1969). "High-resolution frequency-wavenumber spectrum analysis." *Proceedings of the IEEE*, 57, 1408-1418.

- Corona, A., Marchesi, M., Martini, C., and Ridella, S. (1987). "Minimizing Multimodal Functions of Continuous Variables with Simulated Annealing Algorithm." *ACM Transaction on Mathematical Software*, 12(3), 262-280.
- Coduto, D. P. (1994). *Foundation Design: Principles and Practices*. Prentice-Hall, Inc., Englewood Cliffs, New Jersey.
- Crice, D. (2002). "Borehole shear-wave surveys for engineering site investigations." < <http://www.georadar.com/Shearwaves2.pdf> > (viewed May 1, 2006).
- Dal Moro, G., Forte, E., Pipan, M., and Sukan, M. (2006). "Velocity spectra and seismic-signal identification for surface-wave analysis." *Near Surface Geophysics*, 4(4), 243-251.
- Dobrin, M. B., and Savit, C. H. (1988). *Introduction to Geophysical Prospecting*, Fourth Edition. McGraw-Hill Company, New York.
- Dziewonski, A. M., and Hales, A. L. (1972). "Numerical analysis of dispersed waves." *Methods in Computational Physics*, edited by Bolt, B. A., Academic Press, New York, 11, 39-85.
- Feng, S., Sugiyama, T., and Yamanaka, H. (2005). "Effectiveness of multi-mode surface wave inversion in shallow engineering site investigations." *Exploration Geophysics*, 36, 26-33.
- Foinquinos-Mera, R. (1991). *Analytical study and inversion for the Spectral-Analysis-of-Surface-Waves method*. Master's thesis, University of Texas at Austin.
- Forbriger, T. (2003a). "Inversion of shallow-seismic wavefields: 1. Wavefield transformation." *Geophysical Journal International*, 153, 719-734.

- Forbriger, T. (2003b). "Inversion of shallow-seismic wavefields: 2. Inferring subsurface properties from wavefield transformation." *Geophysical Journal International*, 153, 735-752.
- Foti, S. (2000). *Multistation methods for geotechnical characterization using surface waves*. Ph. D. Dissertation, Politecnico di Torino, Italy.
- Foti, S., and Strobbia C. (2002). "Some notes on model parameters for surface wave data inversion." *Proceedings of the Symposium on the Application of Geophysics to Engineering and Environmental Problems (SAGEEP)*, Environmental and Engineering Geophysical Society, Denver, CD-ROM, 12SEI6.
- Gabriels, P., Snieder, R., and Nolet, G. (1987). "In situ measurements of shear-wave velocity in sediments with higher-mode Rayleigh waves." *Geophysical Prospecting*, 35, 187-196.
- Ganji, V. (1996). *An automated inversion procedure for surface wave testing*. Ph. D. dissertation, Rutgers University, New Brunswick, N. J.
- Ganji, V., and Gucunski, N. (1998). "Automated inversion procedure for Spectral Analysis of Surface Waves." *Journal of Geotechnical and Geoenvironmental Engineering*, 124, 757-770.
- Gazetas, G. (1992). "Evaluation of in situ effective shear modulus from dispersion measurements: Discussion of Paper by C. Vrettos and B. Prange." *Journal of Geotechnical Engineering*, 118, 1120-1122.
- Gile, L. H. (1961). "A Classification of Calcium Horizons in Soils of a Desert Region, Doña Ana County, New Mexico." *Soil Science Society of America Proceedings*, 25, 52-61.

- Gilbert, J. W. (2004). *Shear wave velocity profiling of poorly characterized geologic units in Salt Lake Valley, Utah*. Master's Thesis, Utah State University.
- Gucunski, N., Ganji, V., and Maher, M. H. (1996). "Effects of obstacles on Rayleigh wave dispersion obtained from the SASW test." *Soil Dynamics and Earthquake Engineering*, 15, 223-231.
- Gucunski, N., and Woods, R. D. (1991a). "Inversion of Rayleigh wave dispersion curve for SASW test." *1<sup>st</sup> International Conference on Soil Dynamics and Earthquake Engineering*, Computational Mechanics Publications, Southampton, England, 127-138.
- Gucunski, N., and Woods, R. D. (1991b). "Use of Rayleigh modes in interpretation of SASW test." *Proceedings of the 2<sup>nd</sup> International Conference on Recent Advances in Geotechnical Earthquake Engineering in Soil Dynamics*, edited by Prakash, S, University of Missouri-Rolla, Rolla, Missouri, 1399-1408.
- Gucunski, N., Shokouhi, P. (2005). "Wavelet transforms in surface wave analysis." *Proceedings of the Sessions of the Geo-Frontiers 2005 Congress*, edited by Rathje, E. M., Geotechnical Special Publication 134, American Society of Civil Engineers, Reston, VA.
- Hadidi, R., and Gucunski, N. (2003). "Inversion of SASW dispersion curve using numerical simulation." *Proceedings of the Symposium on the Application of Geophysics to Engineering and Environmental Problems (SAGEEP)*, Environmental and Engineering Geophysical Society, Denver, CD-ROM, 1289-1311.
- Haegeman, W., and Van Impe, W. F. (1997). "Stiffness parameters for soils - SASW experiences." *3<sup>rd</sup> International Geotechnical Engineering Conference*, Cairo, Egypt, 675-698.

- Haskell, N. A. (1953). "The dispersion of surface waves on multilayered media." *Bulletin of the Seismological Society of America*, 43, 17-34.
- Heath, K., Louie, J. N., Biasi, G., Pancha, A. and Pullammanappallil, S. (2006). "Blind tests of refraction microtremor analysis against synthetics and borehole data." < <http://www.seismo.unr.edu/ssa2006/16.pdf> > (viewed November 1, 2006).
- Hiltunen, D. R. (1991). "Nondestructive evaluation of pavement systems by the SASW method." *Geotechnical News*, Bitech Publishers Ltd., Vancouver, B. C., 22-25.
- Hiltunen, D. R., and Gucunski, N. (1994). Annotated Bibliography of SASW method, *Geophysical Characterization of Sites*, edited by Woods, R. D., Oxford & IBH Pub. Co., New Delhi, India, 27-34.
- Hiltunen, D. R., Marosi, K. T. and Gardner, J. M. (2006). "Methodologies to assess SASW shear wave velocity uncertainty." *Proceedings, ASCE Geocongress 2006*, edited by DeGroot, D. J., DeJong, J. T., Frost, J. D. and Baise, L. G., ASCE Press, Reston, VA.
- Hisada, Y. (1994). "An efficient method for computing Green's functions for a layered half-space with sources and receivers at close depths," *Bulletin of the Seismological Society of America*, 84(5), 1456-1472.
- Hossain, M. M., and Drnevich, V. P. (1989). "Numerical and optimization techniques applied to surface waves for back calculation of layer moduli." *Nondestructive testing of pavements and backcalculation of moduli*, ASTM STP 1026, edited by Bush, A. J. and Baladi, G. Y., American Society For Testing and Mat. Philadelphia, 649-669.
- Huynh, M., Luke, B., and Calderón-Macías, C., (2003). "Fine-tuning the inversion of seismic surface wave data sets to resolve stiff layers." *Proceedings, 38<sup>th</sup> Symposium on*

- Engineering Geology and Geotechnical Engineering*, edited by Elfass, S., Norris, G., and Watters, R., Idaho State University, Pocatello, 233-251.
- International Building Code, (2003). International Code Council.
- Ivanov, J. (2002). *JASR-Joint Analysis of Surface-Waves and Refractions*. Ph. D. Dissertation, University of Kansas.
- Ivanov, J., Park, C. B., Miller, R. D., and Xia, J. (2000a). "Joint analysis of surface-wave and refraction events from river-bottom sediments." *Soc. Explor. Geoph. Expanded Abstract*, 1307-1310.
- Ivanov, J., Park, C. B., Miller, R. D., and Xia, J. (2000b). "Mapping Poisson's ratio of unconsolidated materials from a joint analysis of surface-wave and refraction events." *Proceedings of the Symposium on the Application of Geophysics to Engineering and Environmental Problems (SAGEEP)*, edited by Powers, M. H., Ibrahim, A. B., and Cramer, L., Environmental and Engineering Geophysical Society, Denver, 11-19.
- Jin, X., Tecle, M., Luke B., Fossett, E., and Taylor, W. (2003). "Shear wave velocity profiling for fault investigation by SASW method," *Proceedings, 38<sup>th</sup> Symposium on Engineering Geology and Geotechnical Engineering*, edited by Elfass, S., Norris, G., and Watters, R., Idaho State University, Pocatello, 319-333.
- Jin, X., Luke, B., Louie, J. (2006). "Comparison of Rayleigh wave dispersion relations from three surface wave measurements in a complex-layered system." *Proceedings, ASCE Geocongress 2006*, edited by DeGroot, D. J., DeJong, J. T., Frost, J. D. and Baise, L. G., ASCE Press, Reston, VA.
- Jin, X., Luke, B. (2006). "Comparison of three surface wave measurements and a seismic downhole measurement in a complex-layered system." *Site and geomaterial*

- characterization: American Society of Civil Engineers, Geotechnical Special Publication 149, edited by Puppala, A., Fratta, D., Alshibli, K., and Pamukcu, S., 212-219.*
- Joh, S. H. (1996). *Advances in interpretation and analysis techniques for spectral-analysis-of-surface-waves (SASW) measurements*. Ph. D. dissertation, University of Texas at Austin.
- Joh, S.-H., Rosenblad, B. L., and Stokoe, K. H. (1997). "Improved data interpretation method for SASW tests at complex geotechnical sites." *Proceedings, 7<sup>th</sup> International Offshore and Polar Engineering Conference*, International Society of Offshore and Polar Engineers (ISOPE), Golden, CO, 1, 875-881.
- Joh, S.-H., Stokoe, K. H., II, Lee, W., Kang, T. H., Rosenblad, B., and Bay, J. (2006). "Joint inversion for apparent phase velocities of Rayleigh and Love waves." *Proceedings, ASCE Geot congress 2006*, edited by DeGroot, D. J., DeJong, J. T., Frost, J. D. and Baise, L. G., ASCE Press, Reston, VA.
- Kalinski, M. E., Stokoe, K. H., II, Jirsa, J. O. and Roësset, J. M. (1994). "Nondestructive identification of internally damaged areas of concrete beam using the SASW method." *Transportation Research Record*, 1458, 14-19.
- Kausel, E., and Roësset, J. M. (1981). "Stiffness Matrices for Layered Soils." *Bulletin of the Seismological Society of America*, 71, 1743-1761.
- Kim, D. S., Bang, E. S. and Kim, W. C. (2004). "Evaluation of various downhole data reduction methods for obtaining reliable VS profile." *Geotechnical Testing Journal*, 27 (6), 1-13.

- Lai, C. G. (1998). *Simultaneous Inversion of Rayleigh Phase Velocity and Attenuation for Near-Surface Site Characterization*. Ph. D Dissertation, Georgia Institute of Technology, Atlanta.
- Lai, C. G., Rix, G. J., Foti, S., and Roma, V. (2002). "Simultaneous measurement and inversion of surface wave dispersion and attenuation curves." *Soil Dynamics and Earthquake Engineering*, 22, 923-930.
- Lancaster, P., and Šalkauskas, K. (1986). *Curve and surface fitting: an introduction*. Academic Press Inc., London.
- Larsen, S. C., and Schultz, C. A. (1995). "ELAS3D: 2D/3D elastic finite-difference wave propagation code." *Lawrence Livermore National Laboratory Report*, UCRL-MA-121792.
- Larsen, S., and Grieger J. (1998). "Elastic modeling initiative, Part III: 3-D computational modeling." *Soc. Explor. Geoph. Expanded Abstract*, 1803-1806.
- Lee, B. (1996). *Analytical Studies of Surface Wave Propagation along the Seafloor for Application to Spectral-Analysis-of-Surface-Waves (SASW) Testing*, Ph. D Dissertation. The University of Texas at Austin, Texas.
- Levander, A. R. (1988). "Fourth-order finite-difference P-SV seismograms." *Geophysics*, 53, 1425-1436.
- Liu, H., Luke, B., and Calderón-Macías, C. (2002). "A scheme to generate starting models for interpretation of shallow surface wave data." *Proceedings, Symposium on the Application of Geophysics to Engineering and Environmental Problems (SAGEEP)*. Environmental and Engineering Geophysical Society, Denver, CD-ROM, 12SEI4.



- Liu, H. (2002). *Improving Resolution of Stiff Layers in Soil Profiles Through Multi-step Inversion of SASW Data*. Master's Thesis. The University of Nevada Las Vegas.
- Liu, H. P., Boore, D. M., Joyner, W. B., Oppenheimer, D. H., Warrick, R. E., Zhang, W., Hamilton, J. C., and Brown L. T. (2000). "Comparison of phase velocities from array measurements of Rayleigh waves associated with microtremors and results calculated from borehole shear-wave velocity profiles." *Bulletin of the Seismological Society of America*, 90. 666-678.
- Liu, Y., Luke, B., Pullammanappallil, S., Louie, J., and Bay, J. (2005). "Combining active- and passive source measurements to profile shear wave velocities for seismic microzonation." *Earthquake Engineering and Soil Dynamics*, edited by Boulanger, R. W., Dewwolkar, M., Gucunski, N., Juang, C., Kalinski, M., Kramer, S., Manzari M., and Pauschke, J., Geotechnical Special Publication 133, American Society of Civil Engineers, Reston, VA, 977-990.
- Liu, Y. (2006). *Site response projections and earthquake microzonation for the Las Vegas Basin*. Ph. D Dissertation. The University of Nevada Las Vegas.
- Long, L. T., Kocaoglu, A. H., and Martin, J. (2000). "Shallow S-wave structure can be interpreted from surface-wave group-velocity tomography." *Proceedings, Symposium on the Application of Geophysics to Engineering and Environmental Problems (SAGEEP)*, edited by Powers, M. H., Ibrahim, A., B., and Cramer, L., Environmental and Engineering Geophysical Society, Denver, 39-46.
- Long, L.T., Kocaoglu, A. H., Doll, W. E., Chen, X. Q., and Martin, J. (1999). "Surface-wave group-velocity tomography for shallow structures at a waste site." *Soc. Explor. Geoph. Expanded Abstract*, Annual Meeting, Houston.

- Long, L. T., and Kocaoglu, A. H. (2001). "Surface-wave group-velocity tomography for shallow structures." *Journal of Environmental and Engineering Geophysics*, 6, 71-81.
- Louie, J. (2001). "Faster, better: shear-wave velocity to 100 meters depth from refraction microtremor arrays." *Bulletin of the Seismological Society of America*, 91(2), 347-364.
- Luke, B., Calderón-Macías, C., Stone, R. C., and Huynh, M. (2003a). "Non-uniqueness in inversion of seismic surface-wave data." *Proceedings, Symposium on the Application of Geophysics to Engineering and Environmental Problems (SAGEEP)*, Environmental and Engineering Geophysical Society, Denver, CD-ROM, 1342-1347.
- Luke, B., Calderón-Macías, C., and Huynh, M. (2003b). "Inverting surface wave data from a site containing cemented inclusions." *Proceedings, Soil and Rock America 2003*, edited by Culligan, P. J., Einstein, H. H., and Whittle, A. J., Verlag Glückauf GmbH, Essen, Germany, 157-162.
- Luke, B., and Calderón-Macías, C. (in press). "Inversion of seismic surface wave data to resolve complex profiles." *Journal of Geotechnical and Geoenvironmental Engineering*.
- Luke, B., Lipinska-Kalita, K., Calderón-Macías, C. and Jin, X. (2006). "Interpreting complex layered systems by constrained optimization of surface wave data." *Proceedings, 8<sup>th</sup> SEGJ International Symposium on Imaging and Interpretation*, edited by Mikada, H., Society of Exploration Geophysicists of Japan, Tokyo, 615-620.
- Luke, B., and Stokoe, K. H., II (1998). "Application of the SASW Method Underwater." *Journal of Geotechnical and Geoenvironmental Engineering*, ASCE, 124(6), 523-531.
- Luke, B., Tsarev, G. (2000). "Detection of buried drums using seismic surface waves -- Toward a rapid-screening approach." *Proceedings, 35<sup>th</sup> Symposium on Engineering*

- Geology and Geotechnical Engineering*, edited by Robinson, L., Idaho State University, Pocatello, Idaho, 210-220.
- Martinez, M. D., Lana, X., Olarte, J., Badal, J., and Canas, J. A. (2000). "Inversion of Rayleigh wave phase and group velocities by simulated annealing." *Physics of the Earth and Planetary Interiors*, 122, 3-17.
- McMechan, G. A., and Yedlin, M. J. (1981). "Analysis of dispersive waves by wave field transformation." *Geophysics*, 46, 869-874.
- Menke, W. (1989). *Geophysical data analysis: Discrete inverse theory*, Acad. Press, San Diego.
- Mussett, A. E., Khan, M. A. (2000). *Looking into the Earth: An Introduction to Geological Geophysics*. Cambridge University Press.
- Nasseri-Moghaddam, A., Cascante, G., and Hutchinson, J. (2005). "A new quantitative procedure to determine the location and embedment depth of a void using surface waves." *Journal of Environmental and Engineering Geophysics*, 10, 51-64.
- Nazarian, S., and Desai, M. R. (1993). "Automated surface wave method: field testing." *Journal of Geotechnical Engineering*, ASCE, 119(7), 1094-1111.
- Nolet, G. (1981). "Linearized inversion of (teleseismic) data." *The solution of the inverse problem in geophysical interpretation*, edited by Cassinis, R., Plenum Press, New York, 9-37.
- Nowatzki, E. A., and Almasmoum, A. A. (1988). "A method for estimating the excavatability of caliche." *Geotechnical Testing Journal*, 11 (2), 148-154.
- Okada, H. (2003). *The Microseismic Survey Method*. Geophysical monograph series, Number 12, Society of Exploration Geophysicists, Tulsa, OK.

- O'Neill, A. (2003). *Full-waveform reflectivity for modeling, inversion and appraisal of seismic surface wave dispersion in shallow site investigations*. Ph. D. Dissertation. University of Western Australia.
- O'Neill, A. (2004a). "Shear velocity model appraisal in shallow surface wave inversion." *Proceedings, Symposium on the Application of Geophysics to Engineering and Environmental Problems (SAGEEP)*, Environmental and Engineering Geophysical Society, Denver, CD-ROM, 1544-1555.
- O'Neill, A. (2004b). "Full-waveform reflectivity for inversion of surface wave dispersion in shallow site investigations." *Proceedings, Symposium on the Application of Geophysics to Engineering and Environmental Problems (SAGEEP)*, Environmental and Engineering Geophysical Society, Denver, CD-ROM, 1565-1576.
- O'Neill, A. (2005). "Seismic surface waves special issue guest editorial." *Journal of Environmental and Engineering Geophysics*, 10 (2), 67-86.
- Park, C. B., Miller, R. D., and Xia, J. (1998a). "Imaging dispersion curves of surface waves on multichannel record." *Soc. Explor. Geoph. Expanded Abstract*, 1377-1380.
- Park, C. B., Miller, R. D., and Xia, J. (1998b). "Ground roll as a tool to image near-surface anomaly." *Soc. Explor. Geoph. Expanded Abstract*, 874-877.
- Park, C. B., Miller, R. D., and Xia, J. (1999a). "Detection of near-surface voids using surface waves." *Proceedings of the Symposium on the Application of Geophysics to Engineering and Environmental Problems (SAGEEP)*, edited by Powers, M. H., Cramer, L., and Bell, R. S., Environmental and Engineering Geophysical Society, Denver, 281-286.

- Park, C. B., Miller, R. D., and Xia, J. (1999b). "Multichannel analysis of surface waves (MASW)." *Geophysics*, 64, 800-808.
- Park, C.B., Miller, R. D. and Xia, J. (2000). "Detection of higher mode surface waves over unconsolidated sediments by the MASW method." *Proceedings of the Symposium on the Application of Geophysics to Engineering and Environmental Problems (SAGEEP)*, edited by Powers, M. H., Ibrahim, A., B., and Cramer, L., Environmental and Engineering Geophysical Society, Denver, 1-9.
- Park, C.B., Ivanov, J., Miller, R.D., Xia, J. (2001a). "Offset and resolution of dispersion curve in multichannel analysis of surface waves (MASW)." *Proceedings of the Symposium on the Application of Geophysics to Engineering and Environmental Problems (SAGEEP)*, Environmental and Engineering Geophysical Society, Denver, CD-ROM, SSM-4.
- Park, C.B., Ivanov, J., Miller, R.D., Xia, J., and Rydén, N. (2001b). "Seismic investigation of pavements by MASW method-geophone approach." *Proceedings of the Symposium on the Application of Geophysics to Engineering and Environmental Problems (SAGEEP)*, Environmental and Engineering Geophysical Society, Denver, CD-ROM, RBA-6.
- Park, C.B., Rydén, N., Miller, R.D., and Ulriksen, P. (2002). "Time break correction in multichannel simulation with one receiver (MSOR)." *Proceedings of the Symposium on the Application of Geophysics to Engineering and Environmental Problems (SAGEEP)*, Environmental and Engineering Geophysical Society, Denver, CD-ROM, 12SEI3.

- Phillips, C., Cascante, G., and Hutchinson, J. (2004). "Evaluation of horizontal homogeneity of geomaterials with the distance analysis of surface waves." *Canadian Geotechnical Journal*, 41, 212-226.
- Phillips, C., Moghaddam, A. N., Moore, T., Cascante, G., and Hutchinson, J. (2003). "A simple automated method of SASW analysis using multiple receivers." *Proceedings of the Symposium on the Application of Geophysics to Engineering and Environmental Problems (SAGEEP)*, Environmental and Engineering Geophysical Society, Denver, CD-ROM, 1328-1347.
- Reeves, C. C. (1976). *Caliche: origin, classification morphology and uses*. Estacado Books, Lubbock, Texas.
- Richart, F. E., Hall, J. R., and Woods, R. D. (1970). *Vibrations of Soils and Foundations*, Prentice Hall, Englewood Cliffs.
- Rix, G. J., Lai, C. G., and Foti, S. (2001). "Simultaneous measurement of surface wave dispersion and attenuation curves." *Geotechnical Testing Journal*, 24, 350-358.
- Roberts, J. C., and Asten, M. W. (2004). "Resolving a velocity inversion at the geotechnical scale using the microtremor (passive seismic) survey method." *Exploration Geophysics*, 35, 14-18.
- Roësset, J. M., Chang, D. W., and Stokoe, K. H., II. (1991). "Comparison of 2-D and 3-D models for analysis of surface wave tests." *Proceedings, 1<sup>st</sup> International Conference on Soil Dynamics and Earthquake Engineering*, Computational Mechanics Publications, Southampton, England, 112-126.
- Rydén, N., Ulriksen, P., Park, C. B., Miller, R. D., Xia, J., and Ivanov, J. (2001). "High frequency MASW for non-destructive testing of pavements-accelerometer approach."

- Proceedings of the Symposium on the Application of Geophysics to Engineering and Environmental Problems (SAGEEP)*, Environmental and Engineering Geophysical Society, Denver, CD-ROM, RBA-5.
- Rydén, N., Park, C. B., Ulriksen, P., and Miller, R. D. (2002a). "Branching of dispersion curves in surface wave testing of pavement." *Proceedings of the Symposium on the Application of Geophysics to Engineering and Environmental Problems (SAGEEP)*, Environmental and Engineering Geophysical Society, Denver, CD-ROM, 12SEI7.
- Rydén, N., Ulriksen, P., Park, C. B., and Miller, R. D. (2002b). "Portable seismic acquisition system (PSAS) for pavement MASW." *Proceedings of the Symposium on the Application of Geophysics to Engineering and Environmental Problems (SAGEEP)*, Environmental and Engineering Geophysical Society, Denver, CD-ROM, 13 IDA7.
- Rydén, N. (2004). *Surface wave testing of pavements*. Ph. D Dissertation, Lund University, Lund, Sweden.
- Safari, J., O'Neill, A., Matsuoka, T., and Sanada, Y. (2005). "Applications of Love wave dispersion for improved shear-wave velocity imaging." *Journal of Environmental and Engineering Geophysics*, 10(2), 135-150.
- Schmidt, H., (1999). *OASES version 2.2 user guide and reference manual*.  
<<http://acoustics.mit.edu/faculty/henrik/oases/oases.html>> (viewed November 22, 2006)
- Sen, M., and Stoffa, P. L. (1995). *Global optimization methods in geophysical inversion*. Elsevier, Amsterdam.

- Sedighi-Manesh M. (1991). *Theoretical Investigation of the Spectral Analysis of Surface Waves (SASW) Technique for Application Offshore*. Ph. D Dissertation, University of Texas at Austin.
- Sharma, P.V. (1997). *Environmental and Engineering Geophysics*. Cambridge University Press: New York.
- Sheriff, R. E. (2002). *Encyclopedic Dictionary of Applied Geophysics*, Fourth Edition. Society of Exploration Geophysicists, Tulsa, Oklahoma.
- Stephenson, W. J., Louie, J. N., Pullammanappallil, S., Williams, R. A., and Odum, J. K. (2005). "Blind shear-wave velocity comparison of ReMi and MASW results with boreholes to 200 m in Santa Clara Valley: Implications for earthquake ground motion assessment." *Bulletin of the Seismological Society of America*. 95, 2506-2516.
- Stokoe, K. H., II, and Nazarian, S. (1983). "Effectiveness of ground improvement from Spectral Analysis of Surface Waves." *Improvement of Ground: Proceedings of the 8th European Conference on Soil Mechanics and Foundation Engineering*, A. A. Balkema, Rotterdam, Netherlands, 91-94.
- Stokoe, K. H., II, and Nazarian, S. (1985). "Use of Rayleigh waves in liquefaction studies." *Proceedings, Measurement and Use of Shear Wave Velocity for Evaluating Dynamic Soil Properties*, edited by Woods, R. D., ASCE, Geotechnical Engineering Division, 1-17.
- Stokoe, K. H., II, and Santamarina, J. C. (2000). "Seismic wave based testing in geotechnical engineering." *International Conference on Geotechnical and Geological Engineering, GeoEng2000*, Melbourne, Australia, 1490-1536.



- Stokoe, K. H., II, Wright, S. G., Bay, J. A., and Roësset, J. M. (1994). "Characterization of geotechnical sites by SASW method." *Geophysical Characterization of Sites*, edited by Woods, R. D., Oxford & IBH Pub. Co., New Delhi, India, 15-25.
- Stoll, R. D., Bryan, G. M., and Bautista, E. O. (1994). "Measuring lateral variability of sediment geoacoustic properties." *Journal of the Acoustical Society of America* 96(1), 427-438.
- Stone, R. C., and Luke, B., (2001). "An overview of engineering with cemented soils in Las Vegas." *Proceedings, 36<sup>th</sup> Symposium on Engineering Geology and Geotechnical Engineering*, edited by Luke, B., Jacobson, E., and Werle, J., Idaho State University, Pocatello, 135-144.
- Suzuki, H., and Hayashi, K. (2003). "Shallow S-wave velocity sounding using the microtremors array measurements and the surface wave method." *Proceedings of the Symposium on the Application of Geophysics to Engineering and Environmental Problems (SAGEEP)*, Environmental and Engineering Geophysical Society, Denver, CD-ROM, 1371-1376.
- Suzuki, H., and Takahashi, T. (2002). "Deep S-wave velocity sounding by the microtremors array measurements at Tsukuba city in Japan." *Proceedings of the Symposium on the Application of Geophysics to Engineering and Environmental Problems (SAGEEP)*, Environmental and Engineering Geophysical Society, Denver, CD-ROM.
- Tecle, M. T., Giorgis, A. Y. and Luke, B. (2003). "Comparison of Seismic Downhole to Crosshole Measurements in a Complex-Layered System." *Proceedings, 38<sup>th</sup>*

- Symposium on Engineering Geology and Geotechnical Engineering*, edited by Elfass, S., Norris, G., and Watters, R., Idaho State University, Pocatello, 217-232.
- Tokimatsu, K. (1995). "Geotechnical site characterization using surface waves." *Proceedings, 1st International Conference on Earthquake Geotechnical Engineering, IS-Tokyo '95*, Balkema, Rotterdam, 1333-1368.
- Tokimatsu, K., Miyadera, Y., and Kuwayama, S. (1992a). "Determination of shear wave velocity structures from spectrum analyses of short-period microtremors." *Proceedings, 10<sup>th</sup> World Conference on Earthquake Engineering*, 253-258.
- Tokimatsu, K., Shinzawa, K., and Kuwayama, S. (1992b). "Use of short-period microtremors for Vs profiling." *Journal of Geotechnical Engineering*, ASCE, 118(10), 1544-1558.
- Tokimatsu, K., Tamura, S., and Kojima, H. (1992c). "Effects of multiple modes on Rayleigh wave dispersion characteristics." *Journal of Geotechnical Engineering*, ASCE, 118(10), 1529-1543.
- Tsarev, G. (2003). *Rapid screening approach for cavity detection using surface-based seismic measurements*. Master's Thesis. University of Nevada Las Vegas.
- Tselentis, G. A., and Delis, G. (1998). "Rapid assessment of S-wave profiles from the inversion of multichannel surface wave dispersion data." *Annali Di Geofisica*, 41, 1-15.
- Turner, G. (1990). "Aliasing in the tau-p transform and the removal of spatially aliased coherent noise." *Geophysics*, 55, 1496-1503.
- Wathelet, M. (2005). *Array recordings of ambient vibrations: surface-wave inversion*. Ph. D. dissertation, University of Liège, Belgium.

- Wyman, R. V., Karakouzian, M., Valentine, V. B., Slemmons, D. B., Peterson, L., and Palmer, S. (1993). "Geology of Las Vegas, Nevada, United States of America." *Bulletin of the Association of Engineering Geologists*, 30 (1), 33-78.
- Williams, T. P., and Gucunski, N. (1995). "Neural networks for backcalculation of moduli from SASW test." *Journal of Computing in Civil Engineering*, ASCE, 9 (1), 1-8.
- Van Wijk, K. (2003). *Multiple scattering of surface waves*. Ph. D. dissertation, Colorado School of Mines.
- Xia, J., Miller, R. D., and Park, C. B. (1999). "Estimation of near-surface shear-wave velocity by inversion of Rayleigh waves." *Geophysics*, 64, 691-700.
- Xia, J., Miller, R. D., and Park, C. B. (2000). "Advantages of calculating shear-wave velocity from surface waves with higher modes." *SEG 70<sup>th</sup> international meeting, expanded abstracts*, 1295-1298.
- Xia, J., Miller, R. D., Park, C. B., and Tian, G. (2003). "Inversion of high frequency surface waves with fundamental and higher modes." *Journal of Applied Geophysics*, 52, 45-57.
- Xia, J., Xu, Y., Miller, R. D., and Chen, C. (2006). "New developments in analysis of high-frequency Rayleigh waves." *Proceedings of the 2<sup>nd</sup> International Conference on Environmental and Engineering Geophysics*, edited by Xu, Y., Xia, J., and Chen, C., Science Press, Monmouth Junction, NJ, 1, 10-18.
- Yoon, S., and Rix, G. J. (2004). "Combined active-passive surface wave measurements for near-surface site characterization." *Proceedings of the Symposium on the*

- Application of Geophysics to Engineering and Environmental Problems (SAGEEP)*, Environmental and Engineering Geophysical Society, Denver, CD-ROM, 1556-1564.
- Zerwer, A., Cascante, G., and Hutchinson, J. (2002). "Parameter Estimation in Finite Element Simulations of Rayleigh Waves." *Journal of Geotechnical and Geoenvironmental Engineering*, 128 (3), 250-261.
- Zhang, S., X., and Chan, L. S. (2003). "Possible effects of misidentified mode number on Rayleigh wave inversion." *Journal of Applied Geophysics* (53). 17-29.
- Zywicki, D. J. (1999). *Advanced signal proceeding methods applied to engineering analysis of seismic surface waves*. Ph.D. Dissertation, Georgia Institute of Technology.
- Zywicki, D. J., and Rix, G. J. (1999). "Frequency-wavenumber analysis of passive surface waves." *Proceedings of the Symposium on the Application of Geophysics to Engineering and Environmental Problems (SAGEEP)*, edited by Powers, M. H., Cramer, L., and Bell, R. S., Environmental and Engineering Geophysical Society, Denver, 75-84.

## VITA

Graduate College  
University of Nevada, Las Vegas

Xiaohui Jin

### Home Address:

1600 E University Ave. # 220, Las Vegas, NV, 89119

### Degrees:

Bachelor of Engineering, Structural Engineering, 1997  
Tian Jin University, China

Master of Engineering, Geotechnical Engineering, 2002  
Tian Jin University, China

Dissertation Title: DELINEATING ANOMALOUS LAYERS IN SOIL PROFILES  
USING SEISMIC SURFACE WAVE METHODS

### Dissertation Examination Committee:

Chair, Barbara Luke, Ph. D., P. E.  
Committee Member, Catherine Snelson, Ph.D.  
Committee Member, Carlos Calderon-Macias, Ph.D.  
Committee Member, Jacimaria Batista, Ph.D.  
Graduate Faculty Representative, Wanda Taylor, Ph. D.